In Situ 3D Electron Diffraction to Investigate Redox Reactions of Perovskite-Based Energy Materials

Daphne Vandemeulebroucke

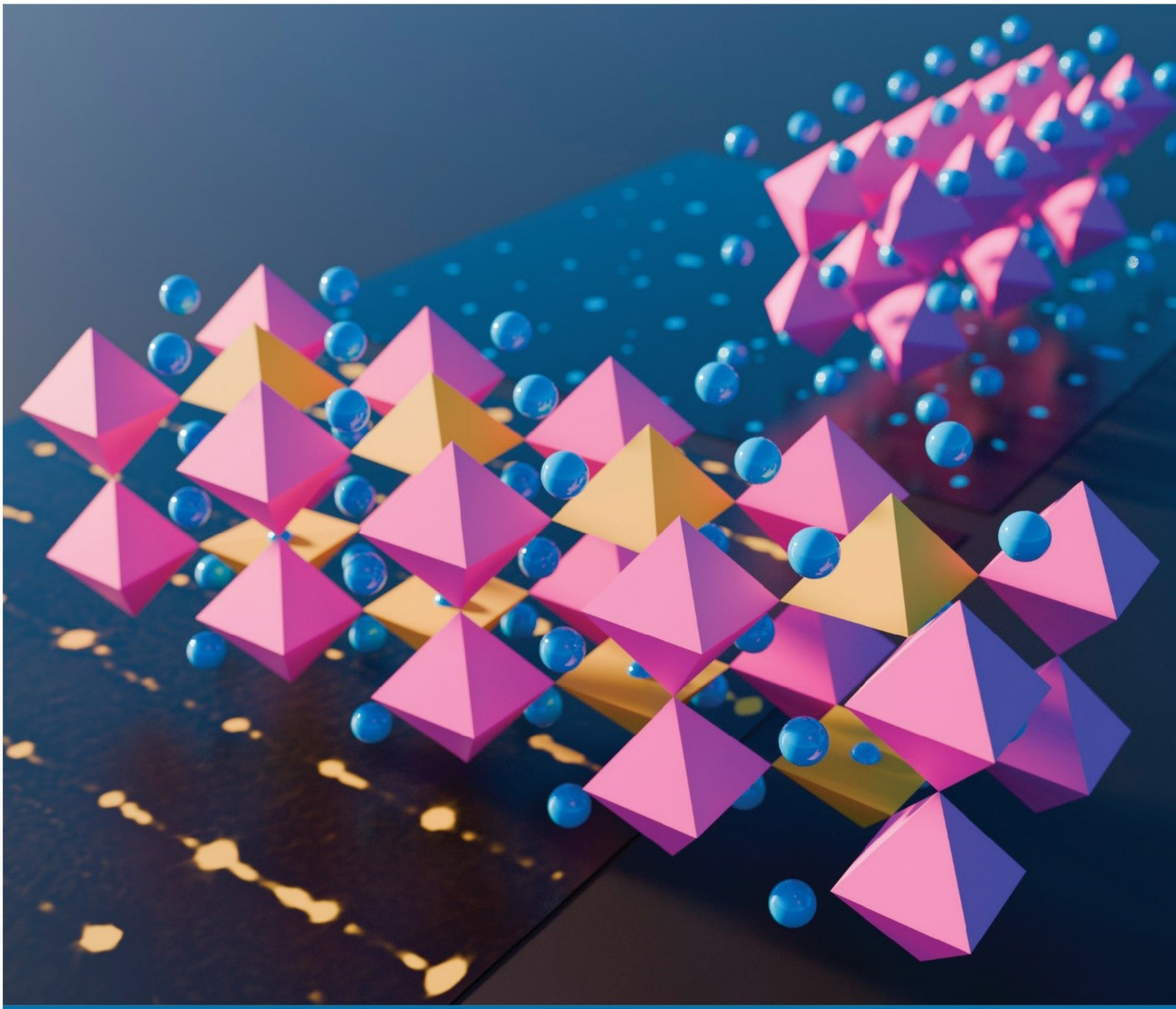

Supervisor **Prof. Dr. Joke Hadermann**

Thesis submitted for the degree of Doctor of Science: Physics
Faculty of Science | Antwerp, 2024

University
of Antwerp

University of Antwerp

Faculty of Science

In Situ 3D Electron Diffraction to Investigate Redox Reactions of Perovskite-Based Energy Materials

Thesis submitted in fulfilment of the requirements for the degree of
doctor in Physics
at the University of Antwerp

Daphne Vandemeulebroucke

Supervisor
Prof. Dr. Joke Hadermann

Antwerpen, 2024

Jury

Prof. Dr. Jan De Beenhouwer, University of Antwerp, Belgium

Supervisor
Prof. Dr. Joke Hadermann, University of Antwerp, Belgium

Members
Prof. Dr. Dirk Lamoen, University of Antwerp, Belgium
Dr. Pascal Roussel, UCCS, University of Lille, France
Dr. Philippe Boullay, CRISMAT, ENSICAEN, Caen, France

Contact
Daphne Vandemeulebroucke

University of Antwerp
Faculty of Science
EMAT
Groenenborgerlaan 171, 2020 Antwerpen, België
daphne.vandemeulebroucke@uantwerpen.be

Dutch title:

Onderzoek van redoxreacties met *in situ* 3D-elektronendiffractie in energiematerialen afgeleid van de perovskietstructuur

Summary

Many alternative energy applications involve inorganic crystalline solids exposed to redox conditions, for instance solid oxide fuel cells (SOFCs) or chemical looping with oxygen uncoupling (CLOU). In this research area, the development of *in situ* 3D electron diffraction (3DED) at elevated temperatures in gas and vacuum unlocks great new potential, as this technique can unravel atomic structure transformations in operational conditions, to understand the origins of e.g. high performance and degradation properties. A particularly interesting group of energy materials is based on the perovskite structure with ABX_3 as chemical formula, where A and B are cations and X is an anion. This project investigated the influence of high temperature reducing atmospheres on the atomic structure of two perovskite-based groups of energy materials : $La_xSr_{2-x}MnO_{4-\delta}$ and $(Ca,Sr)(Fe,Mn)O_{3-\delta}$.

Ruddlesden-Popper (RP) $La_xSr_{2-x}MnO_{4-\delta}$ are promising electrode materials for symmetric SOFCs due to their electronic and chemical properties. They consist of an ordered arrangement of layers with the perovskite structure (ABO_3) and rock salt structure (AO). Previously, they were reported from *in situ* X-ray and neutron diffraction to remain stable upon heating to 700°C in H_2 for $0 < x \leq 0.6$. However, anomalously large atomic displacement parameters were found. Further, while all these structures have the same I4/mmm lattice, the $x = 0.5$ compound shows a higher conductivity in reducing environment that breaks the trend of the rest of the $La_xSr_{2-x}MnO_{4-\delta}$ series. [1] This has not been explained yet in literature. With 3DED, we discovered new incommensurately modulated structures for $La_{0.25}Sr_{1.75}MnO_{4-\delta}$ and $La_{0.5}Sr_{1.5}MnO_{4-\delta}$ upon annealing in hydrogen gas, which have never been reported before. But the amount of order in the crystals differs for different La content. Further, atomic resolution electron microscopy images showed a difference in defect structure: where the $x = 0.5$ composition exhibits many higher order RP $n = 2$ layer defects, this is not the case for the $x = 0.25$ material. Those structural differences can be linked to the trend-breaking conductivity for $La_{0.5}Sr_{1.5}MnO_{4-\delta}$. For the 2D incommensurately modulated $x = 0.25$ phase, a dynamical structure refinement was performed based on 3DED data. Moreover, *in situ* high-resolution images and 3DED also detected the formation of a perovskite phase on the surface of both materials at 700°C. The layer is observed to be La rich, which leads to differences in thermodynamics between the surface and the bulk structure.

As a second group of materials, $(Ca,Sr)(Fe,Mn)O_{3-\delta}$ was studied. They are perovskites with an application as oxygen carrier in the CLOU process, which is a carbon capturing combustion technique that inherently separates expelled CO_2 from air. The cycling stability and oxygen release temperature of $CaMnO_{3-\delta}$ can be significantly improved by A or B site doping with e.g. strontium or iron, but until the current project, it had not yet been found why. [2] [3] Using *in situ* 3DED, we discovered differences in ordering behaviour of the oxygen vacancies that form upon reduction in vacuum and hydrogen

gas. For $CaFe_{0.2}Mn_{0.8}O_{3-\delta}$ and $Ca_{0.75}Sr_{0.25}MnO_{3-\delta}$, only transformations to disordered oxygen deficient structures were observed in between the fully oxidized and fully reduced compounds. On the other hand, for undoped $CaMnO_{3-\delta}$, the already reported [4] ordered supercell of the intermediate phase $CaMnO_{2.75}$ was found. But we could successfully solve and refine its structure for the first time ever, based on an electron diffraction technique that combines scanning and 3DED *in situ* in vacuum at 300°C.

However, at the highest temperatures during the *in situ* experiments in gas atmospheres, a reaction of the oxide samples with the silicon nitride support from the heating chips gave rise to a SiO_2 shell around the crystals. This led to discrepancies between the results of *in situ* and *ex situ* annealing and experimental limitations. Therefore, a systematic investigation was performed into graphene coating the Si_3N_4 chips to prevent this reaction with silicon. Unfortunately, this did not lead to a satisfying solution, probably due to incomplete graphene coverage and humidity and/or residual oxygen inside the closed gas cell. However, *ex situ* and - at sufficiently low temperatures, before the interference of the silica layer - *in situ* 3DED combined with other electron microscopy techniques indeed gave new insights on structure-property relations in $La_xSr_{2-x}MnO_{4-\delta}$ and $(Ca,Sr)(Fe,Mn)O_{3-\delta}$ for energy applications.

Nederlandstalige samenvatting (Summary in Dutch)

In veel alternatieve energietoepassingen spelen redoxreacties en anorganische kristallen een belangrijke rol. Zo zijn er bijvoorbeeld brandstofcellen met een vaste stof als elektrolyt (in het Engels *solid oxide fuel cells (SOFC)* genoemd). Of het zogenaamde CLOU-proces, dat staat voor *chemical looping with oxygen uncoupling* of "chemisch cyclen met zuurstofontkoppeling". Dit is een verbrandingsproces dat koolstofdioxide scheidt van de uitgestoten lucht. De ontwikkeling van *in situ* driedimensionale elektronendiffractie (3DED) op hoge temperatuur in gas of vacuüm opent nieuwe deuren in het onderzoek naar structurele veranderingen in het atoomrooster van materialen in reële toepassingen. Zo kan deze techniek bijvoorbeeld helpen om de oorzaak van degradatie of juist bijzonder goede prestaties van een materiaal bloot te leggen, met het oog op de ontwikkeling van steeds betere energiematerialen. Een cruciale groep energiematerialen is gebaseerd op de zogenaamde perovskietstructuur. Deze verbindingen hebben ABX_3 als chemische formule, waarbij A en B kationen zijn en X een anion is. In dit project bestudeerden we de invloed van hoge temperaturen in een reducerende atmosfeer op twee groepen materialen die afgeleid zijn van deze perovskietstructuur: $La_xSr_{2-x}MnO_{4-\delta}$ en $(Ca,Sr)(Fe,Mn)O_{3-\delta}$.

Ruddlesden-Popper (RP) $La_xSr_{2-x}MnO_{4-\delta}$-materialen wekken steeds meer belangstelling als elektroden voor symmetrische SOFC's, dankzij hun elektronische en chemische eigenschappen. Ze bestaan uit een ordening van lagen met de perovskiet- en de steenzoutstructuur (respectievelijk ABO_3 en AO). Volgens de literatuur blijven ze stabiel bij opwarming tot 700°C in waterstofgas voor de varianten met $0 < x \leq 0.6$, zoals men vaststelde met *in situ* X-stralen- en neutronendiffractie. Toch vond men onverklaarbaar grote afwijkingen van atomen van hun gemiddelde posities. Bovendien hebben alle verbindingen uit deze reeks dezelfde symmetrie (met I4/mmm als ruimtegroep), maar toch heeft de variant met x = 0.5 een grotere geleidbaarheid in een reducerende omgeving dan de rest. [1] Tot voor kort was dit fenomeen nog niet verklaard. In de loop van dit onderzoek ontdekten wij echter nieuwe incommensurabel gemoduleerde structuren voor $La_{0.25}Sr_{1.75}MnO_{4-\delta}$ en $La_{0.5}Sr_{1.5}MnO_{4-\delta}$ na reduceren op 700°C in waterstofgas, die nooit eerder zijn gerapporteerd. We voerden een dynamische verfijning uit voor het materiaal met x = 0.25 op basis van 3DED-data. Maar de hoeveelheid orde in deze kristallen verschilt naargelang de lanthaaninhoud. Verder zagen we met elektronenmicroscopiebeelden van atomaire resolutie dat er een verschil is tussen de defecten in beiden materialen. In de variant met x = 0.5 observeren we vele laagdefecten met een andere RP-configuratie, maar dit is niet het geval voor de verbinding met x = 0.25. Deze structurele verschillen kunnen we linken aan de afwijkende geleidbaarheid voor de fase met x = 0.5. Daarnaast toonden *in situ* hogeresolutiebeelden en 3DED ook aan dat er op het oppervlak van beide materialen een perovskietlaag wordt gevormd van 2-3 nm dik. Die is namelijk rijk aan lanthaan, wat leidt tot thermodynamische verschillen tussen het oppervlak en de bulkstructuur.

Als tweede groep materialen, onderzochten we (Ca,Sr)(Fe,Mn)$O_{3-\delta}$. Deze perovskieten worden gebruikt als zuurstofdrager in het CLOU-proces. Men vond dat doperen met strontium of ijzer de stabiliteit verhoogt na talrijke zuurstofcycli, en de temperatuur verlaagt waarop zuurstofafgifte plaatsvindt. Maar tot voor dit onderzoek was het niet duidelijk waarom dit het geval is. [2] [3] Met behulp van *in situ* 3DED legden we verschillen bloot in de ordening van zuurstofvacatures bij reductie in vacuüm en waterstofgas. Voor $CaFe_{0.2}Mn_{0.8}O_{3-\delta}$ en $Ca_{0.75}Sr_{0.25}MnO_{3-\delta}$ blijven de zuurstofvacatures wanordelijk in alle intermediaire fasen, dus behalve in de volledig geoxideerde en volledig gereduceerde verbinding. Maar dat is niet het geval voor het ongedopeerde $CaMnO_{3-\delta}$, dat zowel *in situ* in vacuüm als in waterstofgas transformeerde naar een geordende superstructuur voor $CaMnO_{2.75}$. Hoewel deze supercel voordien al was waargenomen in de literatuur [4], konden wij voor het eerst de structuur oplossen en verfijnen, en dit op basis van een techniek die 3DED en scannen combineert, *in situ* op 300°C in vacuüm.

Echter, bij de hoogste temperaturen *in situ* in gas treedt een reactie op tussen de bestudeerde materialen en het Si_3N_4-membraan van de chip waarop *in situ* wordt verwarmd. Dat zorgt voor de vorming van een SiO_2-schil rond de kristallen op hoge temperatuur in gas, die interfereert met de *in situ*-experimenten. Daardoor komen bepaalde observaties *in situ* en *ex situ* niet overeen, en is de *in situ*-techniek niet toepasbaar voor de hoogste temperaturen. Om dit te omzeilen bestudeerden we op systematische wijze het effect van een grafeencoating op de Si_3N_4-chips. Helaas leidde dit niet tot de gehoopte resultaten, waarschijnlijk doordat de grafeenlaag niet volledig dekkend was en door de aanwezigheid van water en/of resterende zuurstof in de gascel. Toch leverde *ex situ* en - bij lagere temperaturen - *in situ* 3DED in combinatie met andere elektronenmicroscopietechnieken interessante nieuwe inzichten op, met name over de relatie tussen de atomaire structuur en macroscopische eigenschappen van $La_xSr_{2-x}MnO_{4-\delta}$ en (Ca,Sr)(Fe,Mn)$O_{3-\delta}$ als energiematerialen.

Contents

List of Abbreviations

3DED	three-dimensional electron diffraction
ABO_3	perovskite (layer) with A and B as cations and O as anion
ADF	annular dark field
ADP	atomic displacement parameter
ADT	automated electron diffraction tomography
AO	rock salt (layer) with A as cation and O as anion
BF	bright field
calc	calculated
CBD	cooperative breathing distortions
CCD	charge coupled device
CLOU	chemical looping with oxygen uncoupling
e^-	electron
ED	electron diffraction
EDX	energy-dispersive X-ray spectroscopy
EELS	electron energy-loss spectroscopy
ETEM	environmental transmission electron microscope
F	structure factor
GOF	goodness of fit
HAADF STEM	high-angle annular dark field STEM
I	intensity
IT-SOFC	intermediate temperature solid oxide fuel cell
mono STEM-EELS	monochromated STEM electron energy-loss spectroscopy
KF flanges	Kleinflansch flanges
MEMS	micro-electromechanical systems
MIEC	mixed ionic and electronic conductor
MO	metal oxide
ND	neutron diffraction
~~O~~	indication of the origin on sections from 3DED
obs	observed
RED	rotation electron diffraction
RP	Ruddlesden-Popper
RT	room temperature
S/m	siemens per meter, unit of electrical conductivity
SAED	selected area electron diffraction
SEM	scanning electron microscope/microscopy
SOFC	solid oxide fuel cell
STEM	scanning transmission electron microscopy
TEM	transmission electron microscope/microscopy
TGA	thermogravimetric analysis
U_{ij}	component of harmonic atomic displacement factor
U_{iso}	isotropic atomic displacement factor
XRD	X-ray diffraction

Chapter 1

Introduction

1.1 Perovskite-Based Energy Materials

Climate change is one of the biggest challenges for science of the twenty-first century. The development of new, green technologies that lower the carbon footprint has never been more pressing. Energy materials play a crucial role here, for production, storage and conversion of energy. Nowadays, a tremendous amount of research is conducted to discover, synthesize and characterize numerous edge-cutting materials for e.g. batteries, fuel cells, solar cells, supercapacitors, biofuels, hydrogen storage and many other applications. [5]

One group of materials that are particularly interesting as energy materials are the so-called perovskites. Historically, this name originates from 1839, with the discovery of a new mineral in the Ural mountains. The German crystallographer Gustav Rose called this new material "perovskite", after the mineralogist Lev von Perovski. [6] [7] Chemically, this mineral had the formula $CaTiO_3$, and later the name "perovskite" came into use for the broader class of compounds with the ABX_3 structure. Here, A and B are metals - usually with respectively +II and +IV as oxidation states - and X(-II) is a nonmetal, often oxygen. [8] A schematic representation of a perovskite with the ideal cubic symmetry is shown in Figure 1.1. Where the B cations are smaller and sit in the center of a cube, the larger A cations are located on the corners of that cube. The X^{2-} anions surround the B cations as corner-sharing octahedra (sixfold coordination, BX_6). [9]

However, many real perovskites do not possess this perfect cubic "prototype" symmetry, but are distorted to various degrees. One mechanism for such distortion is rotation or so-called "tilting" of the octahedra. But tilting one octahedron implies tilting of adjacent octahedra as well. This can happen either "in-phase" - if the octahedra above and below tilt in the same sense - or "antiphase" - if they tilt in the opposite sense. [10] Other types of distortions exist as well, e.g. cooperative breathing distortions (CBD) which consist of a combination of dilatation and contraction of the BX_6 octahedra. [11] The simple ABX_3 formula can also be extended to more complex structures if the A and/or B site are doped, e.g. in $LaSrMnRuO_6$ (i.e. $La_{0.5}Sr_{0.5}Mn_{0.5}Ru_{0.5}O_3$). In this case, the valence states are La^{3+}, Sr^{2+}, Mn^{3+} and Ru^{4+} (as reported from X-ray absorption near edge spectroscopy). Synchrotron X-ray diffraction and electron diffraction showed that the Mn^{3+}

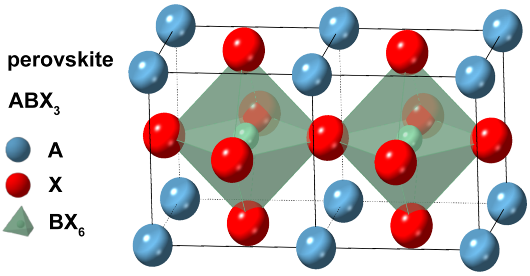

Figure 1.1: Two unit cells of the cubic perovskite structure, with ABX_3 as chemical formula. A and B metal cations are given in blue and green respectively, X anions in red. The BX_6 corner-sharing octahedra are shown in green.

and Ru^{4+} are organized in a disordered way. [12] But in the so-called double perovskites, there is an ordered alternation of BO_6 and $B'O_6$ units, for instance in Sr_2FeOsO_6. [13] In addition to that, many other configurations exist that are perovskite-based, for instance layered arrangements of perovskite and other phases.

Many perovskite-based materials possess interesting physical properties. One famous example is superconductivity. In 1986, this property was discovered for $Ba_xLa_{5-x}Cu_5O_{5(3-y)}$ at 30 K with x = 1 and 0.75 and y > 0. This material consists of three phases, amongst which a perovskite-like structure with mixed Cu^{2+} and Cu^{3+} valence. [14] Later, many more Cu-based oxides were found that are superconductive at higher temperatures. This is an example of the many cases where oxygen non-stoichiometry plays an important role. This means that not all oxygen positions in the lattice are filled, leading to vacancies - i.e. oxygen deficiency - or that extra oxygen is added at interstitial positions - which means in between the normal oxygen positions. Typically, such non-stoichiometry is indicated with the symbol δ in the chemical formula. The origin of a non-zero δ is the requirement of electroneutrality. If the material has cations with varying valence state - like Cu^{2+}/Cu^{3+} or La^{3+}/Sr^{2+} - the total charge is compensated by oxygen vacancies or interstitials. [15] But this might affect the material's properties as well. For instance, $YBa_2Cu_3O_{7-\delta}$ is superconductive for $\delta < 0.5$ but not for $\delta > 0.5$. [16]

Moreover, a lot of perovskites show a high electrical conductivity, e.g. $La_{0.50}Sr_{0.50}CoO_{3\pm\delta}$ has a conductivity of 4.4×10^3 S cm^{-1} at room temperature. For comparison: the conductivity of copper is 5.96 10^4 S cm^{-1}. [17] But in addition to electronic conductivity, also ionic conductivity - by means of ion transport instead of electron transport - is observed in many perovskites. For example, Bak et al. showed that for $CaTiO_3$ at 1050°C in $p(O_2)$ = 710 mbar, the components of the ionic and electronic conductivity become equal in their contribution to the total conductivity. [18] Because of these high conductivities, various perovskite-based materials are used as energy materials, for instance in solid oxide fuel cells as solid electrolyte (e.g. $La_{0.8}Sr_{0.2}Ga_{0.8}Mg_{0.2}O_{3-\delta}$ [19]) or as cathode (e.g. $La_{1-x}Sr_xCoO_{3-\delta}$ [20]). Another widely known example of energy related applications are perovskite solar cells. They are usually based on halide perovskites (with X = Cl, Br or I), due to their light absorption in the visible and near infrared spectrum, combined with their high charge carrier mobility, e.g. $CH_3NH_3PbI_3$. [21]

But perovskites also have redox properties that allow applications as e.g. catalysts or gas sensors. One example from the field of hydrogen production by water splitting is $Sr_2CoNb_{0.30}Ti_{0.70}O_{6-\delta}$. It has a simple cubic perovskite structure, a high hydrogen production rate and a low degradation rate throughout thermochemical water splitting cycles. Its H_2 production after 8 cycles at 700°C was one of the highest ever reported: 410 $\mu mol_{H2} g^{-1}$. [22]

In the scope of this project, the structure-property relations of two groups of perovskite-based materials, that are used in alternative energy applications, were intensively studied. The first group is the $La_xSr_{2-x}MnO_{4-\delta}$ series, which are promising electrode materials for symmetric solid oxide fuel cells (SOFC). These fuel cells are based on redox reactions and have a solid electrolyte. Since the operating conditions of the symmetric SOFCs are harsh - high temperatures in both reducing and oxidizing conditions - studies of structural transformations in these environments are important. Further, differences in performance for varying La/Sr content have not yet been explained by structural characterization techniques until this project. [1] The second group that is examined, are the $(Ca,Sr)(Fe,Mn)O_{3-\delta}$ compounds, which are used in the CLOU process - chemical looping with oxygen uncoupling. This is an energy production process that inherently separates CO_2 from air in its expelled products. [2] [3] Here, the role for the perovskite manganites is that of the oxygen carrier that releases O_2 and reincorporates it. Doping the A or B site can significantly lower the oxygen release temperature and increase the stability upon cycling. But before this research, it had not been discovered yet why this is the case. To examine the structural transformations at high temperatures of these perovskite manganites in reducing atmospheres - as at the anode of an SOFC or for O_2 release of the oxygen carrier in the CLOU process - the technique of *in situ* three-dimensional electron diffraction (3DED) was used, which will be discussed in the next chapter.

1.2 General Outline

In this thesis, the structural transformations of two types of perovskite-based manganites were studied in high-temperature reduction conditions with (*in situ*) 3DED and other TEM techniques. These were linked to their performance properties as energy materials.

Chapter 2 will cover the working principles of the applied methods. The main technique in this project is (*in situ*) 3DED. But in addition to that, also high-resolution HAADF-STEM, EDX, (monochromated) STEM-EELS, 4D-STEM tomography and powder XRD were used.

In Chapter 3, the structural transformations of $La_xSr_{2-x}MnO_{4-\delta}$ in solid oxide fuel cell anode conditions will be discussed. These were studied by *in situ* 3DED in vacuum and hydrogen gas, *ex situ* 3DED, high-resolution HAADF-STEM (also *in situ* in vacuum), monochromated STEM-EELS, EDX and powder XRD for x = 0, 0.25, 0.5, 0.75 and 1.

Chapter 4 is dedicated to the *in situ* 3DED studies of $(Ca,Sr)(Fe,Mn)O_{3-\delta}$ as an oxygen carrier for the CLOU process. $CaMnO_{3-\delta}$, $Ca_{0.75}Sr_{0.25}MnO_{3-\delta}$ and $CaFe_{0.2}Mn_{0.8}O_{3-\delta}$ were investigated *in situ* when heated in vacuum, inert gas and hydrogen gas, uncovering differences in oxygen vacancy ordering behaviour with or without doping.

However, at very high temperatures, a reaction occurred between the samples and the Si_3N_4 support of the Nano-Reactors for *in situ* heating in gas in the TEM. Therefore, coating these silicon nitride chips with graphene was explored as a potential solution to prevent a SiO_2 layer formation around the crystals, as discussed in Chapter 5.

Chapter 2

Methods

2.1 Diffraction to Study Crystalline Materials

For more than 100 years, diffraction has been an indispensable experimental tool to study crystalline materials. According to the International Union of Crystallography (IUCR), a crystal is a solid that consists - on average - of a long-range ordered arrangement of atoms. [23] In 1912, William Lawrence Bragg - son of William Henry Bragg - discovered that the spots from diffracting X-rays through a crystal on a photographic plate, could be considered as reflections from lattice planes of the crystal. [24] This led to the famous Bragg condition for diffraction:

$$n\lambda = 2dsin(\theta) \tag{2.1}$$

where n is an integer, λ the wavelength of the X-ray, d the distance in between the lattice planes and θ the angle of incidence of the ray, as illustrated in Figure 2.1. It means that if the difference in path length AB + BC for two incident waves equals an integral number of wavelengths, there is constructive interference. [25]

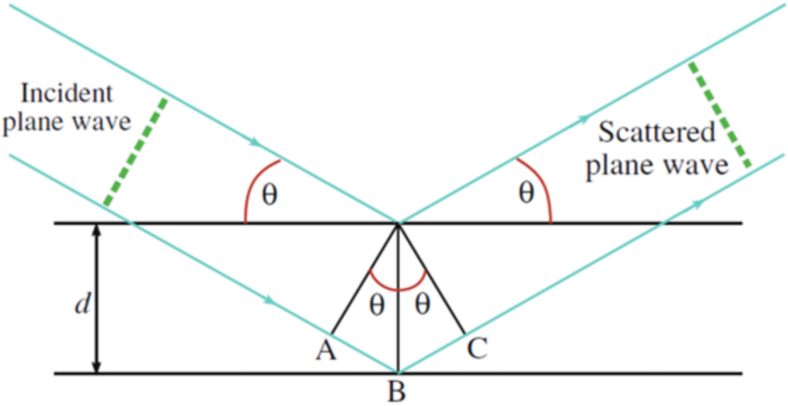

Figure 2.1: Illustration of the Bragg description of diffraction with d the distance in between the lattice planes and θ the angle of incidence. Image by [25]

In the century that followed, a theoretical framework was developed in the field of crystallography that allows to determine the precise ordering of atoms in a lattice, based on the diffraction of rays through a crystal. A crucial element is the concept of reciprocal space, which was independently discovered by Bravais (1850), Gibbs (1881) and Ewald and Laue (1911-1914). [25] In this description, every crystal has the so-called unit cell as its repeated, smallest asymmetric building block, and has two lattices. One lattice - the *direct lattice* - exists in direct space, which is space as we know it, and contains the parallel atomic planes. A point on this direct lattice is indicated by the lattice vector

$$\vec{r_n} = n_1\vec{a} + n_2\vec{b} + n_3\vec{c} \tag{2.2}$$

with $\vec{a}$, $\vec{b}$ and $\vec{c}$ the vectors that define the unit cell, and n_1, n_2 and n_3 integers. As shown in Figure 2.2, the plane ABC through the points A, B and C in direct space, can be indicated by the *Miller indices* hkl, defined in a way that the lengths of the vectors $\vec{OA}$, $\vec{OB}$ and $\vec{OC}$ are a/h, b/k and c/l. The indication (hkl) refers to the set of all equally spaced lattice planes that are parallel to this plane. The second lattice - the *reciprocal lattice* - exists in reciprocal space. There, lattice vectors are described by

$$\vec{r_m^*} = m_1\vec{a^*} + m_2\vec{b^*} + m_3\vec{c^*} \tag{2.3}$$

with m_1, m_2 and m_3 integers and

$$\vec{a^*} = \frac{\vec{b} \times \vec{c}}{V}; \vec{b^*} = \frac{\vec{a} \times \vec{c}}{V}; \vec{c^*} = \frac{\vec{a} \times \vec{b}}{V}; \tag{2.4}$$

with V the volume of the unit cell. Thus, each point in reciprocal space is connected with a plane in direct space. A special reciprocal lattice vector is then $\vec{g}$, defined as

$$\vec{g} = h\vec{a^*} + k\vec{b^*} + l\vec{c^*} \tag{2.5}$$

It can be shown that the distance d_{hkl} between parallel planes with Miller indices hkl - i.e. the (hkl) planes-, is equal to

$$d_{hkl} = \frac{1}{|\vec{g}|} \tag{2.6}$$

The diffraction spot caused by constructive interference due to the (hkl) planes, is called the hkl *Bragg reflection*, and determining the relation between each diffraction spot and the hkl lattice nodes, is called *indexing* the diffraction pattern. [25] Where the positions of the reflections give information on the form and size of the unit cell of the crystal, the intensities of the reflections are connected with the atomic content of the cell. This is described by the so-called structure factor F:

$$F(hkl) = \sum_{j=1}^{M} f_j e^{2\pi i(hx_j + ky_j + lz_j)} \tag{2.7}$$

where f_j are the atomic form factors of all atoms in the unit cell, each with relative coordinates x_j, y_j and z_j in direct space. Here, the atomic form factor is the Fourier transform of the nuclear and/or electron charge distribution of an atom (depending on the radiation type) and is a measure for how much the scattering amplitude deviates from that of a point source. [26] The amplitude of the structure factor will be only

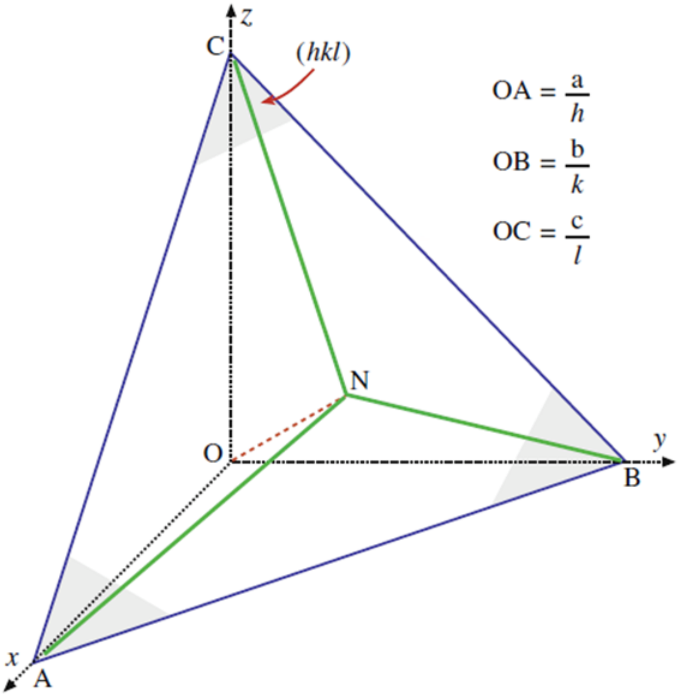

Figure 2.2: Illustration of the plane ABC in direct space, with Miller indices hkl. The lengths of the vectors $\vec{OA}$, $\vec{OB}$ and $\vec{OC}$ are a/h, b/k and c/l with a, b and c the length of the vectors defining the unit cell. Image by [25]

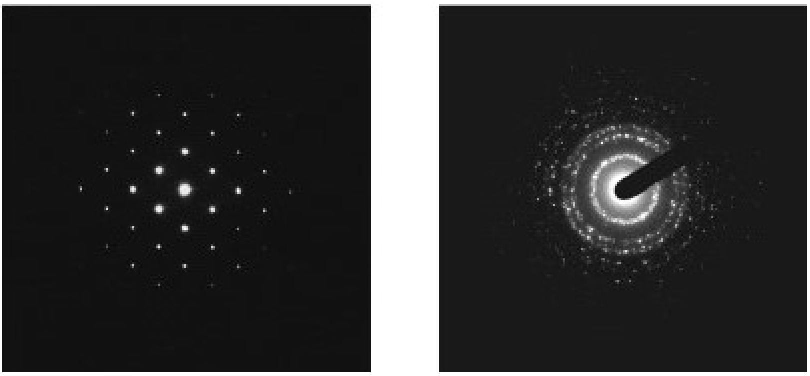

Figure 2.3: Electron diffraction patterns of (left) crystalline Si and (right) polycrystalline Si. Image by [27]

nonzero for certain integer hkl values, depending on the crystal lattice.

Thanks to the extensive mathematical framework that was developed over the years, crystallography can quantitatively describe the atomic arrangements of crystalline materials, based on all reflection positions and intensities measured by diffracting radiation through a crystal.

2.2 Electron Diffraction (ED)

Conventionally, the diffracted radiation consists of X-rays or neutrons, but since the last decade, the value of electron crystallography is more and more appreciated as well. Here, accelerated electrons (in a transmission electron microscope, see next section) are diffracted by a crystal, resulting in an electron diffraction pattern as illustrated in Figure 2.3 from crystalline (left) and polycrystalline (right) silicon. [27] Where crystal sizes of several micron or millimeter are required to obtain single-crystal diffraction patterns (with discrete Bragg reflections, as in Figure 2.3 on the left) for X-rays and neutrons respectively, crystals of a few tens of nanometers already suffice in the case of electron diffraction. The reason for this is that the interaction of electrons with matter is much stronger, since it is based on a different physical process. For X-rays, which are high-energy electromagnetic waves, this interaction happens mainly with the electron cloud around the atom. Neutrons on the other hand, are neutral particles that scatter from the nucleus of the atom through the strong nuclear force. But electrons possess a negative charge, so the Coulomb force comes into play, and they interact with both the electron cloud and nucleus of the atom. As a result, the interaction is more than a million times stronger. [28] [29]

Since X-ray and neutron diffraction (XRD and ND) require large crystals that are not always very practical to grow, powder XRD and ND are widely used. As the name suggests, there the radiation is sent through a powder sample instead of a single crystal, so averaging happens over many crystals and crystal orientations. Instead of discrete Bragg reflections as in single-crystal diffraction patterns, a ring pattern is now obtained (like the one in Figure 2.3 on the right, although this one is in fact acquired by ED but the domain sizes are very small). Then, one integrates the pattern along the circles and plots it as a one-dimensional powder profile, which can be more difficult to interpret than the two-dimensional electron diffraction pattern that can be acquired from the same nanometer crystal sizes. For instance, reflections with similar d values will overlap in a powder pattern, which can make it difficult to determine the unit cell parameters and the space group. Thus, some ordering features could be missed in powder XRD or ND experiments, that can easily be picked up by electron diffraction, where they would e.g. only appear in powder XRD or ND as peak broadening. [29]

2.3 The Transmission Electron Microscope (TEM)

Electron diffraction is acquired using a transmission electron microscope (TEM), where electrons are emitted from either a field emission or thermionic source into vacuum. In the first case, electrons are extracted by an electrostatic field, where in the second case, they get enough thermal energy to escape by heating an electrode. Then, they are accelerated through a high voltage (here 200 or 300 kV) in these ultra-high vacuum conditions of at least 10^{-7}Pa to assure a sufficiently long mean free path. [25] The path of the high-energy electrons is manipulated using electromagnetic lenses, as illustrated in Figure 2.4. [30] From top to bottom, there is first the system of condenser lenses, then the objective lens and finally the projector lens system. The condenser lenses focus the beam to the desired size and convergence onto the sample. For electron diffraction, usually, a parallel electron beam is used. Then, the objective lens - the most important lens of the TEM - again focuses the beam after it went through the specimen and forms a magnified image at its image plane and a diffraction pattern at its back focal plane. If the imaging lens system selects the back focal plane of the objective lens as object, we see a diffraction pattern as final result. On the other hand, if the image plane of the objective lens is selected, we obtain an image. [25] That means that in contrast to XRD and ND, the TEM also offers the possibility to combine diffraction with imaging. But even more - analytical - techniques are possible with the TEM, like high-resolution HAADF-STEM, EDX and EELS, which will be explained later in this chapter. That way, even more information can be gathered on the examined materials. For electron diffraction, often a selected area (SA) aperture is used. In that case, an aperture is placed in the image plane of the objective lens, which selects only one particle or a part of it, and at the end, the resulting diffraction pattern we see stems from that region on the specimen (see Figure 2.4).

2.4 Three-Dimensional Electron Diffraction (3DED)

The development of three-dimensional electron diffraction (3DED) has hugely added to the value of electron crystallography, especially for quantitative solutions and refinements of atomic parameters in the crystal structure. [28] This technique was first developed by Kolb et al. [31] in 2007 as ADT (automated electron diffraction tomography). In the most simple version, a parallel electron beam is supplied by a TEM, and the sample holder is stepwise rotated inside this beam around a random axis, while

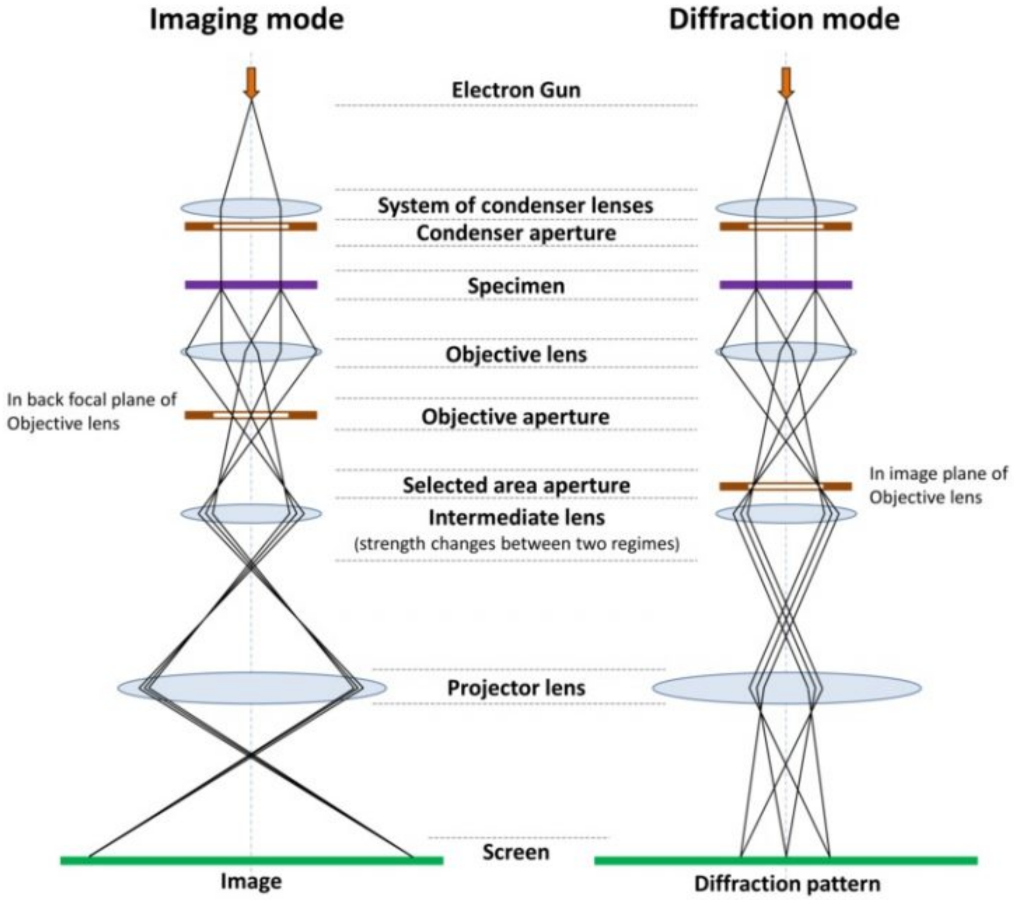

Figure 2.4: Schematic illustrating the basic system of a transmission electron microscope. Image from [30]

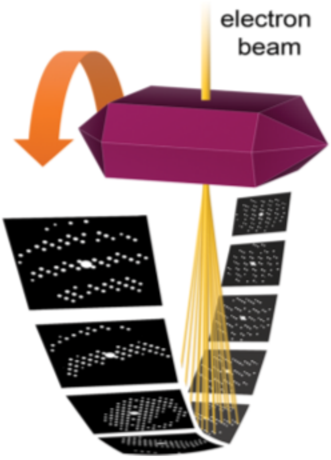

Figure 2.5: Schematic illustrating the principle of 3DED. Image by [32]

at each tilting step a diffraction pattern of the material is acquired. This is illustrated in Figure 2.5. [32] Then, a specialized software such as PETS2 [33] or ADT3D [34] is used to reconstruct the three-dimensional reciprocal space from this. In the past twenty years, many advances were made to improve the method, for instance rotation electron diffraction (RED) by Zhang et al. [35] and most recently continuous acquisition modes like e.g. cRED by Wang et al. [36].

In the current project, 3DED data were acquired in a stepwise manner with tilt steps of 0.5° and with a CCD camera (Gatan US1000XP) or if mentioned explicitly with a direct electron detector (ASI CheeTah). The total angular tilting range was about -20° to 20° for the DensSolutions Climate holder, -30° to 30° for the DensSolutions single tilt Wildfire heating holder and -70° to 70° for the Fischione tomo holder. The acquisition was done manually (acquisition time about 30′-45′) or semi-automatically, using either an in-house written Digital Micrograph script that allows intermediate manual crystal position adjustment (acquisition time 15′-20′), or the fast-ADT software [37] with prior crystal tracking in image mode (acquisition time about 10′). All 3DED experiments were recorded in TEM mode with a parallel electron beam at a Thermo Fisher Tecnai G2 or Titan^3 at a voltage of 200 kV and 300 kV respectively. To select only the diffraction signal from the desired crystal area, a 200 nm selected area aperture or a 300-600 nm parallel beam was used, depending on the required size. 4D-STEM tomography (see below) allowed to select an area of 8 nm x 9 nm. If specified explicitly, the data were acquired while precessing the beam at 100 Hz with a 1° semi-angle, using the Nanomegas system. On one hand, this is a way to collect more reflections and thus cover a larger part of the reciprocal lattice. But it is also a way of integration that is necessary for dynamical refinements, which will be explained later in this chapter. After data acquisition, all diffraction patterns were processed with the PETS2 software [33] to reconstruct the three-dimensional reciprocal space and make two-dimensional reconstructions of selected crystallographic sections.

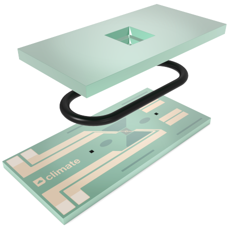

Figure 2.6: Schematic illustrating the design of the DensSolutions Nano-Reactor, used for *in situ* 3DED in gas in this project. Images by [38]

2.5 *In situ* TEM in a Gas Atmosphere

As mentioned above, the transmission electron microscope requires ultra-high vacuum conditions for its operation. So, traditionally, experiments involving chemical reactions on a sample in a certain gas environment happen outside the microscope, and the effect is studied by TEM afterwards. However, two types of TEM experimental settings have been developed that allow studying materials *in situ* under different gas atmospheres: the environmental TEM (ETEM) and the *in situ* gas TEM holders with a sealed nanoreactor. The first option is a dedicated transmission electron microscope where a limited area around the sample can be filled with a gas of choice. The second one is a specialized TEM holder containing a sealed nanoreactor for gaseous atmospheres that can be used in a normal high-vacuum TEM, and contains electrodes that permit *in situ* heating. In this research, the latter equipment was used for all *in situ* 3DED acquisition at high temperatures in gas conditions .

For this, we used the Climate holder and an EDX compatible Nano-Reactor from DensSolutions. This Nano-Reactor is a MEMS (micro-electromechanical system) based device consisting of a bottom chip with heating electrodes and a top chip, creating a sealed gas environment with a spacing of 10 microns. Both top and bottom chip contain an electron transparent Si_3N_4 window, of 50 nm and 30 nm thickness respectively. A schematic representation is given in Figure 2.6. [38] Before heating in gas, 3DED series of the pristine sample were taken at room temperature in vacuum (10^{-7} mbar), in air or nitrogen gas (700 mbar). The reducing agent H_2 was diluted with He or Ar. The concentration is explicitly mentioned at the different experiments. Before introducing the gases, each gas line was vacuum pumped 1 to 3 times in order to eliminate as much remaining oxygen as possible. Inside the sealed Nano-Reactor, the gas pressure was 700 mbar.

The technique of *in situ* TEM offers a lot of advantages. First, it is now also possible to study the material at intermediate stages during chemical reactions, which opens the possibility for discovering previously unseen intermediate phases. Second, it is possible to track the structural changes of one individual crystal at different temperatures and in different gas environments. However, the currently available commercial *in situ* TEM holders can only rotate over one single tilt axis. Therefore, sample orientation into the required crystallographic zones for conventional electron diffraction or high-resolution imaging of the atomic columns is impossible. But with 3DED, the rotation is performed around a random axis, after which the 3D reciprocal space can be constructed. So, no

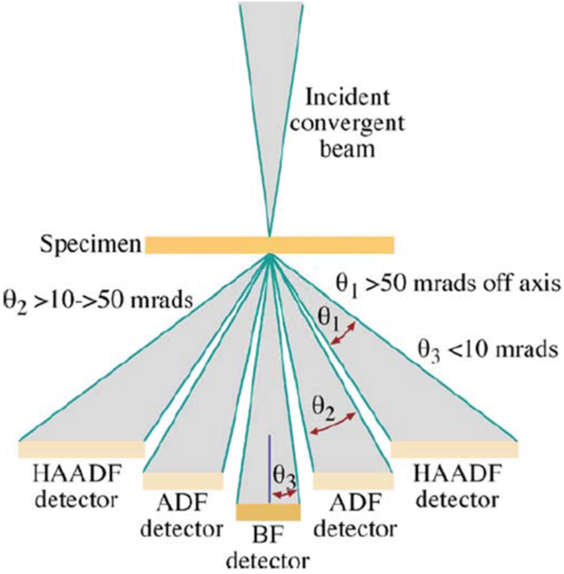

Figure 2.7: Schematic illustrating principle of BF (bright field), ADF (annular dark field) and HAADF (high-angle annular dark field) STEM. Image by [25]

double tilt holder is required for this, which makes 3DED in many cases the only *in situ* TEM technique that can provide information on structural transformations in a gas environment.

2.6 High-Resolution HAADF-STEM Imaging

In addition to creating a parallel electron beam, the lens system of the TEM can also create also a highly focused probe, that can be scanned over the specimen by means of scanning coils, as illustrated in Figure 2.7. In that case, it is called scanning transmission electron microscopy (STEM). Depending on the collecting angles of the detector behind the specimen, this can be bright field (BF) STEM or annular dark field (ADF) STEM. For the highest angles - high-angle annular dark field or HAADF-STEM - the collected electrons are mainly Rutherford scattered. This is incoherent, elastic scattering by the Coulomb force of the nucleus of the atoms. Here, the scattering is strongly dependent on the atomic number Z, which is why HAADF-STEM imaging is also called Z contrast imaging. It allows a straight-forward interpretation where the contrast is linked to the Z number of the atoms.

In this project, atomic resolution HAADF-STEM images were recorded at an aberration-corrected Thermo Fisher Titan^3 microscope at 300 kV. For the *in situ* HAADF-STEM heating experiment in vacuum, a Wildfire double-tilt heating holder from DensSolutions was used. High-resolution HAADF-STEM imaging was only possible at constant temperature (700°C) after sample stabilization, but not during the heating process. This is because the sample drifted while heating.

2.7 4D-STEM Tomography

In 4D-STEM, an electron probe is scanned over the specimen (two spatial dimensions) and a diffraction pattern is collected at each point (another two dimensions). This can be combined with tomography and is then called 4D-STEM tomography. Conventionally, this is used with convergent beam patterns to create the direct space images (e.g. [39]). At EMAT, this has also been used to perform 3DED studies instead, a technique developed as part and to be included in the Ph.D. thesis by Saleh Gholam later this academic year. This technique was also used for the current thesis. At every tilt step, a 4D-STEM scan was performed, which means that a collection of 3DED datasets was obtained, each linked to a spatial position (consisting of two coordinates). Here, data were collected with an ASI Cheetah direct electron detector.

2.8 Energy-Dispersive X-ray Spectroscopy (EDX)

When electrons interact with a specimen in a TEM, X-rays are created as well. This is because electrons in the electron shells from the sample atoms are excited to higher energy levels, leaving electron holes behind. When the hole gets filled by an electron of a higher level, an X-ray is emitted with an energy equal to the energy difference between the higher and lower level. The energy levels in the electron shell are discrete, and the emitted X-ray energy is unique to each excited atom, which is why this is called a characteristic X-ray. Detection and mapping of these characteristic X-rays enable us to gain information on the elemental distribution of the sample. This is called energy-dispersive X-ray spectroscopy (EDX). Here, EDX was performed in STEM mode at 300 kV at a Thermo Fisher Titan^3 instrument or at 200 kV at a Tecnai G2 with a Super X detector. All spectra were processed using the Esprit software.

2.9 (Monochromated) Electron Energy-Loss Spectroscopy (EELS)

Another type of spectroscopy that can be done with a TEM is electron energy-loss spectroscopy (EELS). This is an analysis of the energy distribution of inelastic scattered electrons through the sample. In its high-loss spectrum (> 50 eV), EELS also provides information on inner-shell ionization of atoms, by measuring the energy loss of the incident electrons. One advantage compared to EDX is that it is also sensitive to ionization events where a secondary electron is emitted instead of an X-ray. But more importantly, EELS can detect lighter elements (even Li), where EDX is only sensitive to heavier elements. Moreover, EELS can give information on the valence state of elements, by examining the edge energy positions and shapes. However, a high energy resolution - below 1 eV - is required to detect this fine structure. To limit the energy spread of the initial electron beam, the beam is first dispersed in energy - as light through a prism - and then a narrow energy band is selected by a slit, after which the electron beam is compressed again to a narrow probe. This is called monochromated STEM-EELS. In both cases - monochromated or not - the electron beam is dispersed by a magnetic prism at the end, and spread on a CCD or direct electron detector. [40]

For the current research, (monochromated) STEM-EELS experiments were performed at a Thermo Fisher Titan^3 at 300 kV with a Quantum 966 or Enfinium Gatan Image Filter and a US1000XP CCD camera. If the monochromator was used, it was excited to excitation value 0.7. For energy calibration, dual EELS was performed to include the zero-loss peak. The energy resolution was around 1 eV without monochromator and 0.3-0.65 eV with monochromator. All EELS spectra and maps were processed with the Digital Micrograph software. For plotting multiple EELS spectra on the same graph, Dr. Olesia Karakulina kindly provided us with a specialized Excel script.

2.10 TEM Sample Preparation

To prepare the TEM specimens, the sample powders were crushed with mortar and pestel for about one minute. Then, a suspension in ethanol was made and sonicated for about 30 minutes in an ultrasonic bath, cooled with icepacks to prevent sample heating. After that, this suspension was drop casted on a carbon coated copper grid (*ex situ* TEM characterization), a DensSolutions EDX compatible Nano-Reactor consisting of an O-ring sealed top and bottom chip with electron transparent Si_3N_4 windows (*in situ* gas heating) or a DensSolutions Nanochip for heating (*in situ* heating in vacuum).

It was found that in case of the *in situ* Nano-Reactor, the bottom chip should not be plasma cleaned before drop casting the sample to make sure that enough crystals attach to the Si_3N_4 windows for TEM examination. However, after drop casting, both top and bottom chip were plasma cleaned for 4 times 5 seconds in a 25% O_2/Ar mixture at 30% power to reduce contamination.

2.11 Scanning Electron Microscopy (SEM)

For a more general overview of the Nano-Reactor electron transparent windows, lower resolution images were acquired with a scanning electron microscope (SEM), in our case a Fisher Quanta 250 FEG SEM at 5 or 20 kV. Since the electrons do not have to go through the sample, but only be reflected or knocked-off from the sample, much lower voltages are required for an SEM than a TEM (1-30 kV versus 80-300 kV). As in STEM, a probe scans the surface of the specimen, but the resolution is much worse than for a TEM. Where the optimal resolution obtainable in the best SEMs is $\approx$ 0.5 nm, this is $<$ 50 pm for TEM. [41]

2.12 Powder X-ray Diffraction (XRD)

In this thesis, powder XRD was acquired as a first check of the average structure of the synthesized and annealed samples, after which TEM studies were done to study the materials on a more local scale. Powder XRD was acquired with a Huber powder diffractometer with a pure Cu-K$_{\alpha 1}$ source equipped with a G670 Imaging Plate Guinier Camera at EMAT, Antwerp. To mount the sample, a suspension is made from the powder in ethanol and this is put onto a sample holder with a transparent film, after which it is dried. The diffractometer provides the X-rays that are diffracted by the powder, and are captured by an image plate. This is a foil that is covered by crystallites of a luminescent storage material containing phosphor. After the X-ray exposure, the imaging plate is scanned by a red laser beam, and the areas that were exposed to X-rays, now emit blue photo-stimulated luminescence. This signal is then collected and converted to a digital signal. [42] Powder XRD for *ex situ* hydrogen annealed $\mathrm{La_{0.25}Sr_{1.75}MnO_{4-\delta}}$ was performed with a high-flux Rigaku rotated Cu anode with Ni filter in Bragg-Brentano geometry in the lab of Dr. Pascal Roussel at the University of Lille, France.

2.13 Le Bail fit from powder XRD

The Le Bail fit is a method to extract all peak intensities from a complete powder diffraction pattern - a so-called whole powder pattern decomposition (WPPD) method- , which was first applied in 1988 by Armel Le Bail [43]. It allows to refine the cell parameters, but not the atomic positions, occupancies or displacement parameters. The "goodness of fit" (GOF) and the R-factors describe how well the model fits the experimental data. The explicit formulas for the profile R-factor (R_p), weighted profile R-factor (wR_p) and GOF are [44]:

$$R_p = \sqrt{\frac{\sum_i |y_i(obs) - y_i(calc)|}{\sum_i y_i(obs)}} \cdot 100 \tag{2.8}$$

$$wR_p = \sqrt{\frac{\sum_i w_i(y_i(obs) - y_i(calc))^2}{\sum_i w_i y_i(obs)^2}} \cdot 100 \tag{2.9}$$

with observed and calculated intensities $y_i(obs)$ and $y_i(calc)$, and weights w_i from the standard uncertainties of the profile intensities:

$$w_i = \frac{1}{\sigma^2 y_i(obs)} \tag{2.10}$$

$$GOF = \frac{wR_p}{R_{exp}} \tag{2.11}$$

with R_{exp} the experimental R-factor:

$$R_{exp} = \sqrt{\frac{\sum_i w_i y_i(obs)^2}{n - p}} \cdot 100 \tag{2.12}$$

where n is the number of profile points and p is the number of refined parameters. All Le Bail fits in this project were performed using the software Jana2020. [45]

2.14 Refinements: Rietveld/Single-Crystal and Kinematical/Dynamical

In 1969, Hugo Rietveld published a method for structural analysis called the Rietveld refinement. It consists of modelling a powder diffraction pattern by a set of parameters, which can be simultaneously refined by the least-squares method. That way, the differences between the experimental pattern and calculated pattern are minimized. [46] The resulting match is quantified and rated by means of the so-called R-factor: the standard measure of quality for the agreement between the calculated and observed intensities, given by the formula [47]:

$$R = \frac{\sum|\sqrt{I(obs)} - \sqrt{I(calc)}|}{\sum|\sqrt{I(obs)}|} \tag{2.13}$$

In a Rietveld refinement, there are four categories of parameters. The first group is that of the structural parameters, which we are actually interested in: atomic positions, occupancies and atomic displacement parameters that describe the deviations of atoms from their average positions. Then, there are also the cell parameters, the instrumental parameters and specimen specific parameters, like e.g. the size of the crystallites. In contrast, only the structural parameters are refined in a single-crystal refinement. [48] Refinements from ED of powder materials are single-crystal refinements, since single-crystal electron diffraction patterns can be obtained from sub-micron particles.

For single-crystal diffraction, there are two different kinds of refinements: a (traditional) kinematical refinement and a dynamical refinement. The difference is that the latter takes the dynamical effects of electron diffraction into account. While the interaction of X-ray and neutrons with matter can be approximated as a single scattering event, this is not the case for electrons. The latter interact much more strongly with matter and are often scattered multiple times, which is also called dynamical diffraction. For XRD and ND, the calculation of the model intensities uses the kinematical relation $I \sim |F^2|$, with I the intensity and F the structure factor, as defined in section 2.1. But in a dynamical refinement, these calculations are based on dynamical diffraction theory [49] instead. However, this method requires techniques like e.g. precession or continuous 3DED to have data at enough angles for the integration of the diffracted intensities. Here, precession 3DED was used, which consists in acquiring the tomography series in a stepwise manner, and precessing the electron beam around the optical axis at high frequency (here at 100 Hz with a 1° precession semi-angle and a tilt angle of 0.5°) for each tilt angle.

Different types of refinements were done in the scope of this thesis: Rietveld refinement from powder XRD, kinematical refinement from 4D-STEM tomography and dynamical refinement from 3DED. For all of them, Jana2020 was used (including Dyngo for dynamical refinement). [45]

Chapter 3

$La_xSr_{2-x}MnO_{4-\delta}$ as a Solid Oxide Fuel Cell Electrode

3.1 Introduction to $La_xSr_{2-x}MnO_{4-\delta}$ as an Electrode Material for Symmetric Solid Oxide Fuel Cells

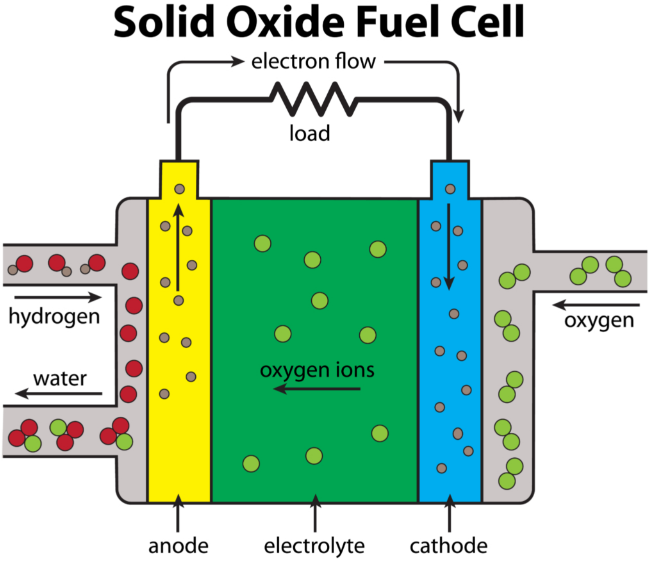

Figure 3.1: Diagram of how a solid oxide fuel cell works. [50]

One type of alternative energy sources are the solid oxide fuel cells (SOFCs). In this fuel cell, electricity is not generated by combustion, but directly by means of an oxidation-reduction reaction pair, also called redox reactions. Various types of these electrochemical conversion devices exist, differing by their mobile charge carriers and the electrolyte. In the case of a SOFC, this is a solid ceramic electrolyte which conducts oxygen ions or protons, but no electrons. At the anode of the cell, a fuel - e.g. hydrogen gas or methane -

is oxidized, and free electrons move via an external circuit to the cathode where they participate in the reduction of oxygen from air. That way an electrical current is produced and a stable system is formed. [51] [52] This process is illustrated in Figure 3.1. [50] As the ionic conductivity in ceramics increases with temperature, the first SOFCs could only operate at very high temperatures: from 750°C to 1000°C. Since then, many efforts have been made to reduce the performance temperature, and intermediate temperature solid oxide fuel cells (IT-SOFCs) have been created, working between 500°C and 750°C. [51] One way to optimize the performance of the solid oxide fuel cell, is to use Mixed Ionic and Electronic Conductors (MIEC) as cathode materials, since they exhibit both electron and oxide ion mobility. In pure electronic conductors, the oxygen reduction reaction can only happen at the triple phase boundary point between cathode, electrolyte and air. There, the cathode only provides the electrons for reducing the oxygen molecules. But in MIECs, oxide ions can also be incorporated at the electrode surface and travel through the electrode bulk to the electrolyte. [53] [54]

Most MIEC materials are based on the ABO_3 perovskite lattice. However, to obtain ionic conductivity, defects are required, which can be in the form of lattice impurities, interstitials or vacancies. Oxygen vacancies are usually described by the so-called oxygen non-stoichiometry or deficiency δ. Often, such defects are introduced by doping of the A and/or B site with cations having a different valence. [54] An example of such heterovalent cation substitution is $La_{1-x}Sr_xCo_{1-y}Fe_yO_{3-\delta}$. Here, e.g. different ratios of La^{3+} and Sr^{2+} on the A site result in different oxygen deficiencies and different electronic and ionic conductivities, as illustrated in Figure 3.2 [55] The aforementioned family of $(La,Sr)(Co,Fe)O_{3-\delta}$ is an example of MIECs cathode materials that possess very high electronic (σ_e) and ionic conductivities (σ_i): e.g. (σ_e) ~ 100 S cm^{-1} and (σ_i) ~ 0.1 S cm^{-1} at 800°C in air for $La_{0.8}Sr_{0.2}Co_{0.8}Fe_{0.2}O_{3-\delta}$, compared to ($\sigma_i$) ~ 0.01 S cm^{-1} for yttria-stabilized zirconia (YSZ) in the same conditions. [55].

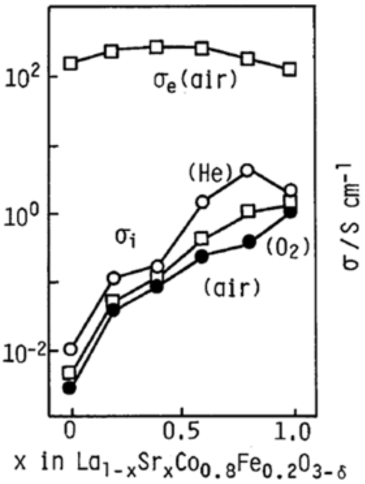

Figure 3.2: The effect of different A cation substitution on the electronic and ionic conductivity in $La_{1-x}Sr_xCo_{0.8}Fe_{0.2}O_{3-\delta}$. The vertical axis shows the electronic σ_e and ionic σ_i conductivity in air, helium and pure oxygen in function of the strontium concentration. [55]

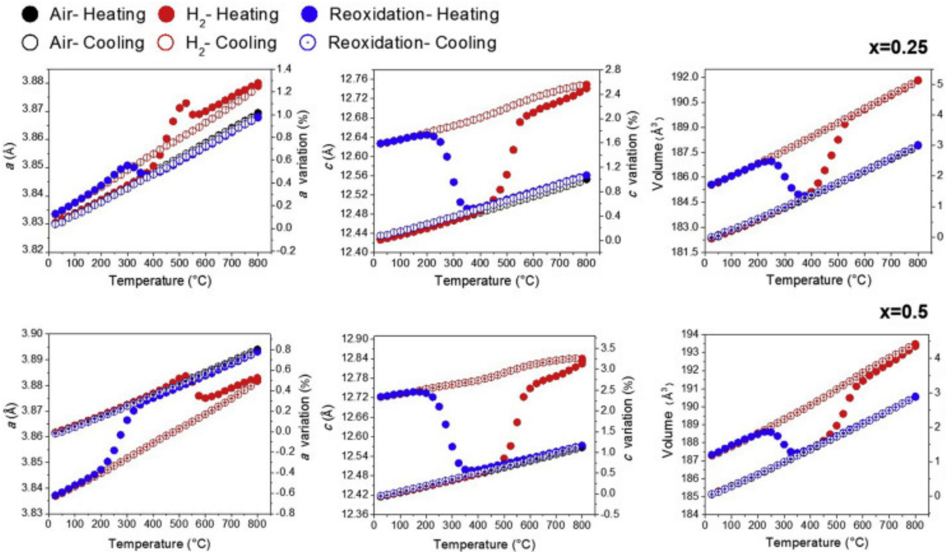

Figure 3.3: Cell parameters from *in situ* XRD by Sandoval et al.[1] for $La_{0.25}Sr_{1.75}MnO_{4-\delta}$ and $La_{0.5}Sr_{1.5}MnO_{4-\delta}$ upon heating (filled circles) and cooling (empty circles) in (black) air, (red) 3% H_2/N_2 and (blue) air again.

Another improvement in the field was the introduction of symmetrical SOFCs. Here, the cathode and the anode are made from the same material, which can simplify the production process and decrease the mechanical stress due to different thermal expansion coefficients. However, such electrodes must be stable in both reducing and oxidizing conditions, exhibit mixed ionic and electronic conducting behaviour and have the right thermomechanical properties. [53] A particular group of MIECs complying with those requirements is the $La_xSr_{2-x}MnO_{4-\delta}$ series. It was reported that the $La_xSr_{2-x}MnO_{4-\delta}$ compositions with $0 \leq x \leq 1.4$ have comparable thermal expansion properties to most common electrolytes, and possess a good stability up to 800°C in air, as in cathode conditions. [56] From this series, $La_{0.5}Sr_{1.5}MnO_{4-\delta}$ possesses the best combination of conductivities in oxidizing and reducing conditions at 800°C, i.e. 35.6 S cm $^{-1}$ (air) and 1.9 S cm $^{-1}$ (3% H_2/Ar). With these values, it breaks the decreasing (in air) and increasing (in hydrogen gas) conductivity trends of the other compositions with increasing La content. For x= 0.25, 0.4 and 0.6, these are 38.6 S cm^{-1}, 33.6 S cm^{-1} and 28.8 S cm^{-1} in air, and 0.4 S cm^{-1}, 0.5 S cm^{-1} and 0.8 S cm^{-1} in 3% H_2/Ar, all at 800°C. [1] The reasons for this were not yet uncovered before the current work.

Concerning the stability in reducing anode conditions, it was reported from *in situ* powder XRD and ND by Sandoval et al. [1] that $La_xSr_{2-x}MnO_{4-\delta}$ with $0.25 \leq x \leq 0.6$ remains stable under flowing hydrogen gas at 800°C, as in the operational environment at the anode. However, these *in situ* powder XRD and ND experiments displayed complex cell parameter changes upon heating and cooling in diluted hydrogen gas, as can be seen in Figure 3.3. This graph shows the a and c cell parameters for $La_{0.25}Sr_{1.75}MnO_{4-\delta}$ and $La_{0.5}Sr_{1.5}MnO_{4-\delta}$ upon heating (filled circles) and cooling (empty circles) in (black) air, (red) 3% H_2/N_2 and (blue) air again. During reduction upon heating in hydrogen, non-linear steep changes happen for a and c between 400°C and 600°C, which are reversed between 250°C and 350°C upon reoxidizing in air. Further, anomalous values were obtained for the anisotropic atomic displacement parameters (ADP) upon heating in hydrogen in these *in situ* diffraction experiments by Sandoval et al. [1] ADPs represent the displacements of atoms from their average positions in the lattice, because of temperature vibrations but also due to other deviations of the perfect structure. They can be isotropic, but are ellipsoids in general. In the study by Sandoval et al., one component of the ellipsoid was significantly larger than expected for thermal expansions, which indicates that some structural transformation happened that could not be further quantified by *in situ* powder XRD or ND experiments.

The $La_xSr_{2-x}MnO_{4-\delta}$ series structurally belongs to the class of the layered K_2NiF_4-type Ruddlesden-Popper (RP) materials, which can be derived from the perovskite lattice. RP structures consist of an alternation between one rock salt layer AO and n perovskite layers ABO_3 (a single perovskite structure is shown in Figure 3.4a), leading to the general formula $A_{n+1}B_nO_{3n+1}$ or $(AO)(ABO_3)_n$ with n = 1, 2, 3, 4, ... The A cation can be an alkali, alkaline earth (here strontium) or rare earth metal (here lanthanum) and B is a transition metal (here manganese). While the A cations are located in both the perovskite and the rock salt slabs, the B cations are only positioned at the center of the anion octahedra in the perovskite blocks. A schematic representation is shown in Figure 3.4.

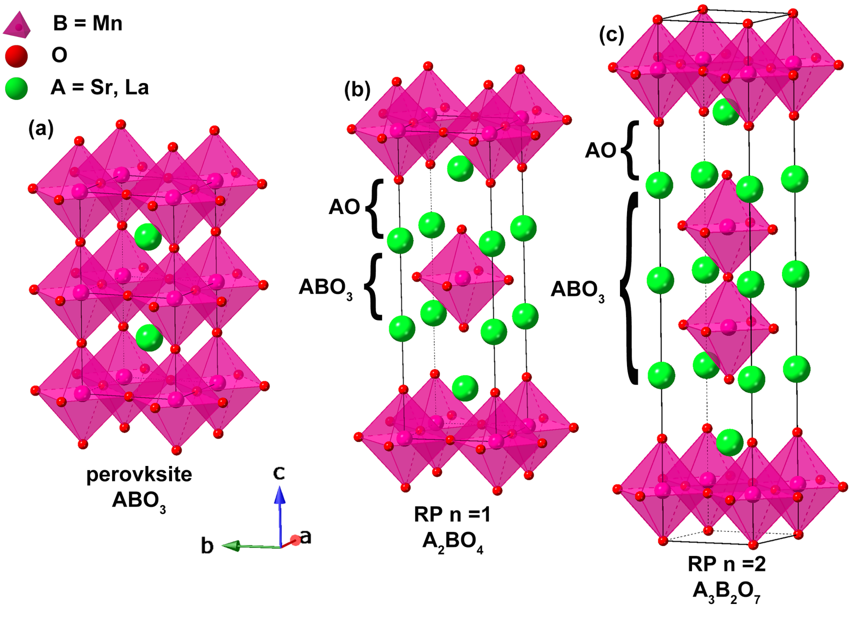

Figure 3.4: Schematic representation of a single perovskite with chemical formula $AMnO_3$ (a) and Ruddlesden-Popper structures A_2MnO_4 with n = 1 (b) and $A_3Mn_2O_7$ with n = 2 (c). Here, A is Sr or La, and B is Mn.

In the case of $La_xSr_{2-x}MnO_{4-\delta}$, n equals 1, so each rock salt layer is followed by a single perovskite layer. Several La-doped compositions will be treated in the scope of this thesis, i.e. x=0, 0.25, 0.5, 0.75 and 1. All these materials have the K_2NiF_4 structure in their pristine state with I4/mmm as a spacegroup, as the structure in Figure 3.4b. However, as mentioned above, their conductivities differ. Especially the x = 0.5 has a strongly deviating conductivity in reducing conditions that breaks the trend of the other compositions in the series. But the reportedly large ADP values seen during *in situ* powder XRD and ND experiments, suggest that some structural ordering could have occurred upon hydrogen annealing that was missed by those techniques, but that might be picked up by 3DED (for reasons discussed in section 2.4). It is known that ordering of oxygen vacancies has a significant effect on ionic transport properties. As an example, for $SrCo_{0.8}B'_{0.2}O_{3-\delta}$ (with B'= Cr, Fe, Co, Cu) and for $La_{0.6}Sr_{0.4}CoO_{3-\delta}$, the transition from a vacancy-ordered state to a disordered perovskite leads to an increase in oxygen permeability with 5 to 6 orders of magnitude (up to $3 \cdot 10^{-7}$ mol cm^{-2} s^{-1}). [57].

With this research, we investigated whether differences in structural order might explain the differences in SOFC electrode performance for $La_xSr_{2-x}MnO_{4-\delta}$ with different La content. In addition to 3DED, we also performed HAADF-STEM, EDX, EELS and powder XRD. First, we analyzed pristine, as-synthesized $La_xSr_{2-x}MnO_{4\pm\delta}$ with x = 0, 0.25, 0.5, 0.75 and 1. Then, we examined those samples after annealing in diluted hydrogen gas. Finally, we also performed *in situ* TEM heating experiments on the x= 0, 0.25 and 0.5 compositions, in vacuum and in hydrogen atmosphere. $Sr_2MnO_{4-\delta}$ is known not to be stable in reducing conditions, and therefore it is not interesting as a SOFC electrode. However, because of its well-documented and clearly observable structural transformation from tetragonal I4/mmm to a monoclinic $P2_1/c$ supercell [58] [59], we selected this composition as a reference material, to test the validity of the *ex situ* and *in situ* annealing experiments.

A sidenote regarding notation: even in the oxidized form, the doped materials from this series usually exhibit oxygen non-stoichiometry, due to the difference in valence state between the A site cations. For instance, Sandoval et al. [1] found a composition of $La_{0.25}Sr_{1.75}MnO_{4.07}$ as a starting point before reduction. Since we did not perform thermogravimetric analysis of the samples at any stage, the materials will be referred to as $La_xSr_{2-x}MnO_{4\pm\delta}$ in their pristine state, and as $La_xSr_{2-x}MnO_{4-\delta}$ during or after reduction treatment.

3.2 Pristine $La_xSr_{2-x}MnO_{4\pm\delta}$ for x = 0, 0.25, 0.5, 0.75 and 1

3.2.1 Synthesis

Sr_2MnO_4, $La_{0.25}Sr_{1.75}MnO_{4\pm\delta}$ and $La_{0.5}Sr_{1.5}MnO_{4\pm\delta}$ were all synthesized by means of the solid state reaction. For the synthesis of Sr_2MnO_4, stoichiometric amounts of $SrCO_3$ (Sigma Aldrich 99.9%) and Mn_2O_3 (Sigma Aldrich 99.9%) powder were pressed into pellets of 1 cm in diameter using a hydraulic press, and heated for 18h hours at 1500°C in air. However, it is known that pure K_2NiF_4 type Ruddlesden-Popper Sr_2MnO_4 - also called β-Sr_2MnO_4 - is difficult to obtain. Simultaneously, also α-Sr_2MnO_4 is formed, which consists of a mixture of SrO and $Sr_7Mn_4O_{15}$. [60] In literature, it was found that heating α-Sr_2MnO_4 for 30 minutes to 1650°C in air can transform it to β-Sr_2MnO_4 [61], but when we tried this, the high temperature melted the sample instead. Different numbers of heating cycles at different temperatures and for different durations were tried, but the best purity of β-Sr_2MnO_4 was achieved by heating for 18 hours at 1500°C in air. Powder XRD data and refinements will be discussed in the next section. Since $Sr_7Mn_4O_{15}$ also has $P2_1/c$ as a spacegroup and similar cell parameters to the reduced phase (a = 6.8125 Å, b = 9.6228 Å, c= 10.3801 Åand β = 91.8771 ° for $Sr_7Mn_4O_{15}$ [62] versus a= 6.8517 Å, b = 10.8063 Å, c = 10.8134 Å, and β = 113.287 ° [59] for $Sr_2MnO_{3.55}$), 3D ED data were acquired of the pristine material at room temperature in vacuum or air to select crystals of the tetragonal β-phase as a first step of all *in situ* TEM vacuum and gas experiments.

$La_{0.25}Sr_{1.75}MnO_{4\pm\delta}$ and $La_{0.5}Sr_{1.5}MnO_{4\pm\delta}$ were synthesized at the lab of Dr. Pascal Roussel in at the University of Lille, France. For this, stoichiometric amounts of La_2O_3 (Alfa Aesar 99.9%), $SrCO_3$ (Sigma Aldrich 98%) and $MnCO_3$ (Sigma Aldrich 99.9%) were mixed and milled in an agate mortar for 2 hours. The resulting powders were uniaxially pressed into pellets of approximately 10 mm diameter. Then, the powders were calcined using three successive heating cycles at 1300 °C for 6h for x = 0.5. The x = 0.25 composition required three cycles at 1300°C for 6h, followed by 3 cycles at 1450°C for 6h and 1 cycle at 1450°C for 18h, performing intermediate grinding steps in all cases (pellets were always put on a sacrificial bed of powder to avoid any possible diffusion between the alumina crucible and the pellet).

$LaSrMnO_4$ and $La_{0.75}Sr_{1.25}MnO_{4\pm\delta}$ were provided by Prof. Dr. Michael Hayward from the University of Oxford. They were prepared via the citrate gel method where La_2O_3 (99.999%, dried at 900°), $SrCO_3$ (99.994%) and MnO_2 were dissolved in a minimum quantity of 1:1 mixture of 6M nitric acid and distilled water. 5 ml ethylene glycol and $2\frac{1}{3}$ mole equivalents of citric acid were added. The solution was stirred constantly to heat and encourage polymerization. Then, the gel was ground into a fine powder, and heated in a Al crucible to 1000°C in air at 1°C/minute. The thus obtained powder was pressed into pellets of 13 mm and heated under a $2\%H_2/N_2$ flow at 1300°C twice for 2 days, with intermediate grinding. [63]

3.2.2 Powder XRD

The phase, quality and cell parameters of as-synthesized $La_xSr_{2-x}MnO_{4\pm\delta}$ with x = 0, 0.25, 0.5, 0.75 and 1 were examined with powder XRD. For Sr_2MnO_4, powder XRD was also acquired after annealing the sample in pure nitrogen gas at 550°C for 1 hour. The raw XRD patterns are shown for all samples in Figure 3.5, and in a more detailed way - including calculated patterns from the Le Bail fit and zoomed areas - in Figures 3.6, 3.7, 3.8, 3.9, 3.10 and 3.11. For all materials, a tetragonal cell was found, as expected. On top of that, the predicted monoclinic impurity phase was found for Sr_2MnO_4 that agrees with the structure of $Sr_7Mn_4O_{15}$ from literature [62]. The compounds with x = 0.75 and 1 have less agreement between the raw experimental and calculated phase, as visible from the broadened and extra peaks in Figure 3.10 and 3.11. This is probably because of aging of the samples, and will be disscussed further when comparing the cell parameters. All cell parameters - as listed in Table 3.1 - , were refined from the Le Bail fit.

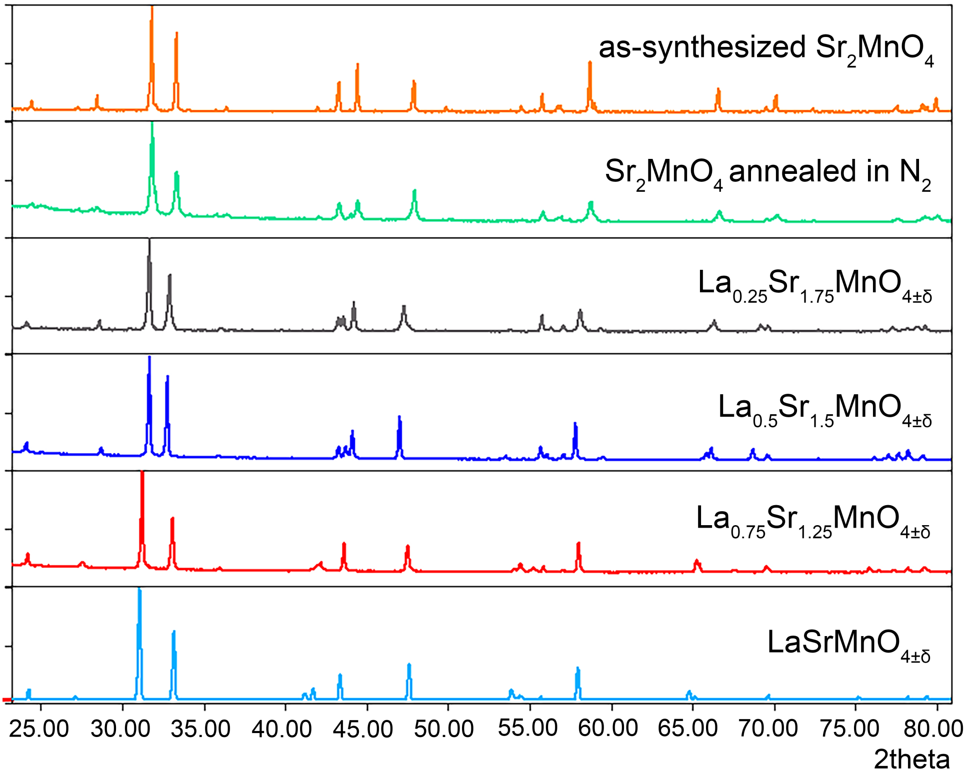

Figure 3.5: Comparison of raw powder XRD patterns for as-synthesized $La_xSr_{2-x}MnO_{4\pm\delta}$ with x = 0, 0.25, 0.5, 0.75 and 1, and for Sr_2MnO_4 after annealing at 550°C in N_2. Calculated patterns from the Le Bail fit and zoomed areas are given in the following figures.

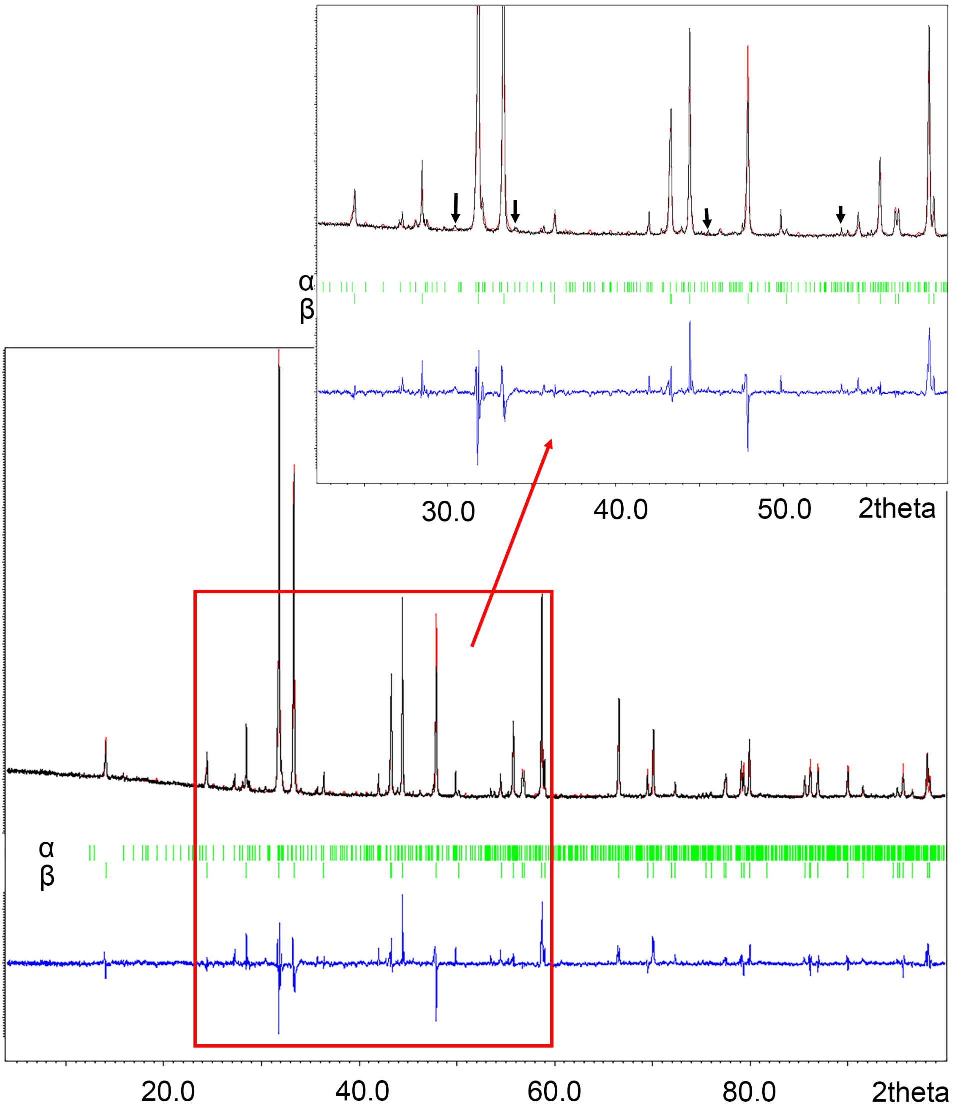

Figure 3.6: Raw (black), calculated (red) and difference (blue) powder XRD patterns for as-synthesized Sr_2MnO_4. The calculated pattern was obtained from the Le Bail fit. In green, the calculated peaks are indicated from both β-Sr_2MnO_4 (I4/mmm) and $Sr_7Mn_4O_{15}$ in the impurity α-Sr_2MnO_4 phase. The black arrows indicate impurity peaks in the observed pattern that do not match with the calculated pattern.

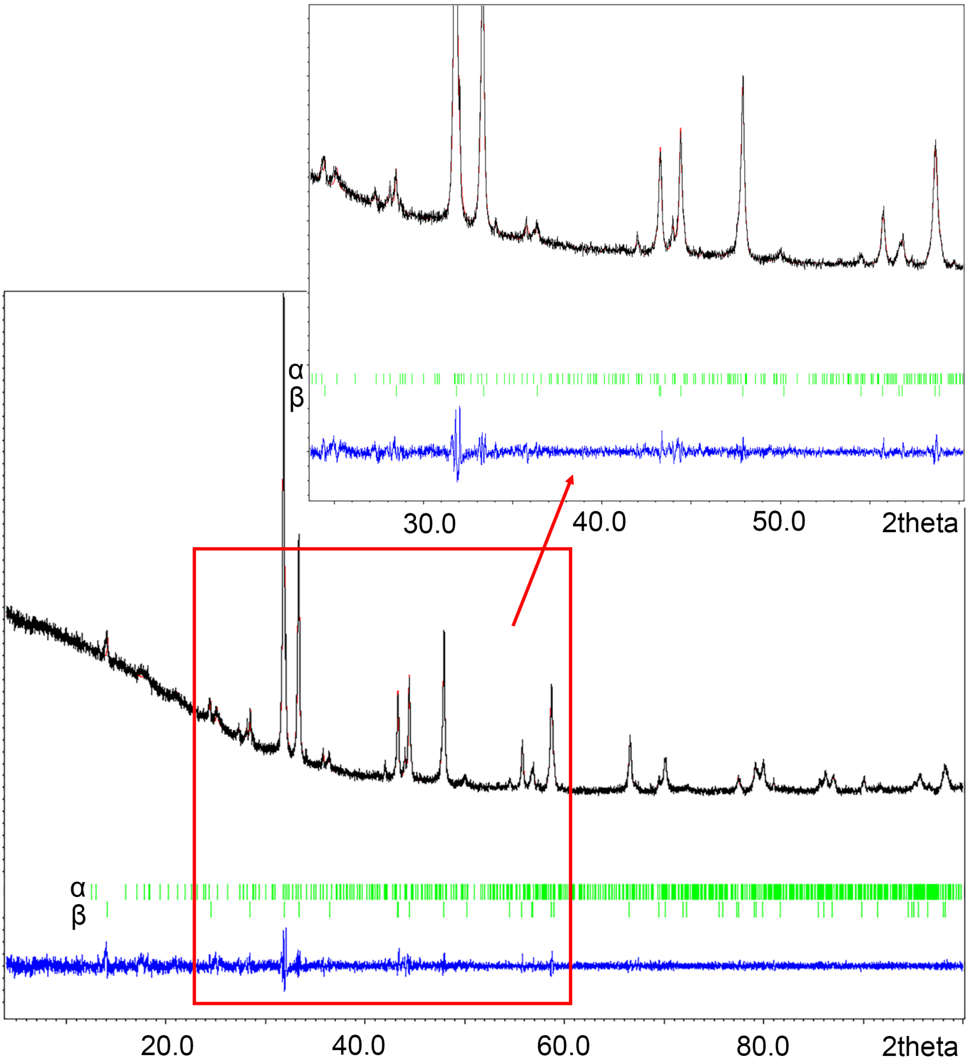

Figure 3.7: Raw (black), calculated (red) and difference (blue) powder XRD patterns for Sr_2MnO_4 upon annealing in N_2. The calculated pattern was obtained from the Le Bail fit. In green, the calculated peaks are indicated from both β-Sr_2MnO_4 (I4/mmm) and $Sr_7Mn_4O_{15}$ in the impurity α-Sr_2MnO_4 phase.

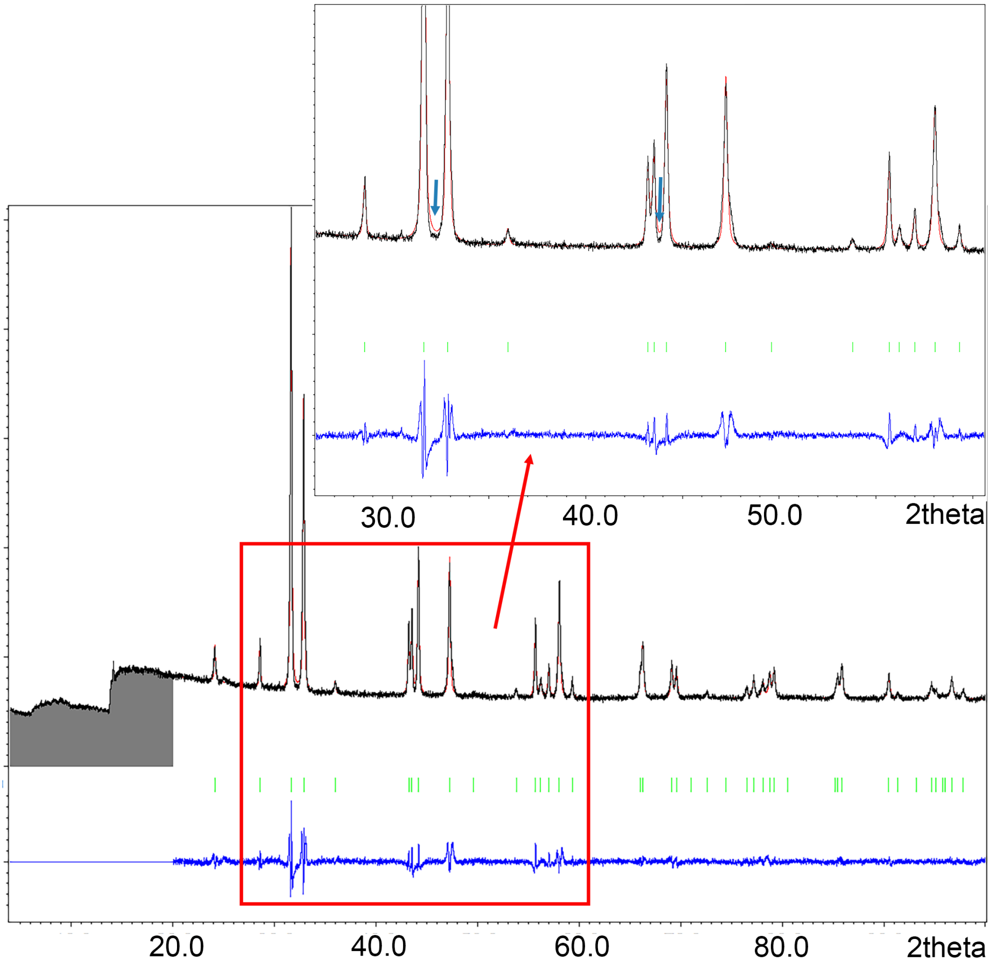

Figure 3.8: Raw (black), calculated (red) and difference (blue) powder XRD patterns for $La_{0.25}Sr_{1.75}MnO_{4\pm\delta}$. The calculated pattern was obtained from the Le Bail fit. The blue arrows show small mismatches between the Le Bail fit and the experimental pattern, that could not be improved.

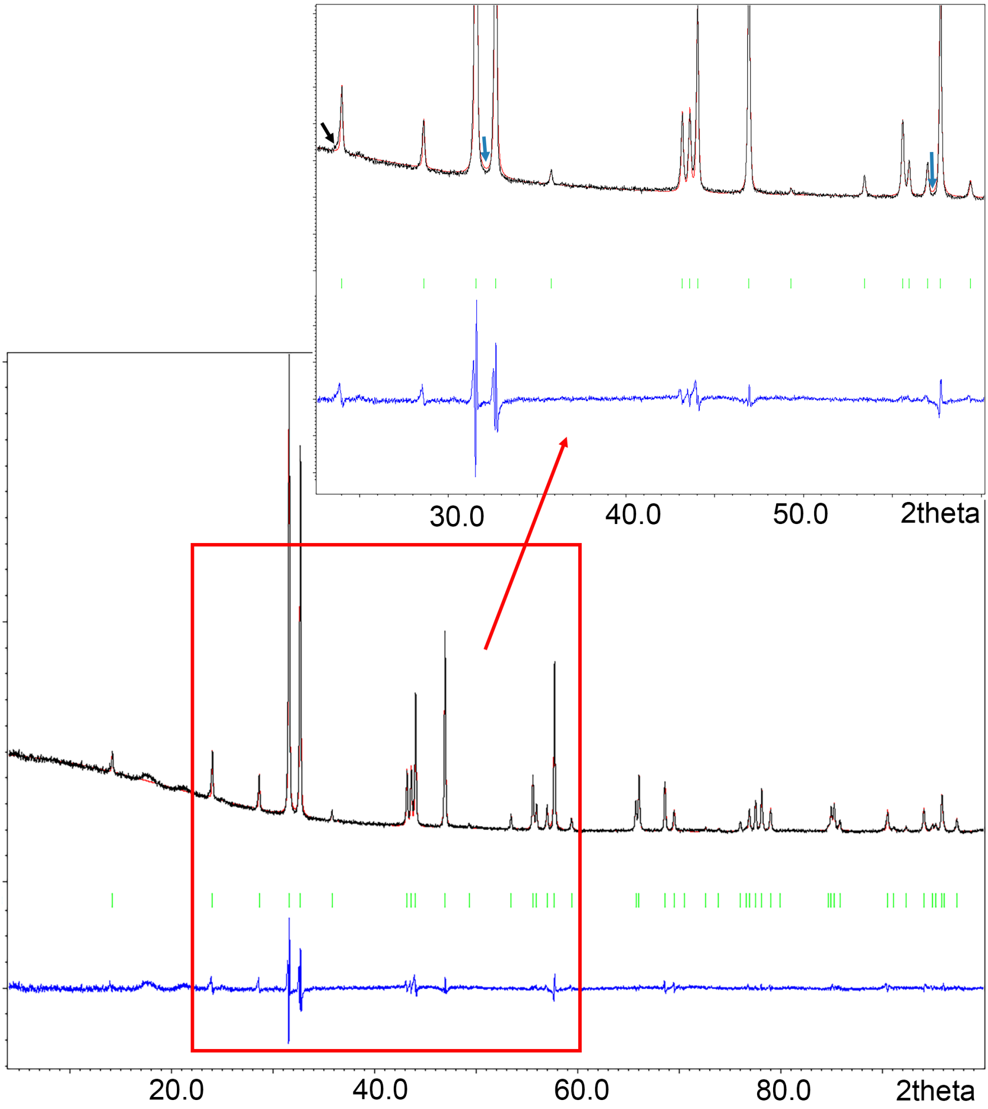

Figure 3.9: Raw (black), calculated (red) and difference (blue) powder XRD patterns for $La_{0.5}Sr_{1.5}MnO_{4\pm\delta}$. The calculated pattern was obtained from the Le Bail fit. The black arrow indicates a broadened peak, perhaps due to sample aging. The blue arrows show small mismatches between the Le Bail fit and the experimental pattern, that could not be improved.

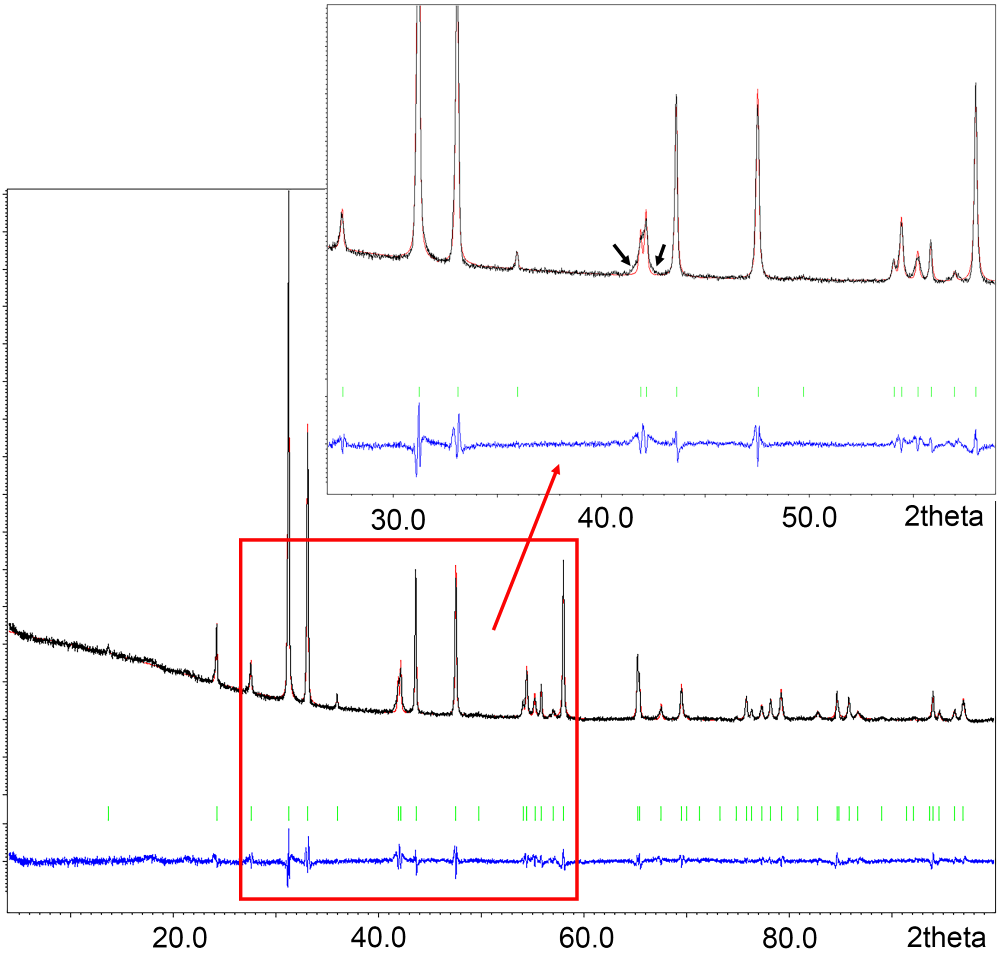

Figure 3.10: Raw (black), calculated (red) and difference (blue) powder XRD patterns for $La_{0.75}Sr_{1.25}MnO_{4\pm\delta}$. The calculated pattern was obtained from the Le Bail fit. The black arrows show peak broadening, probably due to aging of the sample.

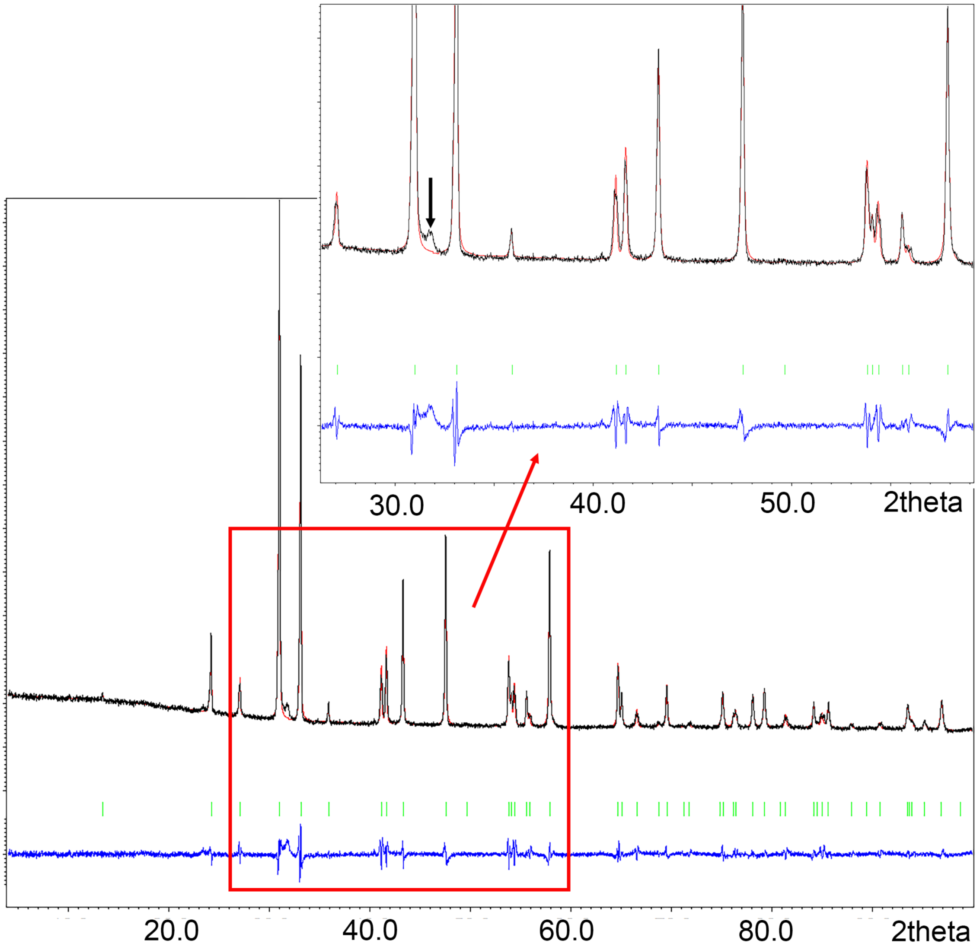

Figure 3.11: Raw (black), calculated (red) and difference (blue) powder XRD patterns for $LaSrMnO_{4\pm\delta}$. The calculated pattern was obtained from the Le Bail fit. The black arrow indicates a peak from an impurity phase.

x	0	0.25	0.5	0.75	1
literature	[58]	[1]	[1]	[64]	[63]
a (Å)	3.81829(6)	3.8289(3)	3.8616(2)	3.840	3.80
c (Å)	12.58165(2)	12.4263(13)	12.4211(11)	12.651	13.15
	[62]				
a (Å)	6.8125				
b (Å)	9.6228				
c (Å)	10.3801				
β(°)	91.8771				
phase 1					
a (Å)	3.78839(6)	3.8324(3)	3.86007(7)	3.81784(4)	3.81624(2)
c (Å)	12.4955(3)	12.422(1)	12.4135(5)	12.9040(3)	13.1324(2)
phase 2					
a (Å)	6.7931(4)				
b (Å)	9.6120(7)				
c (Å)	10.4258(5)				
β(°)	92.053(5)				
GOF	1.11	0.66	1.02	0.80	0.88
R_p	2.39	2.27	1.83	1.58	2.02
wR_p	3.83	3.50	2.78	2.22	3.00
annealed for 1h in N_2 at 550°C					
phase 1					
a (Å)	3.79577(8)				
c (Å)	12.5338(4)				
phase 2					
a (Å)	6.8102(4)				
b (Å)	9.6741(5)				
c (Å)	10.3877(6)				
β(°)	91.981(4)				
GOF	0.48				
R_p	1.62				
wR_p	2.14				

Table 3.1: Parameters from Le Bail fit on powder XRD data of as-synthesized $La_xSr_{2-x}MnO_{4\pm\delta}$ with x = 0, 0.25, 0.5, 0.75 and 1, compared to literature. For Sr_2MnO_4 also the cell parameters are given after an extra annealing cycle at 550°C in pure N_2.

For the x = 0.5 and 1 compositions, the literature values are from the actual samples that we studied, as we received them from Dr. Pascal Roussel and Prof. Dr. Michael Hayward. However, we see a small difference in cell parameters (<0.017 Å) from our own powder XRD data than the ones that were published. This can be either due to the error from the experimental method, combined with the Le Bail refinement, or from the "aging" of the sample, since those publications were from 2017 and 2010 respectively, and the samples were kept in an Ar glovebox only from 2020 onwards. Some surface oxidation effects or adsorption of humidity might have affected the samples at some point. Before all *ex situ* and *in situ* experiments that will be described below, a prior heating cycle in pure N_2 was performed to desorb all those potential water or other

molecules. It was always checked with 3DED that this did not alter the structure.
The sample with composition x = 0.25 was resynthesized in the lab of Dr. Pascal Roussel in 2023, especially for our experiments. Here, the differences between our powder XRD measurement and the reported structure are < 0.004 Å.
Further, for the x = 0.75 sample, the deviations from the literature values are very large (for c even ∼ 0.25 Å). This might be because of differences in synthesis method (powder by the citrate gel method as described in section 3.2.1 versus crushed single crystals [64] [65]) and perhaps differences in oxygen deficiency after long-term storage. However, this sample will not be as extensively studied as the other ones, since it does not show any structure transformations upon hydrogen reduction, as will be discussed later in this chapter.
Finally, also for the self-synthesized Sr_2MnO_4 the differences between the cell parameters reported by literature and the ones observed by us are quite large (< 0.09 Å), both for the tetragonal phase (phase 1) as the impurity (phase 2). However, as shown on the bottom of 3.1, after an extra desorption heating cycle of 1 hour in nitrogen gas at 550°C, the cell parameters get closer to the literature values (< 0.05 Å).

3.2.2.1 Trend in Cell Parameters with Composition

Lanthanum has a valence that equals +3, where that of strontium is only +2. To preserve charge neutrality, different La/Sr ratios for different members of the $La_xSr_{2-x}MnO_{4\pm\delta}$ series can lead to different average manganese oxidation states and/or varying oxygen content. For the pristine samples with x = 0, 0.25 and 0.5, the Mn oxidation state in literature from iodometric titration [1] is +4, +3.79(3) and +3.64(3) respectively. However, the valence of an ion refers to the number of bonds it can make, and it can only have an integer value. Thus, in reality, we obtain a mixture of Mn^{4+} and Mn^{3+}. From the aforementioned three compositions, $La_{0.5}Sr_{1.5}MnO_{4\pm\delta}$ contains the largest amount of Mn^{3+}, which is known to be a Jahn-Teller active ion. That means that the octahedron is elongated in order to split two degenerate orbitals - i.e. having equal energy - as illustrated in Figure 3.12. This phenomenon can have a considerable effect: e.g. in $LiMnO_2$, the Jahn-Teller distortion can induce a bond length difference of up to 20 %. [66]

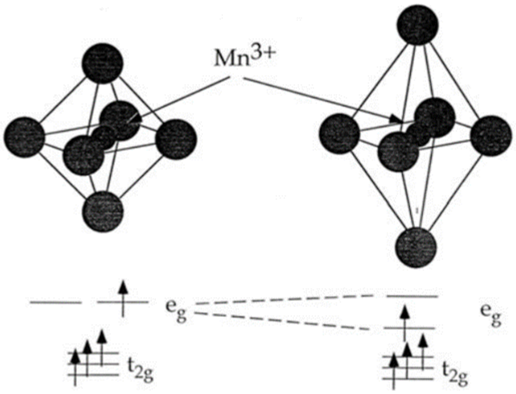

Figure 3.12: The Jahn-Teller effect: splitting of the degenerate e_g levels in an octahedron around Mn^{3+}. [66]

Taking this Jahn-Teller elongation into account, we would expect that the c parameter of the x = 0.5 composition would be longer than for x = 0 and 0.25. But, on contrary, the opposite is true: c = 12.53, 12.42 and 12.41 Å, for x = 0, 0.25 and 0.5 respectively. Apparently, another effect must play a role here. From literature [1], we know that there is also decreasing trend in the axial La/Sr-O bondlength, with increasing amount of lanthanum: 2.508(2), 2.437(1), 2.435(5), 2.426(7) Å, for x = 0, 0.25, 0.4 and 0.5. However, for the x = 0.6 composition, the bondlength increases again to 2.452(6) Å, and c = 12.451(1) Å. It is possible that $La_{0.5}Sr_{1.5}MnO_{4\pm\delta}$ has the smallest c parameter of the $La_xSr_{2-x}MnO_{4\pm\delta}$ series because of the competition between the Jahn-Teller elongation depending on the Mn^{3+} content and the smaller ion size with higher La content. However, it could also be caused by deviations in the defect structure or elemental distribution, which will be discussed in the next sections.

3.2.3 3D Electron Diffraction

3DED data of the $La_xSr_{2-x}MnO_{4\pm\delta}$ series for x = 0, 0.25, 0.5, 0.75 and 1 in the pristine state confirm the 4/mmm Laue class. The reflection conditions here can all be reduced to

$$hkl : h + k + l = 2n \tag{3.1}$$

from the body-centered lattice, which is indeed always fulfilled in the experimental sections from 3DED. Below, experimental [001], [010], [110] and [111] zones - indexed as I4/mmm - are given for pristine $La_{0.5}Sr_{1.5}MnO_{4\pm\delta}$ in Figure 3.13. In the synthesized Sr_2MnO_4 powder, 3DED indeed detected the presence of some $Sr_7Mn_4O_{15}$ impurity crystals.

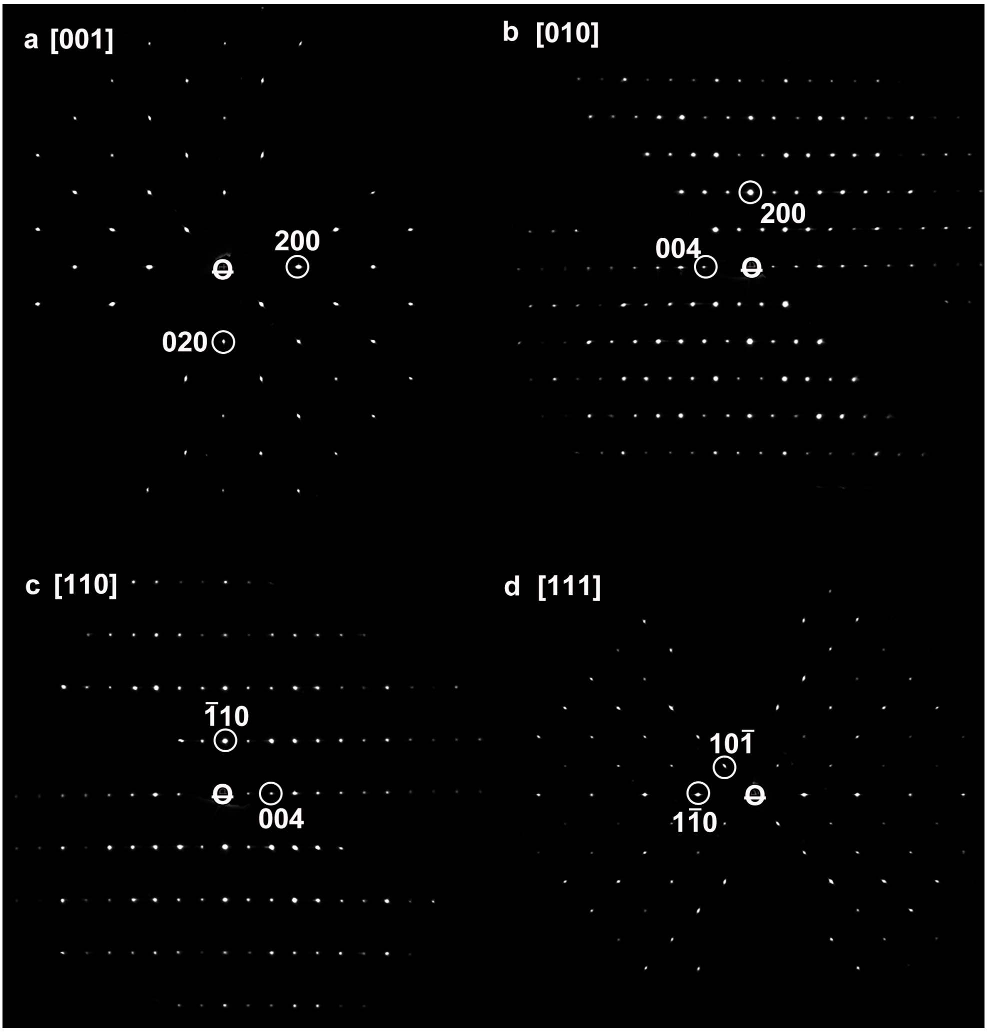

Figure 3.13: 2D reconstructed sections from 3DED of pristine $La_{0.5}Sr_{1.5}MnO_{4\pm\delta}$, indexed as I4/mmm. The origin is indicated with the symbol Θ, also in all sections below.

3.2.4 Defect Structure by high-resolution HAADF-STEM

High-resolution HAADF-STEM images of pristine $La_{0.5}Sr_{1.5}MnO_{4\pm\delta}$ detect the systematic presence of an amorphous surface layer of 2-3 nm (Figure 3.14a, red arrow). Previously Gonell et al. [67] already reported such amorphous edge in $La_{0.5}Sr_{1.5}MnO_{4\pm\delta}$ formed during synthesis. From high-resolution EDX (Figure 3.14b), it is clear that this is indeed no carbon contamination, but a form of lanthanum strontium manganite that is La rich compared to the bulk RP n=1 phase. Quantitative EDX analysis shows that the relative La concentration at the surface is $\langle La/Sr \rangle = 1.0$ ($\sigma = 0.1$), which is more than twice as large as in the bulk RP $n = 1$ structure: from EDX $\langle La/Sr \rangle = 0.36$ ($\sigma = 0.03$), theoretically $\langle La/Sr \rangle = \frac{1}{3}$. Note that for the quantification of the composition of the bulk RP n=1 structure, only non-oriented low magnification maps were taken into account. This is because quantification of EDX (as for EELS) of in-zone-oriented crystals is unreliable due to the excitation of guided light modes and relativistic losses. [68]

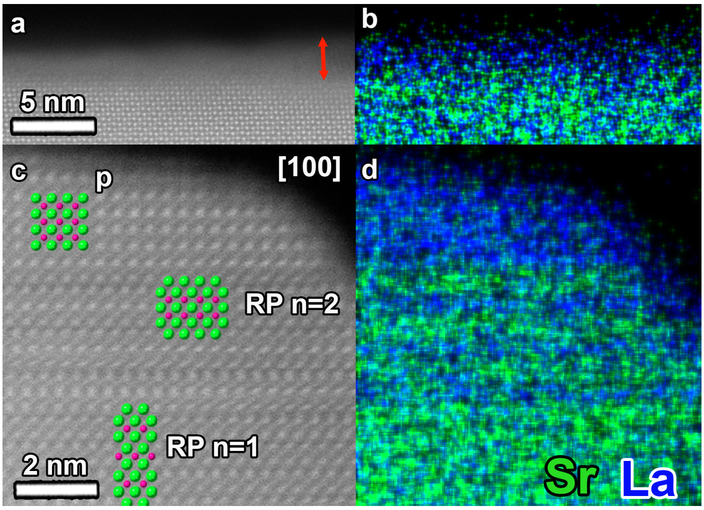

Figure 3.14: High-resolution HAADF-STEM images and EDX maps (in counts) of pristine $La_{0.5}Sr_{1.5}MnO_{4\pm\delta}$. In the EDX maps, lanthanum is represented as blue, strontium as green. In the models on top of the high-resolution images, La/Sr atoms are shown in green, Mn atoms in pink. (a,b) An amorphous layer is visible at the surface (red arrow) with a higher La content than the bulk structure. (c,d) Some crystals show perovskite on the edge, and many show Ruddlesden-Popper (RP) $n = 2$ layer defects, both in the bulk as at the surface. All areas deviating from RP $n = 1$ are La-rich.

Additionally, many higher order RP $n = 2$ layer defects were observed in the pristine material at the surface and in the bulk area, as can be seen in Figure 3.14c. As mentioned above, the Ruddlesden-Popper n = 2 structure has 2 subsequent perovskite layers in between 2 rock salt layers (as illustrated in the model in Figure 3.4c), compared to 1 perovskite layer for the RP n = 1 lattice (Figure 3.4b). Figure 3.14c also shows that for those RP n = 2 defects, the middle A cation (Sr, La) layer in between two perovskite layers has a brighter contrast. For HAADF-STEM images, we know that this contrast is Z-contrast: the heavier the atom, the more intense the scattering signal. [69] Since Z[Sr] = 38 and Z[La] = 57, it means that this A cation layer contains relatively more lanthanum

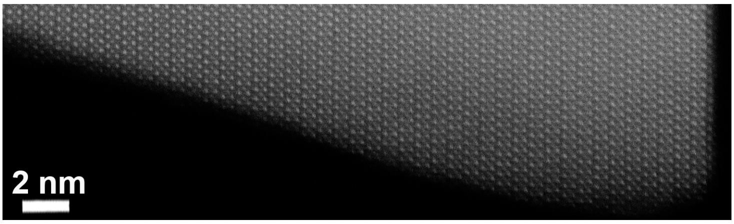

Figure 3.15: High-resolution HAADF-STEM image of pristine $La_{0.25}Sr_{1.75}MnO_{4\pm\delta}$ where no amorphous surface layer or RP n = 2 layer defects are observed.

than the n = 1 structure, which is confirmed by high-resolution EDX (see 3.14d). In some pristine $La_{0.5}Sr_{1.5}MnO_{4\pm\delta}$ crystals, perovskite blocks (La,Sr)MnO_3 are also present that epitaxially grew during synthesis on the {001} face of the RP n =1 phase (Figure 3.14c) and also have a higher lanthanum content than the RP n=1 bulk (Figure 3.14d). In contrast, high-resolution HAADF-STEM images of pristine $La_{0.25}Sr_{1.75}MnO_{4\pm\delta}$ systematically do not show any amorphous layer, RP n = 2 defects or perovskite domains, as illustrated in Figure 3.15. There, the RP n=1 bulk phase always stretches until the very edge of the crystals.

3.3 3DED of Hydrogen Annealed $La_xSr_{2-x}MnO_{4-\delta}$

To investigate the reasons behind the abovementioned anomalously large atomic displacement parameters [1] reported from powder XRD and ND upon heating in diluted hydrogen, we annealed samples of $La_xSr_{2-x}MnO_{4-\delta}$ for x = 0 , 0.25, 0.5, 0.75 and 1 in 5% H_2/Ar at high temperatures. These are the relevant extreme conditions of an SOFC anode. After annealing, we acquired 3DED data and powder XRD data to observe whether any structural transformations occurred.

3.3.1 Experimental Description

For the annealing experiments, powders of $La_xSr_{2-x}MnO_{4\pm\delta}$ for x = 0, 0.25, 0.5 and 1 were pressed uniaxially into pellets of 0.5-1 cm in diameter with a hydraulic press and placed in separate ceramic crucibles. Those were placed in a horizontal tube furnace with a ceramic tube inside, surrounded by insulating glass wool. Between the exhaust and the tube, a glass flask was partially filled with glycerin, giving a non-quantitative indication of the gas flow. To seal the set-up from air, the connections were tightened by KF (Kleinflansch) flanges: standardized connectors for vacuum applications.

On Sr_2MnO_4, three separate heating experiments were performed. First, the sample was heated directly in 5% H_2/Ar to 550°C for 1 hour, at a heating rate of 16°C/min, and cooled down to room temperature. In the second experiment, Sr_2MnO_4 was heated in N_2 to 550°C for 1 hour, with the same heating rate, and cooled down to room temperature. The third experiment consisted of performing a 5% H_2/Ar heating cycle to 550°C on part of the sample that was previously heated in nitrogen, again for 1 hour at the same heating rate, after which it was cooled down to room temperature. Powder XRD and 3DED data were acquired after each of the three experiments. 550°C was chosen as the maximum temperature, since it is known that the full reduction to $Sr_2MnO_{3.55}$ has already been reached at that point, and $Sr_2MnO_{4-\delta}$ decomposes above 600°C [59]. Annealing experiments in $5\%H_2/Ar$ on the La containing samples (x = 0.25, 0.5, 0.75 and 1) were performed with the same parameters, with a prior heating cycle in N_2 at 550°C for 1 hour, and with 700°C as a maximum temperature. 3DED and powder XRD data were taken at the end of each experiment. It was checked with 3DED that heating these samples in nitrogen gas at 550°C does not cause any structural transformation. For $La_{0.5}Sr_{1.5}MnO_{4-\delta}$, also the *in situ* powder XRD hydrogen annealing experiment from Sandoval et al. [1] was repeated at the University of Lille in the lab of Dr. Pascal Roussel. Here, the sample was heated in 3% H_2/N_2 to 800°C with a heating rate of 5°C/min. In this case, the prior heating cycle was performed in air at 800°C. This hydrogen annealed sample was also examined with 3DED at EMAT.

The reason why for the in-house annealing experiments of the La containing samples a temperature of 700°C was chosen, instead of 800°C as in the experiments of Sandoval et al. [1], is twofold. First, the non-linear section in the temperature dependence of the cell parameters (as visible in Figure 3.3) is situated in the region between 400 and 600°C. Thus, the potential structural transformation giving rise to this behaviour should already have taken place at 700°. Second, for the *in situ* TEM experiments, the decomposition can sometimes already happen at a lower temperature than *ex situ*. To be certain to avoid this and at the same time keep as many parameters equal between the *in situ* and *ex situ* set-up, we opted for 700°C as a maximum temperature in our experiments (except as a test in two additional gas and vacuum *in situ* heating experiments, as will be discussed further in this chapter).

3.3.2 Powder XRD

3.3.2.1 Sr_2MnO_4 as a Reference Sample

As a reference to check the validity of all annealing experiments, Sr_2MnO_4 was chosen. It is known from *in situ* powder neutron diffraction that this material transforms from its pristine tetragonal lattice (I4/mmm, a= 3.788925(2) Å, c = 12.4991(1) Å) to a monoclinic supercell when it is heated to 550°C under a 5% H_2/He flow ($P2_1/c$, a = 6.8517(2) Å, b = 10.8063(3) Å, c = 10.8134(3) Å and β=113,287(2)°), with as a composition $Sr_2MnO_{3.55}$ [59] [58]. The transformation matrices describing this structural change are given by

$$P = \begin{pmatrix} -0.5 & -2 & 2 \\ -0.5 & 2 & 2 \\ 0.5 & 0 & 0 \end{pmatrix} \tag{3.2}$$

and

$$Q = \begin{pmatrix} 0 & 0 & 2 \\ -0.25 & 0.25 & 0 \\ 0.25 & 0.25 & 0.5 \end{pmatrix} \tag{3.3}$$

with

$$\begin{pmatrix} a & b & c \end{pmatrix} P = \begin{pmatrix} a' & b' & c' \end{pmatrix} \tag{3.4}$$

and

$$Q\begin{pmatrix} u \\ v \\ w \end{pmatrix} = \begin{pmatrix} u' \\ v' \\ w' \end{pmatrix} \tag{3.5}$$

where a, b, c and a', b', c' are the old and new cell parameters respectively, and u, v, w and u', v', w' the old and new crystal orientations. This is also the transformation which was seen from our hydrogen annealing experiments.

3.3.2.2 Powder XRD Patterns and Cell Parameters

The powder X-ray diffraction patterns of the samples annealed in N_2 and 5% H_2 - as described in section 3.3.1 - are given in Figure 3.16, except for Sr_2MnO_4 annealed in N_2 only, which was already included in section 3.2.2. More detailed patterns, including calculated patterns from the Le Bail fit and zoomed areas, are given in Figures 3.17, 3.18, 3.19, 3.20 and 3.21. Table 3.2 lists the cell parameters from the Le Bail fit. For hydrogen annealed $La_{0.25}Sr_{1.75}MnO_{4-\delta}$ and $La_{0.5}Sr_{1.5}MnO_{4-\delta}$, extra reflections are present in the patterns which cannot be indexed in the I4/mmm space group of the pristine phase, as indicated by the black arrows in Figure 3.18 and 3.19.

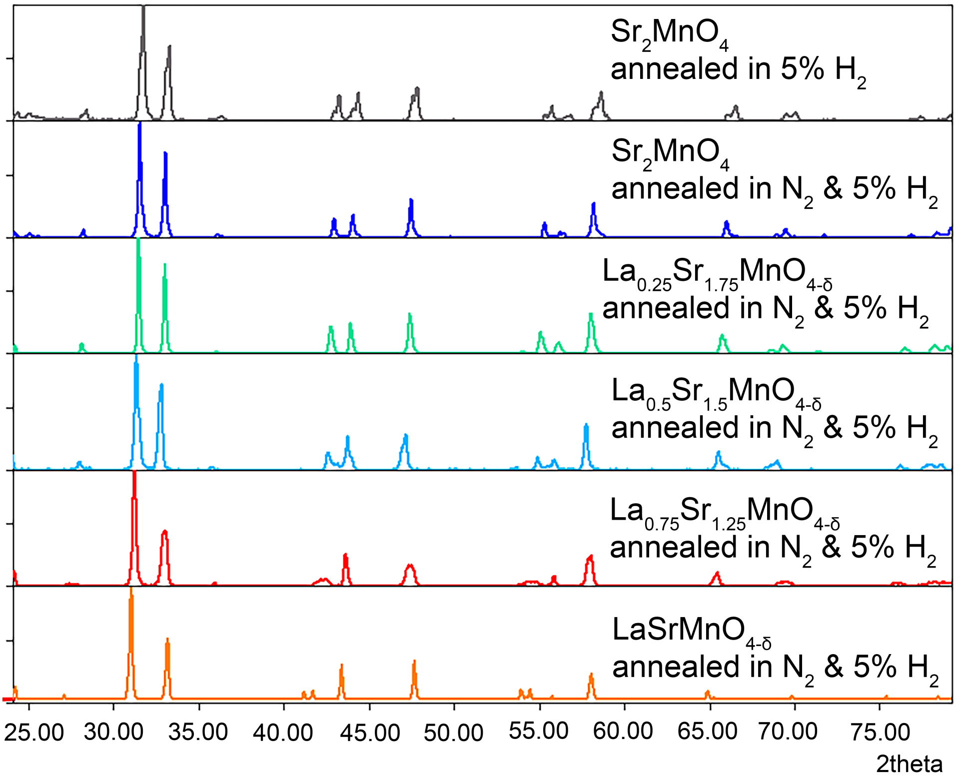

Figure 3.16: Power XRD patterns for $La_xSr_{2-x}MnO_{4-\delta}$ with x = 0, 0.25, 0.5, 0.75 and 1 after annealing in N_2 and 5% H_2/Ar.

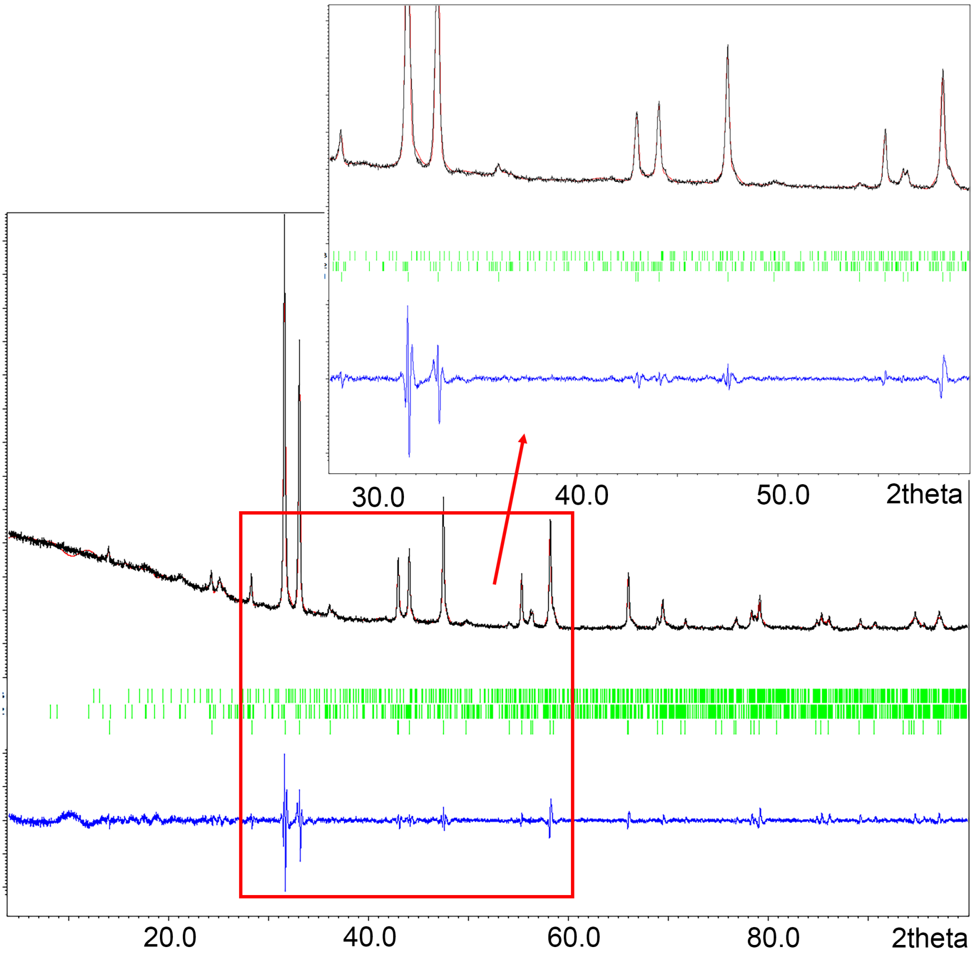

Figure 3.17: Raw (black), calculated (red) and difference (blue) powder XRD patterns for $Sr_2MnO_{4-\delta}$ after annealing in N_2 and H_2. The calculated pattern was obtained from the Le Bail fit.

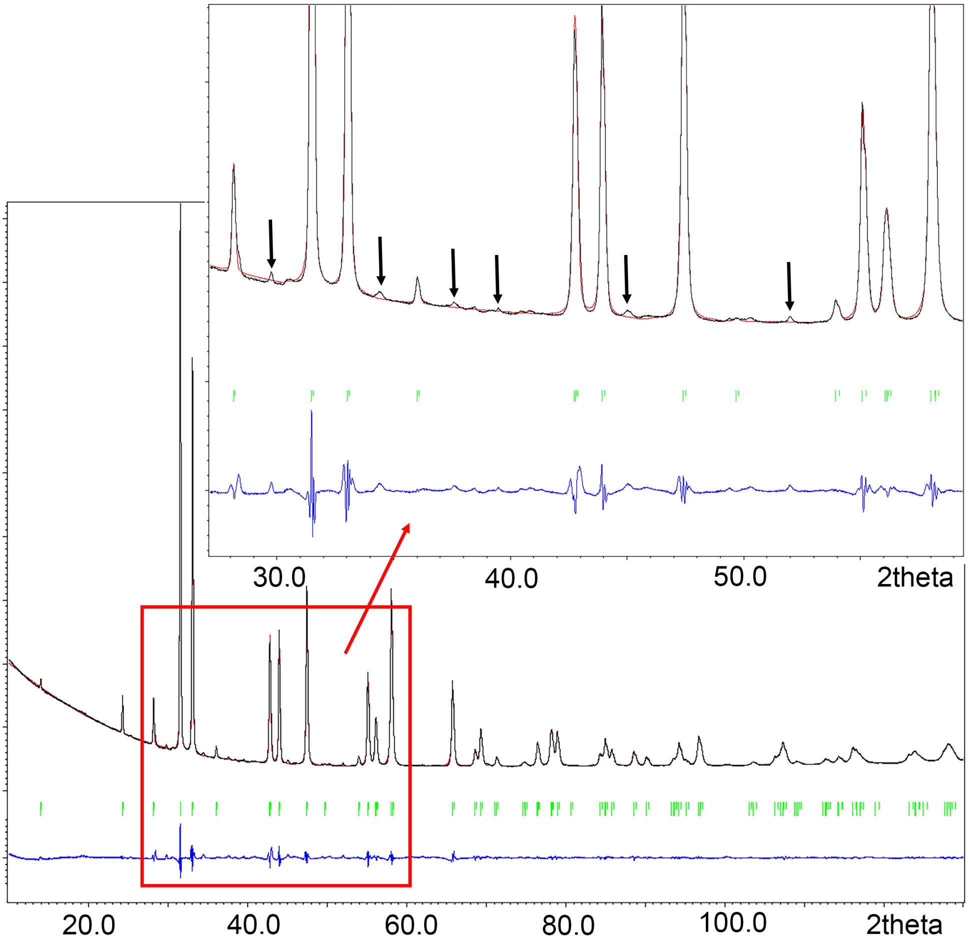

Figure 3.18: Raw (black), calculated (red) and difference (blue) powder XRD patterns for $La_{0.25}Sr_{1.75}MnO_{4-\delta}$ after annealing in N_2 and H_2. The calculated pattern was obtained from the Le Bail fit. The black arrows indicate reflections that are not present in the I4/mmm structure of the model.

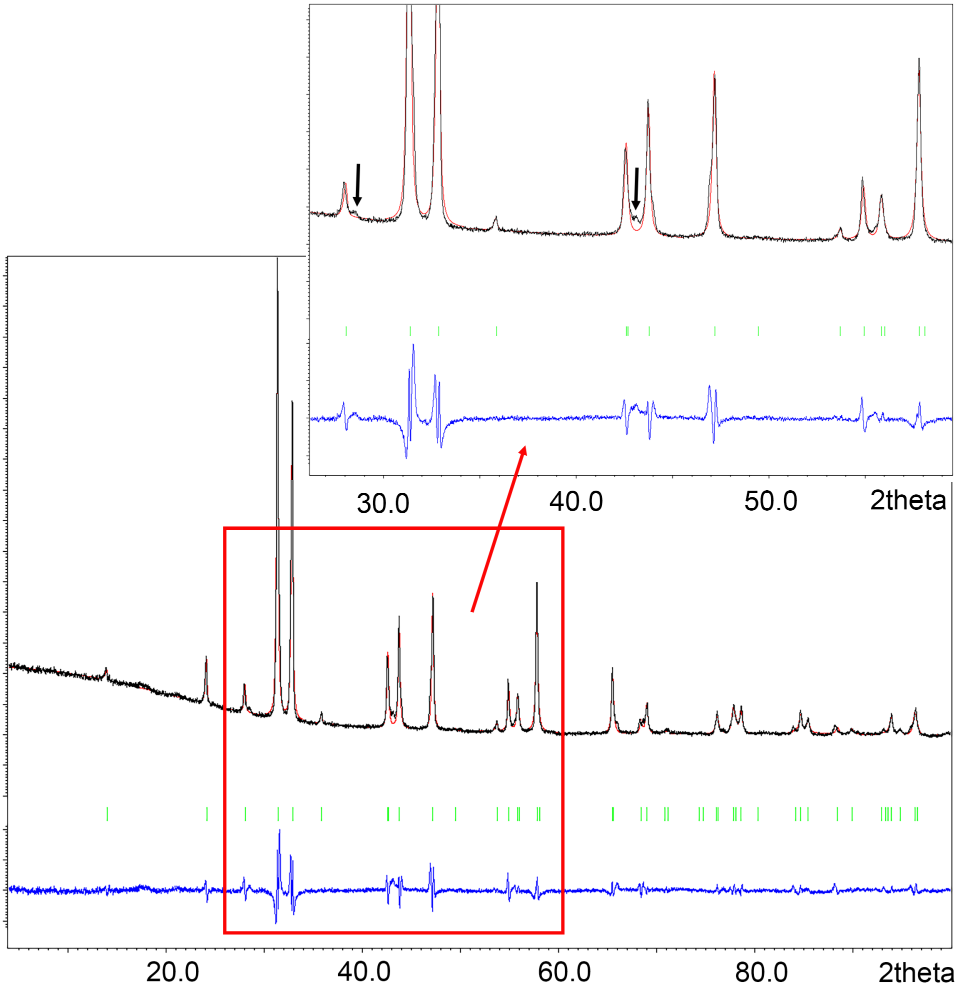

Figure 3.19: Raw (black), calculated (red) and difference (blue) powder XRD patterns for $La_{0.5}Sr_{1.5}MnO_{4-\delta}$ after annealing in N_2 and H_2. The calculated pattern was obtained from the Le Bail fit. The black arrows indicate reflections that are not present in the I4/mmm structure of the model.

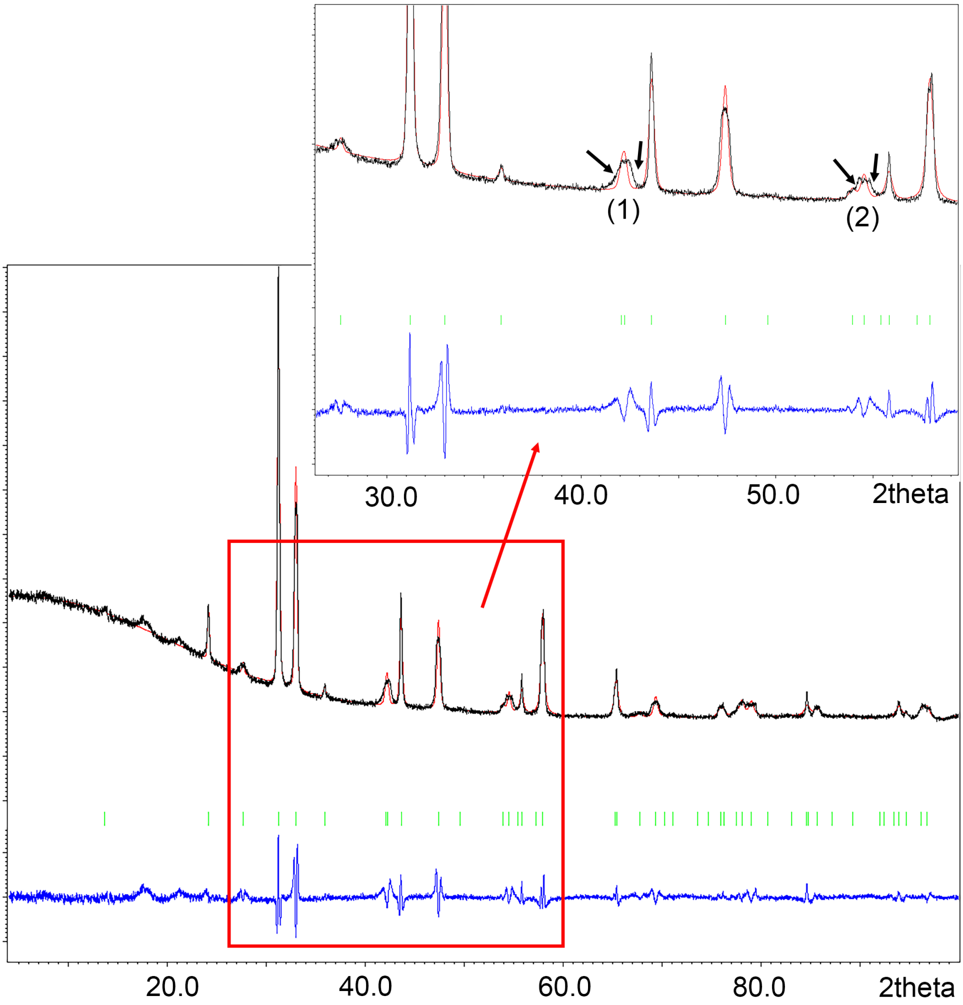

Figure 3.20: Raw (black), calculated (red) and difference (blue) powder XRD patterns for $La_{0.75}Sr_{1.25}MnO_{4-\delta}$ after annealing in N_2 and H_2. The calculated pattern was obtained from the Le Bail fit. The peak indicated with (1) was already broadened from the pristine state (see Figure 3.10), while the broadening at (2) happened during the reduction treatment.

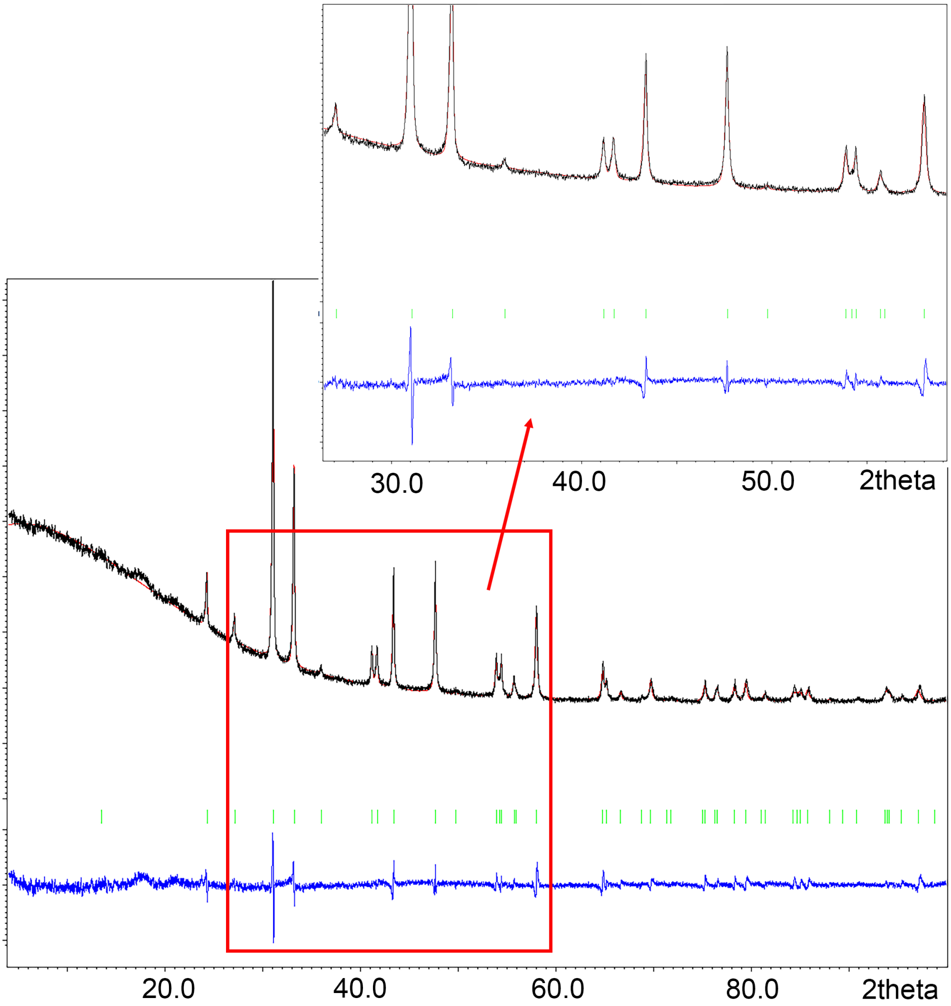

Figure 3.21: Raw (black), calculated (red) and difference (blue) powder XRD patterns for $LaSrMnO_{4-\delta}$ after annealing in N_2 and H_2. The calculated pattern was obtained from the Le Bail fit.

x	0	0.25	0.5	0.75	1
phase 1					
a (Å)	3.8247(1)	3.8324(7)	3.8476(7)	3.8224(2)	3.80592(7)
c (Å)	12.6039(9)	12.6725(5)	12.684(4)	12.84(1)	13.1152(4)
phase 2					
a (Å)	6.773(3)				
b (Å)	9.682(4)				
c (Å)	10.382(5)				
β(°)	91.97(3)				
phase 3					
a (Å)	6.82(1)				
b (Å)	10.89(1)				
c (Å)	10.95(2)				
β(°)	113.5				
GOF	1.16	3.92	1.59	1.18	0.61
R_p	2.30	1.39	2.92	2.05	1.34
wR_p	3.54	2.16	4.32	3.26	1.71

Table 3.2: Parameters from Le Bail fit on powder XRD data of $La_xSr_{2-x}MnO_{4-\delta}$ with x = 0, 0.25, 0.5, 0.75 and 1, first annealed in N_2 and then 5% H_2/Ar.

For $Sr_2MnO_{4-\delta}$, after the heat treatment, the transformation from the oxidized to the reduced phase was not complete, as illustrated in Figure 3.22. In this figure, the red and green experimental diffraction patterns (first and third) are from as-synthesized and N_2 annealed Sr_2MnO_4 respectively. These powders consist of a mixture of the tetragonal β-Sr_2MnO_4 (calculated peaks in red) and a monoclinic impurity (database peaks in light blue). The small peak shift between those powders is due to the difference in cell parameters, as was listed in Table 3.1. After annealing in 5% H_2/Ar only (second pattern, dark blue), additional peaks appear that agree with the reduced monoclinic phase of $Sr_2MnO_{4-\delta}$, of which the exact oxygen deficiency is not completely certain. But the peaks of tetragonal Sr_2MnO_4 remain present as well, indicating this is a mixture of three phases (including the original impurity). As can be seen from the orange (bottom) pattern, the combination of a N_2 and a 5% H_2/Ar results in a much larger fraction of the reduced phase. Further, the cell parameters then agree quite well with the ones from literature for $Sr_2MnO_{3.55}$, as in Table 3.2, which will be discussed in the next section. No successful cell parameter refinement could be performed for the sample that was only annealed in hydrogen gas. It is possible that more intermediate phases were present in this sample, due to the incomplete reduction. Therefore, also for the lanthanum doped samples, the prior nitrogen cycle was included before the hydrogen cycle in the reduction treatment.

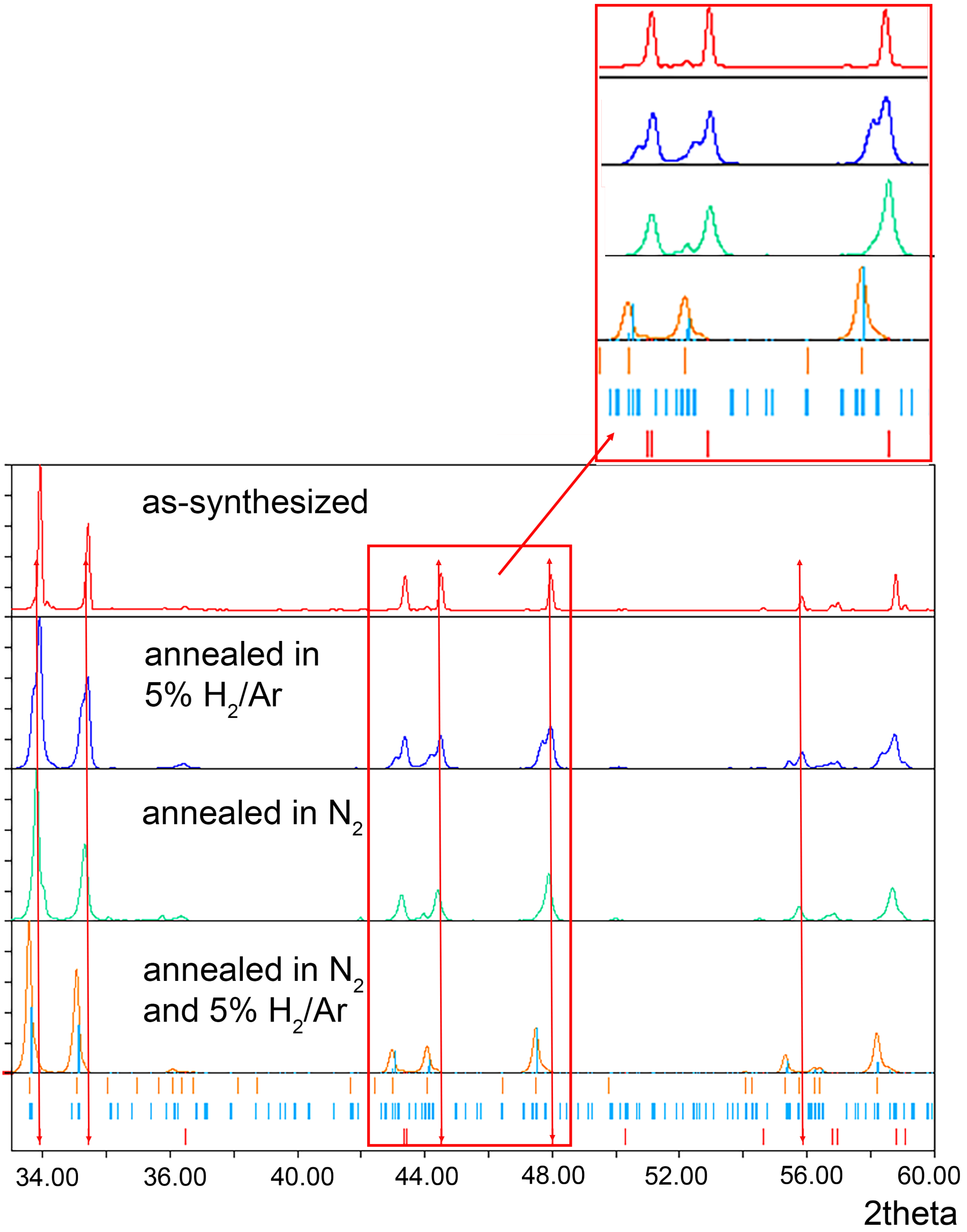

Figure 3.22: Comparison of different heat treatments for $Sr_2MnO_{4-\delta}$. As-synthesized (red), annealed in 5% H_2/Ar (dark blue), annealed in N_2 (green) and in both N_2 and 5% H_2/Ar (orange). Calculated peaks for Sr_2MnO_4 are given in red, for the $Sr_7Mn_4O_{15}$ impurity in light blue and for $Sr_2MnO_{3.55}$ in orange.

3.3.2.3 Discussion of the Cell Parameter Evolution upon Hydrogen Annealing

Figure 3.23 shows the cell parameter evolution of $La_xSr_{2-x}MnO_{4-\delta}$ for *a* and *c* upon annealing in diluted hydrogen atmosphere, both from our experiments (for x = 0.25, 0.5, 0.75 and 1) as from literature (only for 0.25 and 0.5) [1]. In all compositions, the *a* parameter slightly decreases after the reduction treatment. Only for $La_{0.25}Sr_{1.75}MnO_{4-\delta}$, both the experimental and the literature value for *a* remain the same. On the other hand, the *c* parameter significantly increases for both $La_{0.25}Sr_{1.75}MnO_{4-\delta}$ and $La_{0.5}Sr_{1.5}MnO_{4-\delta}$ (both experimentally as in literature), but slightly decreases for the x = 0.75 and x = 1 compounds.

The elongation of the *c* parameter for x = 0.25 and 0.5 could be explained by the aforementioned Jahn-Teller effect, since part of the Mn^{4+} ions are reduced to Jahn-Teller active Mn^{3+} ions. However, upon reduction, a part of the already existing Mn^{3+} ions transforms into Mn^{2+} as well, which is not Jahn-Teller active. From iodometric titration, it is known that the average Mn valence of $La_{0.25}Sr_{1.75}MnO_{4-\delta}$ is reduced from +3.79 to +2.91 upon heating to 740°C in 3%H_2/N_2, and to +2.82 upon further heating to 850°C. [1] For $La_{0.5}Sr_{1.5}MnO_{4-\delta}$, no data is available for the intermediate temperature, but upon reduction at 850°C, the Mn oxidation state changes from +3.64 to +2.90. Calculating the changes in percentage of Mn^{3+} with respect to the total Mn content for both samples, we get a 63% increase for x = 0.25 and only a 54% increase for x = 0.5. Note that the $La_{0.25}Sr_{1.75}MnO_{4-\delta}$ is reduced more strongly than $La_{0.5}Sr_{1.5}MnO_{4-\delta}$ in the same conditions. Based on these numbers, it makes sense that the *c* parameter length increases, due to the Jahn-Teller elongation of the axial Mn-O bondlength. However, the increase for x = 0.25 would be expected to be largest, while in reality it is slightly larger for x = 0.5. Further, no experimental data is available to explain the decrease in c for $La_{0.75}Sr_{1.75}MnO_{4-\delta}$ and $LaSrMnO_{4-\delta}$ based on the amount of Mn^{3+} before and after annealing. Also the decrease of the *a* parameters can be linked to the Jahn-Teller distortion [1], although, there again, the effect is larger for x = 0.5 than for x = 0.25 while the increase in active Mn^{3+} content is larger for the x = 0.25 composition. Since the cell parameters obtained by XRD could not completely be explained using structural information from powder XRD alone, it was necessary to look in more detail. Therefore, the hydrogen annealed samples were also examined with 3DED, which will be discussed in the next section.

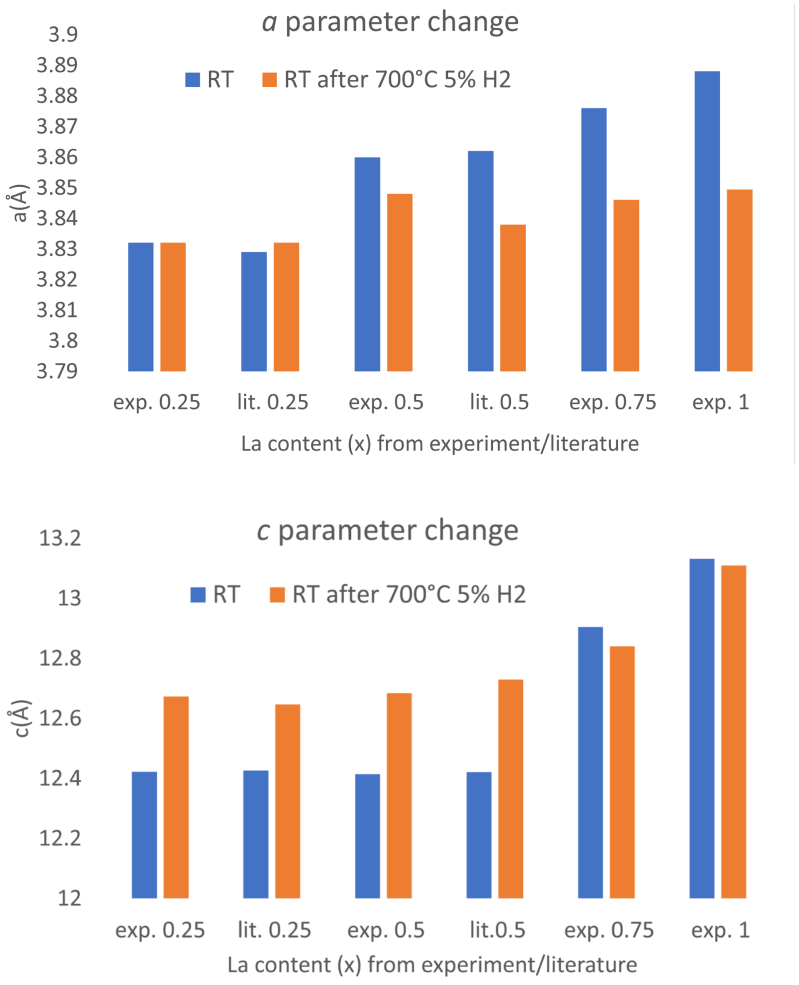

Figure 3.23: Comparison of the experimental and literature [1] values of the a and c parameters before and after annealing at 700°C in diluted hydrogen atmosphere.

3.3.3 3DED: 2D Incommensurately Modulated $La_{0.25}Sr_{1.75}MnO_{4-\delta}$

After the nitrogen and hydrogen treatment of $La_{0.25}Sr_{1.75}MnO_{4-\delta}$ at 700°C, precession 3DED revealed the transformation to an incommensurate 2D modulated structure with cell parameters a = 3.8324(7) Å and c = 12.6725(5) Å, and superspace group I4/mmm($\alpha\alpha$0)0000(α-α0)0000 where α = 0.2848(1). Figures 3.24b, 3.24e and 3.24h, show the reconstructed hk0 and h0l sections from 3DED and the modulation vectors $\vec{q}_1$ and $\vec{q}_2$. What this means, is that the structure cannot be described by a conventional three-dimensional periodic space group. To describe the atoms on the lattice, modulation waves are needed, which are considered as a periodic deformation in higher dimensional space, that is aperiodic in three-dimensional space. This leads to a description in a higher dimensional space, depending on the number of required modulation waves. [70] In diffraction patterns, the modulation results in so-called satellite reflections, which are usually weaker than the main reflections, and positioned at a fixed distance from those main reflections. The weaker reflections in Figure 3.24 are such satellites. Since these are not situated at rational positions in between the main reflections - and are consequently not leading to a periodic lattice -, the modulation is called incommensurate. This is the case for reduced $La_{0.25}Sr_{1.75}MnO_{4-\delta}$. No three-dimensional supercell can be found, and the only way to index the satellites of an incommensurately modulated structure is by using one or more additional vectors, called q vectors. They start at the reflections originating from the average structure and are related to the periodicity of the modulation itself, which is not commensurate with the periodicity of the average structure. For indexing the diffraction patterns of reduced $La_{0.25}Sr_{1.75}MnO_{4-\delta}$, two q vectors are required: $\vec{q}_1 = 0.2848(1) \cdot (\vec{a}^* + \vec{b}^*)$ and $\vec{q}_2 = 0.2848(1) \cdot (\vec{a}^* - \vec{b}^*)$. Now, we need 5 indices $hklmn$ for complete indexation, as can be seen in Figure 3.24b, 3.24e and 3.24h. Here, the reflection conditions on hkl are the same as for I4/mmm, i.e. hkl: $h+k+l = 2n$. No reflection conditions are observed on the fourth and fifth indices m and n. This corresponds to the (3+2)-dimensional super space group I4/mmm($\alpha\alpha$0)0000(α-α0)0000 in the notation developed by Yamamoto [71]. α equals in this case 0.2848(1), and indicates the length of the q vector components along the $\vec{a}^*$ and $\vec{b}^*$ direction. Here, the lengths are equal, and the fourfold symmetry is retained. The symbol "0000" means there is no extra translation. For clarity, representations of the cell in reciprocal space from Pets 2 are added in Figure 3.25. This supports and illustrates the indexation of the satellites with the two q vectors $\vec{q}_1$ and $\vec{q}_2$.

Note that it can sometimes be difficult to decide for diffraction data whether the structure is 2D modulated or we have a superposition of two twins that are only 1D modulated. A twinned structure is a symmetrical intergrowth of crystals, having the same structure but oriented in a way that can be described by a twin law, e.g. a rotation or a mirror plane. [72] However, in the current case, the satellites in the h0l section (3.24e) can only be indexed by a combination of $\vec{q}_1$ and $\vec{q}_2$, which excludes the possibility of a twinned four-dimensional structure with only one q vector.

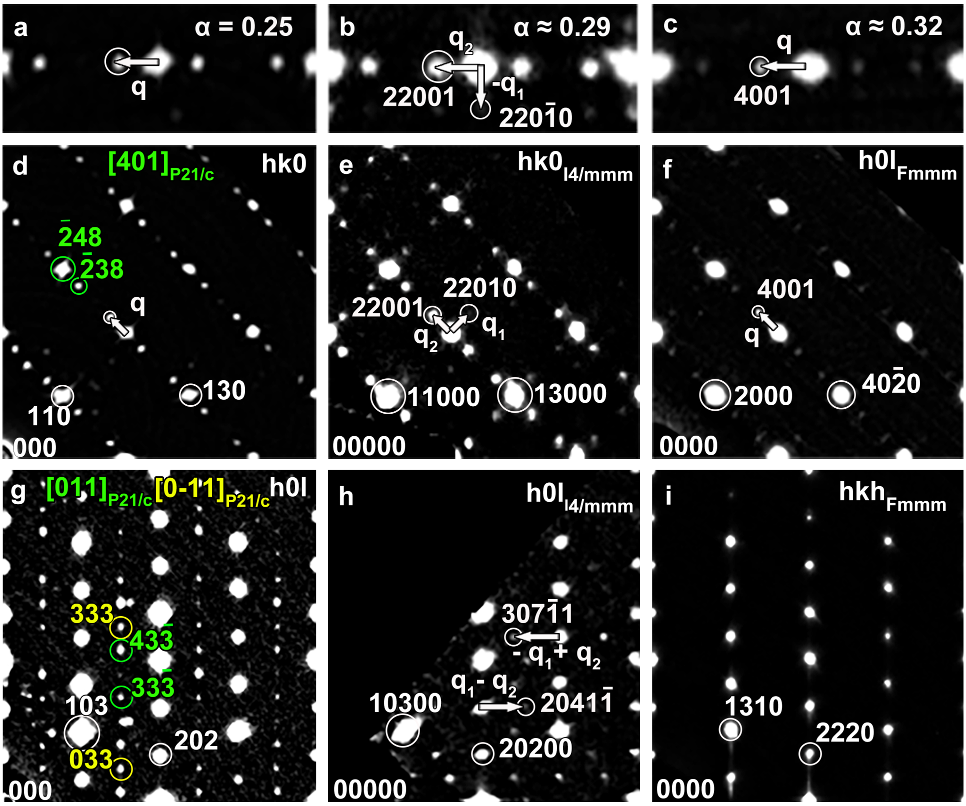

Figure 3.24: Reconstructed hk0, h0l and hkh sections from 3DED for annealed $La_xSr_{2-x}MnO_{4-\delta}$ at 700°C in 5% H_2/Ar with x = 0 (d, g), 0.25 (e, h) and 0.5 (f, i). The q vectors are indicated by arrows. Two twins of $P2_1/c$ are indexed in green and yellow. In a-c, details from the hk0 or h0l sections in d-f are given to illustrate the trend in the modulation wavelength. α is 0.25, 0.29 and 0.32 for x = 0, 0.25 and 0.5 respectively.

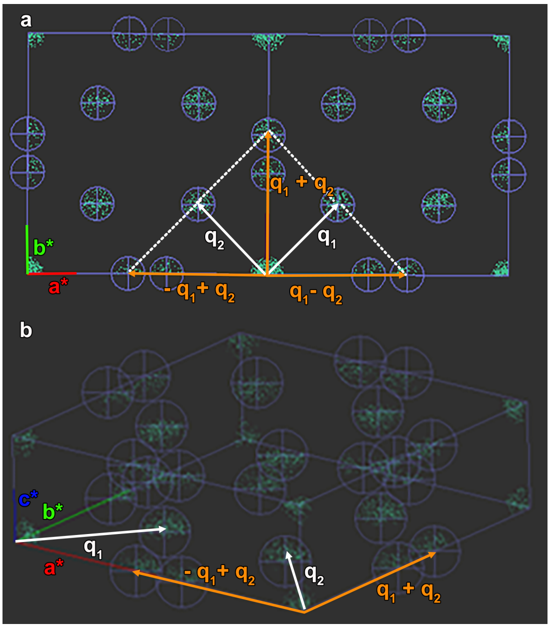

Figure 3.25: Representations of the cell in reciprocal space from Pets2, clarifying the indexation of the satellites with q vectors $\vec{q}_1$ and $\vec{q}_2$ (white). Sum vectors are indicated in orange. The cell in reciprocal space is indicated in purple.

A very similar (3+2)D structure was already found for oxygen deficient $LaSrCuO_{3.5}$ with in-zone electron diffraction by Hadermann et al. [73], with a somewhat different modulation wavelength ($\alpha \approx 0.22$). There, the modulation was driven by oxygen vacancy order. That is also the most likely physical source of the modulation in $La_{0.25}Sr_{1.75}MnO_{4-\delta}$, since reduction in the hydrogen atmosphere takes atomic oxygen from the lattice and creates oxygen vacancies. Starting from a similar model as $LaSrCuO_{3.5}$ and using the precession 3DED data, we could dynamically refine the atomic positions, positional and occupancy modulation parameters and atomic displacement parameters for modulated $La_{0.25}Sr_{1.75}MnO_{4-\delta}$. For the same sample, the Rietveld refinement was done from powder XRD as well. In Table 3.4 and 3.5, the resulting parameters for both refinements are listed. The R-factor was calculated either for all observed reflections (R(obs); all), or only the observed main reflections but not the satellite reflections (R(obs); main). Details on the 3DED data acquisition and data reduction are given in Table 3.3.

Table 3.5 also list some specialized parameters for the dynamical refinement from 3DED. First, there is the maximal diffraction vector g(max), which is the resolution limit on the used reflections for the refinement. Further, $S(g)$(max) is the so-called maximal excitation error, i.e. the maximal deviation of the reflection from the exact Bragg condition (as in equation 2.1). Since the data were taken while precessing the beam, the excitation error varies along the precession path. The parameter $RS(g)$ expresses how well a reflection is "covered" by the precession movement. If the reflection reaches the exact Bragg condition one or two times, $RS(g)$ is equal to or smaller than 1. If it never fulfills the Bragg condition, $RS(g) > 1$. That way, both $S(g)$(max) and $RS(g)$(max) are filters of the program to decide whether a reflection is observed or not. There is still a difference between $S(g)$(max)(matrix) and $S(g)$(max)(refine). Where the former sets a limit on the number of calculated dynamical intensities, the latter selects which reflections from the experimental data are used. Last, the number of integrations steps refers to how many steps are taken for the integration of the intensities over all beam orientations along the precession path. [49]

One discrepancy between the two types of structure refinements is the observation of more satellites by 3DED than XRD: for the latter only satellite reflections with indices l,m = 0,1 or 1,0 are experimentally visible, whereas indices up to 2 can be distinguished by 3DED, including the mixed indices l,m = 1,1. This can be explained by the higher sensitivity of electrons versus X-rays for light elements next to heavy elements. Further, the powder that was used for XRD might contain crystals that did not transform to the modulated structure and even an impurity. This is illustrated in Figure 3.26, which shows the raw (black), calculated (red) and difference (blue) powder pattern after the Rietveld refinement. Some satellites are not observed in the experiment powder data (red arrows), whereas others are (black arrows). The shoulder indicated with the blue arrow suggests the presence of an impurity.

For all atoms, small positional modulation waves were introduced, that describe the atomic displacement from their average position. With t and u as the coordinates of the fourth and fifth dimension, positional modulation waves are given by

$$x(t) = \sum_i xs_i \sin(2\pi i t) + xc_i \cos(2\pi i t) \tag{3.6}$$

$$y(t) = \sum_i ys_i \sin(2\pi i t) + yc_i \cos(2\pi i t) \tag{3.7}$$

$$z(t) = \sum_i zs_i \sin(2\pi i t) + zc_i \cos(2\pi i t) \tag{3.8}$$

where the same holds for u.

Because of the presence of higher order satellites in the 3DED data, a higher number of modulation waves can be used in the 3DED refinement versus the powder XRD refinement. However, because of the tetragonal symmetry of the super space group, in this case pairs of harmonic modulation waves need to be introduced in Jana2020. That means that if satellite reflections are only present up to the first order - as in the powder XRD data-, we need to add not one, but two modulation waves. The same holds for the 3DED data, where satellites up to the second order are visible in the diffraction patterns, but four modulation waves should be introduced.

Parameter	
Temperature (K)	293
Crystal system average structure	tetragonal
Super space group symbol	I4/mmm($\alpha\alpha$0)0000(α-α0)0000
a, c (Å)	3.894(7), 12.61(2)
q_1, q_2	$0.29 \cdot (\vec{a}^* + \vec{b}^*), 0.29 \cdot (\vec{a}^* - \vec{b}^*)$
Electron wavelength (Å)	0.0251
Precession angle (°)	1
Precession frequency (Hz)	100
Tilt range (°)	131
Tilt step (°)	1
Completeness (%)	74
Resolution ($\sin\theta_{max}/\lambda$) (Å^{-1})	1.4
Selected area aperture (nm)	200
Detector	ASI Cheetah direct electron detector
Exposure time (s)	1
Beam stop	yes

Table 3.3: Crystallographic details of 3DED data collection, data reduction and dynamical structure refinement for modulated $La_{0.25}Sr_{1.75}MnO_{4-\delta}$.

Parameter	**3DED**	**powder XRD**
a, c (Å)	3.894(7), 12.61(2)	3.8323(3), 12.672(2)
α (q vector)	0.29*	0.289(7)
La/Sr (x,y,z)	0, 0, 00.3530(1)	0, 0, 0.3544(6)
La/Sr (xs$_{1/2}$/ys$_{1/2}$, zs$_{1/2}$)	0.0187(2), 0*	0.000(8), 0*
La/Sr (xc$_{1/2}$, yc$_{1/2}$, zc$_{1/2}$)	0*, 0*, 0*	0*, 0*, 0.002(3)
La/Sr (xs$_3$, ys$_3$, zs$_3$)	0*, 0.0028(3), 0*	n.a.
La/Sr (xs$_4$, ys$_4$, zs$_4$)	0.0028*, 0*, 0*	n.a.
La/Sr (xc$_{3/4}$, yc$_{3/4}$, zc$_{3/4}$)	0*, 0*, 0.00340(8)	n.a.
La,Sr (occ)	0.125*, 0.875*	0.125*, 0.374(2)
La/Sr (U$_{11}$, U$_{33}$ or U$_{iso}$)	0.0401(6), 0.023(1)	0.001*
Mn (x,y,z)	0, 0, 0	0, 0, 0
Mn(xs$_{1/2}$/ys$_{1/2}$, zs$_{1/2}$)	0.0029(2), 0*	0.01(2), n.a.
Mn (xs$_3$, ys$_3$, zs$_3$)	0*, -0.0185(3), 0*	n.a.
Mn (xs$_4$, ys$_4$, zs$_4$)	-0.0185*, 0*,0*	n.a.
Mn (U$_{11}$, U$_{33}$ or U$_{iso}$)	0.003(4), 0.0006(8)	0.001*
O1 (x,y,z)	0, 0, 0.1570(5)	0, 0, 0.163(4)
O1 (xs$_{1/2}$/ys$_{1/2}$, zs$_{1/2}$)	0.035(1), 0*	0.02(4)
O1 (U$_{iso}$) or (U$_{11}$, U$_{33}$)	0.041(2)	0.041*
O2 (x,y,z)	0, 0.5, 0	0, 0.5, 0
O2 (xs$_{1/2}$, ys$_{1/2}$, zs$_{1/2}$)	0.047(2), 0.016(1), 0*	0.07(3), -0.07(4), 0*
O2 (xs$_3$, ys$_3$, zs$_3$)	0*, 0.003(2), 0*	n.a.
O2 (xs$_4$, ys$_4$, zs$_4$)	0.002(2), 0*, 0*	n.a.
O2 (xc,yc,zc for 1/2/3/4)	0*, 0*, 0*	0*, 0*, 0*
O2 (o, oc$_{1/2}$)	0.66(2), -0.113(8)	0.62(5), -0.4(3)
O2 (oc$_3$, oc$_4$)	-0.04(1), 0.03(1)	n.a.
O2 (os for 1/2/3/4)	0*	n.a.
O2 (U$_{11}$, U$_{22}$, U$_{33}$)	0.028(4), 0.026(4), 0.005(4)	0.028*, 0.026*, 0.005*

Table 3.4: Parameters from the dynamical (3DED) and Rietveld (powder XRD) refinement of modulated La$_{0.25}$Sr$_{1.75}$MnO$_{4-\delta}$. Values with * have not been refined. If the parameter is indicated as 0*, it means that the symmetry requires it to be zero. See the next table for the R-factors and number of reflections.

Parameter	**3DED**	**powder XRD**
GOF (all)	8.42	12.64
R(obs); all	27.30	8.39
wR(obs); all	24.66	11.55
R(obs); main	9.64	7.61
wR(obs); main	11.68	11.61
R(obs); m,n = ± (0,1)	28.62	15.06
wR(obs); m,n = ± (0,1)	27.62	11.52
R(obs); m,n = ± (1,1)	37.45	n.a.
wR(obs); m,n = ± (1,1)	36.58	n.a.
R(obs); m,n = ± (0,2)	75.77	n.a.
wR(obs); m,n = ± (0,2)	83.11	n.a.
R(obs); m,n = ± (1,2)	86.53	n.a.
wR(obs); m,n = ± (1,2)	88.51	n.a.
# reflections; all	3744	258
# main reflections	285	71
# satellites ± (0,1)	1699	187
# satellites ± (1,1)	1377	/
# satellites ± (0,2)	165	/
# satellites ± (1,2)	168	/
# refined parameters	24	13
g(max) ($Å^{-1}$)	1.4	
Sg(max) (matrix) ($Å^{-1}$)	0.01	
Sg(max) (refine) ($Å^{-1}$)	0.1	
RSg(max) ($Å^{-1}$)	0.66	
# integration steps	90	

Table 3.5: R-factors and number of reflections from the dynamical (3DED) and Rietveld (powder XRD) refinement of modulated $La_{0.25}Sr_{1.75}MnO_{4-\delta}$. For the dynamical refinement, some additional specialized parameters are listed that are explained in the main text.

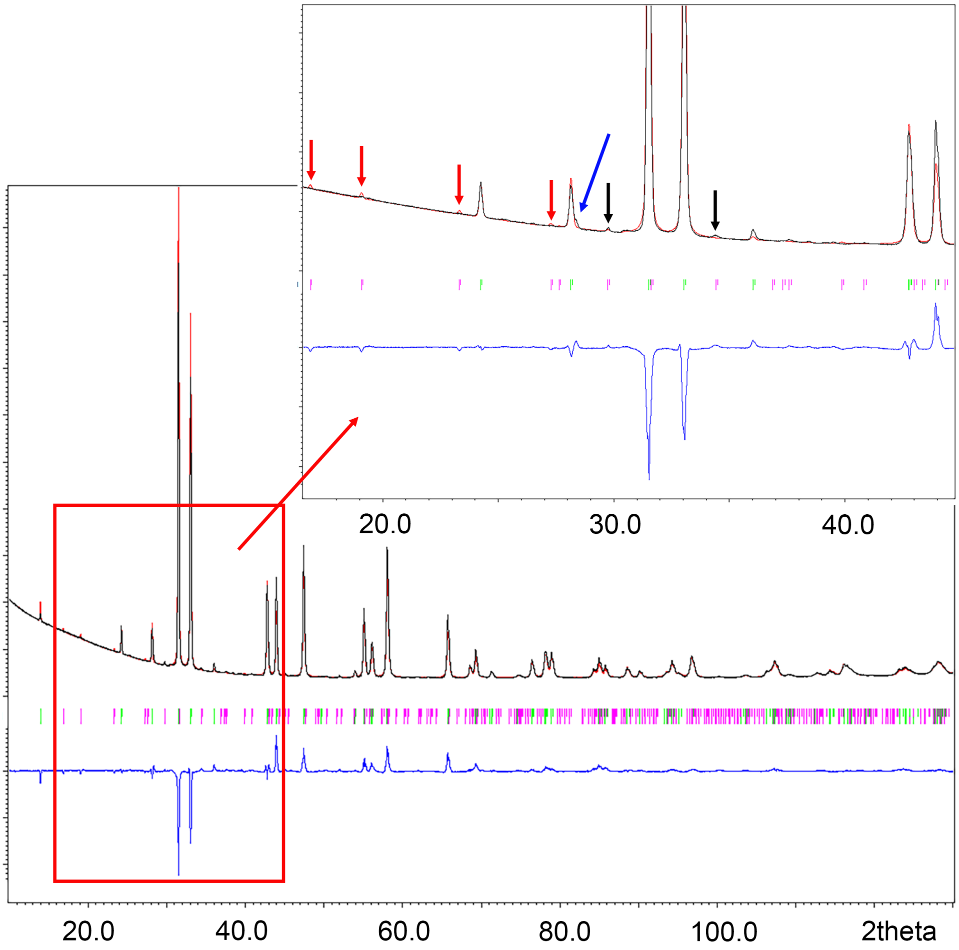

Figure 3.26: Raw (black), calculated (red) and difference (blue) powder XRD pattern after Rietveld refinement of which the parameters are given in Table 3.4 and 3.5. A zoom is given which shows that some satellite reflections are not observed in the raw data (red arrows), whereas others are (black arrows). Further, a peak shoulder is seen (blue arrow) that indicates the presence of an impurity. See text for explanation.

However, the largest modulation is the occupancy modulation of oxygen O2, with occupancy modulation waves given by

$$o(t) = o + \sum_i oc_i \cos(2\pi i t) \tag{3.9}$$

Figure 3.27 plots the occupancy modulation function for O2 as refined from precession 3DED and from powder XRD. No occupancy modulations were used for Mn in the 3DED refinement, since this leads to non-physical values. The large modulation for O2 originates from oxygen vacancy creation by the reduction treatment, leading to an ordered arrangement of octahedra and square pyramids as shown in Figure 3.28. This figure shows the Mn-O plane for the $t = 0$, $u = 0$ section through five-dimensional

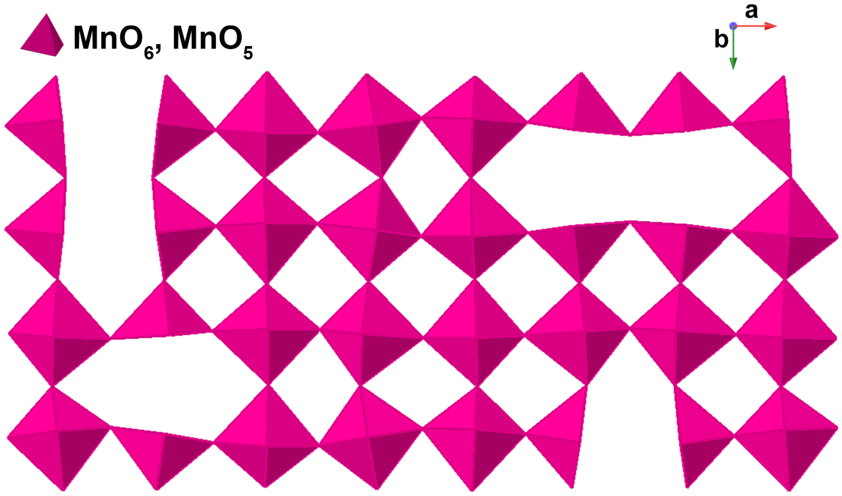

Figure 3.28: Schematic representation of the manganese coordination for the $t = 0$, $u = 0$ section through five-dimensional space of reduced $La_{0.25}Sr_{1.75}MnO_{4-\delta}$, seen along c. A threshold of 56% is applied to plot the oxygen position as filled. The vacancy ordering causes a pattern of octahedra and square pyramids.

space. Vacancy ordering occurs for the equatorial oxygen positions, and gives rise to an alternation between manganese octahedra and square pyramids. In the figure, a threshold of 56% was applied to plot the oxygen positions as filled. In Table 3.4, the refined coefficients of these modulation waves are abbreviated. s_i and c_i represent the coefficients of the sine and cosine terms of the i^{th} positional modulation wave or occupancy modulation wave (with the prefix "o"). Those coefficients can be positive or negative.

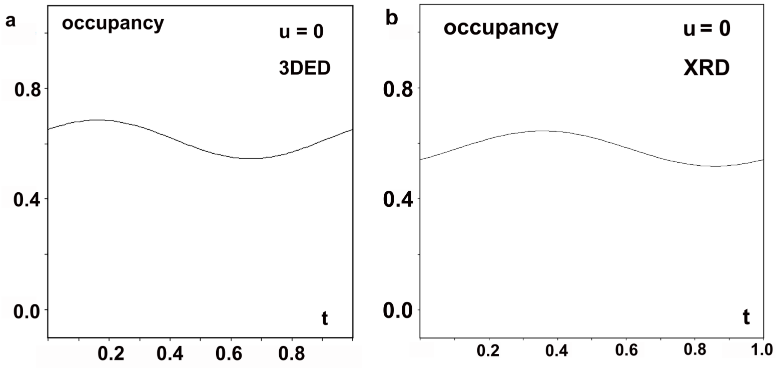

Figure 3.27: Occupancy modulation function of O2 in function of the fourth coordinate t with u = 0 from the dynamical 3DED refinement (a) and powder XRD refinement (b) of hydrogen annealed $La_{0.25}Sr_{1.75}MnO_{4-\delta}$.

The Rietveld refinement from powder XRD did not allow to refine the atomic displacement parameters to valid (positive) values, which is why they have been fixed in the refinement. Further, the occupancies of lanthanum and strontium could not be refined from 3DED (convergence to negative values or values larger than 1), which is why they were fixed as well. In the XRD refinement, the occupancy of Sr converged to a very low value. Probably, the data quality is not good enough to accurately refine the elemental occupancies.

It must be noted that from the reflection conditions only, also I4mm, I422 or I4 would be possible space groups of the average structure. However, in a recent paper from Klar et al. [47], it was shown that dynamical refinement from 3DED data can derive an inversion center and determine the absolute configuration, based on a significant decrease in the R-value. For 2D modulated $La_{0.25}Sr_{1.75}MnO_{4-\delta}$, we compared the refinements of the average structure with I4/mmm, I4mm, I422 and I4, of which I4/mmm gave the lowest R-value. Those R-factors are listed in Table 3.6.

Space group	**R main (%)**
I4/mmm	9.80
I4mm	11.25
I422	11.45
I4	14.72

Table 3.6: Comparison between the R-factors of the dynamical refinement of 2D modulated $La_{0.25}Sr_{1.75}MnO_{4-\delta}$ in I4/mmm, I4mm, I422 and I4.

3.3.4 3DED: 1D Incommensurately Modulated $La_{0.5}Sr_{1.5}MnO_{4-\delta}$

For $La_{0.5}Sr_{1.5}MnO_{4-\delta}$, the identical hydrogen gas heat treatment leads to a 1D incommensurate modulation, with a slightly longer modulation wave vector $\vec{q} = \alpha\ \vec{c}^*$ with α = 0.318(2), an orthorhombic superspace group Fmmm(00α)000 and cell parameters a = 5.4537(6) Å, b = 12.711(2) Å and c =5.4403(5) Å (rotated 45° along the c axis with respect to the I4/mmm parent cell). The reconstructed sections from 3DED are shown in Figure 3.24c, f and i. Again, based on the reflection conditions, also Fmm2, Fm2m, F2mm and F222 could be possible. Since the data quality did not allow dynamical refinement here, we opted for the highest symmetry as the most likely case. For the x = 0.5 composition, the satellites are much weaker than for the x = 0.25 composition (and even weaker after hydrogen treatment without the N_2 cycle). For this particular crystal, some weak reflections also appear along the $\vec{a}^*$ direction in the h0l section, but they stem from twinning and this composition is not two-dimensionally modulated. First, such reflections are not systematically present in all crystals. Moreover, no satellites are observed that arise from the combination of two different q vectors as e.g. in the h0l section of 2D modulated $La_{0.25}Sr_{1.75}MnO_{4-\delta}$ (Figure 3.24h).

3.3.5 3DED: $Sr_2MnO_{3.55}$

As a reference sample, $Sr_2MnO_{4-\delta}$ was annealed in 5% H_2/Ar at 550°C for 1h, with prior N_2 heating cycle as described above. This caused a conversion to the known $P2_1/c$ superstructure of $Sr_2MnO_{3.55}$ as expected from literature [58] [59] with a = 6.82(1) Å, b = 10.89(1) Å, c = 10.95(2) Å and β = 113.5(2)°, as in Figure 3.24a, 3.24d and 3.24g (main reflections in I4/mmm in white, two twins of $P2_1/c$ in yellow and green). The cell declared by Gillie et al. [58] is $a = \frac{1}{2}(-a_t - b_t + c_t)$, $b = 2(-a_t + b_t)$, $c = 2(a_t + b_t)$ (with the index t referring to the tetragonal subcell). The latter two equations correspond to a two-dimensional commensurate modulation with vectors $q_1 = \alpha\ (-\vec{a_t}^* + \vec{b_t}^*)$ and $q_2 = \alpha\ (\vec{a_t}^* + \vec{b_t}^*)$ where α = 0.25, similar to the one we observe for $La_{0.25}Sr_{1.75}MnO_{4-\delta}$, but commensurate instead of incommensurate. Therefore, that cell could be described by a supercell in the original paper. The first equation implies an additional shift of the whole vacancy ordered layer over $\frac{1}{2}(-a_t - b_t + c_t)$. Due to the glide plane perpendicular to c_t with a translation along $a_t + b_t$, satellites in the $\vec{a}_t^* + \vec{b}_t^*$ direction are extinct (Figure 3.24d). The different twin domains originate from lowering the symmetry when going from I4/mmm to the super structure.

3.3.6 Hydrogen Annealed $La_{0.75}Sr_{1.25}MnO_{4-\delta}$ and $LaSrMnO_{4-\delta}$

Additionally, two more compositions with higher lanthanum content x = 0.75 and x = 1, i.e. $La_{0.75}Sr_{1.25}MnO_{4-\delta}$ (I4/mmm, a =3.81784(4) Å and c = 12.9040(3) Å) and $LaSrMnO_{4-\delta}$ (I4/mmm, a = 3.81624(2) Å and c = 13.1324(2) Å) were heated to 700°C in 5% H_2/Ar after a prior nitrogen cycle at 550°C. This gave the cell parameters a =3.8224(2) Å and c = 12.84(1) Å for $La_{0.75}Sr_{1.25}MnO_{4-\delta}$, and a =3.80592(7) Å and c = 13.1152(4) Å for $LaSrMnO_{4-\delta}$, but did not lead to any structural change to the space group observable by 3DED.

3.3.7 Defect Structure of Hydrogen Annealed $La_{0.5}Sr_{1.5}MnO_{4-\delta}$

After annealing $La_{0.5}Sr_{1.5}MnO_{4-\delta}$ in N_2 and in 5% H_2/Ar as described above, high-resolution HAADF-STEM also revealed many perovskite (La,Sr)MnO_3 domains on the surface of the crystals, as illustrated in Figure 3.29. However, those domains are not as sharply demarcated as the perovskite regions in the pristine sample (see Figure 3.14c): in the hydrogen annealed sample, instead of sharp domain boundaries, distorted "transition regions" are present, up to 2 nm in width. This was not observed in the compound before hydrogen treatment. On the other hand, abundant higher-order RP n = 2 layer defects are still present after reduction as in the pristine sample. The higher Z contrast of the middle A cation layer in between the two perovskite blocks, indicates it is lanthanum rich compared to the layers bordering on the rock salt blocks.

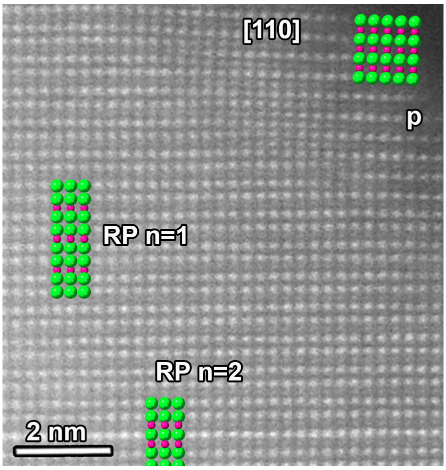

Figure 3.29: High-resolution HAADF-STEM image of $La_{0.5}Sr_{1.5}MnO_{4-\delta}$ after annealing at 550°C in N_2 and at 700°C in 5% H_2/Ar. RP n = 2 layer defects are still present, as in the pristine material. Now, also perovskite domains have grown on the surface, but instead of a demarcated boundary, there is a 2 nm transition region, which was not observed in the pristine sample. La/Sr cations are indicated in green, Mn cations in pink.

3.4 *In Situ* 3DED of $La_xSr_{2-x}MnO_{4-\delta}$ in Hydrogen Gas for x = 0, 0.25 and 0.5

To determine the relation between the features in the pristine crystals and those after reduction, we used *in situ* TEM, which allows to follow single crystals throughout the reduction reaction. Using a closed cell, $La_{0.5}Sr_{1.5}MnO_{4-\delta}$, $La_{0.25}Sr_{1.75}MnO_{4-\delta}$ and $Sr_2MnO_{4-\delta}$ were studied with *in situ* 3DED using the same reduction treatment in diluted hydrogen gas as above, with and/or without prior nitrogen cycle. An overview of all *in situ* experiments and their parameters for $Sr_2MnO_{4-\delta}$, $La_{0.5}Sr_{1.5}MnO_{4-\delta}$ and $La_{0.25}Sr_{1.75}MnO_{4-\delta}$ in (diluted) hydrogen gas is given in Table 3.7 and Table 3.8. 3DED was always acquired during the time intervals with stable temperature. During heating intervals, the morphology and diffraction of the crystals were checked as well.

La content	**N_2 cycle**	**H_2 cycles**	**Extra**
x = 0	no	5% H_2/He: RT -500°C: 1h, 500°C: 2h, 500-600°C: 1h, 600°C: 1h	
x = 0	RT - 500°C: 1h, 500°C: 1h, 500°C - RT: 1h	5% H_2/He: RT- 500°C: 100′, 500-550°C: 30′, 550°C: 1h, 10% H_2/He: 550°C: 16h, 550-600°C: 30′, 600°C: 1h, 600°C-550°C: 30′, 1.06E-5 mbar: 550°C - RT: 2h	
x = 0	RT - 550°C: 30′, 550°C: 1h, 550°C - RT: 2h	5% H_2/Ar: RT- 550°C: 30′, 550°C: 2h, 10% H_2/Ar: 1h, 25% H_2/Ar: 1h, 50% H_2/Ar: 2h, 100% H_2/Ar: 3h, 550°C-RT: 3h, RT-550°C: 90′, 550°C: 8h	- plasma cleaning: Ar instead of 25% O_2/Ar - at the end, the chip broke because of a short circuit in the heating system
x = 0.25	no	5% H_2/Ar: RT-550°C: 30′, 550°C: 2h30′ , 550°C-RT: 2h, RT-700°C: 45′, 700°C: 4h 700°C-RT: 2h30′	

Table 3.7: Parameters of *in situ* experiments of $La_xSr_{2-x}MnO_{4-\delta}$ in (diluted) H_2 for x = 0 and x = 0.25

La content	**N_2 cycle**	**H_2 cycles**	**Extra**
x = 0.5	no	5% H_2/He: RT - 400°C: 30′, 400°C: 2h, 400°C-550°C: 30′, 550°C: 2h, 550°C-700°C: 30′, 700°C: 2h, 700°C-RT:	cycle 20% O_2/He: RT - 250°C: 30′ 250°C: 2h 250-550°C: 30′, 550°C: 2h
x = 0.5	no	5% H_2/He: RT - 700°C: 1h , 700°C: 3h, 700°C-750°C: 15′, 750°C: 3h	cooling: 20% O_2/He: 700°C - RT: 1h
x = 0.5	RT-550°C: 30′, 550°C: 1h, 550°C -RT: 30 ′	5% H_2/Ar: RT - 550°C: 30′ , 550°C: 1h 50% H_2/Ar: 1h 100% H_2: 550-700°C: 20′, 700°C: 16h 700°C-RT: 1h	
x = 0.5	no	5% H_2/Ar: RT-650°C: 3h30′ 650°C: 2h30′ 650°C-RT: 10h50′, RT-690°C: 45′, 690°C: 1h30′ 690-700°C: 5′	with molecular sieve and Zr

Table 3.8: Parameters of *in situ* experiments of $La_{0.5}Sr_{1.5}MnO_{4-\delta}$ in (diluted) H_2

3.4.1 $La_{0.25}Sr_{1.75}MnO_{4-\delta}$ and $La_{0.5}Sr_{1.5}MnO_{4-\delta}$ *In Situ* in Hydrogen

Upon *in situ* reduction in 5% hydrogen gas at 700°C, none of the $La_{0.25}Sr_{1.75}MnO_{4-\delta}$ and $La_{0.5}Sr_{1.5}MnO_{4-\delta}$ crystals exhibited the satellites observed after the *ex situ* reduction treatment described above, so the structures did not display any modulations. From room temperature up to 550°C, the lattice keeps its original I4/mmm symmetry. However, between 550°C and 700°C (depending on the crystal size and position near the heating electrodes) a secondary perovskite phase does form, for both the x = 0.25 and the x = 0.5 compounds. This is evidenced by the appearance of reflections in the 3DED patterns in agreement with a (La,Sr)MnO_3 perovskite structure with $a \approx 3.9$ Å. Figure 3.30 shows the hk0 and 0kl reconstructed sections from one and the same $La_{0.5}Sr_{1.5}MnO_{4-\delta}$ crystal (Figure 3.30a, b, d, e) and $La_{0.25}Sr_{1.75}MnO_{4-\delta}$ crystal (Figure 3.30g, h) at room temperature before heating and at 700°C in 5% H2/Ar. I4/mmm reflections are indexed in white, newly appeared perovskite reflections in green. The simulated hk0 and 0kl patterns are given in Figure 3.30c and f. An important note here is that the formation of the perovskite phase was equally observed in crystals that were previously exposed to the electron beam or not. Moreover, perovskite reflections were never observed at room temperature when using the illumination conditions as we use for 3DED (parallel beam with selected area aperture). So, the 3DED acquisition does not change the sample in a way that would influence the 3DED analysis.

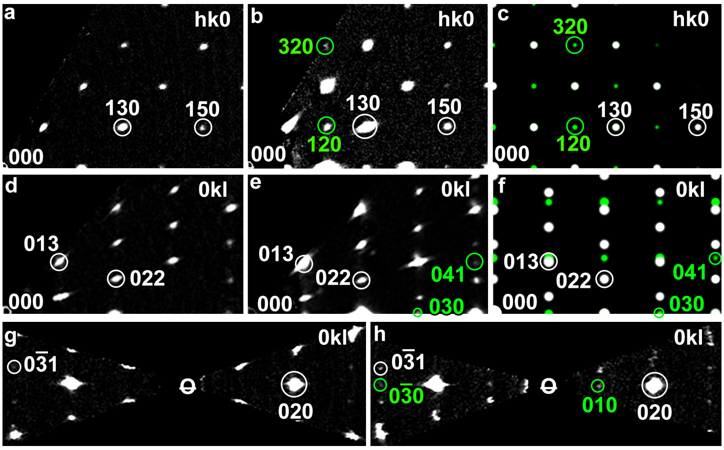

Figure 3.30: Experimental reconstructed hk0 and 0kl sections from 3DED and simulations. $La_{0.5}Sr_{1.5}MnO_{4-\delta}$ at room temperature in the pristine state in air (a, d) and at 700°C in 5% H_2/Ar (b, e). $La_{0.25}Sr_{1.75}MnO_{4-\delta}$ at room temperature in the pristine state in air (g) and at 700°C in 5% H_2/Ar (h). The simulated hk0 and 0kl sections of the multiphase crystal consisting of the RP $n = 1$ and the perovskite structure (c,f). I4/mmm reflections are indexed in white, newly appeared perovskite reflections in green.

For $La_{0.5}Sr_{1.5}MnO_{4-\delta}$, an experiment was done where a molecular sieve (sodium Y zeolite, Sigma Aldrich) and zirconium were added to the chip to absorb potential water or oxygen gas molecules on the surface, assuming those molecules might prevent reduction. Before crushing the molecular sieve, and precipitating and sonicating it in ethanol, it was activated for water absorption by heating in air to 150°C to empty the pores. The sample, Zr and molecular sieve were drop casted onto the chip in separate droplets to avoid agglomeration. However, still no modulated structure was observed in this case, only the partial transformation to perovskite.

Attempted reoxidation by cooling down in 20% O_2 to room temperature, or by another heating cycle in 20% O_2 (with a maximum temperature of 550°C) after cooling down in 5% H_2 did not recover the original pure RP n = 1 structure. After reaching 700°C in reducing atmosphere, the obtained superposition of the tetragonal Ruddlesden-Popper and cubic perovskite phase always remains unchanged for the rest of the experiments. Most likely, this failed reduction and reoxidation are caused by the formation of a SiO_2 around the crystals, as evidenced from EDX, which will be discussed in detail in section 3.4.3.

3.4.2 $Sr_2MnO_{4-\delta}$ *In Situ* in Hydrogen

For the Sr_2MnO_4 reference compound, neither the transformation to the monoclinic $P2_1/c$ supercell, nor to the perovskite phase was observed by *in situ* 3DED upon heating in a closed cell inside the TEM with the same parameters as the *ex situ* hydrogen treatment. Assuming the environmental conditions inside the closed volume formed by the double silicon nitride heating chip were too different from the *ex situ* annealing atmosphere, multiple experiments were performed with varying parameters. The parameters that were varied and examined are: temperature, duration, heating rate, hydrogen concentration (from 5% up to 100%), prior N_2 cycle or not, plasma cleaning (Ar versus 25%O_2/75%Ar). During all stages of the experiments (as listed in Table 3.7), the original I4/mmm space group was retained for $Sr_2MnO_{4-\delta}$, as observed by 3DED.

3.4.3 Silica Layer Growth

As revealed by EDX (see Figure 3.31), the reason for the discrepancies between *in situ* and *ex situ* hydrogen reduction, turns out the be the formation of a silica shell around the crystals during the *in situ* reaction. In Figure 3.31, a HAADF-STEM image and EDX maps are given from a $La_{0.5}Sr_{1.5}MnO_{4-\delta}$ crystal at room temperature after *in situ* heating to 700°C in 5% H_2/Ar. A SiO_2 layer has grown around the particle. This shell originates from Si migration to the crystals from the electron transparent silicon nitride window of the *in situ* heating chips, hindering the reduction of the sample. Most likely, the oxygen in SiO_2 stems from the sample, out of which it diffuses during heating, but it could also be delivered by unwanted humidity or residual O_2 in the closed cell. Possibly, once the silica layer has been formed, oxygen cannot leave the lattice anymore, and the formation of a modulated structure due to oxygen vacancy ordering is prevented. This could also have an influence on the reversibility of the perovskite formation. In the current conditions, *in situ* reoxidation did not alter the structure anymore for $La_{0.5}Sr_{1.5}MnO_{4-\delta}$ and $La_{0.25}Sr_{1.75}MnO_{4-\delta}$, but it is uncertain whether the reaction would also be irreversible without the presence of the silica shell.

Another consequence of this Si migration, is that the silicon nitride membrane gradually gets etched over time, until even holes appeared and a leak is created in the volume containing the gas. This systematically happened at 700°C during experiments with DensSolutions Nano-Reactors of the "newer" design, and at higher temperatures -

from 850°C - with DensSolutions Nano-Reactors from the "older" heating design, which was eventually discontinued by DensSolutions. Probably, the difference between those designs is the precise thickness of the silicon nitride window. Investigations of the possibility to apply graphene coatings to prevent this silica layer growth will be extensively discussed in chapter 5.

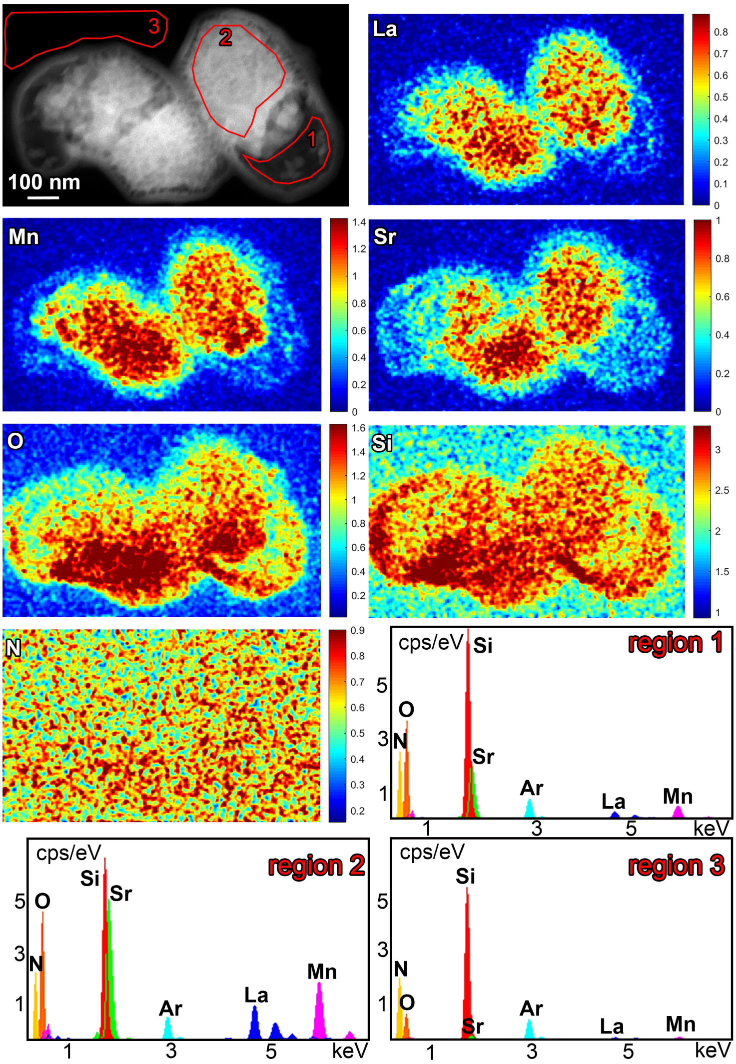

Figure 3.31: HAADF-STEM image and elemental EDX maps of two $La_{0.5}Sr_{1.5}MnO_{4-\delta}$ crystals after *in situ* heating to 700°C in 5% H_2/Ar. All maps are given in counts. On the bottom, the deconvoluted EDX spectra are shown for three regions indicated in red on the HAADF-STEM image. The Ar peak is from the gas environment, N and a part of the Si stem from the support window. A silica shell is formed around the crystals.

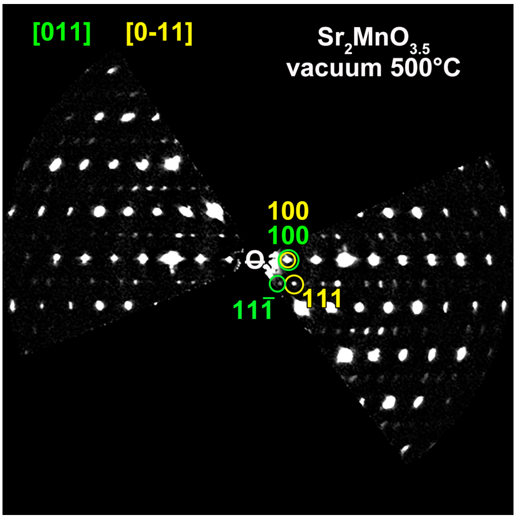

Figure 3.32: Reconstructed section from *in situ* 3DED of $Sr_2MnO_{3.55}$ at 500°C in vacuum. Two twin domains are indexed in $P2_1/c$, in green and yellow.

3.5 *In Situ* Annealing of $La_xSr_{2-x}MnO_{4-\delta}$ for x = 0, 0.25 and 0.5 in Vacuum

3.5.1 *In Situ* 3DED of $Sr_2MnO_{4-\delta}$ in Vacuum

To circumvent the silica shell formation, and still be able to follow the transformation upon reduction, we turned to *in situ* heating in vacuum, which is well-known to be a reducing atmosphere as well. As a test, the reference sample Sr_2MnO_4 was successfully reduced to $Sr_2MnO_{3.55}$ at 500°C in vacuum, as its $P2_1/c$ superstructure could be observed by *in situ* 3DED. This is illustrated in Figure 3.32, for $Sr_2MnO_{4-\delta}$ at 500°C. Again, the crystal is twinned, resulting in a superposition of the [011] and [0-11] zones in $P2_1/c$ (indexed in green and yellow), which agree with the equivalent [010] and [100] zones in I4/mmm.

3.5.2 *In Situ* 3DED of $La_{0.25}Sr_{1.75}MnO_{4-\delta}$ in Vacuum

In situ vacuum heating of $La_{0.25}Sr_{1.75}MnO_{4-\delta}$ did also lead to successful reduction to the 2D incommensurately modulated structure with superspace group $I4/mmm(\alpha\alpha0)0000(\alpha\text{-}\alpha0)0000$, as described in section 3.3.3. Figure 3.33 shows the [001] and [100] zone from *in situ* 3DED of one and the same $La_{0.25}Sr_{1.75}MnO_{4-\delta}$ crystal at room temperature (a,b) and at 550°C (c,d). The modulation already occurs at 550°C, and remains unaltered and stable when heated further to 700°C. Note that this does not imply a difference between the transformation temperatures, because the *ex situ* experiment - which was performed at 700°C - does not have the possibility to track when the transformation actually occurred.

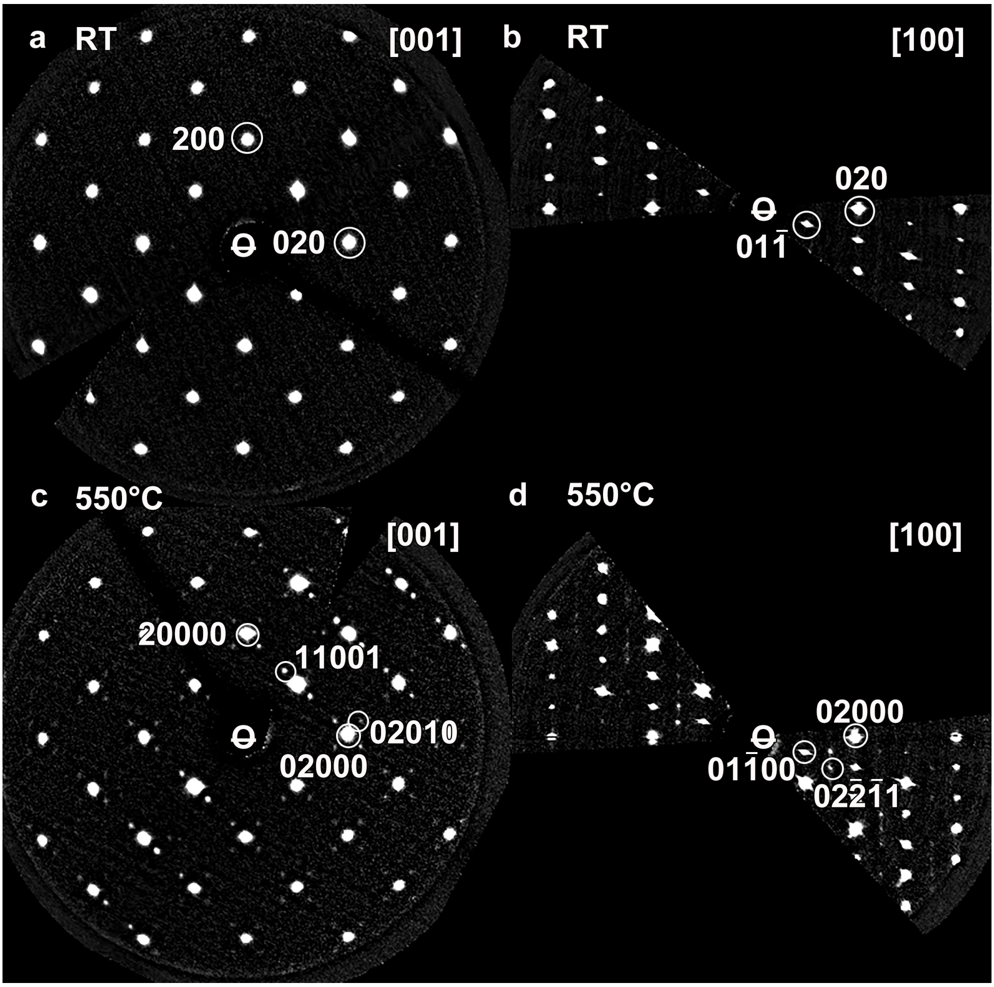

Figure 3.33: Reconstructed [001] and [100] zones from *in situ* 3DED of one and the same $La_{0.25}Sr_{1.75}MnO_{4-\delta}$ crystal at room temperature (a,b) and at 550°C (c,d) in vacuum. The 2D incommensurately modulated structure is indexed with 5 indices hklmn.

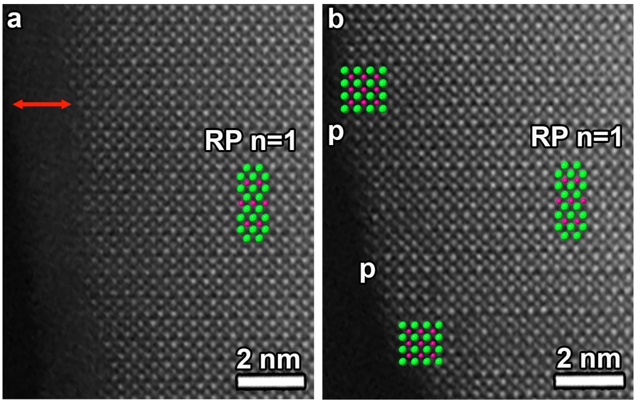

Figure 3.34: High-resolution HAADF-STEM images. (a): Pristine $La_{0.5}Sr_{1.5}MnO_{4\pm\delta}$ at room temperature. (b): The same crystal *in situ* heated in vacuum at 700°C. In (b), perovskite domains (indicated as **p**) were created where the amorphous phase was previously present in (a) (red arrow). La/Sr cations are indicated in green, Mn cations in pink.

3.5.3 *In Situ* 3DED and high-resolution HAADF-STEM of $La_{0.5}Sr_{1.5}MnO_{4-\delta}$ in Vacuum

When $La_{0.5}Sr_{1.5}MnO_{4-\delta}$ was heated *in situ* to 700°C in vacuum, no structural modulation corresponding to an oxygen-vacancy ordering was observed, only the same partial transformation to perovskite as in hydrogen gas at the same temperature (see Figure 3.30). However, since the commercial *in situ* holders for heating in vacuum already exist as double-tilt holders, also *in situ* high-resolution HAADF-STEM could be performed at high temperature in vacuum. Figure 3.34 shows the high-resolution HAADF-STEM image of one and the same $La_{0.5}Sr_{1.5}MnO_{4-\delta}$ crystal at room temperature (a) and at 700°C (b) in vacuum - without electron beam exposure in between. From this image, it can be seen that it is the 2-3 nm amorphous surface layer that crystallizes into perovskite domains, whereas the bulk RP $n = 1$ phase remains unchanged. The amorphous layer is indicated by a red arrow over its width. La/Sr cations are indicated in green, Mn cations in pink.

3.6 Mono STEM-EELS for Determining the Mn Valence

No oxygen vacancy ordering was observed from 3DED for any of the $La_xSr_{2-x}MnO_{4-\delta}$ samples when heated *in situ* in hydrogen gas. For $La_{0.5}Sr_{1.5}MnO_{4-\delta}$ this was even not seen when heated in vacuum either. However, this does not necessarily mean that the material was not reduced. It could be possible that oxygen vacancies were effectively created, but they just did not order. In that case, the structure would keep its unmodulated I4/mmm structure, and no changes would be observed in the sections from 3DED.

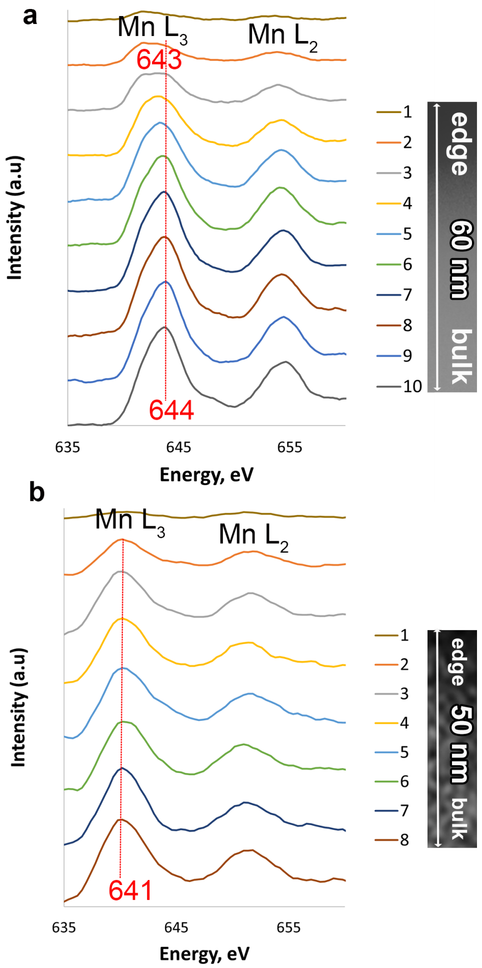

Figure 3.35: The L_2 and L_3 edge of the Mn fine structure from mono STEM-EELS of (a) $La_{0.5}Sr_{1.5}MnO_{4-\delta}$ after *in situ* heating to 700°C in vacuum and (b) $La_{0.5}Sr_{1.5}MnO_{4-\delta}$ after *ex situ* heating to 700°C in 5% H_2/Ar. In the former case, the L_3 peak shift indicates a mixture of Mn^{3+} and Mn^{4+}, with a gradual decrease of amount of Mn^{3+} when moving deeper into the particle. For the latter case, the peak shift to 641 eV indicates the presence of Mn^{2+}.

Therefore, to determine the manganese valence state - and thus the effectivity of the reduction treatment - monochromated STEM-EELS was performed. In Figure 3.35, the L_2 and L_3 edges of the Mn fine structure are given for $La_{0.5}Sr_{1.5}MnO_{4-\delta}$ after *in situ* heating in vacuum to 700°C (3.35a) and *ex situ* heating in 5% H_2/Ar to 700°C (3.35b). In the *in situ* gas heating experiments, the thickness of the double-chip Nano-reactor rendered the signal-to-noise ratio too low for a valid interpretation of the measurements. Since the same structural transformation was observed in the 3DED data for *in situ* heating in hydrogen as in vacuum, the mono STEM-EELS spectra for *in situ* vacuum heated $La_{0.5}Sr_{1.5}MnO_{4-\delta}$ are used in this comparison. For this latter case (3.35a) the Mn L_3 edge is positioned at 643 eV at the outer surface, and gradually shifts to 644 eV at a depth of 60 nm, with an energy resolution of 0.5 eV. Comparing with MnO_2, Mn_2O_3 and MnO reference spectra [74], this gives a mixture of Mn^{3+} and Mn^{4+}, where the amount of Mn^{3+} gradually decreases while moving from the outer surface towards the bulk of the particle, and the amount of Mn^{4+} increases. However, the Mn L_3 edge of *ex situ* annealed $La_{0.5}Sr_{1.5}MnO_{4-\delta}$ in a 5% hydrogen atmosphere is shifted to 641 eV. This indicates a lowering of the Mn valence towards 2+ over the whole edge of the measured crystal (from the surface up to 50 nm into the bulk). Thus, the degree of reduction is much lower for the *in situ* vacuum heated material - where indeed no oxygen-vacancy ordering was observed with 3DED - as opposed to the *ex situ* reduced sample.

3.7 Discussions and Conclusion for $La_xSr_{2-x}MnO_{4-\delta}$

3.7.1 Relation between Structure and Conductivity for $La_xSr_{2-x}MnO_{4-\delta}$ in SOFC Anode Conditions

Although according to literature [1] Ruddlesden-Popper manganites $La_xSr_{2-x}MnO_{4-\delta}$ with $0.25 \leq x \leq 0.6$ have the same I4/mmm structure, the x = 0.5 has a conductivity that breaks the trend of the other compositions. Especially in reducing SOFC anode conditions, its conductivity is large in comparison to the compounds with a higher or lower lanthanum content. With *ex situ* 3D electron diffraction it was now possible to detect an incommensurate modulation in $La_{0.25}Sr_{1.75}MnO_{4-\delta}$ and $La_{0.5}Sr_{1.5}MnO_{4-\delta}$ due to ordering of the oxygen vacancies, when reduced in 5% H_2/Ar at 700°C. While the resulting satellite reflections are very clearly visible in the reconstructed sections from 3DED (see Figure 3.24), the materials were previously reported to retain oxygen-vacancy disorder upon high-temperature reduction [1]. The satellite reflections in modulated $La_{0.5}Sr_{1.5}MnO_{4-\delta}$ are much weaker than in modulated $La_{0.25}Sr_{1.75}MnO_{4-\delta}$ (Figure 3.24), suggesting that a smaller fraction of the overall crystal transforms into the modulated structure and thus the compound is less ordered. For both samples, 3DED data were repeated with a CCD as well as a direct electron detector under the same illumination conditions, giving systematically the same results. Goff et al. [75] showed that for yttria-stabilized zirconia, the ionic conductivity decreases with an increasing degree of order in the oxygen vacancies. Thus, the decreased oxygen-vacancy order might explain the much higher conductivity for $La_{0.5}Sr_{1.5}MnO_{4-\delta}$ at 800°C in diluted hydrogen gas (1.9 S cm $^{-1}$) with respect to compositions with higher and lower lanthanum content : (x = 0.25: 0.4 S cm^{-1}, x = 0.4: 0.5 S cm^{-1} and x= 0.6: 0.8 S cm^{-1}).

Moreover, the x = 0.5 compound of the $La_xSr_{2-x}MnO_{4-\delta}$ series not only breaks the decreasing conductivity trend with La doping in reducing conditions, but also in air: x = 0.25: 38.6 S cm^{-1}, x = 0.4: 33.6 S cm^{-1}, x = 0.5: 35.6 S cm^{-1} and x = 0.6: 28.8 S cm^{-1} [1]. This might be related to the abundant RP $n = 2$ layer defects in $La_{0.5}Sr_{1.5}MnO_{4-\delta}$, whereas they are absent in $La_{0.25}Sr_{1.75}MnO_{4-\delta}$. *In situ* neutron diffraction studies of the vacancy localization and atomic displacement parameters of the $(La,Sr)_{n+1}(Co,Fe)_nO_{3n+1}$ Ruddlesden-Popper series suggest that oxygen transport pathways are rather located in the perovskite layers than the rock salt layers, causing the RP $n = 1$ structure to have to lowest oxygen mobility. [76] However, $La_{0.25}Sr_{1.75}MnO_{4\pm\delta}$ still has a somewhat higher conductivity in the oxidized form than $La_{0.5}Sr_{1.5}MnO_{4\pm\delta}$. Probably, this is because the effect of the defect structure does not outweigh the influence of the doping concentration.

3.7.2 Perovskite Growth in $La_xSr_{2-x}MnO_{4-\delta}$ for x = 0.25 and 0.5

In pristine $La_{0.5}Sr_{1.5}MnO_{4\pm\delta}$, there is also an amorphous La-rich surface layer of 2-3 nm (Figure 3.14a, red arrow). Previously Gonell et al. [67] already reported such amorphous edge in $La_{0.5}Sr_{1.5}MnO_{4\pm\delta}$ formed during synthesis. Crystallization of an amorphous surface layer on a Ruddlesden-Popper manganite into a perovskite phase was observed earlier in RP $Pr_{0.5}Ca_{1.5}MnO_4$ by Mierwaldt et al. [77] after 7 minutes of electron beam exposure in 0.5 Pa H_2O, but the perovskite did not form in vacuum. This suggests that water vapour played an important role in the formation mechanism. However, for $La_{0.5}Sr_{1.5}MnO_{4-\delta}$, perovskite growth upon heating to 700°C was also observed in vacuum conditions with HAADF-STEM, and the addition of a molecular sieve to absorb water molecules (*in situ* in a diluted hydrogen atmosphere) did not prevent perovskite formation either. No amorphous surface layer was observed in pristine $La_{0.25}Sr_{1.75}MnO_{4\pm\delta}$, although *in situ* 3DED upon heating to 700°C in diluted hydrogen gas also showed perovskite growth. This suggests that for $La_{0.25}Sr_{1.75}MnO_{4-\delta}$ in hydrogen gas, the perovskite forms from the layered RP $n = 1$ phase.

For both $La_{0.5}Sr_{1.5}MnO_{4-\delta}$ and $La_{0.25}Sr_{1.75}MnO_{4-\delta}$, the creation of perovskite domains can be explained by thermodynamics and their different elemental distribution at the surface. As shown in Figure 3.14, pristine $La_{0.5}Sr_{1.5}MnO_{4\pm\delta}$ has a lanthanum rich region at the surface compared to the bulk. But the La/Sr ratio has a crucial influence on the stability of phases in the La-Sr-Mn-O system. According to the calculated phase diagrams by Grundy et al. [78] using the compound energy formalism [79], the stable coexisting phases at 800°C in reducing atmosphere ($\log(P(O_2)= 10^{-18})$ for $La_{0.5}Sr_{1.5}MnO_{4-\delta}$, $La_{0.25}Sr_{1.75}MnO_{4-\delta}$ and Sr_2MnO_4 are SrO, MnO and RP $n = 1$ $(La,Sr)_2MnO_4$. But when the lanthanum content locally gets doubled or more - as indeed seen by EDX at the surface of $La_{0.5}Sr_{1.5}MnO_{4-\delta}$ in Figure 3.14 - also the perovskite form $(La,Sr)MnO_3$ and higher order RP $n = 2$ $(La,Sr)_3MnO_7$ become stable. This is why no perovskite formation was observed in the case of Sr_2MnO_4. It must be noted that oxygen non-stoichiometry was not taken into account there, due to a lack of thermodynamic literature data for the relevant Ruddlesden-Popper phases.

The perovskite formation evidenced in our experiments, is not reversible upon either cooling or heating in oxidizing conditions. However, in the *in situ* experiments, this could be caused by faster silica growth kinetics than the potential redox reactions involving the studied sample itself. Thus, the reversibility of the perovskite growth should still be examined *in situ* without the presence of a SiO_2 layer, since it might have an effect on the degradation of the materials as SOFC electrodes. Unfortunately, up till now, it has not been possible yet to completely prevent this layer.

3.7.3 Silica Contamination during *In Situ* TEM

Upon annealing *in situ* in hydrogen gas, none of the samples displayed oxygen vacancy ordering, and EDX detected the formation of a shielding shell containing silicon. This layer around the crystals stems from the silicon nitride window of the heating chip on which the sample is drop casted for *in situ* heating experiments. Wang et al. [80] already recorded the migration of SiO_2 from the support to diverse metal nanoparticles like Pt, Co, Ni, ... upon heating to 750°C in 10% H_2/Ar with *in situ* high-resolution TEM images and EDX. Although the vacuum heating DensSolutions Wildfire chips contain similar silicon nitride electron transparent windows as the gas heating DensSolutions Nano-Reactors, no such shell was detected by EDX upon heating in vacuum. However, as proven by mono STEM-EELS and *in situ* 3DED, the high-temperature vacuum conditions (700°C-800°C) did not suffice to effectively reduce the x = 0.5 compound, although $Sr_2MnO_{4-\delta}$ and $La_{0.25}Sr_{1.75}MnO_{4-\delta}$ were successfully reduced to their oxygen ordered phases in vacuum at 500°C and 550°C. Probably, the reaction with Si takes place in both experimental *in situ* set-ups - gas and vacuum - but the silicon migration happens more slowly under vacuum conditions (10^{-7} mbar) than near-atmospheric pressure (± 700 mbar). Because of the lower reduction temperature for the x = 0 and 0.25 materials compared to the x = 0.5 composition, oxygen vacancies could apparently still be created in vacuum before the silicon shell got too thick to prevent this. Possible solutions to prevent the growth of this silica layer will be discussed in detail in chapter 5.

3.7.4 Conclusion for $La_xSr_{2-x}MnO_{4-\delta}$

Ruddlesden-Popper $La_xSr_{2-x}MnO_{4-\delta}$ solid oxide fuel cell electrode materials were studied for x = 0, 0.25 and 0.5 by different *ex situ* and *in situ* electron microscopy techniques. 3D electron diffraction discovered a structural transformation to an incommensurate 2D ($La_{0.25}Sr_{1.75}MnO_{4-\delta}$) and 1D ($La_{0.5}Sr_{1.5}MnO_{4-\delta}$) modulated structure upon annealing at 700°C in 5% H_2/Ar. This was previously undetected with powder X-ray and neutron diffraction. The systematically weaker satellites for x = 0.5 point to a lower degree of oxygen vacancy order, which can indeed lead to a higher conductivity in reducing anode conditions. [75]

In pristine $La_{0.5}Sr_{1.5}MnO_{4\pm\delta}$, a 2-3 nm amorphous surface layer is systematically observed by high-resolution HAADF-STEM, as well as many higher-order RP $n = 2$ layer defects. The presence of these defects can also play a role in the enhanced conductivity, since they contain more perovskite blocks which are assumed to be the oxygen transport pathways [76], and no such $n = 2$ defects are observed in $La_{0.25}Sr_{1.75}MnO_{4\pm\delta}$.

Upon *ex situ* or *in situ* annealing in reducing environment at 700°C - diluted hydrogen gas or vacuum - also perovskite domains are created. In situ high-resolution HAADF-STEM shows that for $La_{0.5}Sr_{1.5}MnO_{4-\delta}$, these domains originate from the crystallization of an originally amorphous surface layer. Such perovskite formation at high temperature is important to take into account in conductivity and degradation studies for applications as an SOFC electrode. The precise mechanism leading to the perovskite growth is not clear, but based on thermodynamics of the La-Sr-Mn-O system [78], an important role is played by the La rich surface - as observed by EDX - and different structural phases are stable at the edge compared to the bulk structure in reducing environment. However, due to silicon migration of the Nano-Reactors, it was not possible to fully reduce the materials *in situ* and monitor the transformation to the modulated structure by *in situ* 3DED. To completely understand this phenomenon, further research has to be performed, especially into the experimental set-up for *in situ* electron microscopy, so that the reaction with silicon at high-temperatures can be avoided for this group of manganites and individual crystals can be tracked throughout the reaction in actual SOFC anode conditions.

Chapter 4

$(Ca, Sr)(Mn,Fe)O_{3-\delta}$ for Chemical Looping Combustion with Oxygen Uncoupling

---

4.1 Introduction to $(Ca, Sr)(Mn,Fe)O_{3-\delta}$ for Chemical Looping Combustion with Oxygen Uncoupling

To counter global warming, new techniques are required that lower the emission of carbon dioxide: on one hand by energy production alternatives that decrease the need of fossil fuels, and on the other hand by methods to capture CO_2 once it has been emitted. One such example is Chemical Looping Combustion (CLC), a combustion process in which carbon dioxide is inherently separated from air in the reaction products, which would otherwise require an extensive and energy consuming procedure. The crucial elements in this process are oxygen carrying particles that can be cycled - or "looped" - through redox reactions. A schematic representation of the operating principle is shown in Figure 4.1. While the fuel can be solid, liquid or gaseous, e.g. coal, natural gas or biomass, the oxygen carriers are usually solids, and more specifically metal oxides. As can be seen in the figure, from the 1950s, two reactors have been used: the reducer or CO_2 generator, and the oxidizer or metal oxide regenerator. In the beginning, the typical metal oxides (MO) were copper or iron oxide. Those oxygen carriers react with the fuel (if it is a gas) or gasification products created from the fuel and leave a metal (M) behind, depleted from oxygen. Now the oxygen carrier should be reoxidized by O_2 from air in the oxidizer, after which the cycle can begin again. The CO_2 is produced in the reducer and never mixed with air during the entire process. [81] [82] If the fuel is a solid (e.g. coal or biomass), it has to be gasified first to be able to react with the solid oxygen carrier particles. In the Syngas CLC process, this happens in an external gasifier, after which syngas is produced - a mixture of CO and H_2 - and sent to the reducer. This can also be done in one single reactor, as in *in situ* Gasification CLC (iG CLC). In that case, the solid fuel and oxygen carriers are mixed together. However, the gasification of char - the solid remains after removal of syngas and water vapour from solid fuel upon heating - is a slow step in the conversion process. [82] Since this slow gasification step is avoided in Chemical Looping with Oxygen Uncoupling (CLOU), it significantly increases the reaction rates. Here, the oxygen carrier releases oxygen in gas form upon heating in the fuel

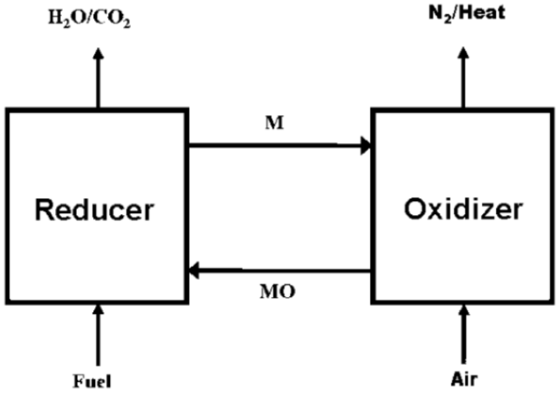

Figure 4.1: Schematic representation of the Chemical Looping Combustion (CLC) process. Image by [81]. M stands for metal and MO for metal oxide.

reactor, which can directly react with the solid fuel. But that means the oxygen carrier has to possess the suitable thermodynamical properties to be reduced in the required conditions. The redox couples Mn_2O_3/Mn_3O_4 or CuO/Cu_2O are good examples, for which the CLOU process is 50 times faster than normal CLC of petroleum coke. [83] In this case, the (average) Mn and Cu valence states are lowered from Mn^{3+} to $Mn^{2.67+}$ (mixed valence state with both Mn^{3+} and Mn^{2+}), and from Cu^{2+} to Cu^{+}, but the material does not reach the fully metallic form. The CLOU principle is illustrated in Figure 4.2.

However, there are some limitations for previously mentioned CLOU oxygen carriers. Copper oxides are not only expensive, but also have a low melting point in the reduced phase, which leads to agglomeration and loss of the reactive phase. [84] Manganites, on the other hand, are cheaper and easily available, but more difficult to reoxidize, since they require very high oxygen partial pressures at high temperatures. [85] Recently, oxygen carriers with the perovskite $ABO_{3-\delta}$ lattice have been intensively investigated for use in the CLOU process, especially the $CaMnO_{3-\delta}$ family. They have the advantage that they can be synthesized from many different abundant and cheap precursors [86]. Moreover, they are useful in the CLOU process: the redox couple $CaMnO_{2.92}/CaMnO_{2.5}$ has an oxygen carrier capacity of 4.92 wt%, compared to 3.38 and 10.06 wt% for Mn_2O_3/Mn_3O_4 or CuO/Cu_2O respectively [87]. But $CaMnO_{3-\delta}$ has the disadvantage of having poor stability in the long term. At high temperatures, it irreversibly transforms to $CaMn_2O_4$ (marokite) and Ca_2MnO_4 (Ruddlesden-Popper n = 1), decreasing its activity.

Nevertheless, this degradation effect can be overcome by cation doping. Galinsky et al. [2][3] showed that doping the A site with Sr or the B site with Fe resulted in a stable orthorhombic perovskite up to 1200°C. They also found that for $CaFe_{0.2}Mn_{0.8}O_3$, the working redox temperature could be lowered to 600°C, compared to > 800°C for $CaMnO_{3-\delta}$. Further, 100 isothermal CLOU redox cycles could be performed for $CaFe_{0.2}Mn_{0.8}O_3$ (at 600°C) and $Ca_{0.75}Sr_{0.25}MnO_3$ (at 850°C) without any observed phase transformation by *in situ* XRD. [2] [3] It has not yet been discovered why this doping strategy improves the stability and working conditions for calcium manganites as a CLOU oxygen carrier. All of them exhibit the same orthorhombic structure as $CaMnO_3$ (Pnma, a = 5.2819(1) Å, b = 7.4547(2) Å, c = 5.2658(1) Å[88]) when fully oxidized. But their performance differences

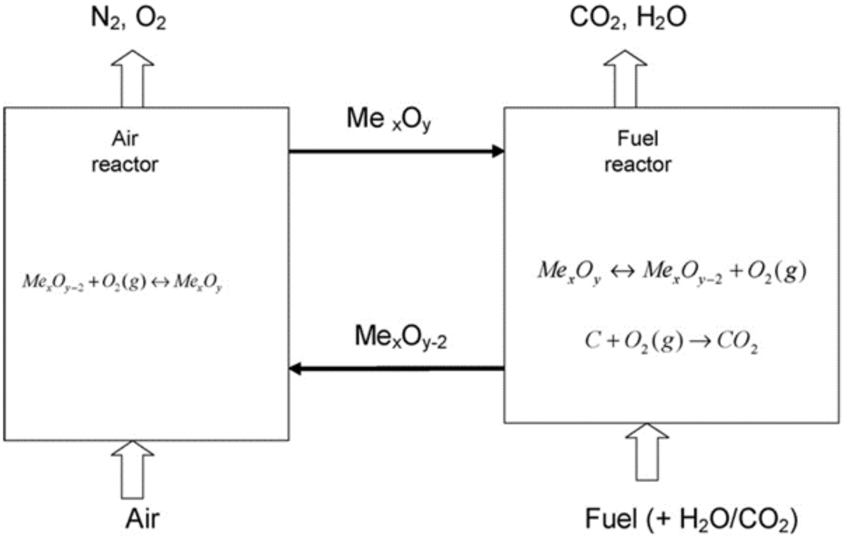

Figure 4.2: Schematic representation of Chemical Looping with Oxygen Uncoupling (CLOU). Image by [83].

are likely related to the evolution of the intermediate structures in between the fully oxidized and fully reduced compounds.

As discussed in section 1.1, oxygen vacancies in perovskite structures can give rise to materials with a large variety of oxygen deficiencies. This is also the case for $CaMnO_{3-\delta}$. While the fully oxidized structure - $CaMnO_3$ - has the classic perovskite arrangement of tilted oxygen octahedra around the Mn cations, these have been replaced by a network of corner-sharing square pyramids for fully reduced $CaMnO_{2.5}$ (Pbam, a = 5.424(2) Å, b = 10.230(4) Å, c = 3.735(2) Å[89]) since all Mn^{4+} cations have been changed into Mn^{3+}, as illustrated in Figure 4.3. Further, although their structures have not been solved yet, it is known (from thermogravimetric analysis or TGA) that oxygen deficient compounds exist with the following oxygen content: $CaMnO_{2.92}$ [88], $CaMnO_{2.89}$ [88], $CaMnO_{2.8}$ [4], $CaMnO_{2.75}$ [90], $CaMnO_{2.655}$ [4] and $CaMnO_{2.56}$ [88]. However, Lichtenthaler [91] reported that the intermediate phases are extremely difficult to synthesize and only $CaMnO_{2.75}$ could be successfully prepared as a single phase.

According to Reller et al. [4] in 1984, the phases with intermediate oxygen deficiency adopt structures with an ordered arrangement of six- and five-coordinated manganese polyhedra (MnO_6 and MnO_5), depending on the ratio of Mn^{4+} versus Mn^{3+}. For instance, for $CaMnO_{2.75}$, exactly half of the polyhedra are octahedra and half are square pyramids. From in-zone electron diffraction, they found a fourfold super cell with a = 5.35 Å, b = 21.0 Å, c = 7.47 Å and one with half the length for b. However, they did not try to solve the structure due to the high polycrystallinity and small domain sizes (below 150-200 nm). Chiang et al. [92] and Lichtenthaler [91] did attempt to solve this structure, with either neutron diffraction or combining conventional powder XRD and in-zone electron diffraction, but they could not find a model that matched with the symmetry from observed reflection conditions and allowed structure refinement with non-negative atomic displacement parameters and chemically possible bond lengths. Concerning the

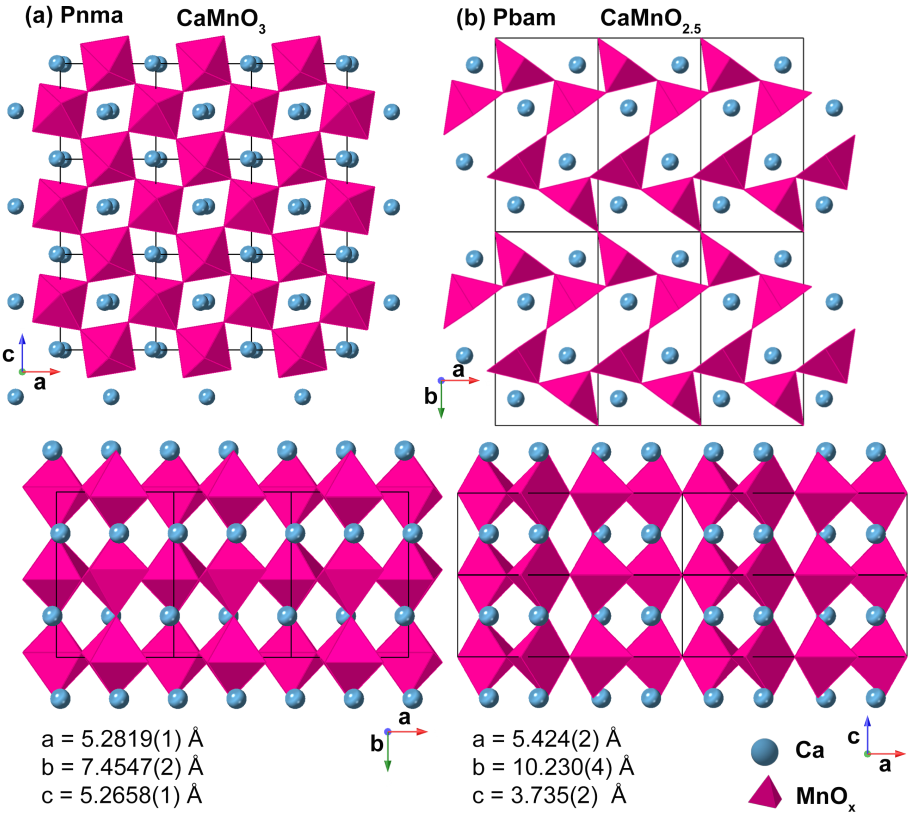

Figure 4.3: Representation of models for (a) $CaMnO_3$ and (b) $CaMnO_{2.5}$. Upon reduction, the tilted oxygen octahedra surrounding the Mn cations turn into a network of square pyramids. MnO_5 and MnO_6 polyhedra are shown in pink, Ca atoms in blue.

other oxygen deficient phases, Reller et al. [4] also found an orthorhombic a = 5.43 Å, b = 16.29 Å, c = 3.74 Å unit cell for $CaMnO_{2.667}$ and a tetragonal cell with a = 8.34 Å and c = 7.46 Å for $CaMnO_{2.8}$, but did not make any structure solution attempts here either.

For $Ca_xSr_{1-x}MnO_3$ with $0.4 \leq x \leq 0.6$, a phase transition from Pnma to I4/mcm upon heating was observed using synchrotron XRD by Zhou et al. [93], with a = 5.3429(1) Å, and c = 7.5840(1) Å for x = 0.5, as shown in Figure 4.4. This tetragonal phase coexists with the original orthorhombic phase from 250°C up to 390°C, after which I4/mcm becomes the sole phase. At 635°C, they saw a further transformation to Pm-3m with a = 3.8010(1) Å. However, the oxygen content was not studied here. If this structure actually contains oxygen vacancies, they are disordered: there is no periodic arrangement of MnO_6 octahedra and MnO_5 square pyramids, or other coordination polyhedra. In 2020, Mastronardo et al. [94] investigated $CaFe_xMn_{1-x}O_3$ for x = 0.1 and x = 0.3 with *in situ* powder XRD upon heating in N_2/O_2 atmospheres with high (pO_2 = 0.18) and low (pO_2 = 0.008) oxygen partial pressures. They observed a direct transformation from the pristine orthorhombic Pnma structure to the cubic phase in both oxidizing and reducing conditions - although at lower temperature in the latter case - without any intermediate tetragonal phase. For undoped $CaMnO_{3-\delta}$ on the other hand, they observed transition to the tetragonal and cubic structure at 894°C and 914°C at high pO_2, to the cubic structure at 800°C at low pO_2, and no phases with vacancy ordering. The phase diagrams from their experiments are given in Figure 4.5. Also Taguchi et al. [88] in 1989 only observed disordered tetragonal and cubic phases for undoped $CaMnO_{3-\delta}$ using *in situ* powder XRD in air. They observed that the weight of the sample decreased upon heating and increased again when cooling down, which means that $CaMnO_{3-\delta}$ can even be reduced in air, but at very high temperatures. Using thermogravimetric analysis, they determined that the chemical composition is $CaMnO_{2.65}$ at 900°C and $CaMnO_{2.56}$ at 920°C in air. From powder XRD, they indexed the structure of $CaMnO_{2.65}$ as a tetragonal cell with a = 5.333 Å and c = 7.534 Å, and the $CaMnO_{2.56}$ compound as a cubic cell with a = 3.774 Å.

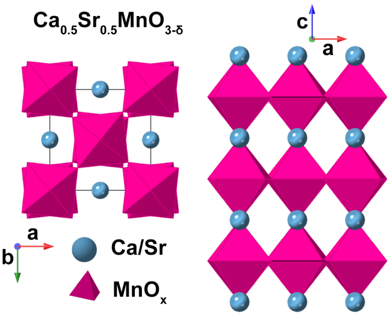

Figure 4.4: Model of $Ca_{0.5}Sr_{0.5}MnO_{3-\delta}$ in I4/mcm by Zhou et al. [93]. Oxygen vacancies are disordered here. MnO_6 octahedra are shown in pink, Ca/Sr cations in blue.

But these disordered oxygen deficient compounds for undoped $CaMnO_{3-\delta}$ reported by Taguchi and Mastronardo contradict the oxygen vacancy ordered super structures observed by Reller et al. [4]. However, this does not necessarily mean that such ordening was not present in their experiments. The technique used by Mastronardo and Taguchi

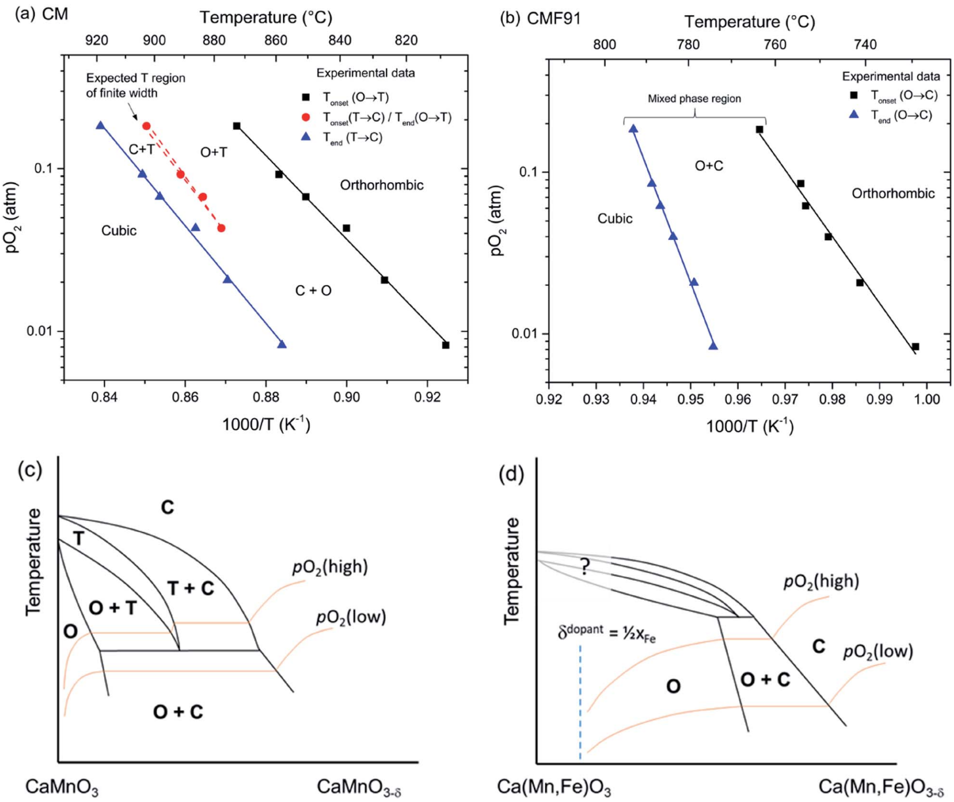

Figure 4.5: Phase diagram for $CaMnO_{3-\delta}$ and $Ca(Fe,Mn)O_{3-\delta}$ by Mastronardo et al. [94] from *in situ* powder XRD. They did not encounter the tetragonal phase for iron doped calcium manganite.

was powder XRD, while Reller studied the material with in-zone electron diffraction and high-resolution images. Possibly, the vacancy ordering was missed because of the high degree of polycrystallinity of the samples, peak broadening and loss of local information by averaging over many crystals inherent to the characterization method. Due to its stronger interaction with matter, electron diffraction is applicable on submicron particles, and thus a suitable method to investigate materials consisting of many small, differently oriented domains, which can easily pick up on such ordering phenomena as the ones found by Reller in $CaMnO_{3-\delta}$. So far, the structural evolution of doped $(Ca,Sr)(Mn,Fe)O_{3-\delta}$ materials upon reduction has not yet been investigated using electron diffraction, meaning that potential ordering schemes for varying oxygen content could have been missed. Now, it is also possible to do this *in situ* at high temperatures in vacuum or gas atmospheres, which allows to track the structural evolutions of individual particles, providing even more accurate information on structure transformations, and specifically on intermediate phases. Adding tomography, 3DED offers the option to also solve and refine structures of oxygen deficient phases, where e.g. for $CaMnO_{2.75}$ this failed with powder techniques. [91] Thus, combining all these methods, we are thoroughly equipped to study ordering phenomena in oxygen deficient members of the polycrystalline $(Ca, Sr)(Mn,Fe)O_{3-\delta}$ family, *in situ* during phase transformations upon reduction, in an attempt to explain higher cycling stability and lower functional temperatures in CLOU applications by doping.

4.2 Synthesis of (Ca, Sr)(Mn,Fe)O$_3$

$CaMnO_3$, $Ca_{0.75}Sr_{0.25}MnO_3$ and $CaFe_{0.2}Mn_{0.8}O_{3-\delta}$ were prepared using the solid state synthesis method. $CaCO_3$ and $SrCO_3$ powders were dried at 500°C for 12h. Then, stoichiometric amounts were mixed and ground in an agate mortar with stoichiometric amounts of Mn_2O_3 and Fe_2O_3. The mixture was pressed into pellets and annealed at 1200°C in air for three times 12h, with intermediate grinding. To check the phases, powder XRD was acquired of the as-prepared samples. An overview of the raw XRD patterns is given in Figure 4.6, and the raw (black), calculated (red) and difference (blue) powder XRD patterns with zooms are given in Figure 4.7, 4.8 and 4.9. The Le Bail fit to this data resulted in the cell parameters, space group and weighted profile R factors wR_p listed in Table 4.1.

	$CaMnO_3$	**$CaFe_{0.2}Mn_{0.8}O_{3-\delta}$**	**$Ca_{0.75}Sr_{0.25}MnO_3$**
Space group	Pnma	Pnma	Pnma
a (Å)	5.2812	5.3034	5.3132
b (Å)	7.458	7.4914	7.4884
c (Å)	5.2682	5.2919	5.3061
wR_p (%)	1.26	1.31	1.39

Table 4.1: Parameters from Le Bail fit to powder XRD data from as-prepared $CaMnO_3$, $CaFe_{0.2}Mn_{0.8}O_{3-\delta}$ and $Ca_{0.75}Sr_{0.25}MnO_3$.

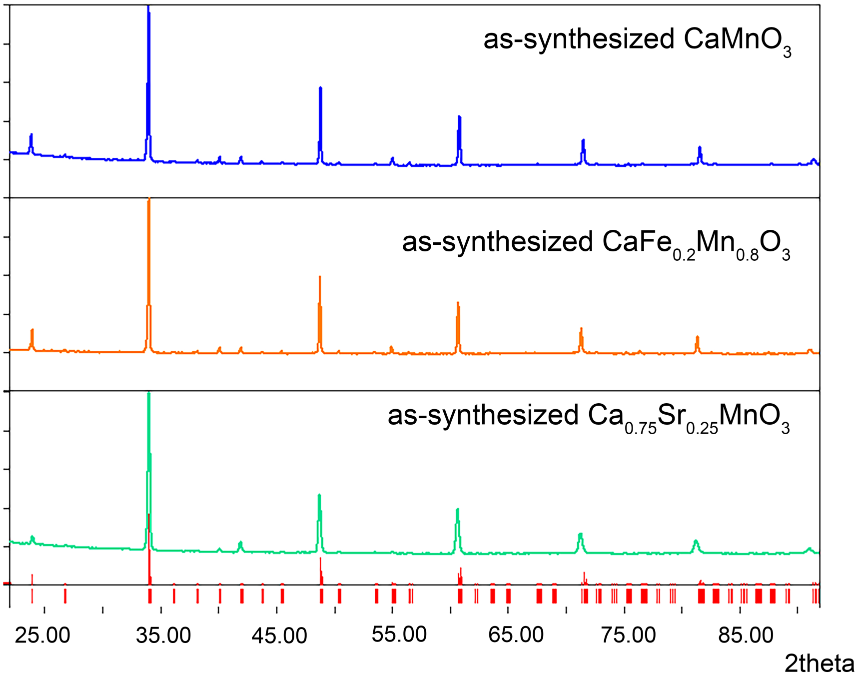

Figure 4.6: Powder XRD patterns of as-prepared $CaMnO_3$, $CaFe_{0.2}Mn_{0.8}O_{3-\delta}$ and $Ca_{0.75}Sr_{0.25}MnO_3$. Calculated patterns from the Le Bail fit and zooms are given in the following figures.

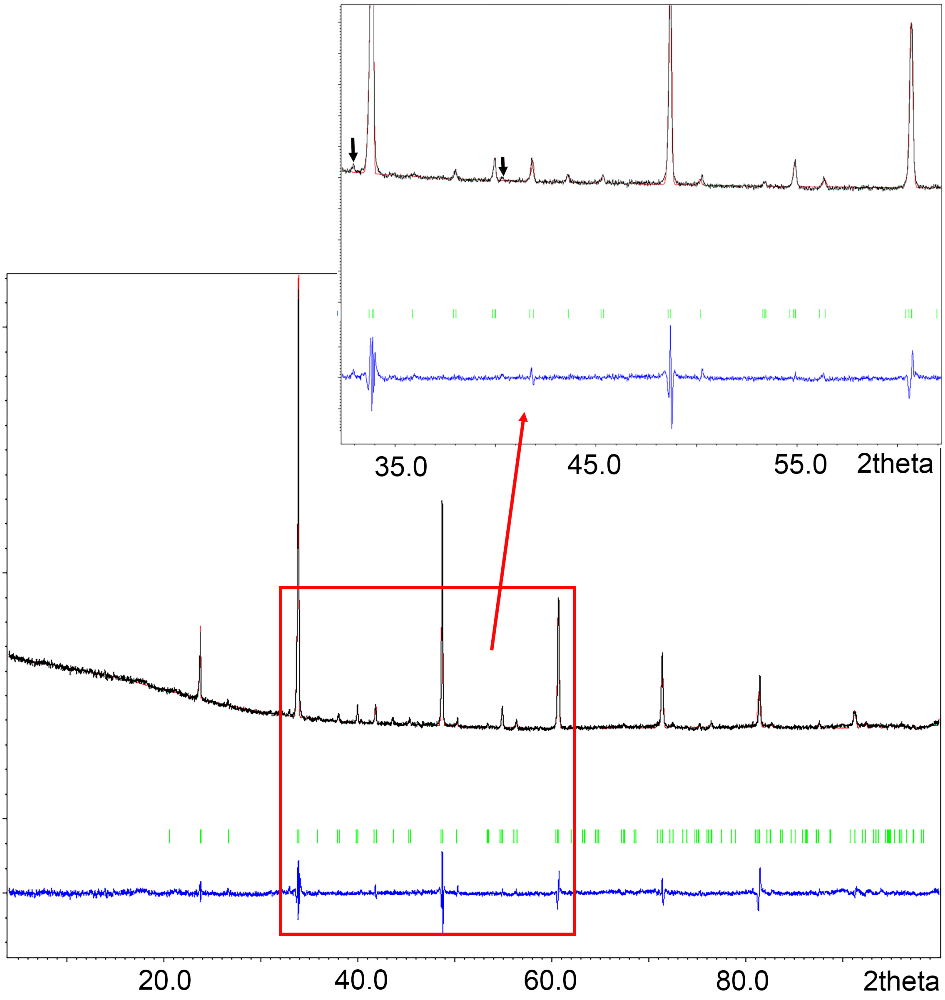

Figure 4.7: Raw (black), calculated (red) and difference (blue) powder XRD patterns for as-synthesized $CaMnO_3$. The calculated pattern was obtained from the Le Bail fit. The black arrows indicate small peaks that belong to a small amount of impurity phase.

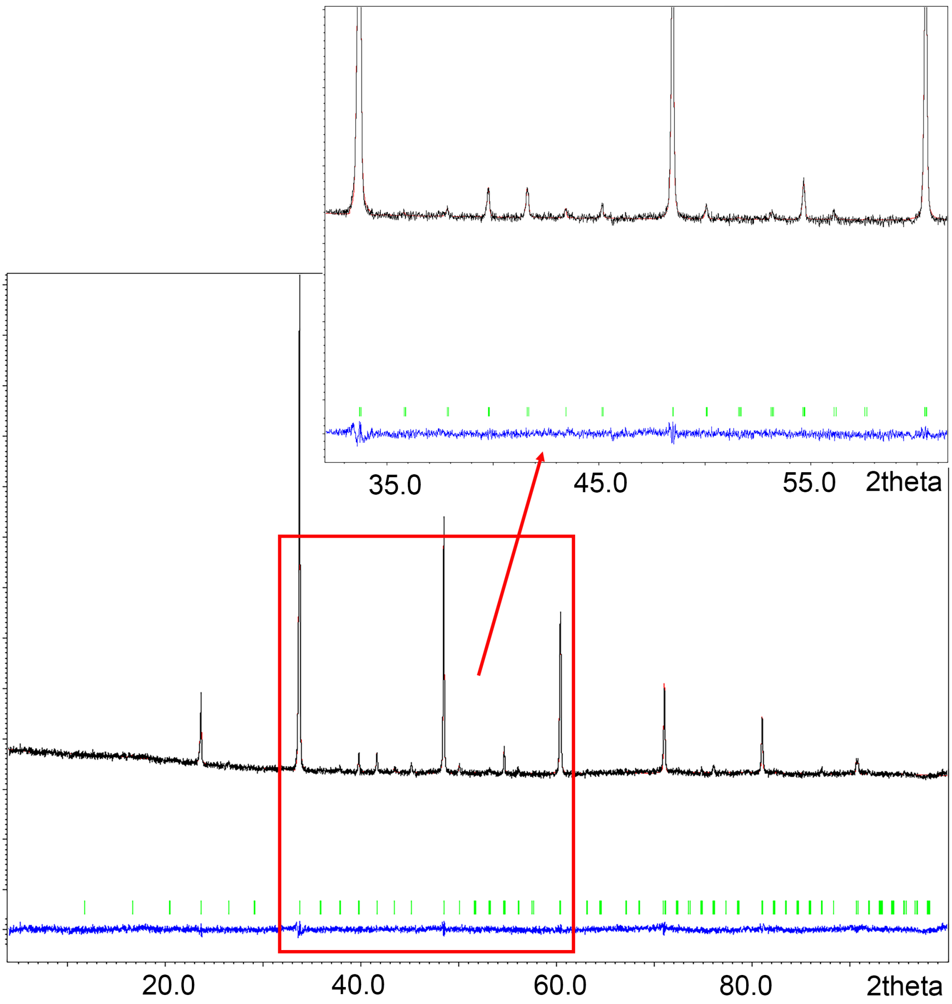

Figure 4.8: Raw (black), calculated (red) and difference (blue) powder XRD patterns for as-synthesized $CaFe_{0.2}Mn_{0.8}O_{3-\delta}$. The calculated pattern was obtained from the Le Bail fit.

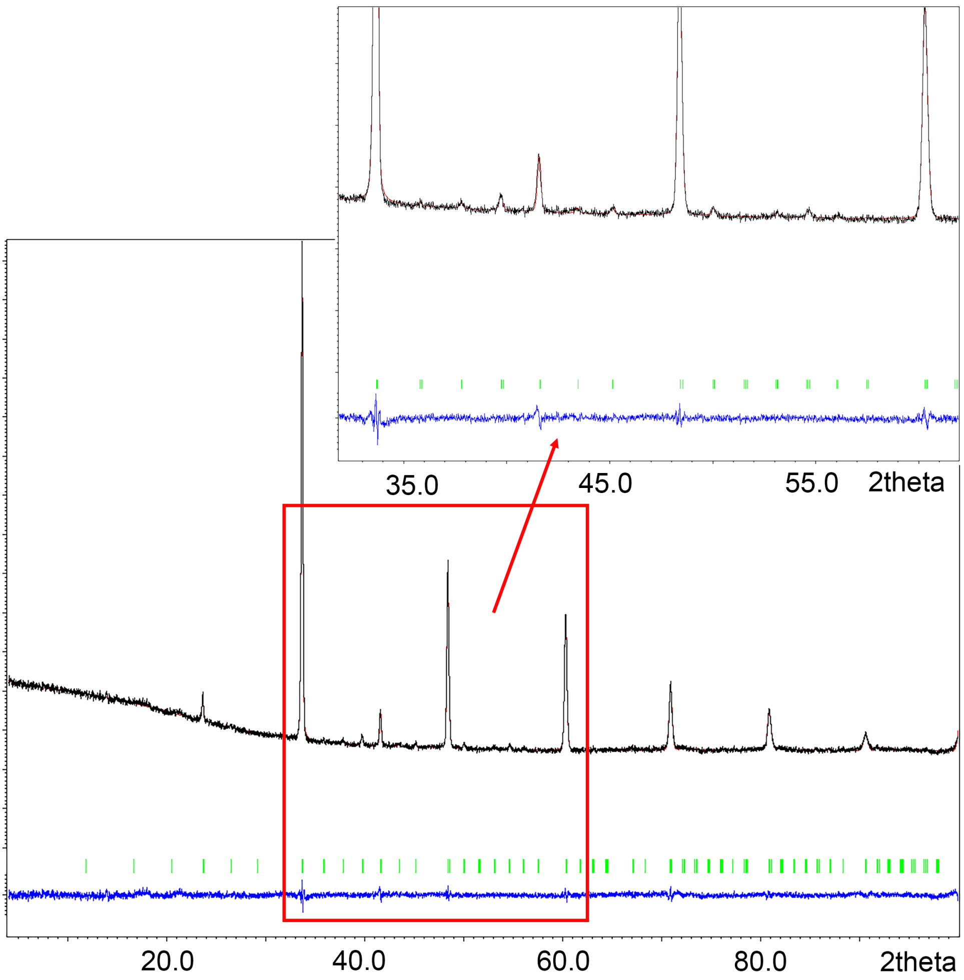

Figure 4.9: Raw (black), calculated (red) and difference (blue) powder XRD patterns for as-synthesized $Ca_{0.75}Sr_{0.25}MnO_3$. The calculated pattern was obtained from the Le Bail fit.

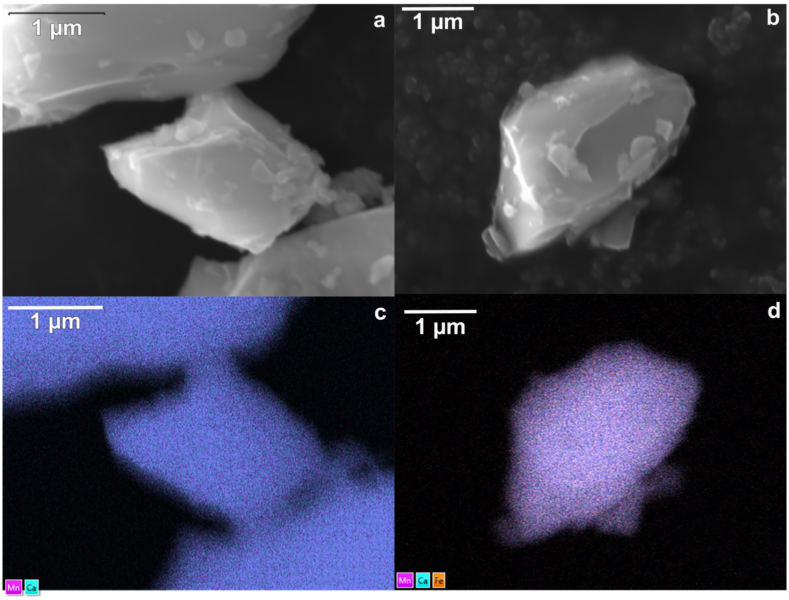

Figure 4.10: SEM images (a,b) and EDX maps (c, d, in counts) of $CaMnO_3$ (a,c) and $CaFe_{0.2}Mn_{0.8}O_{3-\delta}$ (b,d). Ca is given in blue, Mn in pink and Fe in orange.

The elemental distribution was checked with SEM EDX at 20 kV and was found to be homogeneous throughout the crystals, as shown for as-synthesized $CaMnO_3$ and $CaFe_{0.2}Mn_{0.8}O_{3-\delta}$ in Figure 4.10. Further, 3DED was acquired from the pristine materials, as illustrated for $CaMnO_3$ in Figure 4.11. For $Ca_{0.75}Sr_{0.25}MnO_3$, 3DED showed that the crystallinity was too poor - after storage in an Ar glovebox for 1,5 years - to conduct meaningful *in situ* 3DED experiments. Therefore, it was subjected to another heating cycle at 1100°C for 8h, which significantly improved the crystal quality.

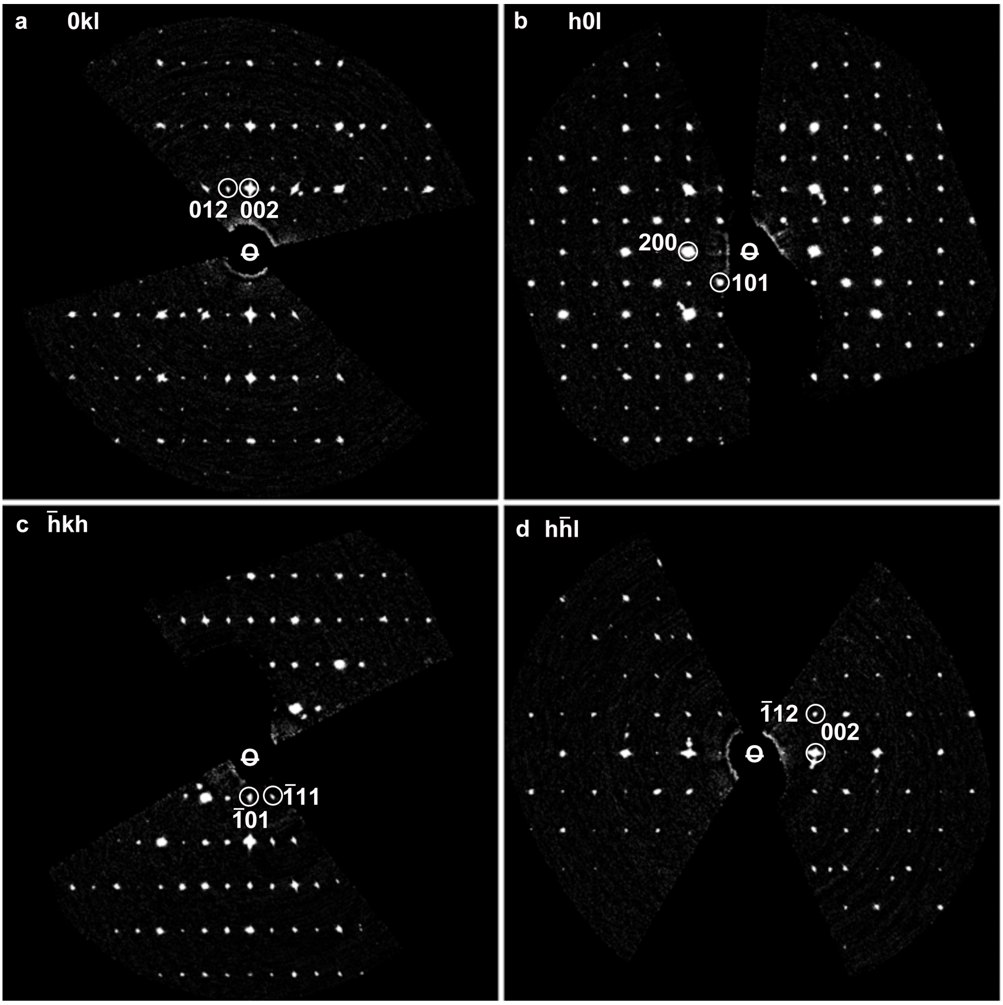

Figure 4.11: Reconstructed (a) 0kl, (b) h0l, (c) -hkh and (d) h-hl sections from 3DED of pristine $CaMnO_3$.

4.3 *In Situ* Reduction of Undoped CaMnO$_{3-\delta}$

4.3.1 *In Situ* 3DED of CaMnO$_{3-\delta}$ in Inert Gas

When CaMnO$_{3-\delta}$ was heated in helium in the TEM, 3DED showed that it retained its orthorhombic Pnma lattice up to 700°C. From 750°C onwards, some crystals decomposed and only few reflections remained, from which no crystal structure could be determined anymore. Additionally, in the range 750-800°C, three crystals transformed to an orthorhombic cell with cell parameters a = 9.24(2) Å, b = 2.874(9) Å, and c = 11.43(3) Å- measured at 800°C by 3DED - for which the reconstructed hk0 and h-kk sections from 3DED are given in Figure 4.12.

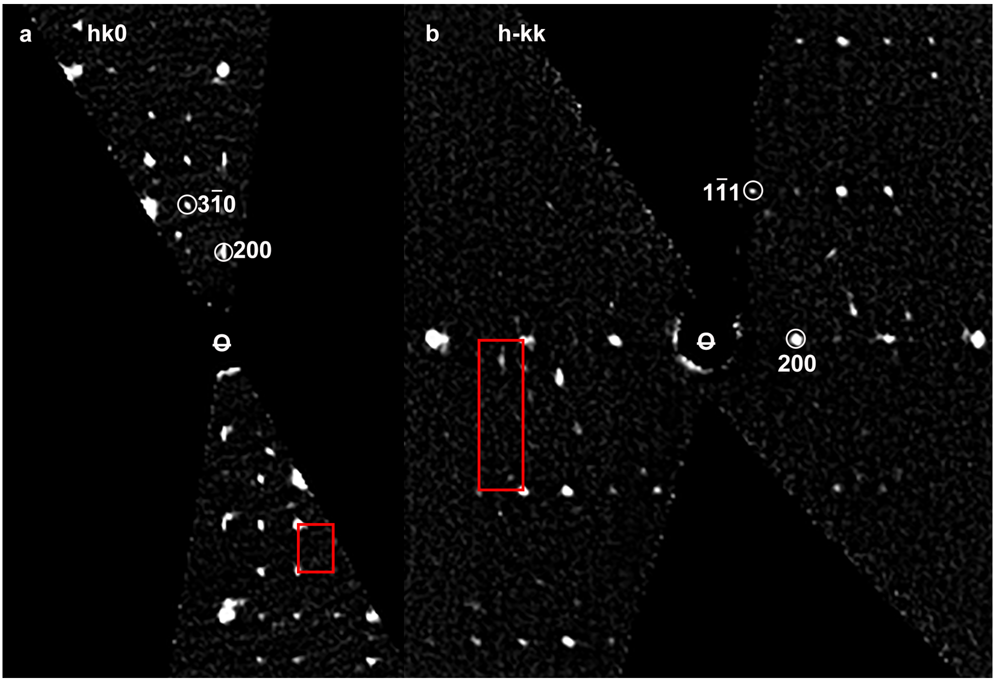

Figure 4.12: Reconstructed hk0 (a) and h-kk (b) sections of a Ca$_x$Mn$_3$O$_6$ crystal from *in situ* 3DED, obtained by heating CaMnO$_{3-\delta}$ at 800°C in helium. The cell in reciprocal space (with a = 9.24(2) Å, b = 2.874(9) Å, and c = 11.43(3) Å, in real space) is indicated in red.

This is a tunnel structure that was already described in 2006 by Hadermann et al. [95] for CaMn$_3$O$_6$ (Ca$_{1-0.67}$MnO$_{3-1}$, see Figure 4.13). In that case, however, only $\frac{1}{3}$ of the calcium positions is occupied and an ordering of Ca vacancies occurs along the tunnel, which transforms the orthorhombic subcell to a monoclinic supercell with a= 10.6940(3) Å, b =11.3258(3) Å, c = 8.4881(2) Å, and β = 122.358(2)°, space group P2$_1$/a and transformation matrix

$$(a_m, b_m, c_m) = (a_o, b_o, c_o)\begin{bmatrix} 1 & 0 & 0 \\ 2 & 0 & -3 \\ 0 & 1 & 0 \end{bmatrix} \tag{4.1}$$

where the subscripts *m* and *o* refer to the monoclinic supercell and orthorhombic subcell respectively. In contrast, instead of the supercell, here the orthorhombic subcell was experimentally seen, so there is no ordered alternation in calcium atoms and vacancies. Probably, this is because these measurements were performed *in situ* at 750-800°C instead of room temperature as by Hadermann et al. [95]. At these elevated temperatures, the calcium content could still be the same, but with disorder between Ca and vacancies. This leads to a space group with a higher symmetry.

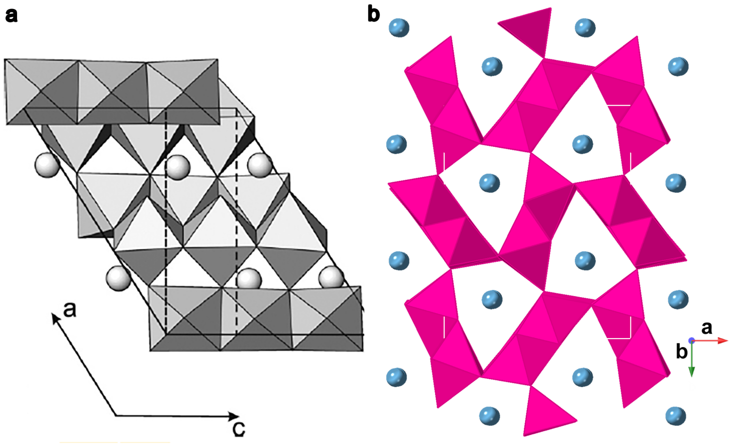

Figure 4.13: a: Schematic representation of the monoclinic superstructure of CaMn$_3$O$_6$, seen along the b direction, with $\frac{1}{3}$ occupancy of the Ca positions and ordering of the vacancies. The orthorhombic subcell is shown by a dashed line. (figure by [95]) In the current observations at 750°C-800°C the vacancies are not ordered, and the subcell is the correct model instead of the supercell. b: Model of CaMn$_3$O$_6$, seen along the c direction. The Ca atoms are situated inside tunnels formed by the Mn octahedra.

On top of that, additional reflections are seen in the sections, which belong to secondary phases. Some crystals also show the CaMn$_7$O$_{12}$ phase (Ca$_{1-0.86}$MnO$_{3-1.29}$) with cell parameters a = 10.76(1) Å, c = 6.596(5) Å, and β = 120° as described by Bochu et al. [96], and one crystal still exhibits remains of the original Pnma structure of CaMnO$_3$. EDX maps acquired in vacuum at room temperature after the experiment, indeed show a segregation of calcium to the edges of the crystals, as in Figure 4.14a and b. Unfortunately, the signal-to-noise ratio for the separate Mn and Ca rich domains was too small to quantify the Ca/Mn/O ratios accurately. This is caused by a combination of the small homogeneous domain sizes and the large background from the double silicon nitride chip. Another part of the crystals transformed to a cell with a = 5.81 Å, b = 9.67 Å and c = 5.80 Å at 800°C, which agrees with the spinel structure of Mn$_3$O$_4$ or Hausmannite described by Aminoff in 1926 [97]. An EDX map of one of these Hausmannite containing particles is shown in Figure 4.14c,d. Again, there is a clear segregation of calcium to the surface. The particle also seems very decomposed by just looking at the morphology by HAADF-STEM. Moreover, bubbles formed, that are most likely filled with He, but this element is too light to be detected by EDX. However, 3DED did not observe any crystalline structure of CaO or other Ca rich phases.

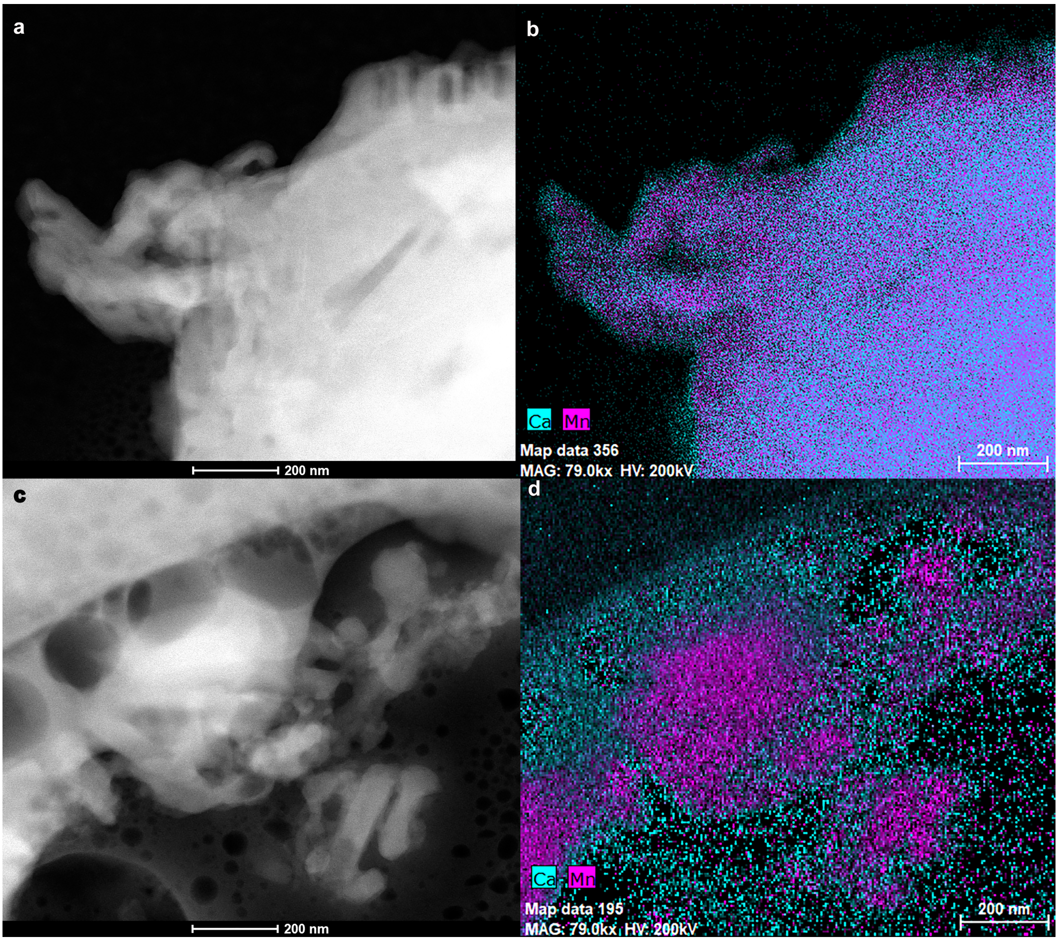

Figure 4.14: HAADF-STEM images and EDX maps at room temperature of crystals after annealing $CaMnO_{3-\delta}$ *in situ* at 800°C in helium. The EDX maps are given in counts, with Ca in blue and Mn in pink. Calcium segregates out of the crystals.

Further, EDX revealed the presence of a silica layer around the crystals, as illustrated in Figure 4.15. Figure 4.15d shows the EDX linescan of the region indicated in Figure 4.15c, indicating that this SiO_2 shell is more or less 40-50 nm thick. After some hours at 850°C, a leak occurred in the closed gas volume, probably due to Si etching at the elevated temperature (see previous chapter), ending the experiment. It must be noted that during the first attempt of this helium *in situ* experiment, a leak occurred already at 785°C. But this experiment was performed with a DensSolutions Nano-Reactor of the so-called "new design", which systematically break at lower temperatures than the "old design" DensSolutions Nano-Reactors during all *in situ* experiments for this project. We assume the silicon nitride window is slightly thinner for the new design Nano-Reactors, and it is etched away more easily. As can be seen in the low magnification TEM images in Figure 4.15a and b, ripples were formed in the Si_3N_4 membrane, bubbles appeared, and holes were created in the window near the particles. The data were taken at room temperature immediately after window breakage.

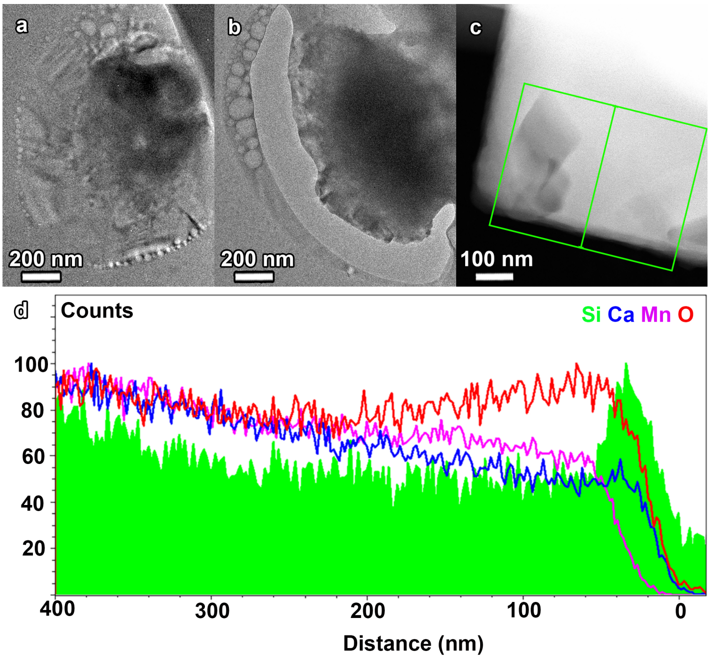

Figure 4.15: (a,b) Low magnification TEM images and (c,d) line scan from EDX of $CaMnO_{3-\delta}$ after heating *in situ* in helium to 850°C. Ripples, bubbles and holes were created in the silicon nitride membrane, eventually leading to a leak in the closed gas cell. A silica layer of more or less 40-50 nm was created on the edge of the crystals.

4.3.2 *In Situ* 3DED of $CaMnO_{3-\delta}$ in Vacuum

In the previous section, it was shown that the silicon nitride windows react with the manganites and get etched away at elevated temperatures. Moreover, the calcium segregates from the particles and they decompose. Thus, another strategy was required to reduce $CaMnO_3$ to $CaMnO_{2.5}$ with ordered oxygen vacancies and the lesser known intermediate oxygen deficient phases. First, $CaMnO_3$ was heated *in situ* in vacuum, as this atmosphere had already proven to be effective in reducing $La_{0.25}Sr_{1.75}MnO_{4-\delta}$ and $Sr_2MnO_{4-\delta}$ as described in the previous chapter.

Upon heating $CaMnO_3$ to 200°C in vacuum, it transformed to an orthorhombic superstructure with *a* multiplied by 4, as shown in the reconstructed sections from *in situ* 3DED in Figure 4.16. At 200°C and 250°C, the newly appeared superstructure reflections appear "streaked" along the h direction, indicating the presence of short-range order, and more specifically that the order within the planes is not periodically repeated among the stacked planes. We previously modelled such type of 2D order in $Li_{1.2}Ni_{0.13}Mn_{0.54}Co_{0.13}O_2$ for the quantification of stacking faults. [98] For $CaMnO_{3-\delta}$, the short-range order stems from the arrangement of oxygen vacancies that form upon reduction. At 300°C and 350°C, the superstructure reflections become sharp and distinct, and the lattice is perfectly periodic again, displaying long-range order in the oxygen vacancies, as can be seen in Figure 4.16d,e. The cell parameters measured at 350°C are a = 21.3(3) Å, b = 7.49(9) Å, and c = 5.35(3) Å. This supercell was already seen for $CaMnO_{2.75}$ by conventional in-zone electron diffraction by Reller et al. as early as 1982 [90]. They described the lattice as consisting of a 50:50 ratio of interconnecting square pyramids (MnO_5) and octahedra (MnO_6). However, while the structure was repeatedly observed and studied by different techniques, e.g. powder XRD by Lichtenthaler [91] and single-crystal neutron diffraction by Dubinin et al. [99] , no structure solution and refinement has been successful for this phase until now. Not even the space group was determined unambiguously as the reflection conditions observed with XRD and in-zone electron diffraction - e.g. by Lichtenthaler [91] - were unclear and inconsistent. They concluded the space group should be either Pmmm (or lower symmetry like Pmm2) since electron diffraction did not show any extinctions, or $Pmn2_1$ from uncertain extinctions in XRD data. They eventually chose $Pmc2_1$ as a space group, but mentioned this was probably not the correct one, as it was contradicted by violations of the reflection conditions.

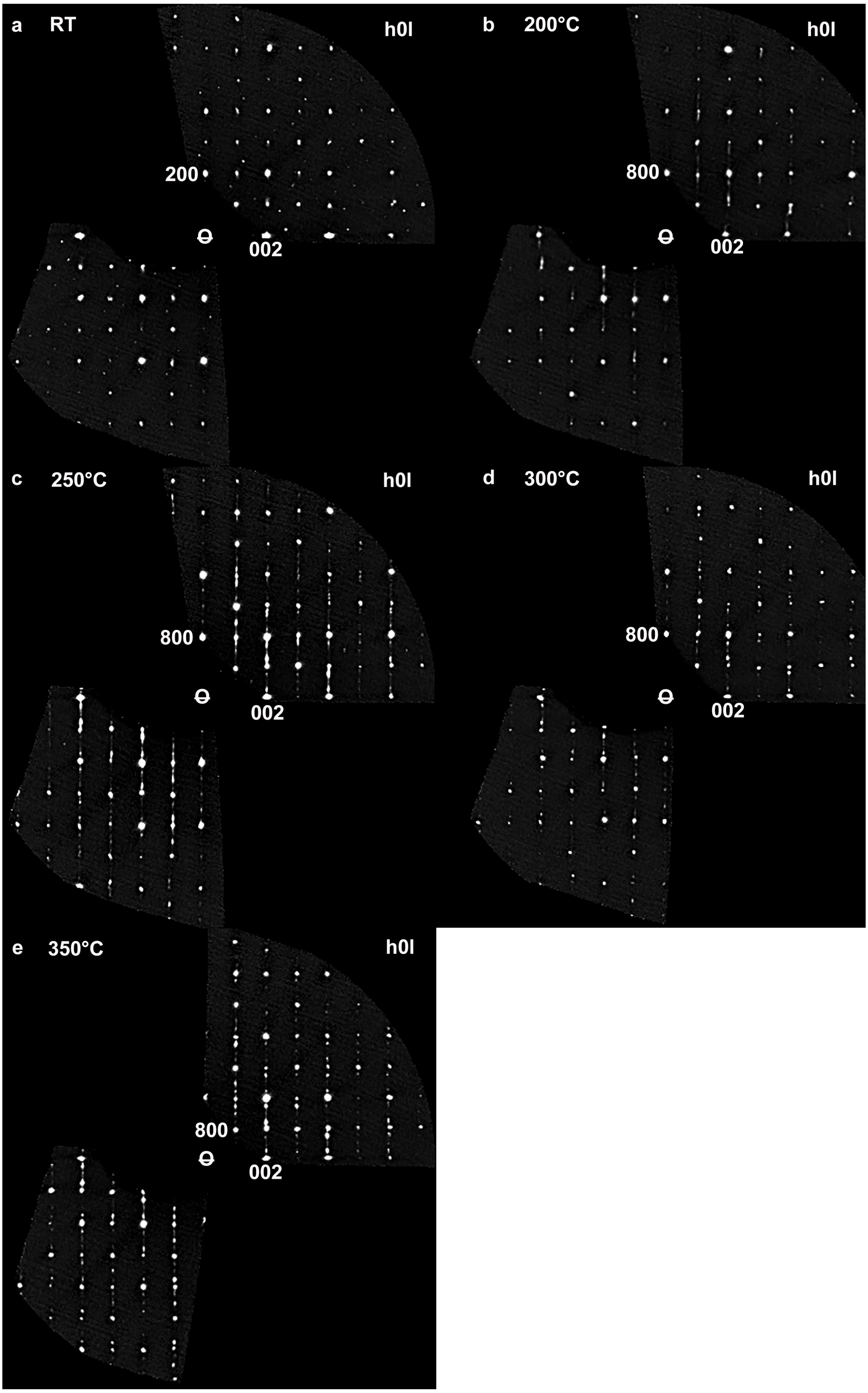

Figure 4.16: Reconstructed h0l section from *in situ* 3DED of CaMnO$_{3-\delta}$ in vacuum at room temperature (a), 200°C (b), 250°C (c), 300°C (d) and 350°C (e).

From our 3DED data, we indeed see inconsistencies in the extinct reflections, as illustrated in Figure 4.17.

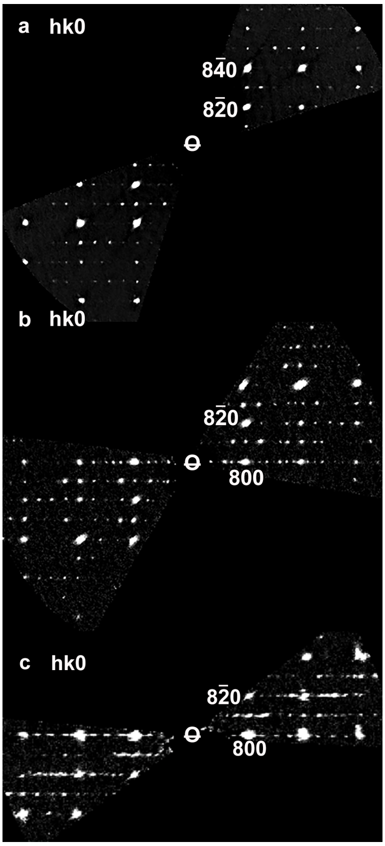

Figure 4.17: Reconstructed hk0 section from *in situ* 3DED in vacuum for three different crystals of $CaMnO_{2.75}$ with cell parameters a = 21.3(3) Å, b = 7.49(9) Å, and c = 5.35(3) Å. In (a), all reflections comply with the condition hk0: h = 2n. However, due to dynamical diffraction in the frames of the 3DED series that lead to this reconstructed zone, in (b) and (c) the condition is violated for many reflections.

Out of the 14 datasets of the $CaMnO_{2.75}$ phase where the hk0 section is present, 5 crystals do not show any reflection conditions. This indeed points toward Pmmm as a space group. However, no model of octahedra and square pyramids can be made that contains the correct number of ordered oxygen vacancies with this symmetry. To accommodate the correct ordered oxygen vacancies, in this case the symmetry should be at least lowered to Pmm2. On the other hand, 3 out of 14 crystals clearly show the restriction hk0: h = 2n without any violation (e.g. Figure 4.17a). For 6 out of 14 crystals this reflection condition holds for a part of the reflections, but there also many reflections for which h is not even (e.g. Figure 4.17b,c). However, multiple scattering can cause reflections to show up in electron diffraction patterns where they should be extinct by symmetry. But when a reflection is systematically absent in a reconstruction, this is caused by the crystal symmetry. The reflection condition being only hk0: h = 2n for an orthorhombic lattice, leads to Pmma, $P2_1ma$ or Pm2a as potential space groups, which all allow a model with the correct oxygen deficiency. In sections 4.3.5 and 4.3.6 , the structure solution and refinement of $CaMnO_{2.75}$ will be discussed further.

4.3.3 *In Situ* 3DED of $CaMnO_{3-\delta}$ in Hydrogen Gas

The applications do not use vacuum, however, but a gas environment with atmospheric pressure. Since the required reduction temperature for inert gas could not be reached *in situ* due to the reaction with Si from the chip, we used diluted hydrogen gas instead. This gas creates an actively reducing atmosphere, and a much lower temperature already suffices for reduction reactions to take place. For instance, Kim et al. [100] could reduce $CaMnO_3$ (Pnma) to $CaMnO_{2.5}$ (Pbam) at 350°C in 5% H_2/Ar.

When we heated $CaMnO_3$ *in situ* in 5% H_2/Ar, it kept its pristine Pnma structure until 150°C. At 250°C, 3DED also detects the intermediate $CaMnO_{2.75}$ phase with unit cell a = 21.6(2) Å, b = 7.70(4) Å, and c = 5.42(2) Å, as shown in Figure 4.18 and Figure 4.19.

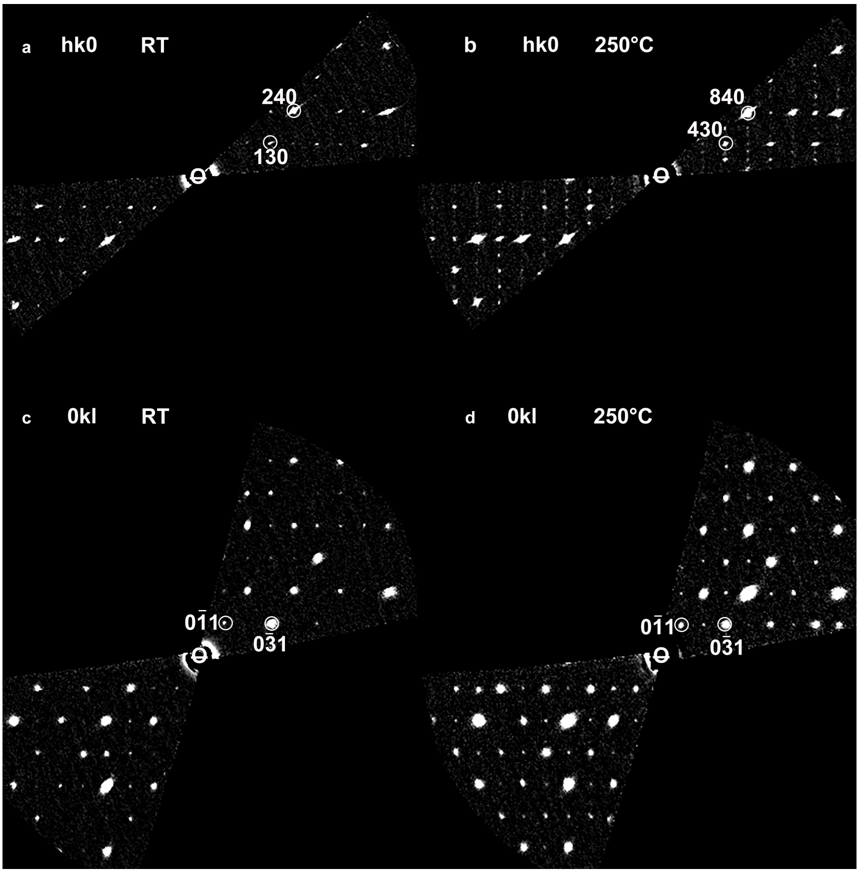

Figure 4.18: Reconstructed hk0 and 0kl sections from *in situ* 3DED of $CaMnO_{3-\delta}$ at room temperature (a,c) and 250°C in 5% H_2/Ar. At 250°C, the material has been reduced to $CaMnO_{2.75}$ with cell parameters a = 21.6(2) Å, b = 7.70(4) Å, and c = 5.42(2) Å.

In the former figure, it is clear from the reconstructed hk0 and 0kl sections from 3DED that the a parameter is quadrupled, but the b and c length remain the same. In the 0kl section, the positions of the reflections stay the same, only their intensities change. Although the reconstructed sections at room temperature in Figure 4.19a,e do not seem complicated on first sight, this crystal consists of four different twin domains. For clarity, a scheme illustrating the relations between the four different twins in direct space is given in Figure 4.20. Here, the ideal cubic perovskite parent cell is given in red. The four twins originate from the disappearance of the mirror planes and fourfold axes that are indicated in black, when lowering the symmetry to the orthorhombic Pnma unit cell.

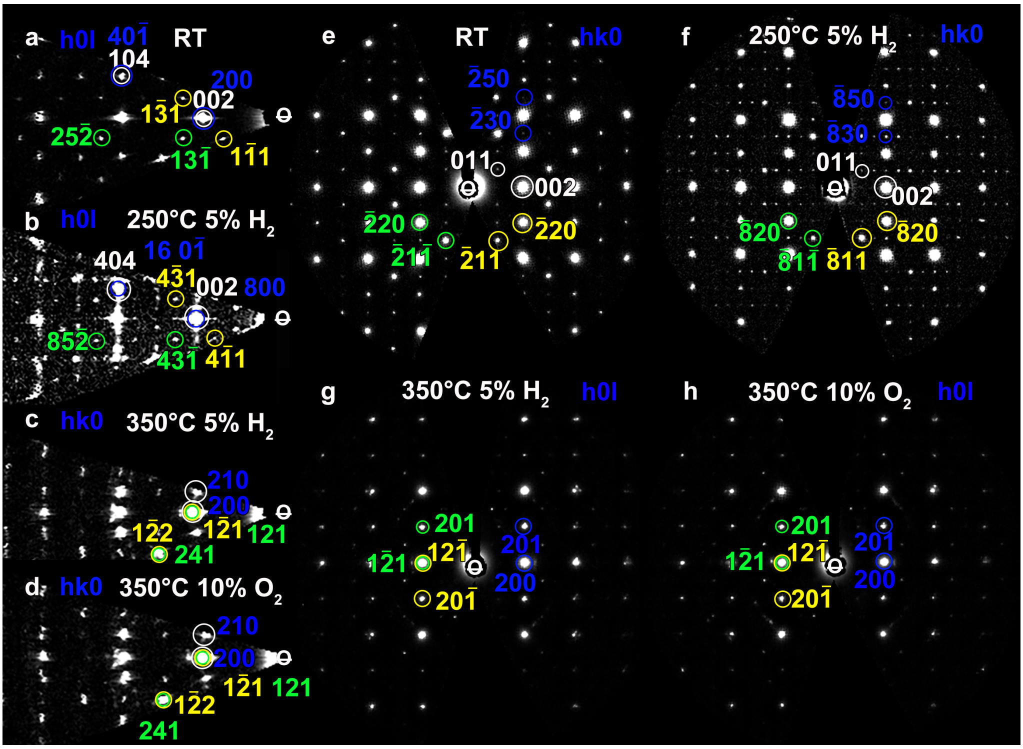

Figure 4.19: Reconstructed sections from *in situ* 3DED of one and the same $CaMnO_{3-\delta}$ crystal at room temperature (a,e) and 250°C in 5% H_2/Ar (b,f), 350°C in 5% H_2/Ar (c,g) and 350°C in 10 % O_2/Ar (d,h). Four twin domains are present in this crystal (indexed in white, blue, yellow and green), amongst which the twin relations must be (and were) conserved during structural transformations upon reduction or oxidation. See the main text for details.

In the reconstructed section in Figure 4.19a, there is a superposition of four zones: two $[010]_{Pnma}$ zones ($h0l_{Pnma}$ sections or $[001]_{Pm-3m}$ zones when indexed in the cubic parent cell), rotated around the $\vec{b}^*$ axis by 90°, and a $[10\text{-}1]_{Pnma}$ ($[010]_{Pm-3m}$) and $[101]_{Pnma}$ ($[100]_{Pm-3m}$) zone, each rotated 45° around the $\vec{b}^*$ axis in clockwise or counterclockwise direction. Thus, all aforementioned zones in Pnma stem from equivalent zones in the cubic parent cell. Since the difference in a and c parameter is small (a = 5.16(4) Å, and

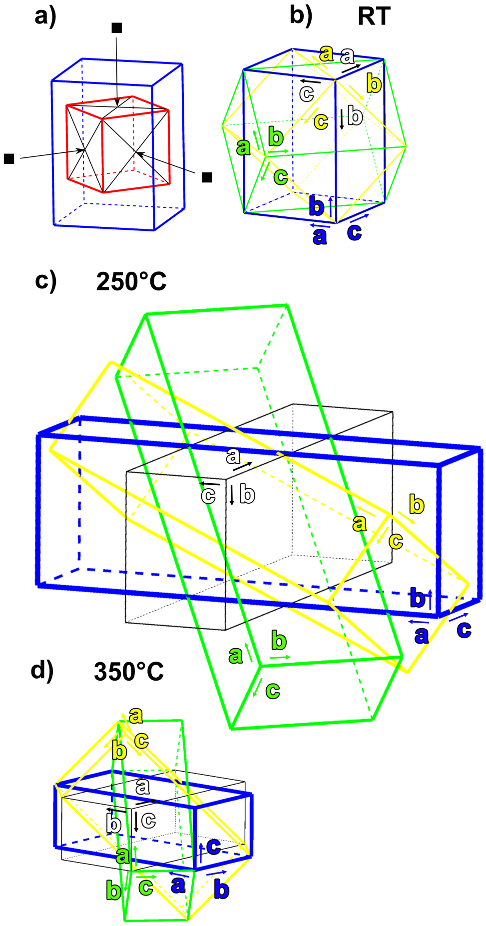

Figure 4.20: Schematics illustrating the relation between all four twins in Figure 4.19. The ideal perovskite parent cell is shown in red (a). The mirror planes and fourfold axes (black) disappear when going from this cubic cell to the orthorhombic Pnma cell, giving rise to the four twins. While the unit cell changes when heating in hydrogen gas from room temperature (b) to 250°C (c) and 350°C (d), the twin relations remain the same through all transformations. See main text for a detailed explanation.

c = 5.13(1) Å), the reflections of the first two twins nearly coincide. The reflections of the twins oriented along the <010>$_{Pnma}$ direction are indexed in white and blue, the last two twins are indexed in yellow and green. Logically, this implies that in Figure 4.19e, there should be a superposition of the [100]$_{Pnma}$ ([110]$_{Pm-3m}$) , [001]$_{Pnma}$ ([1-10]$_{Pm-3m}$), [111]$_{Pnma}$ ([101]$_{Pm-3m}$) and [11-1]$_{Pnma}$ ([011]$_{Pm-3m}$) zones, which is indeed the case. Again, these zones originate from equivalent zones in the more symmetric parent cell. Here, the reflections belonging to the [100]$_{Pnma}$ zone (0kl$_{Pnma}$) are indexed in white, and from the [001]$_{Pnma}$ zone (hk0$_{Pnma}$) in blue. All reflections from the [111]$_{Pnma}$ and [11-1]$_{Pnma}$ zone coincide with reflections from the two other zones, and they are indexed in yellow and green.

When heated to 250°C in diluted hydrogen gas, the different domains in the crystal preserve the same relations as in the pristine state. All four domains transformed to the a = 21.6(2) Å, b = 7.70(4) Å, and c = 5.42(2) Å supercell of $CaMnO_{2.75}$ with the following transformation matrices:

$$(a,b,c)_{4x} = (a,b,c)_{Pnma} \begin{bmatrix} 4 & 0 & 0 \\ 0 & 1 & 0 \\ 0 & 0 & 1 \end{bmatrix} \tag{4.2}$$

and

$$\begin{bmatrix} u \\ v \\ w \end{bmatrix}_{4x} = \begin{bmatrix} 1 & 0 & 0 \\ 0 & 4 & 0 \\ 0 & 0 & 4 \end{bmatrix} \begin{bmatrix} u \\ v \\ w \end{bmatrix}_{Pnma} \tag{4.3}$$

Note that the subscript $4x$ was used here instead of $Pmma$ to avoid confusion with the subscript $Pnma$ of the original cell. The transformation matrix given above transforms the [010]$_{Pnma}$ zones into the [010]$_{4x}$ zones (white and blue) and the [10-1]$_{Pnma}$ and [101]$_{Pnma}$ into the [10-4]$_{4x}$ and [104]$_{4x}$ zone (yellow and green), as shown in Figure 4.19b. Further, the [100]$_{Pnma}$ zone is transformed into the [100]$_{4x}$ zone (or 0kl$_{4x}$ section, white), the [001]$_{Pnma}$ zone into the [001]$_{4x}$ zone (or hk0$_{4x}$ section, blue) and the [111]$_{Pnma}$ and [11-1]$_{Pnma}$ zones into the [144]$_{4x}$ and the [14-4]$_{4x}$ zones of the fourfold supercell (indexed with yellow and green), as can be seen in Figure 4.19f. Note that here the reflection condition hk0: h = 2n is very clearly present, and there is no other logically consistent way to index the newly appeared reflections. This means that the space group should indeed be Pmma, $P2_1ma$ or Pm2a as mentioned in section 4.3.2 , and not Pmm2.

When heated further to 350°C in 5% H_2/Ar, the crystals transform further to fully reduced $CaMnO_{2.5}$ with space group Pbam and cell parameters a = 5.474(8) Å, b = 10.61(8) Å, and c = 3.859(1) Å, as e.g. in Figure 4.19c and g. The transformation from the original Pnma cell to the Pbam cell is as follows:

$$(a,b,c)_{Pbam} = (a,b,c)_{Pnma} \begin{bmatrix} 1 & 0 & 0 \\ 0 & 0 & \frac{1}{2} \\ 0 & -2 & 0 \end{bmatrix} \tag{4.4}$$

and

$$\begin{bmatrix} u \\ v \\ w \end{bmatrix}_{Pbam} = \begin{bmatrix} 2 & 0 & 0 \\ 0 & 0 & -1 \\ 0 & 4 & 0 \end{bmatrix} \begin{bmatrix} u \\ v \\ w \end{bmatrix}_{Pnma} \tag{4.5}$$

Therefore, the expected zones in Figure 4.19c are two $[001]_{Pbam}$ zones (stemming from the $[010]_{Pnma}$ zones), rotated 90° with respect to each other, and the $[210]_{Pbam}$ and $[2\text{-}10]_{Pbam}$ zones (coming from the $[10\text{-}1]_{Pnma}$ and $[101]_{Pnma}$ zones). This is indeed the case, except that only one of the $[001]_{Pbam}$ domains is seen. Lastly, in Figure 4.19g, there is a superposition of the $[010]_{Pbam}$ (from the $[001]_{Pnma}$ zone), $[2\text{-}14]_{Pbam}$ and $[214]_{Pbam}$ zones (yellow and green, from the $[111]_{Pnma}$ and $[11\text{-}1]_{Pnma}$ zones), which all almost completely overlap. Also here, the expected $[100]_{Pbam}$ zone (from the $[100]_{Pnma}$ zone) is not visible anymore in the pattern. Perhaps two domains crystallized into one larger domain at this higher temperature, or the last twin domain accidentally was not inside the SA aperture during this 3DED acquisition. But on top of that, other reflections are seen in the reconstructions that do not fit with any logical twin relation. Maybe the crystal partly started to decompose.

Upon changing the atmosphere to 10 % O_2/Ar at 350°C, no reoxidation took place and the structure did not change anymore, even after waiting for several hours and after cooling down in 10 % O_2/Ar to room temperature (see Figure 4.19d and h). However, this does not necessarily mean that the reaction is not reversible, as will be discussed in the next section.

4.3.4 Mono STEM-EELS of $CaMnO_{3-\delta}$ after *In Situ* Redox Cycling

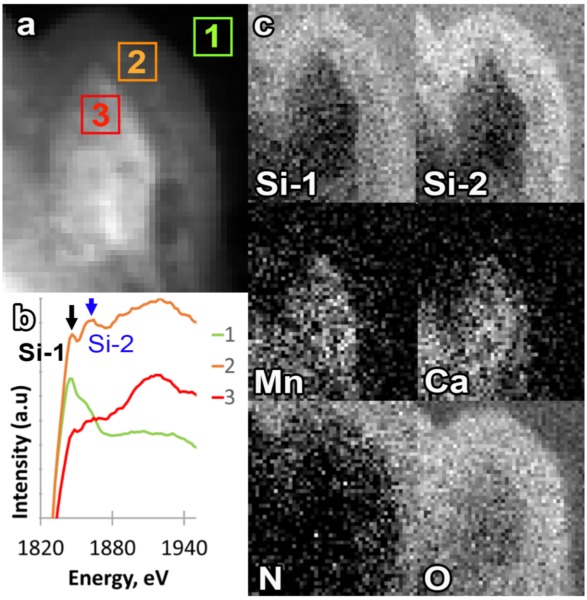

Figure 4.21: ADF image (a), EELS spectrum with the Si K edge (b) and elemental maps (c) from mono STEM-EELS on $CaMnO_{3-\delta}$ after *in situ* cycling in 5% H_2/Ar and 10 % O_2/Ar at 350°C. A SiO_2 shell was formed around the particles. The crystals are supported by a silicon nitride heating chip. Si-1 and Si-2 refer to the first and second peak of the silicon K edge respectively, as indicated with black (Si-1) and blue (Si-2) arrows on the spectrum in (b).

After the *in situ* experiment in hydrogen gas as described in the previous section, mono STEM-EELS was performed to investigate why the material did not reversibly transform back to the pristine Pnma space group of $CaMnO_3$. With mono STEM EELS, not only information on the elemental distribution can be obtained, but also on the manganese valence state, as was e.g. done for $La_xSr_{2-x}MnO_{4-\delta}$ in section 3.6.

Even though the maximum temperature was significantly lower than for the hydrogen reduction of the $La_xSr_{2-x}MnO_{4-\delta}$ samples (350°C versus 700°C), a silica shell formed around the crystals, as illustrated in the elemental EELS maps in Figure 4.21. Region 1 (green) only shows the background signal from the silicon nitride chip. The $CaMnO_{3-\delta}$ crystal itself (region 3, red) is surrounded by a layer consisting of Si and O (region 2, orange). The difference in peak shape from the silicon K edge between region 1 and 2 is shown in the EELS spectra in Figure 4.21b. Si-1 and Si-2 refer to the first and second peak of the silicon K edge respectively, as indicated with black (Si-1) and blue (Si-2) arrows on the spectrum in Figure 4.21b.

In addition to this SiO_2 layer, mono STEM-EELS revealed the presence of gas bubbles containing O_2 in the crystals, as can be seen in Figure 4.22. There, the red arrows indicate a prepeak at around 530 eV from molecular oxygen (reference from [101]) in regions 3, 4 and 5. Also here, the presence of this silica layer surrounding the crystal can be deduced from the lack of manganese at the surface of this particle, compared to the bulk, while oxygen is still abundantly present. Probably, this layer was formed during the oxidation stage of the experiment, entrapping some gas in bubbles inside the crystals, which apparently was not removed again from the crystals in the vacuum atmosphere in which the EELS measurements were performed. An alternative explanation could be that the O_2 is radiation induced because of electron beam damage as in the minerals studied by Garvie [101], but in the present project, no such oxygen gas bubbles were observed by EELS for any of the manganites after a hydrogen gas cycle or vacuum heat treatment, whereas the EELS acquisition conditions were as similar as possible.

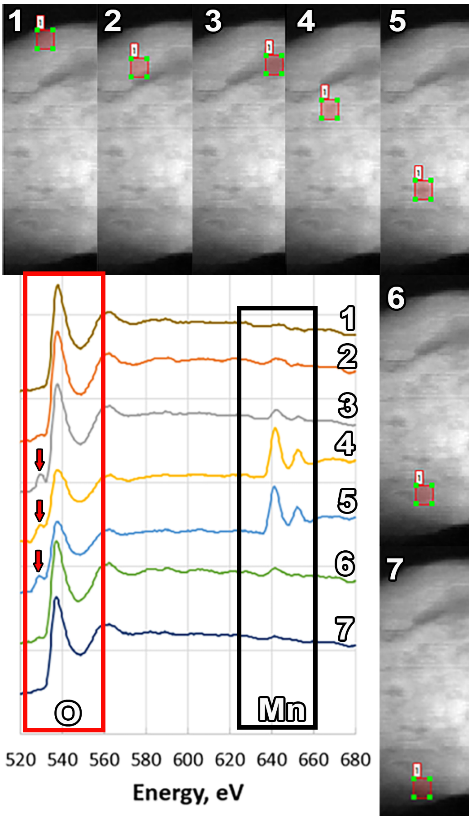

Figure 4.22: Oxygen K (red rectangle) and manganese L (black rectangle) edges from mono STEM-EELS of $CaMnO_{3-\delta}$ after cycling *in situ*, by first heating to 350°C in 5% H_2/Ar and then changing the atmosphere to 10 % O_2/Ar at 350°C. The edges are shown from one surface through the bulk to another surface. In regions 3, 4 and 5, some molecular oxygen is present as bubbles in the crystal, as evidenced by the peaks indicated with the red arrows. While the oxygen signal reaches until the surface of the particle (because of the SiO_2), this is not the case for the Mn signal.

Figure 4.23 shows the variation in manganese valence in a particle from the surface toward the bulk. We see a shift in peak position of the Mn L_3 edge from lower energy at the surface to higher energy inside the bulk, similarly to Figure 3.35 for $La_{0.5}Sr_{1.5}MnO_{4-\delta}$ in section 3.6. Using the same reference EELS spectra [74], we can see that at the edge of the crystal, there is Mn^{2+} present (641 eV) whereas the peak is at the position of Mn^{3+} in the bulk. However, fully oxidized $CaMnO_3$ has a manganese oxidation state of +IV, and thus Mn^{4+} cations. Thus, the silica shell must have prevented reoxidation during the cycle in 10 % O_2/Ar. This also agrees with the 3DED data at this stage: after this cycle, the Pbam structure of $CaMnO_{2.5}$ is found instead of the Pnma of $CaMnO_3$ (see Figure 4.19).

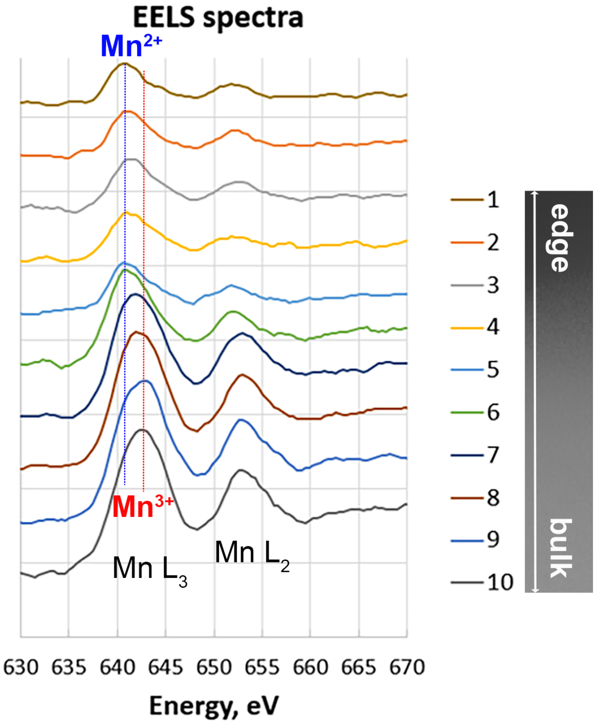

Figure 4.23: Mono STEM-EELS Mn L_2 and L_3 edges from surface toward the bulk of $CaMnO_{3-\delta}$ after cycling *in situ* at 350°C in 5% H_2/Ar and 10 % O_2/Ar. The Mn L_3 peak positions indicate the presence of Mn^{2+} cations at the surface (at 641 eV) and Mn^{3+} cations in the bulk (at 643 eV), which means the silica layer must have prevented reoxidation during the oxygen cycle.

4.3.5 *In Situ* 4D-STEM Tomography of CaMnO$_{3-\delta}$ in Vacuum

In (Ca, Sr)(Mn,Fe)O$_{3-\delta}$, polycrystallinity and twinning are abundant. This was for instance illustrated by the four different twin domains in Figure 4.19, where all of them underwent structure transformations upon reduction. But this highly complicates the structure solution and refinement of CaMnO$_{2.75}$, and was probably one of the reasons the structure had not been solved until now. Even 3DED data seemingly belonging to a single crystal led to serious issues during structure refinement, like unlikely cation positions, negative atomic displacement parameters, wrong bond distances etc. To solve this problem, we used 4D-STEM tomography in vacuum at 300°C. This allowed to search for a 3DED dataset of a small single-crystal area of 8 nm x 9 nm off the microscope, during data processing, from which the structure could successfully be solved and refined (see section 4.3.6).

4.3.6 Structure Solution and Refinement of CaMnO$_{2.75}$

As discussed in section 4.3.2 (see Figure 4.17), some 3DED series from different crystals of CaMnO$_{2.75}$ showed no systematic extinctions, whereas others did display the reflection condition hk0: h = 2n. In the former case the space group should be Pmm2 (or lower symmetry, since Pmmm cannot accommodate the correct amount of ordered oxygen vacancies), but in the latter case it should be Pmma, P2$_1$ma or Pm2a. However, violations of reflection conditions can be explained by dynamical diffraction effects. On the other hand, if reflections are systematically extinct in a diffraction pattern, this must be related to the space group symmetry. So, we decided the hk0: h = 2n condition is the correct one, and solved the structure in Pmma, P2$_1$ma and Pm2a. Nevertheless, multiple structure refinement attempts were made with several potential models in Pmm2, but all of them ran into serious problems (unrealistic cation positions, negative atomic displacement parameters, software crashes, disappearing cations, etc.), and these attempts will not further be discussed here.

The most symmetric potential space group is Pmma, having two mirror planes and a glide plane. Structure solution and kinematical refinement in Pmma leads to the model shown in Figure 4.24a with an R factor of 28.59%. Note that for kinematically refined structures against electron diffraction data, it is normal to have R factors in this range, which is much higher than for XRD. In this unit cell, the oxygen vacancies created upon reduction, are situated on the axial positions. All refined parameters and details are listed in Table 4.3. Some atomic displacement parameters could not be refined. Then, they were fixed to their values in the pristine model of fully oxidized CaMnO$_3$ [102].

Lowering the symmetry, P2$_1$ma is also an option, with one mirror plane replaced by a two-fold screw axis. Structure solution and refinement in this space group lead to the model shown in Figure 4.24b, with the oxygen vacancies ordered in the same way as in the previous model, but with a lower R factor: 25.24%. Refined parameters and R factors are given in Table 4.4. Since a lower symmetry allows to refine more different parameters, this usually results in a lower R factor. Compared to the refined Pmma model, the octahedra look much more distorted and tilted in the refined P2$_1$ma structure. An attempt was made to refine the structure in P2$_1$ma with rigid bodies: keeping all bond angles and distances of the Mn polyhedra rigid in Jana2020. However, this method failed, as this kept all oxygen positions fixed and did not allow for octahedral tilt in the model. Further, the lowest achieved R value using rigid bodies was 30.88%, despite the lower symmetry than Pmma.

The reflection conditions also allow Pm2a as a space group, so the structure solution and refinement was also done with this symmetry. Here, the R-factor was 26.15%, and the octahedra are not tilted, but they are deformed, as can be seen in Figure 4.24c. Again, the oxygen vacancies are arranged in the same manner as in the Pmma and $P2_1ma$ model. Parameters from this refinement are given in Table 4.5.

In all three models, the oxygen vacancies that form the square pyramids, are located in the same plane (see Figure 4.24). Thus, there is an alternation between CaO planes and CaO_{1-x} planes. However, for oxygen deficient $SrFeO_{3-\delta}$ with $\delta = 0.25$ (i.e. $Sr_4Fe_4O_{11}$), Hodges et al. [103] observed oxygen vacancies in alternating planes, as illustrated in Figure 4.25 [104]. We also tried to refine the structure of $CaMnO_{2.75}$ with a similar oxygen vacancy ordering model in $P2_1ma$, but this led to very large atomic displacement parameters, an oxygen content that would be way too low or - if occupancies and atomic displacement parameters were fixed - a final R factor of 41.12%. This indicates that the situation of all oxygen vacancies in the same plane is more plausible.

To decide between the Pmma, $P2_1ma$ and Pm2a structure, bond valence sums were calculated for all of them. This is a method for checking the chemical relevance of structural models, based on the bond lengths and ion valence states. The so-called bond valence v_i is a measure for the strength of a certain bond. According to the bond valence method, the following two equations hold [105]:

$$V = \sum v_i \tag{4.6}$$

$$v_i = e^{\frac{R_0 - R_i}{b}} \tag{4.7}$$

where V is the total valence of the ion, v_i the bond valence of one bond i, R_i the bond length, b an empirical constant and R_0 a parameter that expresses the "ideal" bond length. Values for b and R_0 for bonds between certain elements with specific valence states, can be found in tables e.g. from the International Union of Crystallography [105]. For $CaMnO_{2.75}$, the total average valence of manganese is +3.5. But physically, the oxidation state can only adapt discrete numbers, so this is actually a mixed-valence material. Manganese cations surrounded by an octahedron of oxygen anions are Mn^{4+}, whereas the ones surrounded by a square pyramid are Mn^{3+}. The calculated bond valence sums for all Mn polyhedra in the three different models are listed in Table 4.6. Since the values for Pm2a are deviating very strongly from the real valence states, the deformations of the polyhedra in this model are not likely to be correct. In contast, for both Pmma and $P2_1ma$, the bond valence sums have acceptable values, close to the theoretical ones, which supports their validity. However, this method did not allow to unambiguously choose between them. But although R(obs) is lower for $P2_1ma$, its weighted R-factor wR(obs) is much higher than for Pmma. Moreover, Pmma has a higher symmetry, whereas the octahedra in $P2_1ma$ are very distorted. Thus, we decided that Pmma seems the most likely correct model.

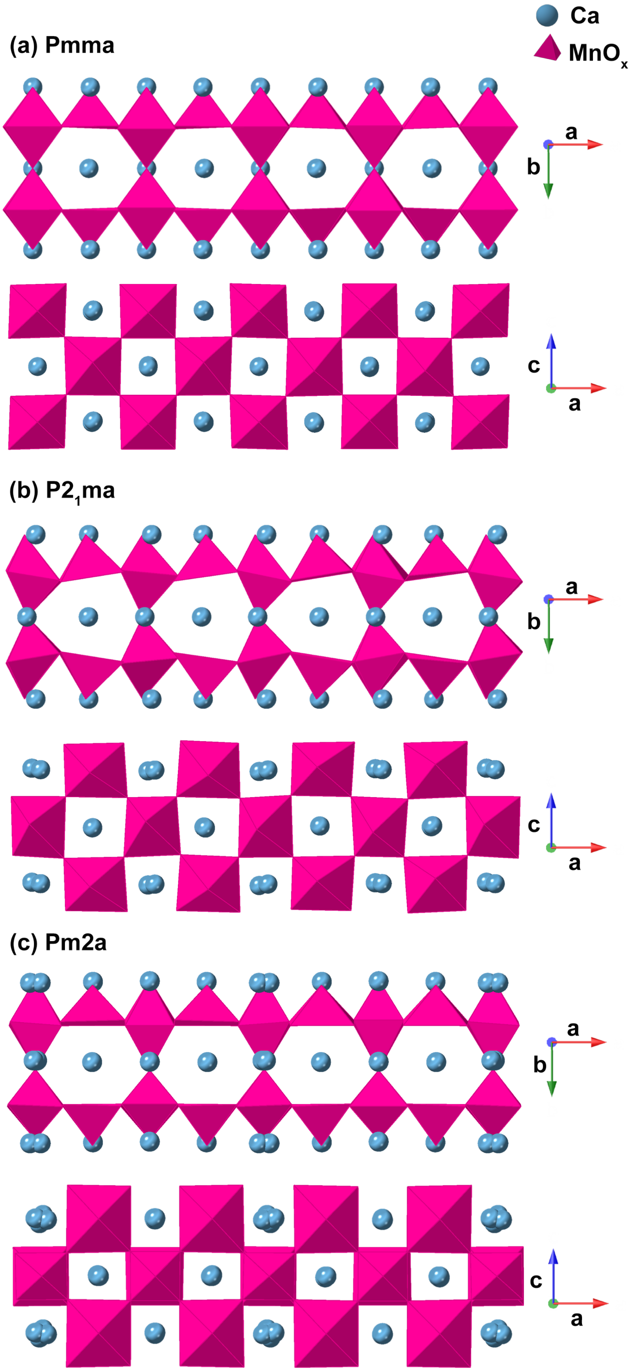

Figure 4.24: Structure model in (a) Pmma, (b) $P2_1ma$ and (c) Pm2a for $CaMnO_{2.75}$ kinematically refined from *in situ* 4D-STEM tomography data at 300°C in vacuum. Mn polyhedra are given in pink, Ca cations in blue.

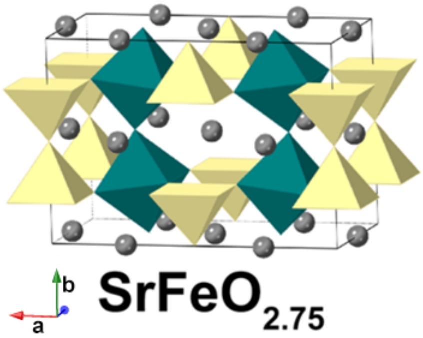

Figure 4.25: Arrangement of the oxygen vacancies in $SrFeO_{2.75}$. Sr atoms are given in grey, FeO_6 octahedra in green and FeO_5 in yellow. Image from Batuk et al. [104]

Parameter	
Temperature (K)	593
Crystal system	orthorhombic
Space group	Pmma
a, b, c (Å)	20.98(5), 7.340(8), 5.2291(1)
Electron wavelength (Å)	0.0251
Tilt range (°)	60
Tilt step (°)	0.5
Completeness (%)	73
Resolution ($\sin\theta_{max}/\lambda$) ($Å^{-1}$)	1.5
Crystal area size (nm x nm)	8 x 9
Beam size (nm)	≈ 5
Detector	ASI Cheetah direct electron detector
Exposure time (μs)	30
Scan size	64 x 64
Beam stop	yes

Table 4.2: Crystallographic details of 4D STEM tomography data collection, data reduction and dynamical structure refinement for $CaMnO_{2.75}$.

4.3.7 *Ex situ* Annealing of $CaMnO_{3-\delta}$

To support the *in situ* experiments, attempts were also made to reduce $CaMnO_3$ *ex situ* in gas. For this purpose, $CaMnO_3$ powder was pressed into a pellet and heated in helium to 850°C with a heating rate of 20°C/min (the same heating rate as used by Galinsky et al. [2]) and kept at this temperature for 1 hour before cooling down. Afterwards, 3DED and EDX were acquired of this sample. In another experiment, $CaMnO_3$ was heated *ex situ* to 240°C in 5% H_2/Ar for 1 hour (heating rate 20°C/min), after which it was checked with precession 3DED. It must be noted that there were temperature fluctuations of ± 10°C for this latter experiment, since the furnace was not designed for this low temperature. For both *ex situ* annealing experiments, the structure found afterwards by 3DED was

Atom	**x**	**y**	**z**	**U$_{iso}$**
Ca1	0.6262(2)	0	0.9893(6)	0.0188(8)
Ca2	0.6232(2)	0.5	0.0039(7)	0.028(1)
Ca3	0.75	0.5	0.4904(6)	0.0079(6)
Ca4	0.5	0.5	0.5	0.0026(5)
Ca5	0.75	0	0.5058(9)	0.025(1)
Ca6	0.5	0	0.5	0.0129(8)
Mn1	0.5	0.2471(2)	0	0.0076
Mn2	0.75	0.2540(2)	0.9896(3)	0.0076
Mn3	0.62491(8)	0.2389(2)	0.4939(2)	0.0076
O1	0.75	0.5	0.0295(1)	0.006
O2	0.5	0.5	0	0.029(2)
O3	0.6862(3)	0.2568(5)	0.7592(8)	0.018(1)
O4	0.5653(5)	0.2444(8)	0.754(1)	0.047(2)
O5	0.75	0	0.015(1)	0.006
O6	0.6892(3)	0.2391(5)	0.2440(8)	0.017(1)
O7	0.5609(3)	0.2436(6)	0.232(1)	0.028(1)
O8	0.5	0	0	0.037(3)
O9	0.6247(3)	0	0.462(1)	0.006

GOF	12.58
R(obs)	28.59
wR(obs)	28.40
# reflections	1496
# refined parameters	41

Table 4.3: Parameters from the kinematical refinement of CaMnO$_{2.75}$ from 4D-STEM tomography in Pmma with cell parameters a = 21.6(2) Å, b = 7.70(4) Å, and c = 5.42(2) Å. (Cell parameters are taken from XRD.)

Atom	**x**	**y**	**z**	**U_{iso}**
Ca1	0.6524(8)	0.5	0.508(1)	0.0038
Ca2	0.7898(8)	0	0.0026(9)	0.0038
Ca3	0.3977(9)	0.5	0.499(1)	0.013(1)
Ca4	0.5384(8)	0	-0.0017(9)	0.0038
Ca5	0.5193(8)	0.5	-0.014(2)	0.016(1)
Ca6	0.2747(8)	0.5	-0.0097(9)	0.0038
Mn1	0.3990(7)	0.2471(3)	-0.0052(6)	0.0076
Mn2	0.7731(8)	0.2504(4)	0.5095(7)	0.0076
Mn3	0.5233(7)	0.2521(4)	0.4841(8)	0.0076
Mn4	0.6486(7)	0.2529(3)	0.0107(8)	0.0076
O1	0.514(2)	0	0.477(6)	0.058(8)
O2	0.769(1)	0	0.451(2)	0.0038
O3	0.407(1)	0	-0.048(2)	0.006
O4	0.647(1)	0	0.025(3)	0.006(2)
O5	0.837(1)	0.282(1)	0.235(2)	0.021(2)
O6	0.846(1)	0.250(2)	-0.256(3)	0.042(4)
O7	0.270(1)	0.5	0.510(3)	0.019(3)
O8	0.521(1)	0.5	0.486(5)	0.031(4)
O9	0.5894(9)	0.278(1)	0.776(2)	0.019(2)
O10	0.4770(9)	0.226(1)	-0.249(2)	0.012(2)
O11	0.730(1)	0.227(2)	0.244(2)	0.019(2)
O12	0.593(1)	0.287(2)	0.235(3)	0.038(4)
O13	0.7214(8)	0.2168(8)	-0.235(1)	0.001(1)
O14	0.4738(8)	0.2184(9)	0.234(2)	0.006(1)

GOF	10.58
R(obs)	25.24
wR(obs)	46.20
# reflections	2463
# refined parameters	81

Table 4.4: Parameters from the kinematical refinement of $CaMnO_{2.75}$ from 4D-STEM tomography in $P2_1ma$ with cell parameters a = 21.6(2) Å, b = 7.70(4) Å, and c = 5.42(2) Å. (Cell parameters are taken from XRD.)

Atom	**x**	**y**	**z**	$\mathbf{U}_{iso}$
Ca1*	0.9884(7)	0.251(1)	0.007(2)	0.019(2)
Ca2	0.25	0.2404(7)	0.008(1)	0.0038
Ca3	0.0038(5)	0.7352(7)	0.037(1)	0.025(1)
Ca4	0.8759(2)	0.7447(5)	0.0.4897(7)	0.0038
Ca5	0.75	0.7427(7)	0.004(1)	0.0038
Ca6	0.1259(2)	00.2447(5)	0.5009(7)	0.0038
Mn1	0.75	0.9965(7)	0.4970(8)	0.0076
Mn2	0.5	0.0070(6)	0.5	0.0076
Mn3	0.1242(2)	0.0094(4)	0.0111(5)	0.0076
Mn4	0.75	0.5275(6)	0.5017(9)	0.0076
Mn5	0.1259(2)	0.5030(5)	0.0380(6)	0.0076
Mn6	0	0.5255(6)	0.5	0.0076
O1	0.6250(5)	0.265(1)	0.998(1)	0.006
O2	0.3136(5)	0.0195(9)	0.750(1)	0.006
O3	0.5	0.781(1)	0.5	0.006
O4	0.75	0.229(1)	0.501(2)	0.006
O5	0.75	0.796(1)	0.497(2)	0.006
O6	0	0.228(1)	0.5	0.006
O7	0.5608(4)	0.0229(9)	0.754(1)	0.006
O8	0.9452(4)	0.493(1)	0295(1)	0.006
O9	0.1957(6)	0.483(1)	0.716(2)	0.016(2)
O10	0.0602(4)	0.0094(9)	0.759(1)	0.006
O11	0.1889(6)	0.006(1)	0.249(2)	0.016(2)
O12	0.1964(6)	0.516(1)	0.288(2)	0.015(2)
O13	0.4429(5)	0.5178(9)	0.298(2)	0.006

GOF	11.00
R(obs)	26.15
wR(obs)	26.36
# reflections	2695
# refined parameters	67

Table 4.5: Parameters from the kinematical refinement of $CaMnO_{2.75}$ from 4D-STEM tomography in Pm2a with cell parameters a = 21.6(2) Å, b = 7.70(4) Å, and c = 5.42(2) Å. (Cell parameters are taken from XRD.)
* The Ca1 position is split with half occupancy.

	Pmma	$\mathbf{P2_1ma}$	**Pm2a**
Mn oct 1	+4.12(3)	+4.02(7)	+5.82(7)
Mn oct 2	+4.12(3)	+4.02(7)	+4.97(6)
Mn oct 3	+4.04(2)	+4.07(8)	+5.55(9)
Mn oct 4	+4.04(2)	+4.07(8)	+5.20(7)
Mn pyr 1	+2.97(2)	+3.09(8)	+1.60(5)
Mn pyr 2	+2.97(2)	+3.09(8)	+2.97(4)
Mn pyr 3	+2.97(2)	+2.85(7)	+1.60(5)
Mn pyr 4	+2.97(2)	+2.85(7)	+2.97(4)

Table 4.6: Bond valence sums for structural models in Pmma, $P2_1ma$ and Pm2a with cell parameters a = 21.6(2) Å, b = 7.70(4) Å, and c = 5.42(2) Å. The abbrevations "oct" and "pyr" mean octahedron and square pyramid.

the pristine Pnma lattice of fully oxidized $CaMnO_3$. One possible explanation is that the environmental conditions were not harsh enough to reduce the material. Or perhaps it immediately reoxidized in air at room temperature after taking it out of the furnace to prepare the TEM grid. It is unlikely that the heating cycle was not long enough for reduction, since oxygen loss is reported to already occur after a couple of minutes at 850°C in helium. [2]

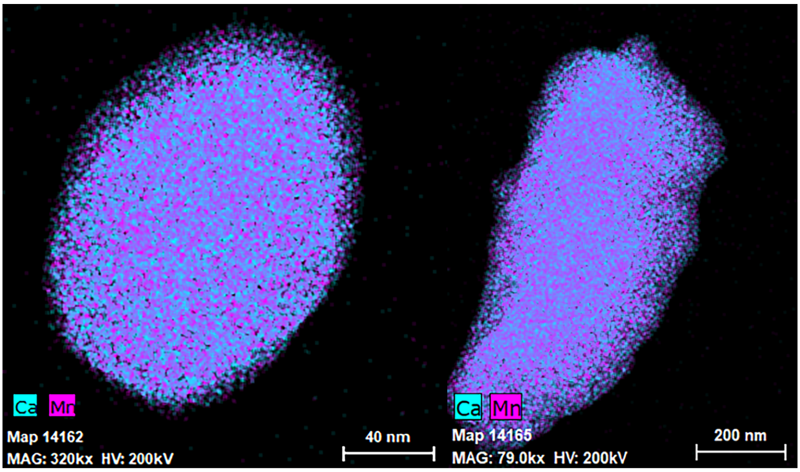

Figure 4.26: EDX maps (given in counts) of $CaMnO_{3-\delta}$ after annealing *ex situ* in helium at 850°C for 1 hour. Ca is shown in blue, Mn in pink. No calcium segregation is visible here, in contrast to the *in situ* experiment with the same environmental parameters (see Figure 4.14).

Interestingly, the sample did not decompose upon heating to 850°C *ex situ* in helium, whereas this was the case for heating *in situ*. By EDX, no calcium segregation was observed either (see Figure 4.26), in contrast to the *in situ* helium experiment at the same temperature as in Figure 4.14. The explanation for this might be related to the difference in particle configuration between the two experiments. *In situ*, isolated nanocrystals have been drop casted on the heating chip, which are locally heated to 850°C by the heating electrodes. On the other hand, the *ex situ* experiments are conducted on a pressed powder pellet with a diameter of 1 cm, and only the outside of this pellet is exposed to the heated surrounding gas (He or 5%H_2/Ar). Possibly, this Ca segregation could be linked to a reaction with water, since the humidity can be quite different in both set-ups. For instance, the flow rate for the *in situ* system can be finely controlled but is limited to 1 ml/min, whereas it is much bigger but not controllable in the *ex situ* set-up, so the efficiency of carrying off potential water molecules might differ. Moreover, the crystals on the *in situ* heating chip are in contact with this potential humidity everywhere except for the side that is lying on the chip. In contrast, most crystals in the pressed pellet for *ex situ* annealing, are inside the bulk and not in direct contact with the surrounding atmosphere, possibly containing reactive water molecules.

4.4 *In Situ* Reduction of CaFe$_{0.2}$Mn$_{0.8}$O$_{3-\delta}$

4.4.1 *In Situ* 3DED of CaFe$_{0.2}$Mn$_{0.8}$O$_{3-\delta}$ in Vacuum

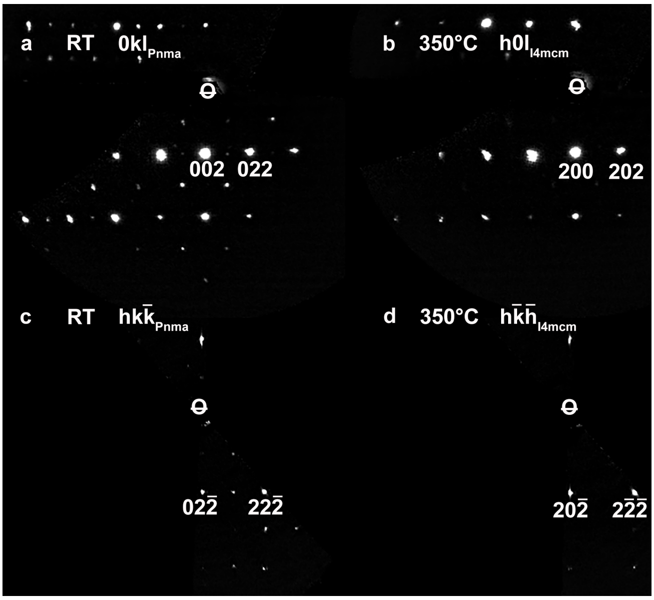

Figure 4.27: Reconstructed sections from *in situ* 3DED of one and the same CaFe$_{0.2}$Mn$_{0.8}$O$_{3-\delta}$ crystal at room temperature (a,c) and at 350°C (b,d) in vacuum. The sections in a and c have been indexed in Pnma, whereas the sections b and d stem from exactly the same crystal orientation, but have been indexed in I4/mcm.

When CaFe$_{0.2}$Mn$_{0.8}$O$_{3-\delta}$ was heated *in situ* in vacuum to 150°C, and then to 250°C (heating rate 5°C/min), it kept the Pnma structure of the pristine material. The 0kl$_{Pnma}$ section or [100]$_{Pnma}$ zone, and hk-k$_{Pnma}$ section or [011]$_{Pnma}$ zone of a CaFe$_{0.2}$Mn$_{0.8}$O$_{3-\delta}$ crystals at room temperature are shown in Figure 4.27a and c. This original cell has the reflection conditions 0kl: k+l = 2n and hk0: h = 2n. However, at 350°C the crystal transformed to a tetragonal cell with cell parameters a = 5.11(3) Å, and c = 7.31(8) Å, as shown in Figure 4.27b and d. Now, the new reflection conditions are hkl: h+k+l = 2n (a body-centered lattice, see e.g. Figure 4.27d) and h0l: h,l = 2n (see Figure 4.27b), indicating I4/mcm as a space group, with the following transformation matrices:

$$(a,b,c)_{I4/mcm} = (a,b,c)_{Pnma} \begin{bmatrix} 0 & 1 & 0 \\ 0 & 0 & 1 \\ 1 & 0 & 0 \end{bmatrix} \tag{4.8}$$

and

$$\begin{bmatrix} u \\ v \\ w \end{bmatrix}_{I4/mcm} = \begin{bmatrix} 0 & 0 & 1 \\ 1 & 0 & 0 \\ 0 & 1 & 0 \end{bmatrix} \cdot \begin{bmatrix} u \\ v \\ w \end{bmatrix}_{Pnma} \tag{4.9}$$

with [uvw] the crystal directions. This transforms the 0kl$_{Pnma}$ section or [100]$_{Pnma}$ zone into the h0l$_{I4/mcm}$ section or [010]$_{I4/mcm}$ zone, and the hk-k$_{Pnma}$ section or [011]$_{Pnma}$

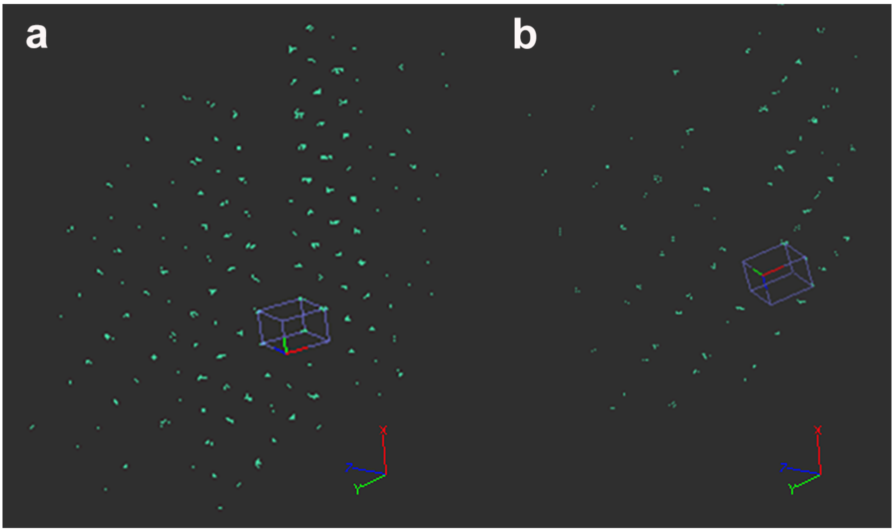

Figure 4.28: Reconstructed reciprocal space from the $CaFe_{0.2}Mn_{0.8}O_{3-\delta}$ crystal of which the section are given in Figure 4.27. (a): at room temperature, (b): at 350°C, both in vacuum.

into the h-k-$h_{I4/mcm}$ section or $[101]_{I4/mcm}$ zone. The reconstructed reciprocal space of this crystal at room temperature and at 350°C in vacuum is given in Figure 4.28. This tetragonal phase was already observed by Taguchi et al. [88] using powder XRD for undoped $CaMnO_{3-\delta}$ upon heating in air to 900°C. Also Mastronardo et al. [94] observed the I4/mcm structure in both low and high partial oxygen pressures for $CaMnO_{3-\delta}$ by *in situ* powder XRD , with $p(O_2)$ ranging from 0.008 atm (pure N_2) to 0.18 atm. However, as mentioned before, they did not encounter this tetragonal phase for the iron doped compositions they studied, i.e. $CaFe_xMn_{1-x}O_{3-\delta}$ with x = 0.1 and 0.3 (see Figure 4.5).

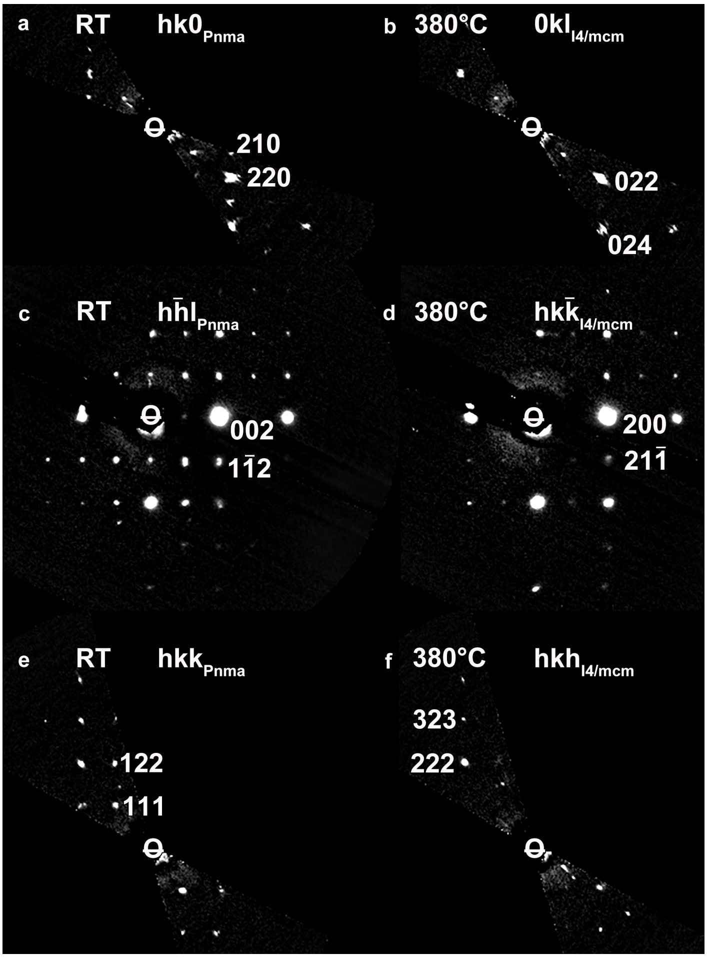

Figure 4.29: Reconstructed sections from *in situ* 3DED of one and the same CaFe$_{0.2}$Mn$_{0.8}$O$_{3-\delta}$ crystal at room temperature (a,c,e) and at 380°C (b,d,f) in argon.

4.4.2 *In Situ* 3DED of CaFe$_{0.2}$Mn$_{0.8}$O$_{3-\delta}$ in Inert Gas

CaFe$_{0.2}$Mn$_{0.8}$O$_{3-\delta}$ was also heated *in situ* in inert gas (in this case argon) as corresponds to the applications. At 380°C, 3DED again shows the transformation to the I4/mcm cell, with cell parameters a= 5.17(2) Å, c = 7.34(8) Å, as can be seen in Figure 4.29. In the $[011]_{I4/mcm}$ zone or hk-k$_{I4/mcm}$ section (Figure 4.29d), some faint reflections are present that violate the body-centering reflection condition (hkl: h +k + l = 2n). They are probably present because the transformation from Pnma to I4/mcm was not complete yet at this stage. But even in this section, it is clear that they are much weaker than in the pristine material, where they are very bright (Figure 4.29c). From 450°C onwards, the crystals decompose. Upon further heating to 750°C, no new crystal phases are formed. EDX at room temperature at the end of the experiment again shows the segregation of calcium to the edge of the particles (see Figure 4.30). On top of the Ca distribution, the distribution of Mn and Fe is not completely homogeneous anymore throughout the crystals either.

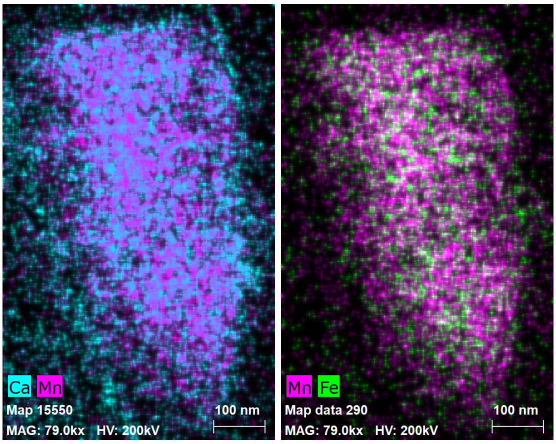

Figure 4.30: EDX maps (given in counts) from $CaFe_{0.2}Mn_{0.8}O_{3-\delta}$ at room temperature after heating to 750°C in argon. Ca is shown in blue, Mn in pink and Fe in green.

4.5 *In Situ* Reduction of $Ca_{0.75}Sr_{0.25}MnO_{3-\delta}$

4.5.1 *In Situ* 3DED of $Ca_{0.75}Sr_{0.25}MnO_{3-\delta}$ in Vacuum

As a last material of this series, $Ca_{0.75}Sr_{0.25}MnO_{3-\delta}$ was also heated in vacuum and studied with *in situ* 3DED, for which the results are shown in Figure 4.31. Again, the pristine crystal with Pnma lattice is twinned at room temperature. In Figure 4.31a, we have superposition of the $[10\text{-}1]_{Pnma}$ zone of one twin (white, $[010]_{Pm-3m}$ in the cubic parent cell), and the $[010]_{Pnma}$ zone of the other twin, 45° rotated (yellow, $[001]_{Pm-3m}$). To be logically consistent, then the $[\text{-}111]_{Pnma}$ zone (yellow, $[0\text{-}11]_{Pm-3m}$) should be superimposed on the $[001]_{Pnma}$ zone (white, $[1\text{-}10]_{Pm-3m}$), which is indeed the case, as shown in Figure 4.31b.

At 250°C, the fading of reflections can indicate a transformation to I4/mcm with unit cell a = 5.22(3) Å, and c = 7.42(9) Å, and transformation matrices as given in equations 4.8 and 4.9. In that case, we see the $[\text{-}110]_{I4/mcm}$ and $[001]_{I4/mcm}$ zones in Figure 4.31c. In I4/mcm these zones have as reflection conditions hkl: h+k+l = 2n ($[\text{-}110]_{I4/mcm}$) and hk0: h+k = 2n ($[001]_{I4/mcm}$). While the first equation holds, the second one is violated by some weak reflections, but they are most likely caused by an incomplete transformation at this temperature. In Figure 4.31d, we have a superposition of the $[100]_{I4/mcm}$ and $[1\text{-}11]_{I4/mcm}$ zone. Here, for I4/mcm, the reflection condition is 0kl: k, l = 2n ($[100]_{I4/mcm}$) and hkl: h+k+l = 2n ($[1\text{-}11]_{I4/mcm}$). The last equation is indeed true, but since the reflections of $[100]_{I4/mcm}$ are completely overlapping with the reflections from the $[1\text{-}11]_{I4/mcm}$ zone, it is not possible to know whether the condition 0kl: k, l = 2n holds.

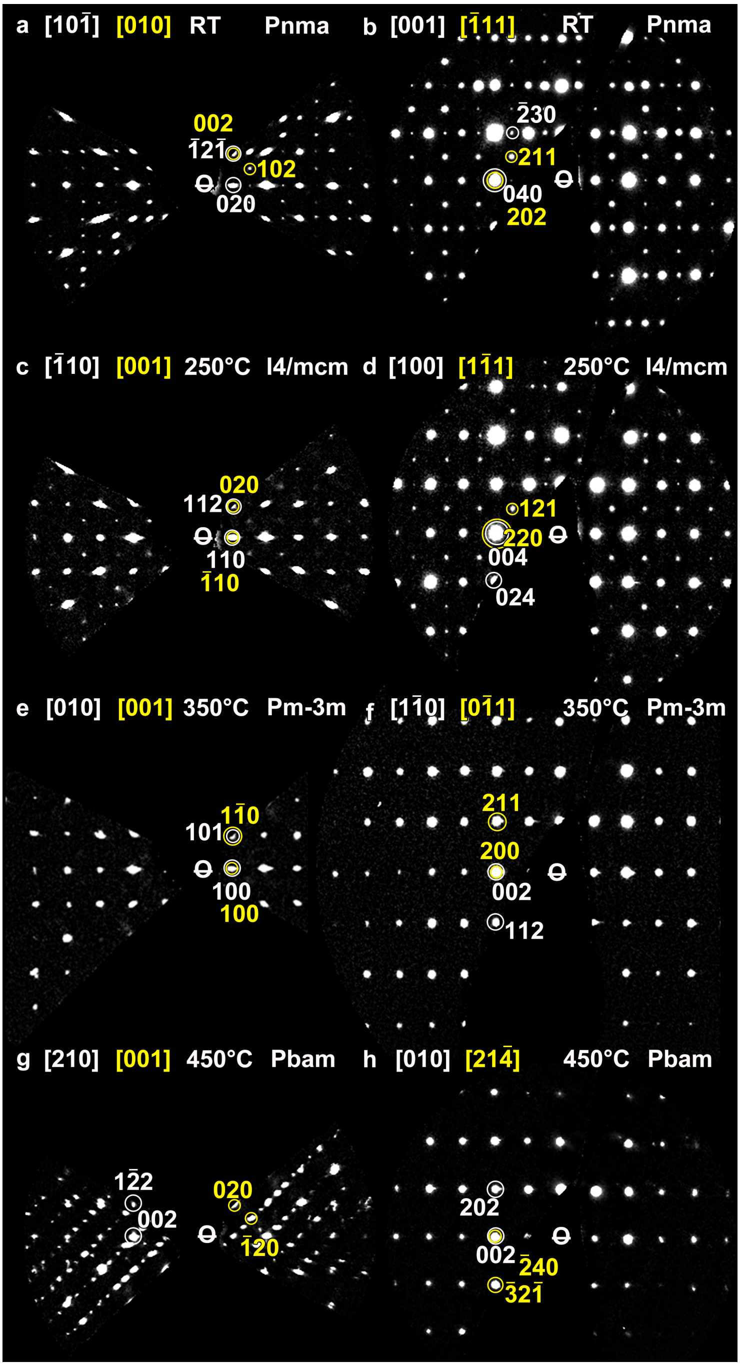

Figure 4.31: Reconstructed sections from *in situ* 3DED of one and the same $Ca_{0.75}Sr_{0.25}MnO_{3-\delta}$ crystal, *in situ* in vacuum (a,b) at room temperature, (c,d) at 250°C, (e,f) at 350°C and (g,h) at 450°C. The crystal transformed from Pnma to I4/mcm, then to Pm-3m and finally to Pbam. Reflections for one twin are given in white, and for the other in yellow.

At 350°C, the crystal transforms to a cubic structure with a = 3.72(2) Å, as shown in Figure 4.31e,f with transformation matrices

$$(a, b, c)_{Pm-3m} = (a, b, c)_{Pnma} \begin{bmatrix} 1 & 1 & 0 \\ 0 & 0 & 1 \\ 1 & -1 & 0 \end{bmatrix} \tag{4.10}$$

and

$$\begin{bmatrix} u \\ v \\ w \end{bmatrix}_{Pm-3m} = \begin{bmatrix} 1 & 0 & 1 \\ 1 & 0 & -1 \\ 0 & 2 & 0 \end{bmatrix} \cdot \begin{bmatrix} u \\ v \\ w \end{bmatrix}_{Pnma} \tag{4.11}$$

Now, Figure 4.31e shows the combination of $h0l_{Pm-3m}$ and the $0kl_{Pm-3m}$ sections, and Figure 4.31f the $[1\text{-}10]_{Pm-3m}$ and $[0\text{-}11]_{Pm-3m}$ zones. In both cases, all reflections of both twins completely overlap as they are equivalent in the higher symmetry.

Finally, at 450°C, the symmetry is lowered again, due to reduction and the ordering of oxygen vacancies. A transformation to Pbam happens with a = 5.4(1) Å, b= 10.61(4) Å, and c = 3.66(3) Å, which is the structure of fully reduced $Ca_{0.75}Sr_{0.25}MnO_{2.5}$, with transformation matrices as given above in equation 4.4 and 4.5. In Figure 4.31g, there is now the combination of the $[210]_{Pbam}$ zone and $[001]_{Pbam}$ zone - the latter 45° rotated, and in Figure 4.31h, the $[010]_{Pbam}$ and the $[2\text{-}14]_{Pbam}$ zone. Again, the twin relations between both twin domains remain unchanged - as they should - during all structure transformations upon heating *in situ* in vacuum.

4.5.2 *In Situ* 3DED of $Ca_{0.75}Sr_{0.25}MnO_{3-\delta}$ in Hydrogen gas

When $Ca_{0.75}Sr_{0.25}MnO_{3-\delta}$ was heated *in situ* to 300°C in 5% H_2/Ar, the larger crystals (≈ 400 nm x 600 nm) transformed from Pnma (Figure 4.32a,b) to the cubic perovskite with a = 3.602(6) Å. This can be seen in Figure 4.32c,d. They still had this same lattice after cooling down, leaving it at room temperature overnight, and reheating to 300°C again, all in the same hydrogen atmosphere. Heating further to 400°C, some of them transformed to I4/mcm, as in Figure Figure 4.32e,f.

Something different happened to the smaller crystals (≈ 150 nm x 150 nm). They changed into the reduced Pbam lattice of $Ca_{0.75}Sr_{0.25}MnO_{2.5}$ at 300°C, as shown in Figure 4.33a. However, after cooling down, leaving it at room temperature in a static 5% H2/Ar environment, and reheating to 300°C in flowing 5% H2/Ar, they adopted the cubic Pm-3m cell (4.33b) and did not change any further upon heating to 400°C and 500°C. This transformation can be seen in Figure 4.33 as the complete disappearance of the 3 superstructure reflections in between two main perovskite reflections on the horizontal lines. However, Mastronardo et al. [94] reported a different sequence in transformations upon reduction, as can be seen from the phase diagrams in Figure 4.5, i. e.: orthorhobmic (Pnma) to tetragonal to cubic upon heating in reducing atmosphere. We also observed this same order for heating $Ca_{0.75}Sr_{0.25}MnO_{3-\delta}$ in vacuum from room temperature to 350°C, as shown in Figure 4.31, with additionally the ordered Pbam phase as a final stage at 450°C. But here - after cooling down in 5% H_2/Ar, leaving the sample in this static atmosphere overnight and reheating in the same hydrogen conditions - the

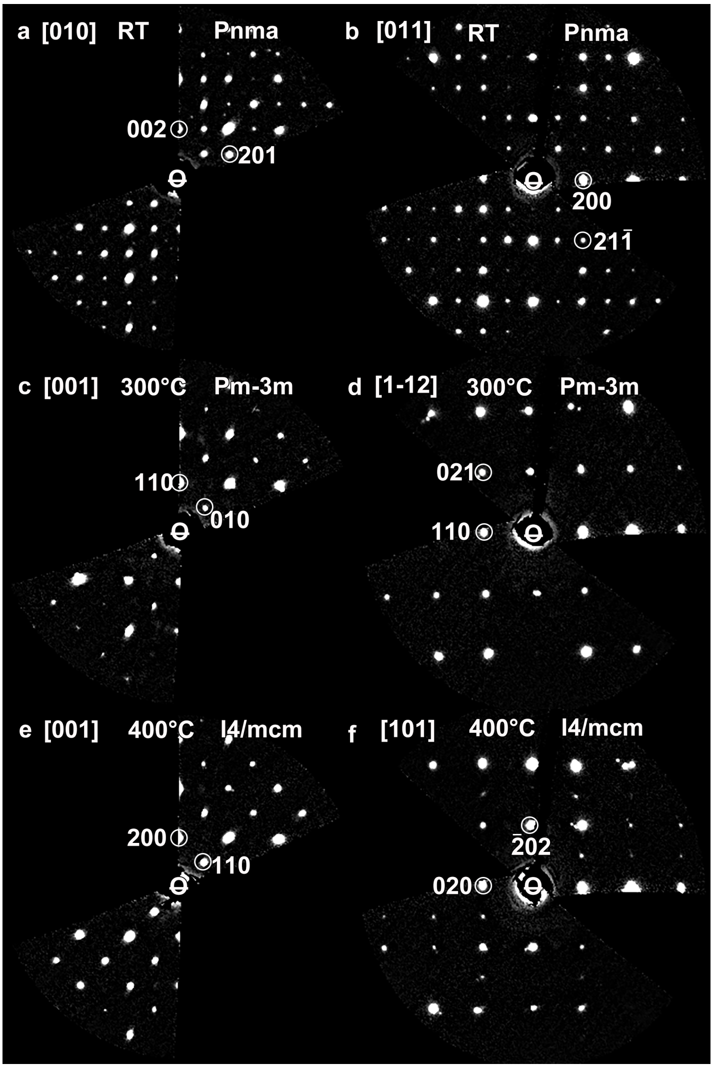

Figure 4.32: Reconstructed sections from *in situ* 3DED of one and the same large (≈ 400 nm x 600 nm) $Ca_{0.75}Sr_{0.25}MnO_{3-\delta}$ crystal in 5% H_2/Ar at (a,b) room temperature, (c,d) 300°C and - after cooling down to RT, leaving it at RT for a night and reheating to (e,f) 400°C. The crystal transforms from Pnma to Pm-3m, and then to I4/mcm.

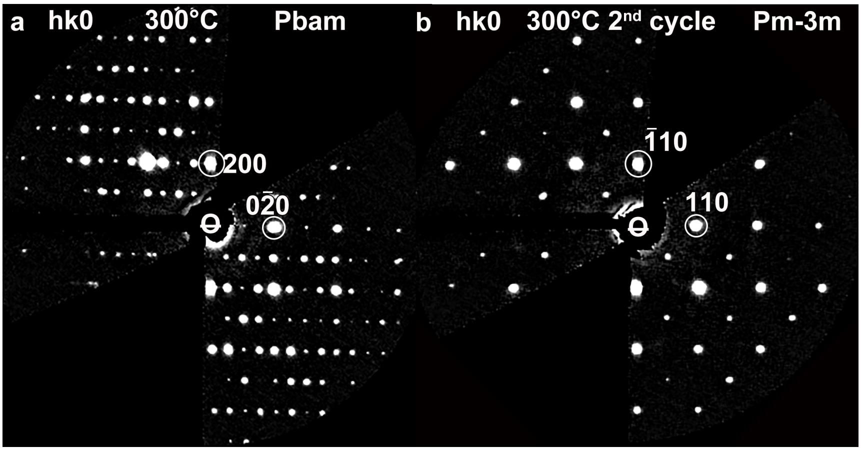

Figure 4.33: Reconstructed hk0 section from *in situ* 3DED of one and the same small (≈ 150 nm x 150 nm) $Ca_{0.75}Sr_{0.25}MnO_{3-\delta}$ crystal in 5% H_2/Ar at (a) 300°C in 5% H_2/Ar and (b) again 300°C after cooling down to room temperature and reheating in the same atmosphere. The structure transforms first to Pbam and then to Pm-3m, and does not change any more upon further heating to 500°C.

occurence of the transformations seems to be reversed. There are two possible explanations here. First, the sample might be reoxidized upon cooling down. E.g. Taguchi et al. [88] reduced $CaMnO_{3-\delta}$ by heating in air, and oxidized it by cooling. The oxygen required for this, might stem from humidity in the gas supply system, or air leaking in overnight when the gas conditions were static at atmospheric pressure instead of in flow conditions with overpressure. Second, the growth of a SiO_2 layer on the particles might have delivered oxygen for reoxidation, or could in another way have interfered with the crystal transformation in the later stage of the experiment.

4.6 Discussions and Conclusion for (Ca, Sr)(Mn,Fe)$O_{3-\delta}$

An overview of all phases that were encountered *in situ* in vacuum and hydrogen/inert gas, is given in Figure 4.34. While *in situ* reduction of (Ca, Sr)(Mn,Fe)$O_{3-\delta}$ in inert atmosphere was not possible due to a reaction of the sample and the silicon nitride heating chip at the required high temperatures, $CaMnO_{3-\delta}$ and $Ca_{0.75}Sr_{0.25}MnO_{3-\delta}$ were successfully reduced to (Ca,Sr)$MnO_{2.5}$ in vacuum and diluted hydrogen gas, because in these harsher atmospheres, lower temperatures suffice for reducing the material. As expected, the structure transformed from the original Pnma cell to the Pbam cell, where all MnO_6 octahedra changed into MnO_5 square pyramids (see Figure 4.3). This validates the technique, but only at sufficiently low temperatures. Even at 350°C, after a successful reduction of $CaMnO_3$ to $CaMnO_{2.5}$, a SiO_2 shell formed at some point, making reoxidation upon cycling in 20% O_2 impossible (as confirmed by 3DED and mono STEM EELS). Strategies to avoid silicon contamination during *in situ* TEM experiments will be discussed in the next chapter.

Both in vacuum and in diluted hydrogen gas, the intermediate $CaMnO_{2.75}$ phase could

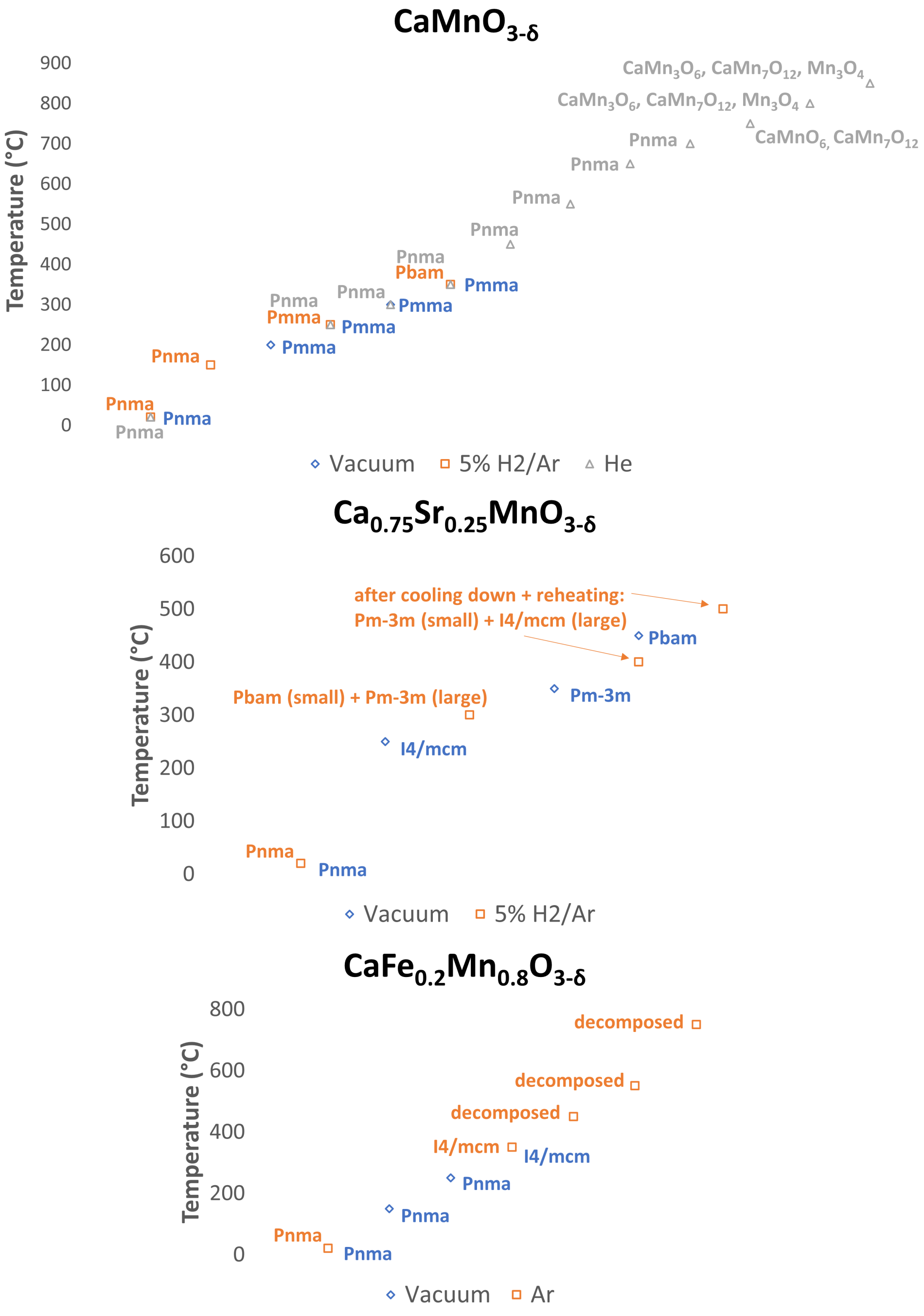

Figure 4.34: Phase diagrams for $CaMnO_{3-\delta}$, $Ca_{0.75}Sr_{0.25}MnO_{3-\delta}$ and $CaFe_{0.2}Mn_{0.8}O_{3-\delta}$ from *in situ* 3DED in vacuum and gas environments. The points at which temperature 3DED were acquired have been plotted in blue, orange and grey, according to the atmosphere.

be captured *in situ*, and its structure was solved and kinematically refined, which was never done before, because of the highly polycrystalline nature and small domain sizes that are specific to the compound. The key element here was the possibility to track individual twin domains by *in situ* 3DED - to determine the correct reflection conditions and symmetry, i.e. Pmma - and 4D-STEM tomography - to collect single-crystal electron diffraction data from a sufficiently small area. For all *in situ* experiments on these samples, this also allowed to verify the conservation of twin relations between different domains and thus the validity of the presumed structural transformations.

Transformations to I4/mcm and Pm-3m were observed for $Ca_{0.75}Sr_{0.25}MnO_{3-\delta}$ and $CaFe_{0.2}Mn_{0.8}O_{3-\delta}$ in vacuum and gas (5% H_2/Ar and Ar respectively). Interestingly, the tetragonal phase was reported by Mastronardo et al. [94] not to occur for $CaFe_xMn_{1-x}O_{3-\delta}$ with 0.1 ≤ and ≤ 0.3 but the structure would directly adopt the cubic lattice, while the I4/mcm structure was observed in our 3DED data *in situ* for $CaFe_{0.2}Mn_{0.8}O_{3-\delta}$, both in vacuum and in argon.

The most important findings resulting from the above mentioned *in situ* 3DED experiments, is that undoped $CaMnO_{3-\delta}$ displays oxygen vacancy ordering for intermediate oxygen content (in between O_3 and $O_{2.5}$) upon reduction, whereas $CaFe_{0.2}Mn_{0.8}O_{3-\delta}$ and $Ca_{0.75}Sr_{0.25}MnO_{3-\delta}$ do not. Where this ordering was missed in oxygen deficient $CaMnO_{3-\delta}$ with powder XRD by e.g. Taguchi [88] in 1989 and even with *in situ* powder XRD by Mastronardo as late as 2020 [94], it was detected by (in-zone) electron diffraction by Reller as early as 1984 [4]. But even with 3DED, we did not see any vacancy ordering for the strontium or iron samples upon heating *in situ* in vacuum or gas atmosphere, except for the final Pbam space group of fully reduced $Ca_{0.75}Sr_{0.25}MnO_{3-\delta}$ and $CaMnO_{2.5}$ where all Mn cations are five-coordinated.

An argument could be that the material was actually not reduced because of the silicon contamination with the Nano-Reactors, but we did observe the same phase transitions to I4/mcm and Pm-3m that were linked to oxygen deficient compounds by Taguchi et al. [88] using thermogravimetric analysis, i.e. $CaMnO_{2.65}$ and $CaMnO_{2.56}$ respectively. Moreover, these phase transformations occurred at temperatures between 250°C and 450°C, which is much lower than the temperature range for reducing $La_xSr_{2-x}MnO_{4-\delta}$ (550°C-700°C) as in the previous chapter, where the silica shell indeed prevented reduction. However, this layer growth probably intervened with transformations in the later stages of the experiment, e.g. the reoxidation cycle for $CaMnO_{3-\delta}$ after reduction in hydrogen gas, or reheating the larger $Ca_{0.75}Sr_{0.25}MnO_{3-\delta}$ crystals in hydrogen gas after cooling down. In the former case, the material kept the oxygen vacancy ordered state of $CaMnO_{2.5}$ upon attempted reoxidation, where in the latter case, the sample remained in the intermediate cubic phase, but could not be further reduced to the Pbam end structure. In vacuum - where the silica formation is much slower - $Ca_{0.75}Sr_{0.25}MnO_{3-\delta}$ completely transformed to Pbam at 450°C. Also, the smaller $Ca_{0.75}Sr_{0.25}MnO_{3-\delta}$ crystals did transform to Pbam in 5% H_2/Ar (before cooling down), but already at the lower temperature of 300°C. All of this suggests that reduction does take place in the beginning of the experiment, until a certain moment, where the silica layer has become significant enough to prevent any further oxygen exchange with the atmosphere, and the structure remains invariable for the rest of the experiment.

While this might be the reason why for $CaFe_{0.2}Mn_{0.8}O_{3-\delta}$ the ordered Pbam phase was not observed in vacuum, nor in inert gas, it is also possible that Pm-3m is the end phase here. For higher levels of Fe, brownmillerite-type structures have been reported upon full reduction, e.g. for $Ca_2Fe_{1.039}Mn_{0.962}O_5$ [106]. There, the manganese and iron positions are ordered, and there are alternating planes of Mn octahedra and Fe tetrahedra. However, this was not reported for any structure with a Mn/Fe ratio larger than 1. Moreover, some materials have a critical concentration δ of oxygen vacancies above which they become ordered on a long range, e.g. in solid solutions of $CaTiO_3$ and $CaFeO_{2.5}$ [107] or $LaFeO_3$ and $CaFeO_{2.5}$. [108] Mastronardo et al. report deficiencies of maximum $\delta = 0.33$ and 0.42 for $CaFe_{0.1}Mn_{0.9}O_{3-\delta}$ and $Ca_{0.5}Sr_{0.5}MnO_{3-\delta}$ at 1200°C in air. But this is lower than the amount of oxygen vacancies in the ordered $CaMnO_{2.5}$ (with $\delta = 0.5$). The exact oxygen content for $Ca_{0.75}Sr_{0.25}MnO_{3-\delta}$ and $CaFe_{0.2}Mn_{0.8}O_{3-\delta}$ could not be determined. With mono STEM EELS, the presence of Mn cations with different valence state can be detected, but with this technique the exact ratio of Mn^{4+}, Mn^{3+} and Mn^{2+} cannot be quantified.

One could argue that the oxygen vacancy ordering only occurs at specific values of δ and that the structure becomes disordered in between those values. In that case, the discrete temperature steps in the *in situ* data acquisition could have caused us to miss the vacancy ordered compounds for the Fe and Sr doped samples. However, in the case of $CaMnO_{3-\delta}$, the Pmma super structure for $CaMnO_{2.75}$ remains present over an at least 150°C wide temperature range in vacuum, as shown in Figure 4.16, which makes the probability to miss this phase rather small, since temperature intervals of 50°C to 100°C were used to check the structure with 3DED.

Moreover, Dubinin et al. [99] find that the satellite reflections for $CaMnO_{2.75}$ start to disappear above 727°C, according to them to the higher oxygen vacancy mobility at high temperature. There is an empirical law [109] which connects the starting temperature for vacancy motion T_s with the melting temperature T_m of the material, i.e.

$$T_s = 0.3 \cdot T_m \tag{4.12}$$

and this vacancy motion destroys the ordered oxygen vacancy structure, but the melting temperatures for $Ca_{0.75}Sr_{0.25}MnO_{3-\delta}$ and $CaFe_{0.2}Mn_{0.8}O_{3-\delta}$ could not be found in literature. We assume, however, that the melting point for the doped samples will not differ more than 1000°C from the undoped material, and that oxygen vacancy ordering would still remain present around 400°C, if there would be any.

One potential explanation why for oxygen vacancy ordering occurs in undoped $CaMnO_{3-\delta}$ but not in the doped samples, might have to do with strain. From DFT calculations, Aschauer et al. [110] discovered that tensile strain in $CaMnO_{3-\delta}$ not only lowers the formation energy but also influences the site preference of oxygen vacancies, creating opportunities for engineering oxygen vacancy ordering in materials. Sr^{2+} has a larger ionic radius than Ca^{2+}, i.e. 0.144 nm versus 0.134 nm. Therefore, its incorporation leads to a less distorted perovskite upon reduction, because Mn^{3+} is also larger than Mn^{4+} (0.065 versus 0.053 nm). Therefore, they balance each other and form a more symmetric lattice, with less strain. [111] [112] This could be one of the reasons why the oxygen vacancies tend to remain disordered for the Sr doped sample. Indeed, powder XRD experiments by Zhou [93] and Mastronardo [94] showed that the transition from the distorted orthorhombic cell with polyhedral tilts to the undistorted cubic perovskite cell happens at a lower temperature for $CaFe_{0.1}Mn_{0.9}O_{3-\delta}$ and $Ca_{0.5}Sr_{0.5}MnO_{3-\delta}$ than for $CaMnO_{3-\delta}$, with or without an additional tetragonal cell in between (although we know from electron diffraction that instead of a cubic cell we actually have a supercell due to oxygen vacancy ordering). For $CaFe_{0.1}Mn_{0.9}O_{3-\delta}$, the transition to Pm-3m has been completed at 780°C if $pO_2 = 0.01$, compared to 860°C for $CaMnO_{3-\delta}$ in the same atmosphere. Similarly, $Ca_{0.5}Sr_{0.5}MnO_{3-\delta}$ has been completely transformed to the cubic phase in air at 850°C, where this is 920°C for $CaMnO_{3-\delta}$ in air. [94] While these temperatures are of course much higher than the ones visited in the *in situ* experiment - due to the problems with silica contamination - it means that the doped phases adopt a higher symmetry earlier, which induces less strain and potentially less ordering in the oxygen vacancies.

For the Fe doped material, another aspect might add to the observed disorder. While for Fe-rich Ca(Fe, Mn)$O_{3-\delta}$ compounds the iron and manganese positions are ordered [106], they remain disordered for lower Fe doping level. But as for brownmillerite ferrites, e.g. $SrFeO_{3-\delta}$ [104], Fe^{3+} tend to be coordinated as tetrahedra, while Mn^{4+} cations tend to be surrounded by octahedra and Mn^{3+} by square pyramids. So we get a disordered arrangement of polyhedra, because of the random Mn/Fe distribution. [113] It must be noted that Mn^{2+} can also be tetrahedrally coordinated (e.g. [114]), and for undoped $CaMnO_{2.5}$, mono STEM EELS did detect the presence of this valence state after *in situ* annealing in H_2 (see Figure 4.23). However, this was only at the surface up to a depth of maximum 10-20 nm, while Mn^{3+} was observed deeper inside the bulk, and from 3DED, no different structure from surface reconstruction was observed.

A crucial implication of the fact that the oxygen vacancies tend to be disordered in the Sr and Fe doped materials but ordered in $CaMnO_{3-\delta}$, is the easier reducibility of the doped materials. For instance, $CaFe_{0.2}Mn_{0.8}O_{3-\delta}$ already releases O_2 at 600°C in working conditions, where this is higher than 800°C for the undoped calcium manganite [3]. But as already mentioned in section 3.7, oxygen vacancy disorder in non-stoichiometric perovskite oxides leads to higher oxygen permeability than ordered oxygen vacancies, as shown by Kruidhof et al. [57] by powder XRD. Therefore, doping of the A and B site with respectively Sr or Fe, improves the operational temperature as an oxygen carrier in the CLOU process.

While it was reported that - in their application for chemical looping with oxygen uncoupling - the doped materials are more stable upon heating than $CaMnO_{3-\delta}$ [2], this is not what we observed when heating them *in situ* in inert atmosphere. $CaMnO_{3-\delta}$ crystals decomposed in helium from 750°C onwards, leading to Mn richer phases as $CaMn_3O_6$, $CaMn_3O_6$ and even Mn_3O_4 due to Ca segregation from the particles. But these phases remained crystalline up to 850°C. On the other hand, the $CaFe_{0.2}Mn_{0.8}O_{3-\delta}$ particles degraded and lost their crystallinity from 450°C when heating *in situ* in argon. However, because of the problems with silica shell formation, these findings might not be transferable to real applications. Attempts to overcome this problem will be discussed in the next chapter.

Chapter 5

Graphene Coating to Prevent SiO_2 Layer Formation while *In Situ* Heating on Si_3N_4 in Gas

5.1 SiO_2 Shell Growth during *In Situ* 3DED in Gas

From the previous chapters, it is clear that *in situ* 3DED can offer interesting results for structural transformations of different perovskite-based manganites in hydrogen gas, but only at sufficiently low temperatures. At a certain temperature - depending on the sample composition and the atmosphere - a silica shell forms around the crystals, stemming from a reaction with the silicon nitride window of the heating chip, as was e.g. shown in Figure 3.31 and Figure 4.21. Because of this layer, the structure remains unchanged for the rest of the experiment. For $La_xSr_{2-x}MnO_{4-\delta}$, this meant that the structures did not display a modulation upon hydrogen treatment. The $(Ca,Sr)(Fe,Mn)O_{3-\delta}$ samples all stopped transforming from a certain point in the experiment onwards: the undoped sample could not be reoxidized from $CaMnO_3$ to $CaMnO_{2.5}$, and $CaFe_{0.2}Mn_{0.8}O_{3-\delta}$ could not be reduced further than the I4/mcm stage.

In TEM, the influence of the electron beam can never be ignored, since it can induce severe damage to samples and provide the energy required for chemical reactions to occur. But at the end of all *in situ* experiments for this project, 3DED and EDX were also acquired from crystals that were not previously exposed to the beam, and there does not seem to be a correlation between electron dose and the reaction with silicon. The EDX or EELS acquisition does not cause the SiO_2 layer either - even though this requires a much higher electron dose than 3DED -, because e.g. in Figure 5.9a the layer is already visible from low magnification TEM images. At a later stage, EDX showed that this was indeed SiO_2 (see Figure 5.12).

The Si reaction is often accompanied by the occurrence of wrinkles in the Si_3N_4 membrane and bubbles, as illustrated in Figure 5.1 for $La_{0.5}Sr_{1.5}MnO_{4-\delta}$ at 700°C in Ar (b), and $CaMnO_{3-\delta}$ at 785°C (a) and 850°C (c) in He. At 700°C (for DensSolutions Nano-Reactors with the more recent "new" design) or 850°C (for the now discontinued "old" design), the silicon nitride membrane even got etched away. This is illustrated in Figure 5.2, for which the images have been acquired after heating $La_{0.5}Sr_{1.5}MnO_{4-\delta}$ to

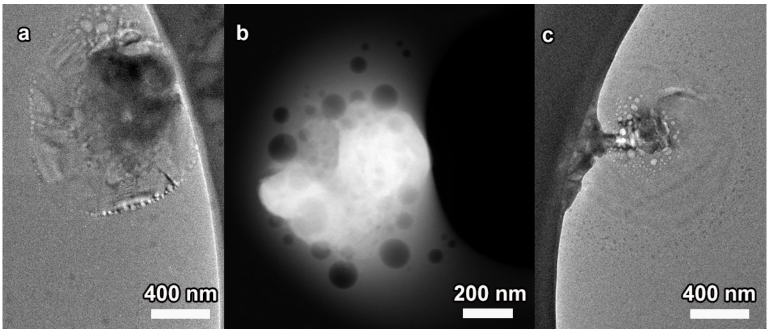

Figure 5.1: Bubbles and wrinkles in the silicon nitride membrane observed after heating (a) $CaMnO_{3-\delta}$ to 785°C in helium, (b) $La_{0.5}Sr_{1.5}MnO_{4-\delta}$ to 700°C in argon and (c) $CaMnO_{3-\delta}$ to 850°C in helium.

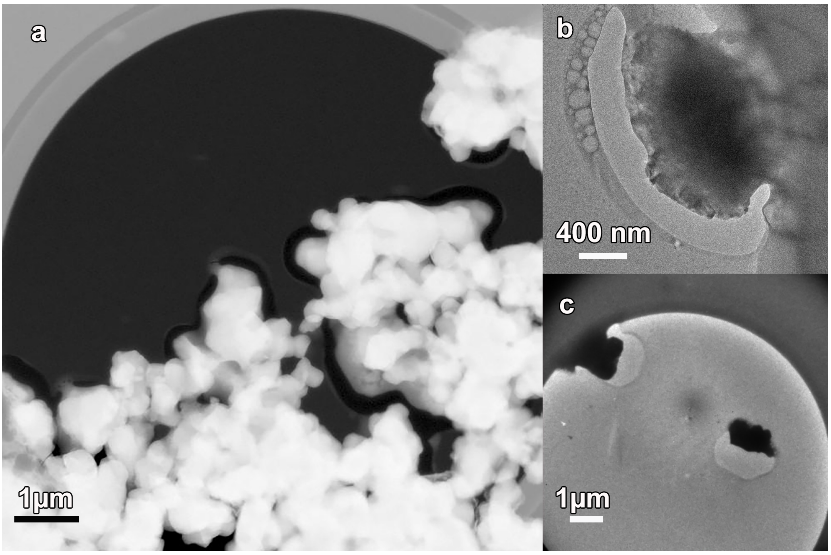

Figure 5.2: HAADF-STEM (a) and TEM (b, c) low magnification images of silicon nitride windows with holes after heating (a) $La_{0.5}Sr_{1.5}MnO_{4-\delta}$ to 700°C in 5 % H_2/Ar, (b) $CaMnO_{3-\delta}$ to 850°C in helium and (c) $La_{0.5}Sr_{1.5}MnO_{4-\delta}$ to 700°C in argon.

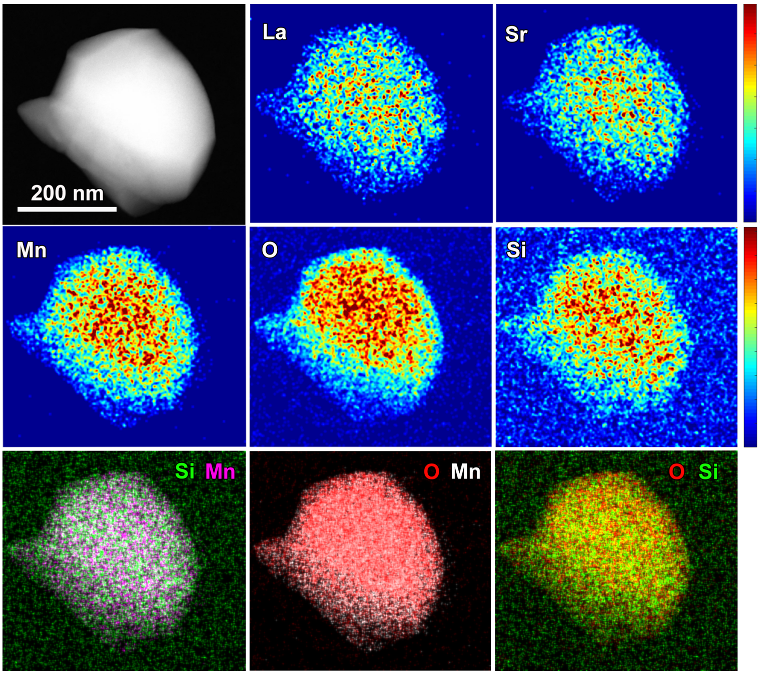

Figure 5.3: HAADF-STEM image and EDX maps (in counts) of La, Sr, Mn, O and Si, and combined maps with Si/Mn, Mn/O and Si/O from $La_{0.5}Sr_{1.5}MnO_{4-\delta}$ after *in situ* annealing in vacuum to a maximum temperature of 800°C.

700°C in either 5 % H_2/Ar (a) or pure Ar (c) and $CaMnO_{3-\delta}$ to 850°C in helium (b). The hole formation happens because of the thinning of the windows due to the reaction with the particles. At that stage, the volume filled with gas is not sealed anymore, and this means the end of the gas heating *in situ* experiment. The Nano-Reactor gets pumped vacuum since it is in contact with the microscope environment, and the microscope column valves have to be closed to protect the microscope.

During *in situ* gas experiments, the silica shell was clearly visible from EDX and EELS (see for instance Figure 3.31 and 4.21). However, the presence of such a layer during *in situ* vacuum heating experiments is much harder to confirm, as the spectroscopy maps there are ambiguous. The silicon nitride support always gives a very strong background signal. Moreover, a Si signal can also be created from the Si crystal in the detector, which is called an internal fluorescence peak, and is unrelated to the real silicon content of the examined material. [115] For example, Figure 5.3 gives the EDX maps of *in situ* vacuum heated $La_{0.5}Sr_{1.5}MnO_{4-\delta}$ to a maximum temperature of 800°C. Nevertheless, $La_{0.5}Sr_{1.5}MnO_{4-\delta}$ could not be reduced in vacuum. On the other hand, Sr_2MnO_4 and $La_{0.25}Sr_{1.75}MnO_{4-\delta}$ did successfully transform to the ordered superstructure of the reduced phase *in situ* in vacuum, at a temperature of 500°C and 550°C respectively. Probably, still some reaction with Si is happening during these experiments, but at a lower rate than in gas atmosphere. Therefore, the lower reduction temperature of the x = 0 and 0.25 members allows the oxygen vacancies to be created before a (thin) protective shell has surrounded the sample. In contrast, for x = 0.5, the reduction temperature is higher, and the Si reaction has evolved too far.

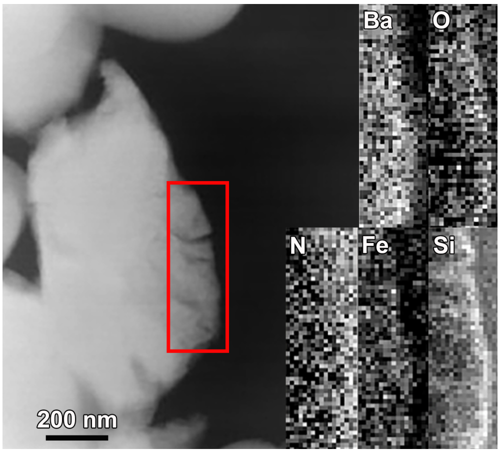

Figure 5.4: EELS map from the Ba, Fe, O, N and Si edge of $BaFeO_{3-\delta}$ (region indicated with red rectangle) at room temperature after heating *in situ* to 700°C in 5 % H_2/Ar.

Thus, there is a temperature threshold above which the shell stops the intended redox reaction. However, this temperature is not an absolute value, but also depends on the sample and the atmosphere. For instance, in previous *in situ* 3DED experiments in our lab [104], $Sr_2Fe_2O_5$ was successfully oxidized at 400°C in O_2, and subsequently reduced again at 700°C in 10 % H_2. Here, no EDX was acquired at any stage during the experiments, but the disappearance and introduction of oxygen vacancies did not seem to be hindered - as evidenced by the disorder and order observed by 3DED. So, if there ever was a reaction with the silicon nitride of the Nano-Reactor, it was weaker and/or slower than in the conditions described in the previous chapters. Moreover, $CaMnO_{2.5}$ could not be reoxidized at the relatively low temperature of 350°C in 20 % O_2, and EELS shows a very thick and clear silica edge after this experiment (see Figure 4.21), where $Ca_{0.75}Sr_{0.25}MnO_{3-\delta}$ and $CaFe_{0.2}Mn_{0.8}O_{3-\delta}$ still underwent transformations linked to reduction above this temperature.

To examine the sample dependence of the Si reaction, an *in situ* EELS experiment was performed simultaneously on perovskite-based manganites and ferrites. For this purpose, five different samples were drop casted on the same heating chip: $Sr_2Fe_2O_5$, $BaFeO_{3-\delta}$, $La_{0.5}Sr_{1.5}MnO_{4-\delta}$, Sr_2MnO_4 and $CaMnO_3$. The Nano-Reactor containing the samples was heated *in situ* in 5% H_2/Ar to 700°C and HAADF-STEM images were acquired to keep track of the morphology of the crystals. Then, the Nano-Reactor was quenched to room temperature, and EELS was acquired. For all five samples, the presence of a silica layer surrounding the crystals was confirmed, so it does not seem sample specific within this test group. As an example, in Figure 5.4, EELS maps for the Ba, Fe, O, N and Si edge are shown for $BaFeO_{3-\delta}$ at room temperature after heating to 700°C in 5% H_2.

Taking all these observations into account, there is clearly a need for a general solution that prevents silica shell formation, regardless the specifics of the experiment. This can enable *in situ* TEM investigations of redox reactions in all types of atmospheres and all temperatures (within the technical limitations of the heating system, i.e. 1000°C).

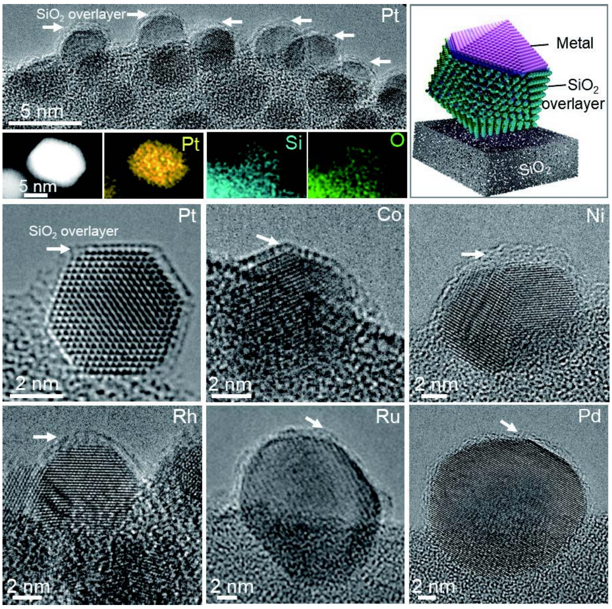

Figure 5.5: High-resolution HAADF-STEM images by Wang et al. [80] of SiO_2 migration and shell formation around metal nanoparticles at 750°C in 10 % H_2/Ar.

5.2 Literature on SiO_2 Growth, Si_3N_4 Membrane Etching and Graphene Coating as a Solution

A very similar - but not identical - reaction was reported by Wang et al. in 2022 [80]. They observed the migration of SiO_2 from the support to metal nanoparticles - Pt, Co , Rh, Pd, Ru, Ni - upon heating *in situ* to 750°C in 10 % H_2/Ar. At the interface with the nanoparticles, the silica is reduced to Si, and diffuses into the crystals, resulting in a thin silicide layer around them at the final stage. This is illustrated in Figure 5.5.

In terms of thermodynamic stability of silicon nitride in pure (dry) hydrogen atmosphere, Herbell et al. [116] found for temperatures between 900°C and 1100°C, that solid Si_3N_4 reacts with H_2 to form N_2 and SiH_4 gas. However, in a humid atmosphere, different output products occur. Depending on the amount of moisture, the final solid can be Si, Si_2N_2O, SiO_2, or a mixture, and the gases can be NH_3, SiO, SiH, SiH_4 or N_2. Lee et al. [117] also observed that SiN_x films for flexible electronics can be oxidized when heated in an environment with high humidity: in their case 60°C-85°C in air with 85%-90% relative humidity. Possibly, the presence of moisture also plays an important role in the present *in situ* experiments in gas conditions, compared to the vacuum heating experiments where all water molecules can be efficiently removed by the pumping systems of the TEM. However, for experiments where oxides are annealed in hydrogen gas - as in the current research -, the formation of water cannot be avoided.

Regarding Si_3N_4 and beam damage, Liu et al. [118] showed how a high dose electron beam at 200 kV degraded nanostructured silicon nitride thin films for semiconductor applications, due to both knock-on damage and ionization damage. They observed thinning of their films and bubble-like defects, comparable to the ones we saw (see Figure 5.1). Howitt et al. [119] also studied the hole drilling power of the electron beam in Si_3N_4 thin films with a thickness of 30 to 60 nm. For intense, focused beams of 10^8 A/m^2, holes were drilled in less than a minute at 300 kV. However, they report that for beam currents of the order of 10^4 A/m^2, it already takes more than a day of constant illumination of the same spot to puncture the film. For comparison, the bottom heating chip from DensSolutions is 30 nm thick, and in the SAED conditions for the aforementioned 3DED experiments a wide, parallel beam (of 200 or 300 kV) is used, with a beam current $\approx 1.5\ 10^4$ A/m^2. Thus, it is unlikely that the Si hole drilling is purely caused by the electron beam. However, although we do not see a local causation of the silica layer by the electron beam, Si knock-on damage might still play a role in the reactions. For *in situ* gas experiments, knocked out atoms or ions are not immediately pumped away as in the vacuum conditions of the TEM, but need to be carried away with the gas flow. This might offer them time to react with crystals on other regions of the heating chip, while being in gaseous aggregation state, e.g. as SiO, SiH or SiH_4.

Li et al. [120] found that the O_2 concentration has a strong influence on Si etching of Si_3N_4 by injecting electrons from a high current Ar plasma. They used a second CF_4/O_2 plasma to functionalize the surface. When they increased the amount of oxygen, oxidation and passivation of the silicon nitride surface was established, which significantly decreased the etching rate. In that case, there was no spontaneous etching by ions anymore, but only slower, controlled etching by the electron beam itself. Therefore, surface oxidation of the silicon nitride chips might explain why no problems with structural transformations upon reduction after oxidation were seen for *in situ* 3DED of $Sr_2Fe_2O_5$ [104].

As a more general solution to avoid the SiO_2 layer growth during high-temperature *in situ*, we tried coating the Nano-Reactors. That way, a physical barrier is introduced in between the oxide particles and the Si_3N_4 membrane, avoiding a reaction caused by direct contact. Additionally, such a coating prevents silicon to be knocked-out by the electron beam and to react in a gaseous state with particles all over the closed cell. The coating should be inert to avoid reaction with the sample, and stable at the required high temperatures for reduction, i.e. 700°C for $La_{0.5}Sr_{1.5}MnO_{4-\delta}$. Further, it should be thin enough so that it does not affect the signal-to-noise ratio for 3DED too much, and ideally not have any crystal structure of which the diffraction spots would interfere with the reflections of the studied sample. As a first attempt, a 3 nm Pt coating was sputtered on the Nano-Reactor (as discussed in 5.4), but this did not lead to good results, and graphene was chosen as a more promising coating option.

Graphene is nowadays increasingly used as a TEM support, especially for high-resolution imaging purposes. Its thickness is that of a single atomic layer (0.34 nm) and it has a low atomic number (for carbon Z = 6), which makes it almost transparent to high-energy electrons and thus background free. Due to its strong mechanical strength, it also prevents specimen motion under the electron beam during imaging, which can significantly improve the image quality at atomic resolution. [121] [122]. Further, graphene is a good electrical conductor (more than six orders of magnitude better than amorphous carbon) which decreases charging of the sample. [122] It is also promising for use at high temperatures. For example, Westenfelder et al. used a free-standing graphene substrate for heating hydrocarbons *in situ* by means of an electrical current, reaching a temperature of 2000 K (= 1727°C). This resulted in a polycrystalline graphene layer, whereas silicon nitride already starts to sublimate at this temperature. [123] Graphene sheets are even used to form enclosed cells for *in situ* TEM experiments, e.g. GLC-EM or graphene liquid cell electron microscopy. There the graphene is not only the material entrapping the liquid, but at the same time also the electron transparent viewing window in the TEM. [124] Thus, its characteristics make graphene a good candidate as a protective coating on the Si_3N_4 membrane to prevent reactions with the drop casted sample while heating *in situ* in gas atmosphere. Different experiments with different parameters (number of graphene layers, electron beam exposure, temperature, coating of the top chip or not) will be discussed in section 5.5.

5.3 H_2 Annealing inside the TEM Without Electron Beam

To study the effect of beam damage without applying any coating, $La_{0.25}Sr_{1.75}MnO_{4-\delta}$ was annealed *in situ* in N_2 to 550°C for 1h and in 5% H_2/Ar to 700°C for 1h without any electron beam exposure during the entire gas experiment. Only after cooling down the sample to room temperature, 3DED and EDX were done in vacuum on the bottom chip alone. We know from the *ex situ* 3DED after hydrogen treatment - as shown in section 3.3.3 - that intermediate exposure to air at room temperature does not reoxidize $La_xSr_{2-x}MnO_{4-\delta}$, but the oxygen vacancy ordering remains intact. However, a leak occurred at 700°C during the *in situ* hydrogen cycle without electron beam, and the sample had to be quenched to room temperature. The resulting windows are shown in Figure 5.6. Even more holes in the membrane and silicon contamination on the particles were present than for the *in situ* gas experiments with intermediate electron beam exposure. Structurally, no transformation to the reduced compound was seen by 3DED either. Therefore, the Si reaction seen during *in situ* reduction in the TEM is not purely caused by the electron beam, and cannot simply be avoided by lowering the electron dose or the voltage.

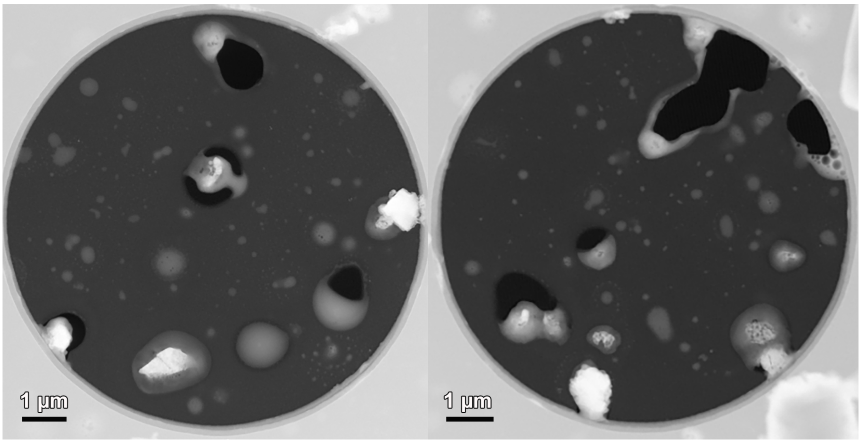

Figure 5.6: Low magnification TEM images of 2 windows with $La_{0.25}Sr_{1.75}MnO_{4-\delta}$ after heating to 550°C in N_2 and 700°C in 5% H_2/Ar without graphene coating and without electron beam exposure during the experiment. Holes got created when the temperature of 700°C was reached.

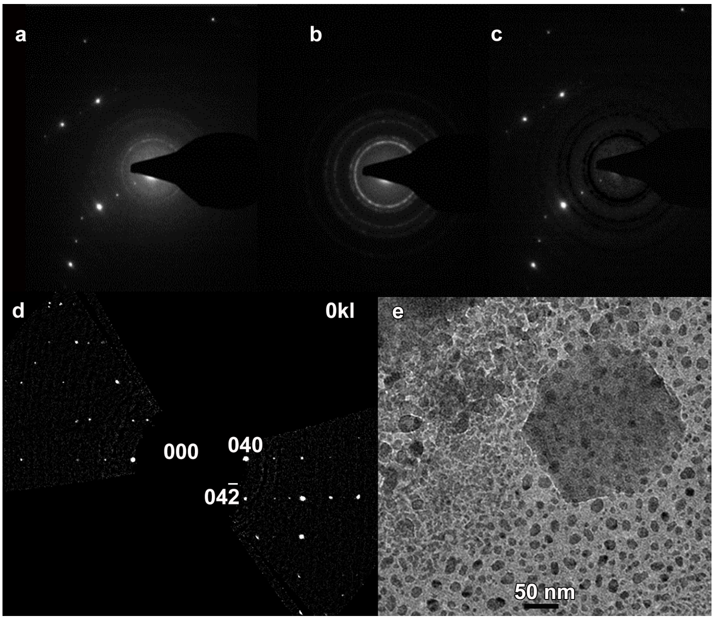

Figure 5.7: Diffraction pattern from 3DED of CaMnO$_{3-\delta}$ on a Pt and C coated Cu TEM grid, (a) before and (c) after background subtraction. The background signal with Pt rings is shown in (b). (d): Reconstructed 0kl section from 3DED. (e) Low magnification TEM image: Pt coating of the silicon nitride DensSolutions Nano-Reactor results in crystalline lumps instead of a continuous amorphous coating.

5.4 *In Situ* 3DED on Platinum Coated Si$_3$N$_4$

As a first try to coat the DensSolutions Nano-Reactor, a 3 nm amorphous platinum layer was sputtered onto the bottom chip, before drop casting CaMnO$_{3-\delta}$ as a test sample. This is the thinnest possible thickness with the sputtering source available in the lab. The coating was first tested on a normal C coated Cu grid for TEM, and 3DED series were acquired, containing both the CaMnO$_{3-\delta}$ reflections and Pt rings, as shown in Figure 5.7a. A Python script was written to subtract the Pt rings from all frames of the 3DED series leading to the frames shown in Figure 5.7c. After that, they were processed with the PETS2 software, resulting in reconstructed sections given in Figure 5.7d. For the subtraction of the rings, a diffraction pattern was taken from the background (Figure 5.7b) during the experiment, and after subtraction negative values were set to zero. Thus, with normal carbon coated grids, Pt coating allowed to still successfully obtain and analyze 3DED data.

However, upon sputtering onto the silicon nitride chip, the platinum clumped together into crystalline lumps, as shown in Figure 5.7e. This effect has two adverse consequences. First, the coverage of the chip is not good anymore, which means the Si can still react with the sample. Second, the crystalline Pt lumps with very intense reflections make it difficult to subtract the signal of the coating from the diffraction frames, since the intensity distribution from platinum will be different for each frame.

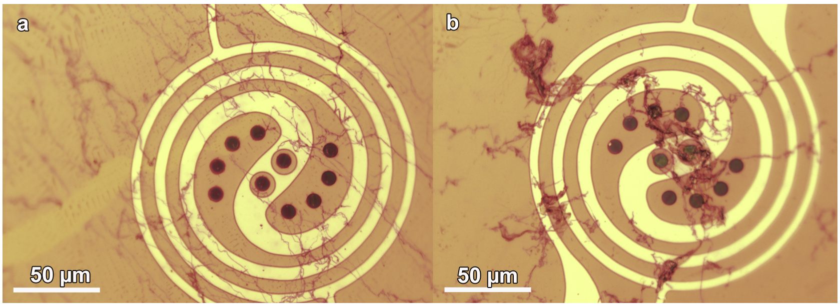

Figure 5.8: Light microscope images of two graphene coated DensSolutions Nano-Reactors, with spiral heating electrodes and ten electron transparent windows that are made from silicon nitride.

As a solution, we explored the potential of a much less strongly diffracting coating, which has already been used frequently in the TEM world: graphene.

5.5 *In Situ* 3DED on Graphene Coated Si_3N_4

5.5.1 Graphene Deposition and Activation

The DensSolutions Nano-Reactors were coated with a single or double - as explicitly mentioned - layer of graphene by Jenthe Verstraelen using a wet transfer method patented at EMAT, of which further details cannot be disclosed. Light microscope images of two different graphene coated DensSolutions Nano-Reactors are shown in Figure 5.8, with spiral heating electrodes and ten electron transparent windows that are made from silicon nitride. After deposition, wrinkles are always present that could not be avoided. But if there are only few present, as in Figure 5.8a, all windows can be used for 3DED without problem. If more are present, as in Figure 5.8b, only the unaffected windows can be used. Some parts of the Nano-Reactor are not covered by graphene, as for instance visible on the left hand side of Figure 5.8a.

Before drop casting the sample on the coated chip, the graphene layer has to be activated. This means that the polymer layer from deposition in between the graphene and the chip has to be removed by heating. For the activation of the bottom chip with a single graphene layer and the activation of the double layer coated top chip, this was done by heating the chip in activated carbon at 300°C for a whole night. However, this gave some carbon contamination on the windows. A cleaner method is heating in vacuum to 450°C for half an hour, which was done in all other experiments in a vacuum pumping station, using the chip's own heating system. For the top chip, this was not possible, since it contains no heating electrodes. In contrast to the other *in situ* heating experiments, no plasma cleaning of the sample was done after drop casting, since this would damage the graphene layer.

5.5.2 *In Situ* 3DED of $La_{0.25}Sr_{1.75}MnO_{4-\delta}$ on Graphene Coated Si_3N_4 in Hydrogen

As a test sample, $La_{0.25}Sr_{1.75}MnO_{4-\delta}$ was chosen to anneal *in situ*. This is because we observed that it transforms to a 2D incommensurately modulated structure upon *ex situ* hydrogen reduction (as described in section 3.3.3), and in the individual frames and reconstructed sections from 3DED many newly appeared reflections are present when the transformation has occurred. This makes it straightforward to verify whether the graphene coating enabled the reduction *in situ* in hydrogen gas. In total, five *in situ* heating experiments were performed on $La_{0.25}Sr_{1.75}MnO_{4-\delta}$ in 5% H_2/Ar with different configurations of graphene, and different environmental parameters. We investigated the effect of a single versus a double graphene layer, and coating of only the bottom chip versus both top and bottom chip of the Nano-Reactor. Coating the top chip was tested to examine whether this might prevent potential Si sputtering from the top chip by the electron beam. Environmentally, the following parameters were varied, to test their influence on the formation of the SiO_2 layer: the maximum temperature, the electron beam exposure, the hydrogen concentration, and whether or not a prior N_2 heating cycle was performed at 550°C for 1h. An overview of all experiments and their parameters is given in Table 5.1. For the experiments without intermediate electron beam exposure, the TEM column valves were never opened before or during annealing in gas. After the completed hydrogen cycle, the holder was extracted, and only the bottom chip - containing the sample - was reinserted into the microscope, where it was examined by (3D)ED and EDX in vacuum at room temperature. It was found that the prior N_2 cycle to desorb attached molecules was required to preserve the crystallinity of the sample, since plasma cleaning could not be done in the presence of graphene. However, in none of these five experiments, the transformation to the 2D incommensurately modulated structure was observed by 3DED, during or after the *in situ* annealing. This means that this graphene coating did not offer a solution for successful *in situ* hydrogen reduction of $La_xSr_{2-x}MnO_{4-\delta}$.

To determine whether or not graphene is present underneath the 3DED examined particles, selected area electron diffraction (SAED) was applied. This is because the graphene coating is too thin for detection by EDX, and also for dark field imaging, which would allow mapping, because the reflections are too weak. An example of an SAED pattern at three different regions near the particles is shown in Figure 5.9, with a selected area aperture of 200 nm. In region 1 (Figure 5.9b), distinct reflections are visible from two graphene layers, rotated a few degrees with respect to each other. A folded ripple is visible on region 2, and there the diffraction pattern gives a ring, since many different orientations are on top of each other in this fold (Figure 5.9b). On region 3, the graphene reflections become very weak and diffuse, and the low magnification image also shows a contrast difference. The systematic study with SAED does not observe the same number of graphene layers near all particles, so the coating is not perfectly homogeneous. Sometimes, there are no graphene reflections visible at all, sometimes only the reflections of a single layer are present, and sometimes there are clearly two graphene layers (as e.g. in Figure 5.9b). However, even for particles that are certainly lying on the graphene, no transformation to the oxygen vacancy ordered structure was observed by 3DED indicating that something was still hindering the reduction.

For a more general overview of the graphene coverage on the chip windows, scan-

Experiment + which chips coated	**# Layers of graphene**	**e^- beam exposure**	**N_2 cycle (550°C)**	**Max. T + H_2 concentration**
1: bottom	single layer	3DED + EDX during exp.	no	700°C, 5%H_2/Ar
2: bottom	double layer	3DED during exp., EDX + EELS after exp.	yes	700°C, 5%H_2/Ar + 100% H_2
3: top + bottom	double layer	3DED during exp., EDX after exp.	yes	700°C, 5%H_2/Ar
4: bottom	double layer	no e^- beam during exp., 3DED + EDX after exp.	no	550°C, 5%H_2/Ar
5: bottom	double layer	no e^- beam during exp., 3DED + EDX after exp.	yes	700°C, 5%H_2/Ar

Table 5.1: Parameters of *in situ* annealed $La_{0.25}Sr_{1.75}MnO_{4-\delta}$ in (diluted) H_2 on a Graphene Coated DensSolutions Nano-Reactor

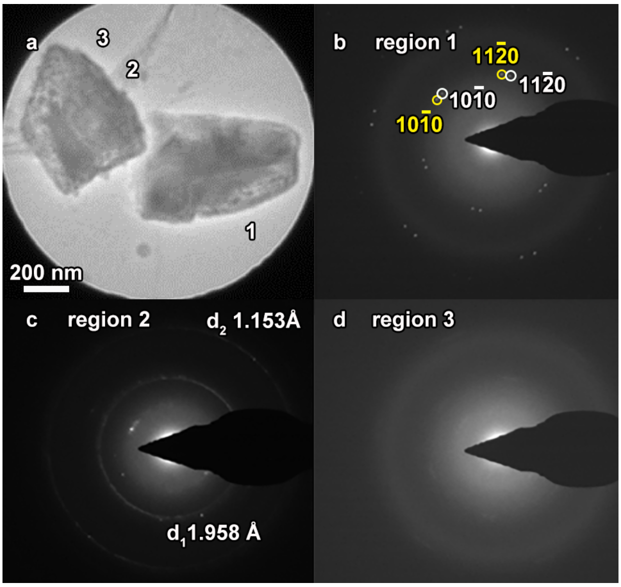

Figure 5.9: SAED patterns at 3 regions near the $La_{0.25}Sr_{1.75}MnO_{4-\delta}$ particle on a Si_3N_4 chip coated with a double graphene layer, with a selected area aperture of 200 nm.

ning electron microscopy (SEM) images were acquired after the previously described experiments with graphene coating. For this, a voltage of 5 kV was used, which allowed to give different contrast for regions with more and less graphene, as for instance in Figure Figure 5.10a. This is an SEM image of $La_{0.25}Sr_{1.75}MnO_{4-\delta}$ crystals on a DensSolutions Nano-Reactor coated with two graphene layers, after heating *in situ* in hydrogen gas to 700°C. The arrow indicates a ripple in the graphene sheet, and the contrast difference suggests that the amount of graphene differs on both sides of this fold. However, it is not certain that "less" graphene means no graphene at all: perhaps it is only a single layer. Another indication of the graphene presence or absence, is (lack of) the charging effect of the SEM specimen. Graphene is a much better electrical conductor than silicon nitride. That means that the effect of local charging by the electron beam will be bigger for parts that have holes in the coating. In Figure 5.10b, an overview SEM image is shown from the ten windows, as well as a zoom on a single window (Figure 5.10c). The white, very bright areas - locally- and the striped features in the scan - for the whole image - result from the accumulation of charge on the chip just outside the windows. Since there seems to be a correlation between these areas and the regions of darker contrast (as shown in Figure 5.10b), this also supports that regions of the Nano-Reactors are still not protected by graphene.

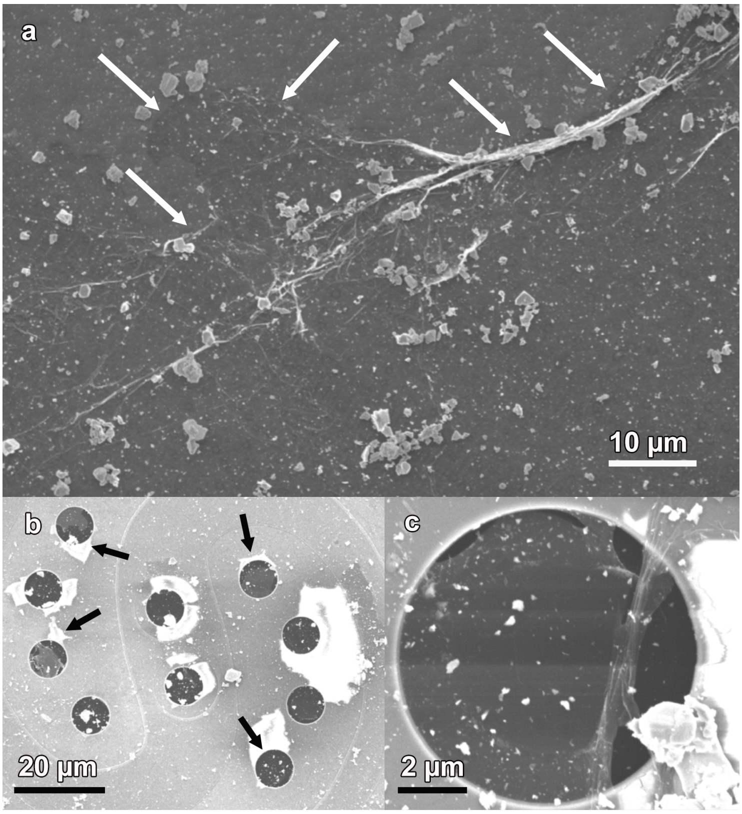

Figure 5.10: SEM images of $La_{0.25}Sr_{1.75}MnO_{4-\delta}$ on a chip coated with a double graphene layer, after heating in 5% H2 to 700°C. See text for the explanation.

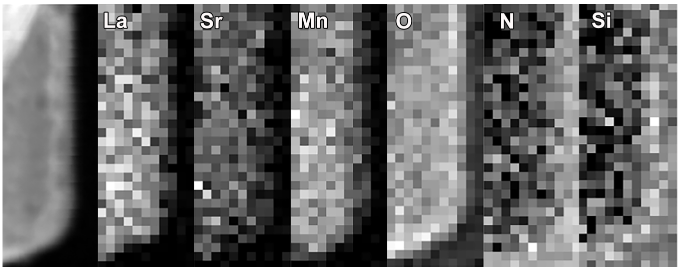

Figure 5.11: Dark field image and signal maps of the La, Sr, Mn, O, N and Si edges from EELS of $La_{0.25}Sr_{1.75}MnO_{4-\delta}$ after *in situ* annealing in N_2 at 550°C, in 5% H_2/Ar at 700°C and 100% H_2 at 550°C on a double graphene layer coated Si_3N_4 Nano-Reactor.

In addition to *in situ* 3DED, also EDX and EELS were acquired during (for EDX) or after the experiment (for EDX/EELS). A silica shell was observed for the experiment with one cycle in N_2 and two hydrogen cycles (in 5% and 100 % H_2) for which maps of the La, Sr, Mn, O, N and Si edges from EELS are shown in Figure 5.11, and EDX maps in Figure 5.12.

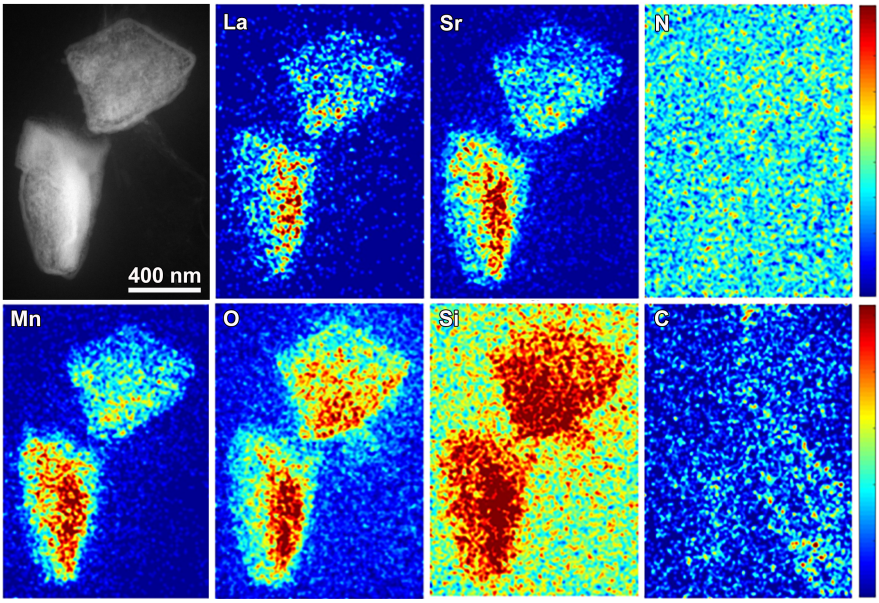

Figure 5.12: HAADF-STEM image and EDX maps (in counts) of La, Sr, Mn, O, N, Si and C from $La_{0.25}Sr_{1.75}MnO_{4-\delta}$ after *in situ* annealing in N_2 at 550°C, in % H_2/Ar at 700°C and 100% H_2 at 550°C on a double graphene layer coated Si_3N_4 Nano-Reactor.

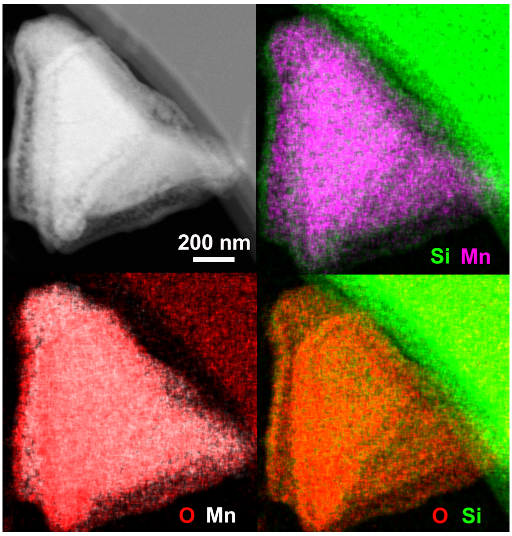

Figure 5.13: HAADF-STEM image and combined EDX maps (in counts) of Si-Mn, Si-O and Mn-O from $La_{0.25}Sr_{1.75}MnO_{4-\delta}$ after *in situ* annealing in N_2 at 550°C and in 5% H_2/Ar at 700°C with both top and bottom chip of the Nano-Reactor coated by a double graphene layer.

A SiO_2 layer was even detected by EDX after the experiment where both the top and bottom chip of the Nano-Reactor were coated by a double graphene layer, as illustrated in Figure 5.13. This experiment consisted of two cycles: one in N_2 and one in 5% H_2/Ar. However, for the other *in situ* hydrogen experiments on graphene coated Si_3N_4, the Si signal from EDX data was ambiguous, similarly to the *in situ* annealing experiments in vacuum (see section 5.1 and Figure 5.3). This is for example illustrated in Figure 5.14, showing EDX maps of $La_{0.25}Sr_{1.75}MnO_{4-\delta}$ on a double graphene layer after annealing in N_2 at 550°C and in 5% H_2/Ar at 700°C without electron beam exposure during the entire experiment. In the low magnification HAADF-STEM image, no layer around the crystal is seen either. In contrast, such layer is clearly visible in the morphology of the particles in Figures 5.11, 5.12 and 5.13. But whether EELS or EDX show clear evidence of a silica layer or not, $La_{0.25}Sr_{1.75}MnO_{4-\delta}$ could not successfully be reduced to its modulated structure *in situ* in any of the experiments in (diluted) hydrogen, with or without graphene coating.

5.5.3 *In Situ* 3DED of $La_{0.25}Sr_{1.75}MnO_{4-\delta}$ on Graphene Coated Si_3N_4 in Vacuum

When $La_{0.25}Sr_{1.75}MnO_{4-\delta}$ was heated *in situ* in vacuum on a graphene coated chip, first to 550°C and then further to 700°C, the structural transformation due to oxygen vacancy ordering did occur. However, as discussed in section 3.5.2, this also happens without graphene coating. Probably, this is because for the x = 0.25 the transition already occurs at a lower temperature (i.e. 550°C) than for x = 0.5, and the Si reaction is much less strong in vacuum, since all knocked-out Si atoms are efficiently pumped away inside the microscope column. Note that for the *in situ* gas experiments, the crystals were

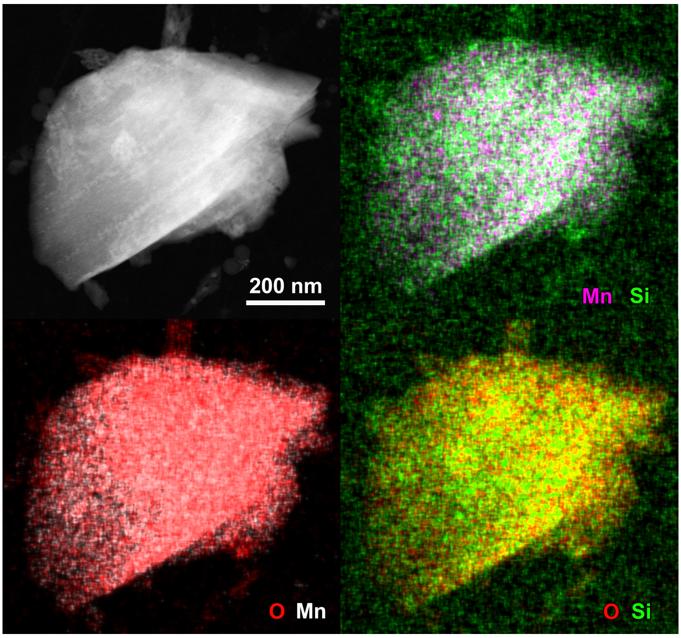

Figure 5.14: HAADF-STEM image and combined EDX maps (in counts) of Si-Mn, Si-O and Mn-O from $La_{0.25}Sr_{1.75}MnO_{4-\delta}$ after *in situ* annealing in N_2 to 550°C and in 5% H_2/Ar to 700°C with the bottom chip of the Nano-Reactor coated by a double graphene layer. The sample was not exposed to any electron beam until after the experiment.

monitored with 3DED at lower temperatures as well and 700°C was only the ending point. This means that chemical reduction is not prevented because of the presence of the highly conductive graphene layer, and it does not interfere with the supply and carrying off of electrons.

5.5.4 Surface Passivation of the Nano-Reactor by Pre-Annealing in Air

Another potential solution instead of coating the Nano-Reactor, is to find a treatment that can make the Si_3N_4 inactive, e.g. a prior oxidation of the surface. We attempted to pre-oxidize the surface of the silicon nitride membrane by heating the bottom chip in air before drop casting the sample. However, very high temperatures are required for this [125] [126], and after heating to 1000°C for 4 hours (the maximum allowed temperature for the DensSolutions Nano-Reactors), the electrode spiral of the *in situ* chip was distroyed, rendering the chip useless for heating experiments.

5.6 Discussion and Conclusion on Preventing Silica Layer Formation *In Situ* by Graphene Coating

As reported in section 5.5, coating the Si_3N_4 DensSolutions Nano-Reactor with graphene did not help to transform $La_{0.25}Sr_{1.75}MnO_{4-\delta}$ *in situ* in hydrogen gas to its reduced, oxygen vacancy ordered structure. In contrast, this was successfully done *ex situ* in hydrogen (see section 3.3.3) and *in situ* in vacuum (see section 3.5.2). After two experiments on graphene coated Si_3N_4 in hydrogen, a clear silica shell was still visible from EDX and/or EELS around the crystals, as shown in Figure 5.11, 5.12 and 5.13. These experiments consisted of 2 or 3 heating cycles: one cycle in N_2 at 550°C, followed by a cycle in 5% H_2/Ar at 700°C, and in one case another cycle in pure hydrogen at 550°C. But the results were ambiguous for the other experiments, suggesting either no or - at least - less reaction with Si. There, only 1 cycle in 5% H_2/Ar was performed, except for the last experiment which also included a prior N_2 cycle. We know, however, that these nitrogen cycles are not the cause of the silica growth, since this also occurred in experiments without prior N_2 heating, as e.g. shown from for $BaFeO_{3-\delta}$ after heating in 5% H_2/Ar (Figure 5.4), or $CaMnO_{3-\delta}$ after heating in 5% H_2/Ar and 10% O_2/Ar (Figure 4.21) or inert gas (Figure 5.2). But the longer total duration at high temperatures might lead to more silica contamination. Most likely, a combination of (at least) two mechanisms causes the SiO_2 growth on the crystals.

First, there is the direct contact reaction between the Si_3N_4 membrane and the manganite particles. Hydrogen annealing of $La_{0.25}Sr_{1.75}MnO_{4-\delta}$ at 700°C on an uncoated Nano-Reactor without any beam exposure (until after the experiment at room in vacuum), showed that this also occurs without the electron beam (see section 5.3 and Figure 5.6). This is very similar to the SiO_2 migration to metal nanoparticles in a 10% H_2/Ar as reported by Wang et al. [80], resulting in a surrounding shell. They do not provide an explanation for the driving force behind their observations. However, in their experiments, the silica was reduced to silicon under the hydrogen atmosphere, which is not what we observe. Possibly, the presence of moisture might play a role for our experiments, or there might be residual O_2 inside the closed cell that is not efficiently removed. But if this was the only active mechanism, graphene coating would have had to be effective in preventing the Si layer growth. Nevertheless, it was observed - by a combination of conventional SAED, 3DED and EDX - that particles lying on the graphene, still did not transform to the modulated structure and (in some cases) still showed the presence of a SiO_2 shell. (In other cases, this silica presence could not be unambiguously confirmed, but still no modulation was observed.)

Thus, there must be also another way Si can be deposited onto the particles. Howitt et al. [119] and Liu et al. [118] showed that silicon can be knocked out from a Si_3N_4 membrane by an electron beam. As discussed in section 5.2, the beam current used for our *in situ* 3DED acquisition is not high enough to directly drill holes into the window, but still some Si atoms can be released by it. However, the Si atoms cannot have been sputtered from the top window, seeing that a double graphene layer on both top and bottom window did not prevent the silica layer growth (see Figure 5.13). Moreover, the hindering of the reduction reaction is not caused by Si being knocked-out by the electron beam from regions that are not covered by graphene and react in a gaseous form with the sample, because for $La_{0.25}Sr_{1.75}MnO_{4-\delta}$ on a graphene coated Nano-Reactor annealed without electron beam exposure, the material did not transform to the modulated structure either.

Since we cannot with 100 % certainty tell from the EDX data (see Figure 5.14) whether there was a silica shell present in that last case because of the Si background and artefact signal, there are two potential explanations for this. In the first case, there is indeed a SiO_2 shell present that stops the oxygen from leaving the sample, and the Si release from the membrane is caused by heating in the gas atmosphere, rather than the electron beam. Then, this is a structural problem in the design of the silicon nitride MEMS devices, but this might be overcome if the entire chip surface can be covered by graphene, not only the central area around the electron transparent windows, in a perfectly homogeneous way. In the second case, there was no silica layer present in this last experiment, because the combination of graphene coating plus decreased electron dose - in this case no electron dose at all - effectively prevented Si from being knocked out or directly reacting with the sample. But in that case, the atmosphere inside the closed cell does not suffice for reduction to happen, perhaps because O_2 is leaking into the gas supply system or cannot be completely removed. Again, the presence of water molecules might interfere. In that case, $La_xSr_{2-x}MnO_{4-\delta}$ - and probably many other systems - cannot be studied at very high temperatures inside the closed gas cell for *in situ* TEM.

Therefore, it remains very important to compare any experimental *in situ* results with *ex situ* tests. For materials that can be reduced at lower temperatures, e.g. for the $(Ca,Sr)(Mn,Fe)O_{3-\delta}$ compounds discussed in the previous chapter, relevant results can still be obtained. In our case, those materials were initially intended to be reduced at higher temperatures (> 800°C) in inert atmospheres, but choosing a harsher atmosphere - i.e. hydrogen gas - allowed to work at lower temperatures. However, this creates severe limitations for the systems that can be studied. In order to remove these restrictions, a potential solution - as an alternative to coating - could be finding a pre-treatment that renders the Si_3N_4 itself inactive, i.e. a type of surface passivation. We already observed that pre-oxidizing the Nano-Reactor by annealing at 1000°C in air distroyed the heating electrodes. But a more practical way to oxidize the surface in advance could be plasma cleaning in an O_2/Ar plasma. However, more experiments are needed to optimize the parameters for this, i.e. duration, gas mixture, power, number of cycles and time before the reduction experiment. If indeed the humidity or residual oxygen inside the Nano-Reactor is the core problem that prevents reduction, perhaps porous materials could be introduced in the gas cell design to absorb these in an efficient way. Or the tubings could be made wider to enable higher gas flow rates through the system, to flush residual molecules away more easily. In any case, more research into the design of the closed-cell *in situ* set-up is required to make it a generally applicable technique that can be safely compared with real operando conditions.

Chapter 6

General Conclusions

The main focus of this thesis was on the use of *in situ* 3DED to study changes in oxygen vacancy ordering upon reduction of two types of perovskite-based energy materials.

As a first group of materials, we studied the Ruddlesden-Popper n = 1 series $La_xSr_{2-x}MnO_{4-\delta}$ for x = 0, 0.25, 0.5, 0.75 and 1. Those symmetric SOFC electrodes materials have of the same pristine structure (I4/mmm) but differ in conducting behaviour in redox conditions. *Ex situ* 3DED discovered the transformation of $La_{0.25}Sr_{1.75}MnO_{4-\delta}$ and $La_{0.5}Sr_{1.5}MnO_{4-\delta}$ to a 2D and 1D incommensurately modulated structure after annealing in hydrogen gas at 700°C, which was never reported before. For x = 0.25, the structure was dynamically refined based on precession 3DED data. The lower amount of ordering in the $La_{0.5}Sr_{1.5}MnO_{4-\delta}$ crystals versus $La_{0.25}Sr_{1.75}MnO_{4-\delta}$ can be related to the higher conductivity of the x = 0.5 compound in reducing conditions. For $La_{0.25}Sr_{1.75}MnO_{4-\delta}$, the transformation to the modulated structure was also seen *in situ* upon heating in vacuum to 550°C. However, it was not possible to reduce the samples *in situ* in hydrogen gas, because of the formation of a SiO_2 shell around the particles, due to a reaction with the Si_3N_4 heating support. In pristine $La_{0.5}Sr_{1.5}MnO_{4-\delta}$, high-resolution HAADF-STEM detected the abundance of RP n=2 layer defects, which are absent in $La_{0.25}Sr_{1.75}MnO_{4-\delta}$. This can also be linked to a conductivity for the x = 0.5 material that breaks the trend of the $La_xSr_{2-x}MnO_{4-\delta}$ series, due to the higher number of perovskite blocks. Moreover, a 2-3 nm lanthanum rich amorphous layer was systematically observed on the surface of $La_{0.5}Sr_{1.5}MnO_{4-\delta}$. *In situ* high-resolution HAADF-STEM and *in situ* 3DED, showed that this layer crystallizes into a perovskite phase upon heating to 700°C in vacuum or hydrogen gas. This is due to the different thermodynamical behaviour at the La rich surface compared to the bulk material.

The second group of materials that were examined, are the $(Ca,Sr)(Mn,Fe)O_{3-\delta}$ compounds for application as oxygen carriers in the CLOU process. They also showed the growth of a silica shell *in situ* in gas at high temperatures, because of which the reduction in inert gases - as in the applications - failed. Nevertheless, at sufficiently low temperatures, different oxygen vacancies ordering configurations could also be observed by *in situ* 3DED in vacuum and hydrogen gas. For $Ca_{0.75}Sr_{0.25}MnO_{3-\delta}$ and $CaFe_{0.2}Mn_{0.8}O_{3-\delta}$, only the disordered I4/mcm and Pm-3m structures were seen as intermediate phases when reduced in vacuum and hydrogen gas. In contrast, undoped $CaMnO_{3-\delta}$ transforms to an ordered Pmma superstructure for $CaMnO_{2.75}$. In the scope of this thesis, this structure could be solved and refined for the first time, based on *in situ* 4D-STEM tomography data at 300°C in vacuum. Those differences in oxygen vacancy ordering can lead to a different degree of oxygen permeability, and thus to oxygen release at lower temperatures for Fe and Sr doped materials compared to $CaMnO_{3-\delta}$. The origin of these different ordering tendencies can be due to the decrease of strain with the incorporation of larger Sr ions, or the disordered arrangement of Fe^{3+} tetrahedra on the one hand and Mn^{3+} square pyramids and Mn^{4+} octahedra on the other hand. However, the reported increased cycling stability upon doping could not be observed in the present *in situ* experiments due to the silica layer interference.

Coating the Si_3N_4 DensSolutions Nano-Reactor with graphene was investigated as a potential solution for the SiO_2 layer growth. This was tested in different graphene layer configurations, and also the influence of the electron beam and the sample composition on the silica growth was studied. However, this did not lead to a successful reduction of $La_{0.25}Sr_{1.75}MnO_{4-\delta}$ *in situ* in hydrogen gas, probably because of a combination of incomplete graphene coverage and humidity and/or residual O_2 inside the closed gas cell. Additionally, platinum coating and pre-oxidation of the heating chips by annealing in air were examined, but did not provide a solution either.

To make *in situ* 3DED a generally applicable technique for studying redox reactions of all types of crystalline oxides, more research is required into the silicon nitride gas heating chips. Improvements for the design could indeed imply graphene coating, but then the coverage should be perfect. Alternatively, a surface passivation treatment could be done, like prior oxidation. But more research is need to decide whether this should be done during the production process or just before the experiment by the user. Because of the high oxidation temperature of silicon nitride and the presence of the heating electrodes, plasma cleaning might be a better option than annealing. Further, efforts should be made to prevent the interference of moisture during the *in situ* reactions, like e.g. the incorporation of porous "water traps". Of course, this is very difficult to achieve when working with hydrogen gas on oxides, but perhaps wider tubes could ensure a better gas flow that efficiently carry all unwanted molecules away. However, even in these less-than-optimal working circumstances, *in situ* and *ex situ* 3DED combined with other electron microscopy techniques already enabled us to obtain some new findings in structural transformation for $La_xSr_{2-x}MnO_{4-\delta}$ and $(Ca,Sr)(Mn,Fe)O_{3-\delta}$. These results are encouraging to optimize *in situ* TEM as a method. Especially since 3DED does not require a high electron dose or double-tilt holder for orienting the sample into crystallographic zones, it can become a very powerful technique to study materials in real operando conditions. But before materials science can profit from all the benefits, thorough design studies must be conducted into the Si_3N_4 MEMS devices to enable reduction of oxides at high temperatures.

Bibliography

[1] Mónica V. Sandoval et al. "In depth study of the RuddlesdenPopper LaxSr2-xMnO4 family as possible electrode materials for symmetrical SOFC". In: *International Journal of Hydrogen Energy* 42 (34 Aug. 2017), pp. 21930–21943. ISSN: 03603199. DOI: `10.1016/j.ijhydene.2017.07.062`.

[2] N. Galinsky et al. "Ca1-xAxMnO3 (A = Sr and Ba) perovskite based oxygen carriers for chemical looping with oxygen uncoupling (CLOU)". In: *Applied Energy* (157 2015), pp. 358–367.

[3] N. Galinsky et al. "CaMn1-xBxO3-d (B = Al, V, Fe, Co, and Ni) perovskite based oxygen carriers for chemical looping with oxygen uncoupling (CLOU)". In: *Applied Energy* (174 2016), pp. 80–87.

[4] Armin Reller et al. "Superstructures Formed by the Ordering of Vacancies in a Selective Oxidation Catalyst: Grossly Defective CaMnO3". In: *Proceedings of the Royal Society A* (1984), pp. 223–241.

[5] Energy Materials. *Energy Materials, About the Journal*. URL: `https://www.oaepublish.com/energymater/about_the_journal`.

[6] Margareth Gagliardi. *Perovskite Solar Cells: Materials, Fabrication, and Global Markets*. URL: `https://blog.bccresearch.com/a-history-of-perovskite-solar-cells`.

[7] E. Katz. "Perovskite: Name Puzzle and German-Russian Odyssey of Discovery". In: *Helvetica Chimica Acta* (103 2020), e2000061.

[8] *Molecule of the Week Archive: Perovskite*. URL: `https://www.acs.org/molecule-of-the-week/archive/p/perovskite.html`.

[9] N. Orlovskaya and N. Browning. *Mixed lonic Electronic Conducting Perovskites for Advanced Energy Systems*. Springer Science + Business Media Dordrecht, 2004.

[10] D. Woodward and I. Reaney. "Electron Diffraction of Tilted Perovskites". In: *Acta Crystallographica B* (61 2005), pp. 387–399.

[11] P. Balachandran and J. Rondinelli. "Interplay of octahedral rotations and breathing distortions in charge ordering perovskite oxides". In: *Physical Review B* (88 2013), p. 054101.

[12] R. Bune et al. "Crystal Structure and Properties of Ru-Stoichiometric LaSrMnRuO6". In: *Chemistry of Materials* (18 2006), pp. 2611–2617.

[13] A. Paul et al. "Lattice Instability and Competing Spin Structures in the Double Perovskite Insulator Sr 2 FeOsO6". In: *Physical Review Letters* (111 2013), p. 167205.

[14] J. Bednorz and K. Muller. "Possible High Tc Superconductivity in the Ba - L a - C u - 0 System". In: *Condensed Matter* (64 1986), pp. 189–193.

[15] M. Pena and J. Fierro. "Chemical Structures and Performance of Perovskite Oxides". In: *Chemical Review* (101 2001), pp. 1981–2018.

[16] T. Ishihara. *Perovskite Oxide for Solid Oxide Fuel Cells*. Springer Science and Business Media, 2009.

[17] H. Kozuka, K. Ohbayashi, and K. Koumoto. "Electronic conduction in La-based perovskite-type oxides". In: *Science and Technology of Advanced Materials* (16 2015), p. 026001.

[18] T. Bak et al. "Electronic and Ionic Conductivity in CaTiO3". In: *Ionics* (10 2004), pp. 334–341.

[19] R. Raghvendra, K. Singh, and P. Singh. "Electrical properties of Ba doped LSGM for electrolyte material of solid oxide fuel cells". In: *AIP Conference Proceedings* (1512 2013), pp. 976–977.

[20] K. Huang, M. Feng, and J. Goodenough. "Electrode Performance Test on Single Ceramic Fuel Cells Using as Electrolyte Sr- and Mg-Doped LaGaO3". In: *Journal of the Electrochemical Society* (144 1997), pp. 3620–3624.

[21] X. Chen, H. Zhou, and H. Wang. "2D/3D Halide Perovskites for Optoelectronic Devices". In: *Frontiers in Chemistry* (9 2021), p. 715157.

[22] M. Azcondo et al. "Novel Perovskite Materials for Thermal Water Splitting at Moderate Temperature". In: *ChemSusChem* (12 2019), pp. 4029–4037.

[23] n.n. *Crystal, Online Dictionary of Crystallography*. URL: `https://dictionary.iucr.org/Crystal`.

[24] T. Welberry and T. Weber. "One hundred years of diffuse scattering". In: *Crystallography Reviews* (22 2016), pp. 2–78.

[25] D. Williams and C. Carter. *Transmission Electron Microscopy*. Springer, 2009.

[26] B. Partoens. *Gevorderde kwantummechanica: Syllabus 2018-2019.*

[27] n.n. *MST: Foundation for Promotion of Material Sicence and Technology of Japan: Electron Diffraction*. URL: `https://www.mst.or.jp/Portals/0/en/en_ed.html`.

[28] M. Gemmi et al. "3D Electron Diffraction: The Nanocrystallography Revolution". In: *ACS Central Science* (5 2019), pp. 1315–1329.

[29] Y. Yun et al. "Three-dimensional electron diffraction as a complementary technique to powder X-ray diffraction for phase identification and structure solution of powders". In: *IUCRj* (2 2015), pp. 267–282.

[30] n.n. *TEM- Transmission Electron Microscopy*. URL: `http://nanofase.eu/show/tem---transmission-electron-microscopy_1454/`.

[31] U. Kolb et al. "Towards automated diffraction tomography". In: *Ultramicroscopy* (107 2007), pp. 507–513.

[32] O. Karakulina et al. "In Situ Electron Diffraction using Liquid-Electrochemical TEM for Monitoring Structural Transformation in Single Crystals Of Cathode Materials for Li-Ion Batteries". In: *Microscopy and Microanalysis* (25 2019), pp. 1946–1947.

[33] Lukas Palatinus. *PETS2 software*. URL: `http://pets.fzu.cz/`.

[34] Ute Kolb. *ADT: Software and useful programs*. URL: `https://www.ak-kolb.chemistry.uni-mainz.de/publications/software/`.

[35] D. Zhan et al. "Collecting 3D electron diffraction data by the rotation method". In: *Zeitschrift fur Kristallografie* (225 2010), pp. 94–102.

[36] Y. Wang et al. "On the quality of the continuous rotation electron diffraction data for accurate atomic structure determination of inorganic compounds". In: *Journal of Applied Crystallography* (51 2018), pp. 1094–1101.

[37] S. Plana-Ruiz et al. "Fast-ADT: A fast and automated electron diffraction tomography setup for structure determination and refinement". In: *Ultramicroscopy* 211 (2020), p. 112951. ISSN: 18792723. DOI: `10.1016/j.ultramic.2020.112951`.

[38] n.n. *DensSolutions Climate Nano-Reactor*. URL: `https://denssolutions.com/products/climate/nano-reactor/`.

[39] M. Hugenschmidt et al. "Low-Dose 4D-STEM Tomography for Beam Sensitive Nanocomposites". In: *ACS Materials Letters* (6 2024), pp. 165–173.

[40] J. Hachtel, A. Lupini, and J. Idrobo. "Exploring the capabilities of monochromated electron energy loss spectroscopy in the infrared regime". In: *Scientific Reports* (8 2018), p. 5637.

[41] n.n. *TEM versus SEM*. URL: `https://www.thermofisher.com/be/en/home/materials-science/learning-center/applications/sem-tem-difference.html`.

[42] n.n. *Huber G670 - Powder Diffraction Camera*. URL: `https://www.xhuber.com/en/products/2-systems/23-x-ray-cameras/g670/`.

[43] A. Le Bail. "Whole powder pattern decomposition methods and applications: A retrospection". In: *Cambridge University Press* 4 (20 2005), pp. 316–326.

[44] V. Petricek. *Profile Functions Used in Jana2006*. URL: `jana.fzu.cz%5Cdoc%5Cpowder%5C_parameters.pdf`.

[45] *Petricek, V. Jana2020 software, http://jana.fzu.cz, version of April 6, 2023.*

[46] T. Runcevski and C. Brown. "The Rietveld Refinement Method: Half of a Century Anniversary". In: *Crystal Growth and Design* (21 2021), pp. 4821–4822.

[47] P.B. Klar et al. "Accurate Structure Models and Absolute Configuration Determination using Dynamical Effects in Continuous-Rotation 3D Electron Diffraction Data". In: *Nature Chemistry* (15 2023), pp. 848–855.

[48] B. H. Toby. *International Table for Crystallography Volume H: Rietveld versus single-crystal refinements*. 2019.

[49] L. Palatinus, V. Petricek, and C.A. Correa. "Structure Refinement Using Precession Electron Diffraction Tomography and Dynamical Diffraction: Theory and Implementation". In: *Acta Crystallographica* (A71 2015), pp. 235–244.

[50] n.n. *PS Special, Power Sources*. URL: `spsources.com%5Cwhy-solid-oxide-fuel-cells`.

[51] Samuel J. Cooper and Nigel P. Brandon. *An Introduction to Solid Oxide Fuel Cell Materials, Technology and Applications*. Elsevier Inc., Jan. 2017. ISBN: 9780128097243. DOI: `10.1016/B978-0-08-101102-7.00001-5`.

[52] S. Hussain and L. Yangping. "Reduction of Sr2MnO4 investigated by high temperature in situ neutron powder diffraction under hydrogen flow". In: *Energy Transitions* (4 2020), pp. 113–126.

[53] Samuel J. Cooper and Nigel P. Brandon. *An Introduction to Solid Oxide Fuel Cell Materials, Technology and Applications*. Jan. 2017. DOI: `10.1016/B978-0-08-101102-7.00001-5`.

[54] S.K. Burnwal, S. Bharadwaj, and P. Kistaiah. "Review on MIEC Cathode Materials for Solid Oxide Fuel Cells". In: *Journal of Molecular and Engineering Materials* 2 (4 2016), p. 1630001.

[55] Y. Teraoka et al. In: *Materials Research Bulletin* (23 1988), pp. 51–58.

[56] Christopher N. Munnings et al. "Structure, stability and electrical properties of the La(2-x)SrxMnO4 solid solution series". In: *Solid State Ionics* 177 (19-25 SPEC. ISS. Oct. 2006), pp. 1849–1853. ISSN: 01672738. DOI: `10.1016/j.ssi.2006.01.009`.

[57] H. Kruidhof et al. "Influence of order disorder transitions on oxygen permeability through selected nonstoichiometric perovskite-type oxides". In: *Solid State Ionics* (63-65 1993), pp. 1816–1822. DOI: `10.1016/0167-2738(93)90202-e`.

[58] L.J. Gillie et al. "Synthesis and characterization of the reduced single-layer manganite Sr2MnO3.5+x". In: *Journal of Solid State Chemistry* 167 (1 2002), pp. 145–151. ISSN: 00224596. DOI: `10.1006/jssc.2002.9636`.

[59] Thibault Broux et al. "Reduction of Sr2MnO4 investigated by high temperature in situ neutron powder diffraction under hydrogen flow". In: *Inorganic Chemistry* 52 (2 Jan. 2013), pp. 1009–1017. ISSN: 00201669. DOI: `10.1021/ic302265f`.

[60] R. Kriegel and A. Feltz. In: *Z. anorg. allg. Chem.* (617 1992), pp. 99–104.

[61] J. Bouloux. In: *Journal of Solid State Chemistry* (38 1981), pp. 34–39.

[62] J.F. Vente, K.V. Kamenev, and D.A. Sokolov. "Structural and magnetic properties of layered Sr7 Mn4 O15". In: *Physical Review, Serie 3. B Condensed Matter* (64 2001), pp. 2144031–21440310.

[63] H. J. Kitchen, I. Saratovsky, and M. A. Hayward. In: *Dalton Transactions* (39 2010), pp. 6098–6105.

[64] D. Senff et al. In: *Physical Review B: Condensed Matter and Materials Physics* (71 2005), pp. 1–8.

[65] P. Reutler et al. "Growth of La1-xSrxMnO4 single crystals and characterization by scattering techniques". In: *Journal of Crystal Growth* (249 2002), pp. 222–229.

[66] G. G. Ceder et al. In: *Modelling Simul. Mater. Sci. Eng.* (8 2000), pp. 311–321.

[67] F. Gonell et al. "Structure Activity Relationship in Manganese Perovskite Oxide Nanocrystals from Molten Salts for Efficient Oxygen Reduction Reaction Electrocatalysis". In: *Chemistry of Materials* (32 2020), pp. 4241–4247. DOI: `10.1021/acs.chemmater.0c00681`.

[68] M. Vatanparast et al. "Bandgap measurement of high refractive index materials by off-axis EELS". In: *Ultramicroscopy* (182 2017), pp. 92–98. DOI: `10.1016/j.ultramic.2017.06.019`.

[69] P. Nellist and S. Pennycook. "The Principles and Interpretation of Annular Dark-Field Z-Contrast Imaging". In: *Advances in Imaging and Electron Physics* (113 2000), pp. 147–203.

[70] T. Janssen et al. In: *International Tables for Crystallography, Vol. C* (9.8.1 2006), pp. 907–913.

[71] A. Yamamoto. In: *Acta Crystallographica* (152 1996), pp. 509–560.

[72] S.A. Nelson. *Twinning, Polymorphism, Polytypism, Pseudomorphism.* URL: `www2.tulane.edu%5Csanelson%5Ceens211%5Ctwinning.htm`.

[73] J. Hadermann et al. "The (3 + 2)D structure of oxygen deficient LaSrCuO3.52". In: *Journal of Materials Chemistry* (17 2007), pp. 2344–2350. DOI: `10.1039/b701449j`.

[74] H. Tan, J. Verbeeck, and G. Van Tendeloo. "Oxidation state and chemical shift investigation in transition metal oxides by EELS". In: *Ultramicroscopy* (116 2012), pp. 24–33.

[75] J. Goff et al. "Defect structure of yttria-stabilized zirconia and its influence on the ionic conductivity at elevated temperatures". In: *Physical Review B* 59 (22 1999), pp. 14202–14219.

[76] A. Tomkiewicz et al. "Oxygen transport pathways in Ruddlesden-Popper structured oxides revealed via in-situ neutron diffraction". In: *Journal of Materials Chemistry A* (3 2015), pp. 21864–21874.

[77] D. Mierwaldt, V. Roddatis, and J. Christian. "Environmental TEM Investigation of Electrochemical Stability of Perovskite and Ruddlesden–Popper Type Manganite Oxygen Evolution Catalysts". In: *Advanced Sustainable Systems* 1 (12 2017), p. 1700109. DOI: `10.1002/adsu.201700109`.

[78] A.N. Grundy, B. Hallstedt, and L.J. Gauckler. "Assessment of the La-Sr-Mn-O System". In: *Computer Coupling of Phase Diagrams and Thermochemistry* (28 2004), pp. 191–201.

[79] Mats Hillert. "The compound energy formalism". In: *Journal of Alloys and Compounds* (320 2001), pp. 161–176.

[80] Lei Wang et al. "Direct Environmental TEM observation of silicon diffusion-induced strong metal-silica interaction for boosting CO2 hydrogenation". In: *Nano Research* 2 (16 2022), pp. 2209–2217. ISSN: 1998-0124. DOI: `10.1007/s12274-022-4991-1`.

[81] L. Fan and F. Li. "Chemical Looping Technology and Its Fossil Energy Conversion Applications". In: *Industrial and Engineering Chemistry Research* (49 2010), pp. 10200–10211.

[82] J. Adanez et al. "Progress in Chemical-Looping Combustion and Reforming technologies". In: *Progress in Energy and Combustion Science* (38 2012), pp. 215–282.

[83] T. Mattisson, A. Lyngfelt, and H. Leion. "Chemical-looping with oxygen uncoupling for combustion of solid fuels". In: *International Journal for Greenhouse Gas Control* (3 2009), pp. 11–19.

[84] M. Arjmand et al. "Prospects of Al2O3 and MgAl2O4 -Supported CuO Oxygen Carriers in Chemical-Looping Combustion (CLC) and Chemical-Looping with Oxygen Uncoupling (CLOU)". In: *Energy and Fuels* (25 2011), pp. 5493–5502.

[85] A. Shulman et al. "Manganese/Iron, Manganese/Nickel, and Manganese/Silicon Oxides Used in Chemical-Looping With Oxygen Uncoupling (CLOU) for Combustion of Methane". In: *Energy and Fuels* (23 2009), pp. 5269–5275.

[86] N Pour et al. "Production and Examination of Oxygen-Carrier Materials Based on Manganese Ores and Ca(OH) 2 in Chemical Looping with Oxygen Uncoupling". In: *American Institute of Chemical Engineers Journal* (60 2013), pp. 645–656.

[87] Magnus Ryden et al. "Combined oxides as oxygen-carrier material for chemical-looping with oxygen uncoupling". In: *Applied Energy* (113 2014), pp. 1924–1932.

[88] H. Taguchi and M. Nagao. “High-Temperature Phase Transition of CaMnO3-d”. In: *Journal of Solid State Chemistry* (78 1989), pp. 312–315.

[89] Kenneth R. Poeppelmeier, M.E. Leonowicz, and J.C. Scanlon. “Structure Determination of CaMnO3 and CaMnO2.5 by X-ray and Neutron Methods”. In: *Journal of Solid State Chemistry* (45 1982), pp. 71–79.

[90] Armin Reller et al. “Three New Ordering Schemes for Oxygen Vacancies in CaMnO3-x Superlattices based on Square-pyramidal Co-ordination of Mn3+”. In: *Journal of the Chemical Society, Chemical Communications* (1982), pp. 1378–1380.

[91] Thor Lichtenthaler. “Ordering of oxygen vacancies in reduced phases of CaMnO3-x and SrMnO3-x.” University of Oslo, Norway, 2005.

[92] C. Chiang and K. Poeppelmeier. “Structural investigation of oxygen-deficient perovskite CaMnO2.75”. In: *Materials Letters* (12 1991), pp. 102–108.

[93] Q. Zhou and B.J. Kennedy. “The nature of the orthorhombic to tetragonal phase transition in Sr1-xCaxMnO3”. In: *Journal of Solid State Chemistry* (179 2006), pp. 3568–3574.

[94] E. Mastronardo et al. “The favourable thermodynamic properties of Fe doped CaMnO3 for thermochemical heat storage”. In: *Journal of Materials Chemistry A* (8 2020), pp. 8503–8517.

[95] J. J. Hadermann et al. “Coupled Cation and Charge Ordering in the CaMn3O6 Tunnel Structure”. In: *Chemistry of Materials* (18 2006), pp. 5530–5536.

[96] B. Bochu et al. “Bond lengths in (Ca Mn3) (Mn4) O12. A new Jahn-Teller distortion of Mn(3+) octahedra”. In: *Solid State Communications* (36 1980), pp. 133–138.

[97] G. Aminoff. “Ueber die Kristallstruktur von Hausmannit (Mn Mn2 O4)”. In: *Zeitschrift fuer Kristallographie* (64 1926), pp. 475–490.

[98] Romy Poppe et al. “Quantitative analysis of diffuse electron scattering in the lithium-ion battery cathode material Li1.2Ni0.13Mn0.54Co0.13O2”. In: *IUCRj* (9 2022), pp. 695–704.

[99] S. F. Dubinin et al. “Ordering of Oxygen Vacancies in a CaMnO3-d Perovskite Single Crystal”. In: *Physics of the Solid State* 47 (7 2005), pp. 1267–1272.

[100] Jaemin Kim et al. “Ca2Mn2O5 as Oxygen-Deficient Perovskite Electrocatalyst for Oxygen Evolution Reaction”. In: *Journal of the American Chemical Society* (136 2014), 14646-14649.

[101] L. Garvie. “Can electron energy-loss spectroscopy (EELS) be used to quantify hydrogen in minerals from the O K edge?” In: *American Mineralogist* (95 2010), pp. 92–97.

[102] A. Mishra and S. Bhattacharjee. “Effect of A- or B-site doping of perovskite calcium manganite on structure, resistivity, and thermoelectric properties”. In: *Journal of the American Ceramic Society* (100 2017), pp. 4945–4953.

[103] J. Hodges et al. “Evolution of oxygen-vacancy ordered crystal structures in the perovskite series Srn Fen O3n-1 (n = 2, 4, 8 and infinity), and the relationship to electronic and magnetic properties”. In: *Journal of Solid State Chemistry* (151 2000), pp. 190–209.

[104] M. Batuk et al. “Topotactic redox cycling in SrFeO2.5+d explored by3D electron diffraction in different gas atmospheres”. In: *Journal of Materials Chemistry A* (11 2023), pp. 213–220.

[105] David Brown. *Accumulated table of bond valence parameters*. URL: `http://www.iucr.org/resources/data/datasets/bond-valence-parameters`.

[106] F. Ramezanipour et al. “Crystal and magnetic structures of the brownmillerite compound Ca2Fe1.039(8)Mn0.962(8)O5”. In: *Journal of Solid State Chemistry* (182 2009), pp. 153–159.

[107] J. Grenier et al. “CARACTERISATION PHYSICO-CHIMIQUE DU FERRITE DE CALCIUM ET DE LANTHANE Ca2LaFe3O8”. In: *Materials Research Bulletin* (12 1977), pp. 79–86.

[108] J. Grenier et al. “MOSSBAUER RESONANCE STUDIES ON THE Ca2Fe205-LaFeO 3 SYSTEM”. In: *Materials Research Bulletin* (17 1982), pp. 55–61.

[109] G. Dienes and G. Vineyard. *Radiation effects in solids*. Interscience Publishers Inc., 1957.

[110] U. Aschauer, R. Prefenninger, and S. Selbach. “Strain-controlled oxygen vacancy formation and ordering in CaMnO3”. In: *Physical Review B* (88 2013), p. 054111.

[111] D. Srivastava et al. “Crystal structure and thermoelectric properties of Sr–Mo substituted CaMnO3: a combined experimental and computational study”. In: *Journal of Materials Chemistry C* (3 2015), p. 12245.

[112] B. Bulfin et al. “Redox chemistry of CaMnO3 and Ca0:8Sr0:2MnO3 oxygen storage perovskites”. In: *Journal of Materials Chemistry A* (5 2017), pp. 7912–7919.

[113] K. Vidyasagar et al. “Novel Oxygen Vacancy-ordered Phases of Ca2Fen-,Mnx05 prepared by the Topotactic Reduction of the Perovskite Oxides, Ca3Fe3-xMnxO9-y (0 < y< 1.5)”. In: *Journal of the Chemical Society, Chemical Communications* (5 1986), pp. 7912–7919.

[114] Thomas Parsons et al. “Synthesis and Structural Characterization of La1-xAxMnO2.5 (A=Ba, Sr, Ca) Phases: Mapping the Variants of the Brownmillerite Structure”. In: *Chemistry of Materials* (21 2009), pp. 5527–5538.

[115] Microscopy Australia. *Energy Dispersive Spectroscopy - EDS spectra artefacts*. URL: `https://myscope.training/EDS_EDS_spectral_artefacts`.

[116] T. Herbell, A. Eckel, and D. Hull. “Effect of Hydrogen on the Strength and Microstructure of Selected Ceramics”. In: *NASA Technical Memorandum* (1990), p. 103674.

[117] W. Lee et al. “Environmental reliability and moisture barrier properties of silicon nitride and silicon oxide films using roll-to-roll plasma enhanced chemical vapor deposition”. In: *Thin Solid Films* (720 2021), p. 138524.

[118] B. Liu et al. “Electron beam radiation induced degradation of silicon nitride and its impact to semiconductor failure analysis by TEM”. In: *American Institute of Physics Advances* (8 2018), p. 115327.

[119] D. Howitt et al. “The electron beam hole drilling of silicon nitride thin films”. In: *Journal of Applied Physics* (103 2008), p. 024310.

[120] C. Li et al. “Electron beam injection from a hollow cathode plasma into a downstream reactive environment: Characterization of secondary plasma production and Si3N4 and Si etching”. In: *Journal of Vacuum Science and Technology A* (38 2020), p. 033001.

[121] X. Gao. et al. "Graphene Membranes for Multi-Dimensional Electron Microscopy Imaging: Preparation, Application, and Prospect". In: *Advanced Functional Materials* (32 2022), p. 2202502.

[122] N. Jain et al. "The application o fgraphene as a sample support in transmission electron microscopy". In: *Solid State Communications* (152 2012), pp. 1375–1382.

[123] B. Westenfelder et al. "Transformations of Carbon Adsorbates on Graphene Substrate". In: *Nano Letters* (11 2011), pp. 5123–5127.

[124] J. Park et al. "Graphene Liquid Cell Electron Microscopy: Progress, Applications, and Perspectives". In: *ACS Nano* (15 2021), pp. 288–308.

[125] S. Meziani et al. "Compositional Analysis of Silicon Oxide/Silicon Nitride Thin Films". In: *Materials Science - Poland* (34 2016), pp. 315–321.

[126] X. Sun, H. Liu, and H. Cheng. "Oxidation behavior of silicon nitride fibers obtained from polycarbosilane fibers via electron beam irradiation curing". In: *Royal Society of Chemistry Advances* (7 2017), p. 47833.

Appendices

Appendix A

List of Author's Contributions

Educational Contributions:

Assistant Fysica 1 for Biology & Biochemistry and Biotechnology 1001WETFYS:
Exercice sessions
Prof. Joke Hadermann
2021-2024

Peer-reviewed Publications:

Vandemeulebroucke D., Batuk M., Hajizadeh A., Wastiaux M., Roussel P. and Hadermann J. (2024) Incommensurate modulations and perovskite growth in $La_xSr_{2-x}MnO_{4-\delta}$ affecting solid oxide fuel cell conductivity. *Chemistry of Materials* 36: 5, 2441-2449. https://doi.org/10.1021/ACS.CHEMMATER.3C03199

Shunsuke S., Souvik G., Cassidy S.J., Dey S., Batuk M., **Vandemeulebroucke D.**, Cibin G., Smith R.I., Holdship P., Grey C.P., Hadermann J. and Clarke S.J. (2023) Anion redox as a means to derive layered manganese oxychalcogenides with exotic intergrowth structures. *Nature Communications* 14 : 1, 1-11. https://doi.org/10.1038/S41467-023-38489-3

Gamon J., Bassat J., Villesuzanne M., Duttine M., Batuk M., **Vandemeulebroucke D.**, Hadermann J., Alassani F., Weill F., Durand E. and Demourgues A. (2023) Impact of anionic ordering on the iron site distribution and valence states in oxyfluoride $Sr_2FeO_{3+x}F_{1-x}$ (x=0.08,0.2) with a layered Perovskite network. *Inorganic Chemistry*, 62 :27, 10822-10832. https://doi.org/10.1021/ACS.INORGCHEM.3C01455

Batuk M., **Vandemeulebroucke D.**, Ceretti M., Werner P. and Hadermann J. (2023) Topotactic redox cycling in $SrFeO_{2.5+\delta}$ explored by 3D electron diffraction in different gas atmospheres. *Journal of Materials Chemistry A*, 11 :1, 213-220. https://doi.org/10.1039/D2TA03247C

Poppe R., **Vandemeulebroucke D.**, Neder R. B. and Hadermann J. (2022) Quantitative analysis of diffuse electron scattering in the lithium-ion battery cathode material $Li_{1.2}Ni_{0.13}Mn_{0.54}Co_{0.13}O_2$. *IUCRj*, 9 :5 (2022) , p. 695-704. https://doi.org/10.1107/S2052252522007746

Oral Presentations:

In Situ 3DED and other TEM Techniques Unravel (Ca,Sr)(Mn,Fe)$O_{3-\delta}$ and $La_xSr_{2-x}MnO_{4-\delta}$ Structure-Property Relations in Redox Conditions
European Microscopy Congress EMC2024
Copenhagen, Denmark, 26/08/2024

(In)commensurate modulations in hydrogen reduced $La_xSr_{2-x}MnO_{4-\delta}$ uncovered by 3D Electron Diffraction
Core-to-Core Project on Mixed-Anion Research: International Conference for Young Researchers
online, 27/09/2023

In Situ High-Temperature Gas and Vacuum 3D Electron Diffraction for Studying Structural Transformations upon Redox Reactions
European Materials Research Society (EMRS) Spring Meeting 2023
Strasbourg, France, 30/06/2023

In Situ and *Ex Situ* 3D Electron Diffraction Investigations of Perovskite-Based Energy Materials in Redox Conditions
EMAT Friday Lecture
Antwerp, 23/06/2023

Ex Situ and *In Situ* Electron Microscopy to Study Anion Ordering in $Sr_2FeO_{3+x}F_{1-x}$, $La_{0.5}Sr_{1.5}MnO_{4-\delta}$ and $CaMnO_{3-\delta}$
Core-to-Core Project on Mixed-Anion Research: Seminar for Young Researchers
online, 31/01/2023

In Situ and *Ex Situ* 3D Electron Diffraction to Study Gas Reduction of $La_xSr_{2-x}MnO_{4-\delta}$
In Situ/Operando Workshop, Canadian Centre for Electron Microscopy (CCEM)
online, 31/03/2022

Kan een QR-code het klimaat helpen redden? (Popular science talk on *In Situ* 3D Electron Diffraction for Studying Redox Reactions)
Press and Speak Science Communication Competition University of Antwerp
Antwerp, 25/02/2022

Investigating Structure Transformations of $La_xSr_{2-x}MnO_{4-\delta}$ using *In Situ* 3D Electron Diffraction in a Gas Environment
EMAT Friday Lecture
Antwerp, 15/10/2021

Poster Presentations:

3D Electron Diffraction Revealing (In)commensurate Modulations and Perovskite Growth in La$_x$Sr$_{2-x}$MnO$_{4-\delta}$ upon Reduction
NANOlab Day
Antwerp, 18/09/2023

In Situ and *Ex Situ* Electron Diffraction Revealing Diverse Structural Transformations of La$_x$Sr$_{2-x}$MnO$_{4-\delta}$ upon Gas Reduction
European Crystallographic Meeting ECM33
Versailles, France, 24/08/2022

Investigating Structure Transformations of La$_x$Sr$_{2-x}$MnO$_{4-\delta}$ using *In Situ* 3D Electron Diffraction in a Gas Environment
International Union of Crystallography (IUCR) Conference
Prague, Czech Republic, 14/08/2021

Scientific Workshop Participations:

18th International Summer School on Crystal Growth
Associazione italiana di cristallographia
Parma, Italy, 24/07/2023-28/07/2023

Electron Crystallography School (ECS)
IUCR, Ensi Caen, Sig4
Caen, France, 29/08/2022-01/09/2022

ESTEEM3 Workshop: ED for solving engineering problems
TEM Gemini Centre, NTNU
Trondheim, Norway, 21/06/2022-23/06/2022

Informatica 1: programmeren in Python
UA, Toegepaste Ingenieurswetenschappen, Prof. Marc Ceulemans
26/09/2021 - 31/01/2022

School on Electron Crystallography
25th IUCR
Prague, Czech Republic, 11/08/2021-14/08/2021

42nd Ad Hoc Jana2020 Workshop - Advanced Topics
Michal Dusek and Vaclav Petricek
online, 27/05/21-02/06/2021

An Introductory Course to 3DED
Royal Society of Chemistry - Interest Group of Porous Materials
online, 12/04/2021-15/04/2021

Basic Workshop Jana2020 and Pets
Lukas Palatinus, Michal Dusek and Vaclav Petricek
online, 24 hours of lectures from 7/12/2020 until 15/01/2021

Appendix B

Acknowledgements

First, I would like to thank my promotor **Prof. Dr. Joke Hadermann** for her scientific guidance. You followed the research process very closely, and were always available for prompt and thorough scientific feedback. Thank you for giving me the opportunity to work on this project.

Further, I thank **Dr. Pascal Roussel** and **Dr. Myriam Wastiaux** for the fruitful collaboration regarding the research on $\mathrm{La}_x\mathrm{Sr}_{2-x}\mathrm{MnO}_{4-\delta}$ and for the synthesis of $\mathrm{La}_{0.25}\mathrm{Sr}_{1.75}\mathrm{MnO}_{4\pm\delta}$ and $\mathrm{La}_{0.5}\mathrm{Sr}_{1.5}\mathrm{MnO}_{4\pm\delta}$.

Many thanks to **Prof. Dr. Michael Hayward** for providing us with the $\mathrm{La}_{0.75}\mathrm{Sr}_{1.25}\mathrm{MnO}_{4\pm\delta}$ and $\mathrm{LaSrMnO}_4$ samples and zirconium for oxygen capture in the reduction process, and to **Dr. Lukáš Palatinus** for helping with many questions regarding PETS2 and dynamical refinements. Also to **Dr. Olesia Karakulina** for providing us with the Excel script for plotting multiple EELS spectra.

My special gratitude goes to all EMAT colleagues who cooperated on and supported this project. **Dr. Maria Batuk** for assisting with high-resolution HAADF-STEM imaging, *in situ* 3DED, the synthesis of $\mathrm{(Ca,Sr)(Fe,Mn)O}_{3-\delta}$ and for teaching me so much about TEM and diffraction techniques. **Amirhossein Hajizadeh** and **Sepideh Rahimi** for all their help in the lab and at the microscope during the *in situ* 3DED experiments. **Matthias Quinteleer** for his help with the microprobe STEM alignment and 4D-STEM acquisition. **Saleh Gholam** for the development of 4D-STEM tomography and frequent assistance with acquisition and processing scripts. **Jenthe Verstraelen** for coating the DensSolutions Nano-Reactors with graphene. **Dr. Romy Poppe** for many discussions on 3DED and the indispensable moral support. **Dr. Saeid Pourbabak** for his help in the lab with both *in situ* and *ex situ* gas annealing experiments. **Dr. Lars Riekehr**, **Dr. Alexander Zintler** and **Dr. Armand Béché** for all their assistance on the microscopes. **Dr. Nicolas Gauquelin** for his help with mono STEM-EELS. **Dr. Tine Derez** and **Dr. Nathalie Claes** for the interesting discussions on the Si contamination during *in situ* experiments.

Financial support is acknowledged from **FWO I003218N**, University of Antwerp **BOF TOP 38689** and the European Commission **NanED Grant number 956099**.

Thanks to **Gert De Bont** for designing the cover.

I especially thank **my parents Jo and Veerle** who gave me the chance to go to the university and the conservatory, and all family and friends who never stopped believing in me. They supported me through all ups and downs of the past four years: **Isabeau and Bavo, Bruno, Nancy and Emma, opa and mammie, Veerle and Dirk, oma Roza, Marie and Vincent, Michael and Didier, Lien and Michaël, Emma, Clara, Sander, Marjolein, Mirte, Diana, Maria, Romy and Ilse**.

And then there is of course **Lucas**, my love and rock for seven years and many more to come. None of this would have been possible without you. Thanks for being there every step of the way, each single day.